



Iron Molybdate Synthesis Using
Dicarboxylate Decomposition Methods
For Methanol Partial Oxidation To
Formaldehyde

Thesis submitted in accordance with requirements of the
University of Cardiff for the qualification of Doctor of
Philosophy

Geoffrey J. F. Pudge

29/09/2017

**NOTICE OF SUBMISSION OF THESIS FORM:
POSTGRADUATE RESEARCH**



**APPENDIX 1:
Specimen layout for Thesis Summary and Declaration/Statements page to be included
in a Thesis**

DECLARATION

This work has not been submitted in substance for any other degree or award at this or any other university or place of learning, nor is being submitted concurrently in candidature for any degree or other award.

Signed (candidate) Date

STATEMENT 1

This thesis is being submitted in partial fulfillment of the requirements for the degree of(insert MCh, MD, MPhil, PhD etc, as appropriate)

Signed (candidate) Date

STATEMENT 2

This thesis is the result of my own independent work/investigation, except where otherwise stated.

Other sources are acknowledged by explicit references. The views expressed are my own.

Signed (candidate) Date

STATEMENT 3

I hereby give consent for my thesis, if accepted, to be available for photocopying and for inter-library loan, and for the title and summary to be made available to outside organisations.

Signed (candidate) Date

STATEMENT 4: PREVIOUSLY APPROVED BAR ON ACCESS

I hereby give consent for my thesis, if accepted, to be available for photocopying and for inter-library loans **after expiry of a bar on access previously approved by the Academic Standards & Quality Committee.**

Signed (candidate) Date

Summary

The formation and subsequent decomposition of iron and molybdenum carboxylate precursors in a molten solvent made of the corresponding carboxylic acid was investigated for the purposes of iron molybdate catalyst production. These catalysts were tested for their ability to partially oxidise methanol to formaldehyde using gaseous oxygen.

The use of oxalic acid was tested first and was found to be successful in production of iron molybdate forming highly active catalysts. These samples were found to be highly sensitive to Fe:Mo ratios with the best in terms of formaldehyde yield were 1:2.2 and 1:1.7 due to the superior mixing of iron and molybdenum on the surface and in the bulk content of the catalyst. Other Fe:Mo ratios tested caused non-homogeneous mixing of the iron and molybdenum resulting in lower formaldehyde yields overall. The oxalate method was found to be highly sensitive to water additions into the oxalate mixture with the formation of large quantities of CO_x selective Fe_2O_3 with small water additions, large additions caused a more coprecipitation approach to be observed.

The use of malonic acid was tested and was found to outperform the oxalic acid examples. This was due to superior mixing of the iron and molybdenum causing a highly homogeneous composition. Similar Fe:Mo study found that a range of ratios (1:1.5, 1:1.9, 1:2.2 and 1:3.0) achieved very high formaldehyde yields. A calcination study showed that the malonate method was highly sensitive to changes in calcination conditions with both composition and performance altered dependent on conditions.

Alterations of iron precursor using the malonate method found significant changes in catalyst composition depending on the anion used. Chloride and nitrate were found to be the best achieving very high yields. Acetate, oxalate, sulphate and phosphate were found to produce less homogeneous samples which negatively affected catalytic performance.

Acknowledgements

I would first like to acknowledge my supervisors, Professor Graham Hutchings and Dr Jonathan Bartley for the opportunity to undertake this PhD. Their supervision and guidance has been instrumental to many of the key developments and their advice has enabled me to progress to where I am as a scientist.

To all the people of the Cardiff Catalysis Institute for their help and friendship in the past few years and the experiences with all of them will stay with me forever. A special thank you to Dr Simon Kondrat and Dr Benjamin Yeo whose advice has served me well in the development of new testing strategies and adaptations to get the best out of my work. Dr Keith Bugler for your friendship and dedication to help me in my hours of need. My students who I have had the privilege of mentoring whose incisive questions have allowed me to expand my own knowledge.

To all the support staff who kept everything running smoothly, Steve Morris, Alun Davis, Chris Morgan, Dr Greg Shaw and Dr Michal Perdjon who I cannot thank enough. Dr David Morgan for his mastery of all things XPS which has allowed for some of the bigger breakthroughs I have experienced.

To both my mum and Julie Thomas for spending the time to proof read my chapters, I cannot thank you enough. I hope now you understand a little of what I have been doing.

To my family and friends who have kept me going in the darker times and celebrated with me in the better times. I honestly think I couldn't have done this without their support especially Bethan who has been there by my side.

Abstract

This work studies the use of simple carboxylic diacids for use as solvents for the production of iron molybdate catalyst. These catalysts were tested for the partial oxidation of methanol to formaldehyde via oxidative dehydrogenation. Oxalic acid was used successfully to produce iron molybdate by the formation and subsequent decomposition of iron and molybdenum oxalates producing iron and molybdenum oxides in the oxalate decomposition method. A solid-state reaction between the oxides during calcination produced high yields of iron molybdate. Catalytic analysis of the sample showed high activity compared to a comparison sample produced by coprecipitation method but less selective towards the target product, formaldehyde.

The effect of Fe:Mo ratio was investigated and found that the oxalate decomposition method was highly sensitive to changes in molybdenum content. Two ratios were shown to be best, 1:2.2 and 1:1.7 both of which outperformed the comparison sample. Other Fe:Mo ratios were shown to produce less homogeneous iron and molybdenum distribution causing lower formaldehyde selectivity. Water addition into the oxalate mixtures was also investigated and was found to change the composition of the sample and by extension the catalytic performance with small additions causing greater Fe_2O_3 and lower formaldehyde selectivity. Higher water additions caused greater $\text{Fe}_2(\text{MoO}_4)_3$ content production and formaldehyde yields.

Investigation into the use of malonic acid as a solvent similar to oxalic acid found that the malonic acid method was superior producing far better iron and molybdenum distribution which allowed for far greater formaldehyde yields over a wider temperature range. The malonate decomposition method was found to be far more robust to changes in Fe:Mo content with only the 1:1.7 ratio achieving under 92.6 % formaldehyde yield. This was thought to be due to the superior iron and molybdenum distribution caused by the superior mixing of the malonates precursors prior to calcination compared to the oxalate examples.

The malonate decomposition method was found to be highly sensitive to calcination conditions both temperature and duration causing significant changes in composition and reactivity. High formaldehyde yields (>93 %) were only attained using 500 °C 2 h, 450 °C 4 h and 600 °C 4 h with others presenting evidence of MoO_3 crystallite formation on the surface and sublimation of MoO_3 on the surface lowering overall distribution.

The effect of iron precursor was studied for its effect on iron molybdate catalysts synthesised using the malonate decomposition method. Iron (III) nitrate and iron (III) chloride were found to be the

best presenting the highest distribution of iron and molybdenum which allowed for the highest formaldehyde yields. Iron (II) oxalate was next best but produced higher Fe_2O_3 content on the surface lowering formaldehyde yield substantially. The use of iron (II) sulphate, iron (III) phosphate and iron (III) acetate had an overall negative effect on the catalyst composition and by extension formaldehyde production with all three samples attaining formaldehyde yields under 88 %. This was due to the lack of ligand substitution during the mixing step which prevented homogeneous mixing.

A calcination study undertaken on malonate decomposition method samples synthesised using chloride and oxalate iron precursors found significant differences. The chloride examples were highly sensitive to extended (> 2 h) high temperature (>500 °C) calcinations with morphologies and compositions shown to deteriorate which lead to lower formaldehyde yields. Instead short high temperature or longer low temperature calcinations were favoured possibly to prevent MoO_3 migration and agglomeration producing iron rich areas. The malonate examples produced using iron oxalate were found to perform better with higher temperature calcinations with over 90 % yield using 600 °C calcinations. This could have been due to the positive effects of thermal spreading of MoO_3 and increased rate of solid-state reaction causing lower exposed Fe_2O_3 content.

Contents

Chapter 1 Introduction	1
1.1 Catalysis	1
1.2 Formaldehyde Applications and Production	2
1.3 Individual Metal Oxide Components of MoO₃/Fe₂(MoO₄)₃ Catalysts	9
1.3.1 Iron Oxide.....	9
1.3.2 Molybdenum (VI) Oxide.....	12
1.3.3 Fe ₂ (MoO ₄) ₃	18
1.4 Optimisation and Deactivation of MoO₃/Fe₂(MoO₄)₃	21
1.4.1 MoO ₃ /Fe ₂ (MoO ₄) ₃ Active Site	21
1.4.2 MoO ₃ /Fe ₂ (MoO ₄) ₃ Deactivation Methods	24
1.4.3 Effect of Iron:Molybdenum Ratio	26
1.4.4 Effect of Calcination Temperature	26
1.5 MoO₃/Fe₂(MoO₄)₃ Preparation Methods	28
1.6 Research Objectives	34
1.7 References	35
Chapter 2 Experimental	40
2.1 Introduction	40
2.2 Catalyst Preparation	40
2.3 Catalyst Characterisation	45
2.3.1 Brunauer-Emmett-Teller (BET)	45
2.3.2 X-Ray Photoelectron Spectroscopy (XPS)	47
2.3.3 Raman Spectral Mapping	49
2.3.4 Powder X-Ray Diffraction (XRD)	51
2.3.5 Thermalgravimetric Analysis (TGA).....	54
2.3.6 Scanning Electron Microscopy (SEM)	55

2.4 Gas Phase Reactions	58
2.5 In-situ XRD Reactions	62
2.6 References	63

Chapter 3 The Use of Oxalate Decomposition Method For Iron Molybdate Synthesis 65

3.1 Introduction	65
3.2 Oxalic Acid Used as a Solvent for Iron Molybdate Synthesis.....	71
3.2.1 Introduction.....	71
3.2.2 Characterisation.....	71
3.2.2.1 BET Surface Area and XPS Surface Analysis	71
3.2.2.2 Powder XRD Crystallography	72
3.2.2.3 Raman Spectral Mapping	73
3.2.2.4 SEM and EDX Elemental Mapping.....	74
3.2.3 Methanol Partial Oxidation and Discussion	76
3.3 Effect of Fe:Mo ratio on samples formed using oxalate decomposition method	77
3.3.1 Introduction.....	77
3.3.2 Characterisation.....	77
3.3.2.1 BET Surface Area and XPS Surface Analysis	77
3.3.2.2 Powder XRD Crystallography	78
3.3.2.3 Raman Spectral Mapping	80
3.3.2.4 SEM and EDX Elemental Mapping.....	82
3.2.3 Methanol Partial Oxidation.....	84
3.3.4 Precalcination Study.....	86
3.3.4.1 XPS of Uncalcined Mixtures	86
3.3.4.2 Thermalgravimetric Analysis	87
3.3.5 Discussion.....	90
3.4 Effect of Water Addition into Oxalate Mixtures	92
3.4.1 Introduction.....	92
3.4.2 Characterisation.....	92
3.4.2.1 BET Surface Area and XPS Surface Analysis	92
3.4.2.2 Powder XRD Crystallography	93
3.4.2.3 Raman Spectral Mapping	95
3.4.2.4 SEM and EDX Elemental Mapping.....	97

3.4.3 Methanol Partial Oxidation	99
3.4.4 Precalcination Study	102
3.4.4.1 XPS of Uncalcined Mixtures	102
3.4.4.2 Raman Spectroscopy.....	103
3.4.4.3 Thermogravimetric Analysis	105
3.4.5 Discussion.....	107
3.5 Conclusion	108
3.5 References.....	109

Chapter 4 The Use of Malonate Decomposition Method(MM) for Iron Molybdate Synthesis	112
4.1 Introduction	112
4.2 Malonic Acid Used as a Solvent for Iron Molybdate Synthesis.....	117
4.2.1 Introduction.....	117
4.2.2 Characterisation.....	117
4.2.2.1 BET Surface Area and XPS Surface Analysis	117
4.2.2.2 Powder XRD Crystallography	118
4.2.2.3 Raman Spectral Mapping	119
4.2.2.4 SEM and EDX Elemental Mapping	120
4.2.3 Methanol Partial Oxidation	122
4.2.3 Discussion.....	123
4.3 Effect of Fe:Mo Ratio on Samples Synthesised Using Malonate Decomposition Method	125
4.3.1 Introduction.....	125
4.3.2 Characterisation.....	125
4.3.2.1 BET Surface Area and XPS surface analysis	125
4.3.2.2 Powder XRD Crystallography	126
4.3.2.3 Raman Spectral Mapping	128
4.3.2.4 SEM and EDX Elemental Mapping	129
4.3.3 Methanol Partial Oxidation	132
4.3.4 Precalcination Study	135
3.3.2.1 XPS of Uncalcined Mixtures	135
3.3.2.2 Thermogravimetric Analysis	136
4.3.5 Discussion.....	139

4.4 Effects of Calcination Conditions on Samples Prepared using the Malonate Decomposition Method	140
4.4.1 Introduction.....	140
4.4.2 Characterisation.....	140
4.4.2.1 BET Surface Area and XPS Surface Analysis	140
4.4.2.2 Powder XRD Crystallography	142
4.4.2.3 Raman Spectral Mapping	144
4.4.2.4 SEM and EDX Elemental Mapping	146
4.4.3 Methanol Partial Oxidation	150
4.4.4 Discussion.....	153
4.5 Conclusion	155
4.6 References	156

Chapter 5 Iron Precursor effect on Molten Malonic Acid Method for Iron Molybdate Synthesis **159**

5.1 Introduction	159
5.2 Effect of Different Iron Precursor on Iron Molybdate Synthesis Using Malonate Decomposition Method	161
5.2.1 Characterisation.....	161
5.2.1.1 BET Surface Area and XPS Surface Analysis	161
5.2.1.2 Powder XRD Crystallography	162
5.2.1.3 Raman Spectral Mapping	164
5.2.1.4 SEM and EDX Elemental Mapping	166
5.2.2 Methanol Partial Oxidation	168
5.2.3 Precalcination Study	172
5.2.3.1 XPS of Uncalcined Mixtures	172
5.2.3.2 Thermogravimetric Analysis	174
5.2.4 In-situ Reduction Study.....	176
5.2.5 Discussion.....	178
5.3 Effect of Calcination Conditions on The Malonate Decomposition Method Using Iron (III) Chloride	180
5.3.1 Introduction.....	180
5.3.2 Characterisation.....	180

5.3.2.1 BET Surface Area and XPS Surface Analysis	180
5.3.2.2 Powder XRD Crystallography	181
5.3.2.3 Raman Spectral Mapping	184
5.3.2.4 SEM and EDX Elemental Mapping	186
5.3.3 Methanol Partial Oxidation	189
5.3.4 Discussion.....	192
5.4 The Effects of Calcination Conditions on The Malonate Decomposition Method Using Iron (II) Oxalate	193
5.4.1 Introduction.....	193
5.4.2 Characterisation.....	193
5.4.2.1 BET Surface Area and XPS Surface Analysis	193
5.4.2.2 Powder XRD Crystallography	194
5.4.2.3 Raman Spectral Mapping	197
5.4.2.4 SEM and EDX Elemental Mapping	199
5.4.3 Methanol Partial Oxidation	202
5.4.4 Discussion.....	205
5.5 Conclusion	206
5.6 References	207
Chapter 6 Conclusion and Future Work.....	210
6.1 Conclusions	210
6.2 Future Work	212
6.3 References	213

Chapter 1

Introduction to Formaldehyde Synthesis from Methanol over $\text{MoO}_3/\text{Fe}_2(\text{MoO}_4)_3$

1.1 Catalysis

The word “catalyst” is defined as “A substance that increases the rate of a chemical reaction without itself undergoing any permanent chemical change”,¹ the act of catalysis means to increase the rate of a chemical reaction by another substance which itself is not consumed in the process.

In order for molecules to react, a minimum activation energy (E_a) must be reached, typically this is the energy required to facilitate a transition state transformation which then leads to the formation of products. The addition of a catalyst allows for a lower energy reaction pathway which causes a greater number of molecules to contain free energy higher than that of the activation energy causing an increase in reaction rate in milder conditions as shown in Fig. 1.1.

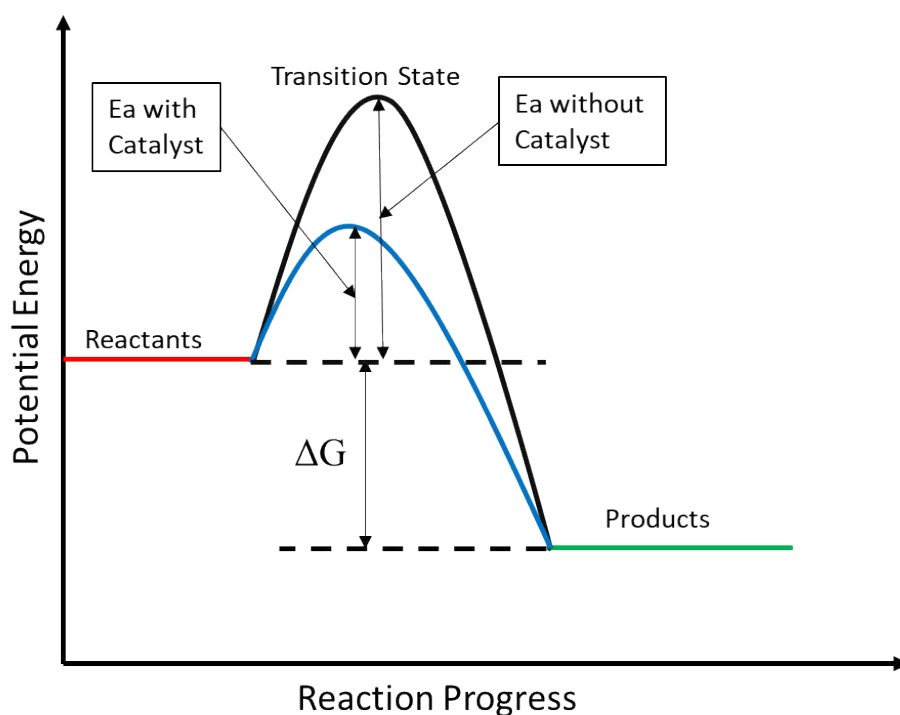


Figure 1.1 Basic illustration of the effect of catalysis and its effects on the activation energy (E_a).

Catalysis is classified in two different ways, homogeneous and heterogeneous.

Homogeneous catalysis features a catalyst and the substrate in the same phase typically in solution based systems where the catalyst and the reactants are both dissolved. Many homogeneous catalyst approaches are highly selective and require relatively low temperatures (<200 °C) to reach high conversions due to great contact with the reactants. The main issues with homogeneous catalysts is separation due to the same phase nature of the catalyst and reactants, this often means distillations and costly separation techniques need to be employed to remove the catalyst which may be lost in the process.²

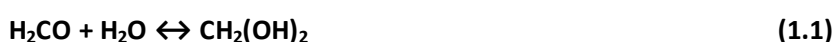
Heterogeneous catalysis typically consists of a solid catalyst with the reactants in either a liquid or gas phase.³ The reactants adsorb to the surface of the catalysts binding to the active site or sites of the catalyst where the reaction occurs, subsequent desorption of the products then facilitates the regeneration of the active site.^{4,5} High conversions are typically achieved at either higher temperature or pressures compared to homogeneous catalysts due to the lower concentration of active sites exposed as part of the active surface. The main benefits of heterogeneous catalytic approaches is ease of separation and reuse and stability which is why most of the industrial catalytic processes are conducted using a heterogeneous approach.⁶

1.2 Formaldehyde Applications and Production

1.2.1 Formaldehyde Characteristics and Applications

Formaldehyde is the simplest of the aldehydes with a chemical formula of H₂CO, in its monomeric form it is a colourless gas at room temperature (b.p. -19.3 °C) with a highly pungent and distinct aroma.⁷ It was first discovered by Hoffman in 1867 after being inadvertently synthesised by Burlerov 10 years previously.

It is not typically observed in its monomeric form instead it tends to polymerise forming compounds such as paraformaldehyde (HO(CH₂O)_nH) where n is between 8-100⁸:





The uses of formaldehyde were initially disinfection and as a preservative in the form of formalin solution with water. It was not until the invention of Bakelite by L. Baekeland^{9,10} that its more commercial applications were utilised. Bakelite comprised of the polymeric resin of phenol-formaldehyde (PF) heated under pressure which produced the first commercial synthetic plastic and a much sought-after replacement for shellac at the time.

Modern uses for formaldehyde are shown in Fig. 1.2 with 44.6 % used in the production urea-formaldehyde (UF) resins. These resins which are used in the production of a variety of wood based products as a binder agent for processed wood such as medium density fibre board (MDF) and parcel board. PF, polyacetal resin, melamine formaldehyde (MF) and diphenylmethane diisocyanate (MDI) also make up a large part of the formaldehyde market share.

Along with resin formation formaldehyde has numerous uses in the bulk and fine chemical sectors as a base feedstock for many chemical processes such as the formation of 1,4 butanediol and pentaerythritol.

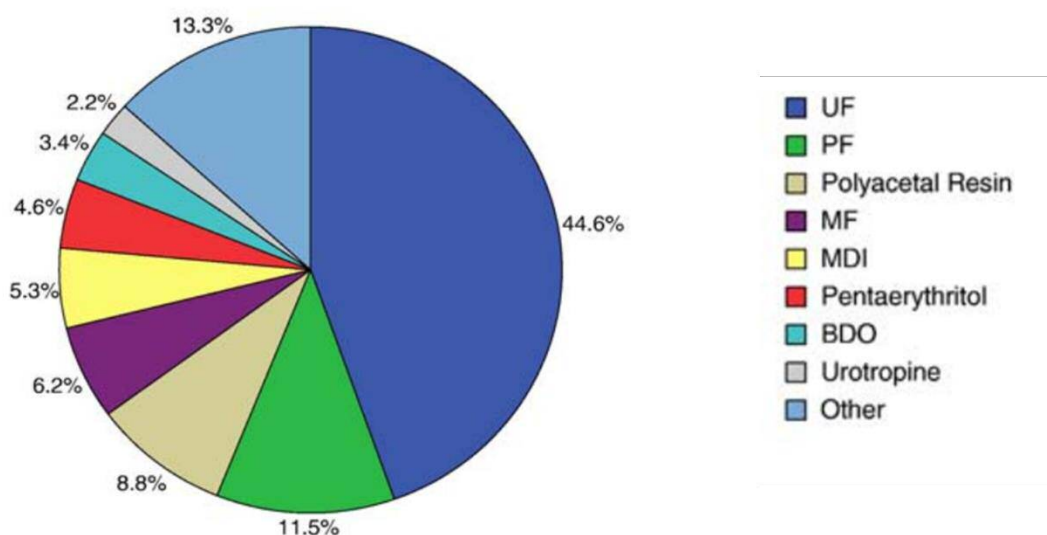


Figure 1.2 Global formaldehyde product distribution. Abbreviations: BDO: 1, 4-butanediol; MDI: Diphenylmethane diisocyanate; MF: Melamine formaldehyde resin; PF: Phenol-formaldehyde resin; UF Urea-formaldehyde resin.¹¹

The projected growth of formaldehyde as measured in formalin (37%) is shown in Fig. 1.3 and it is predicted to see an increase in demand year on year due to the ever-increasing

need for affordable building supplies and consumer products. Steady growth is also expected in the wood market, corresponding to the formaldehyde based resin markets for use in wood composite materials. A sharper increase in the bulk chemical demand is also suggested due to the importance of formaldehyde as a base feedstock for many industrial processes.

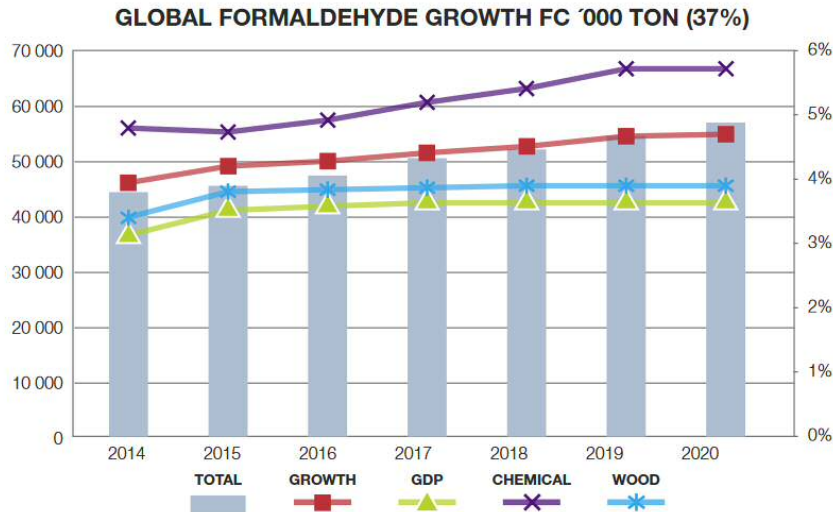


Figure 1.3 Formaldehyde market growth forecast¹²

Formaldehyde production from the partial oxidation of methanol was commercialised using a process where a methanol and water vapour mixture with air was passed over a copper gauze.¹³ Copper was later replaced with silver to increase overall formaldehyde yields.¹⁴ In 1931 Adkins and Peterson proposed the use of a mixed metal oxide of iron and molybdenum using a dilute methanol air mixture to produce high yields of formaldehyde.¹⁵

Modern formaldehyde production is dictated by the cost of methanol which accounts for 94 % of the cost of the process, with catalyst and energy requirements representing 2 % and 4 % respectively.¹⁶ The necessity to keep the costs of both catalyst and energy requirements low have meant constant development of both process and catalyst design are vital.

1.2.2. Thermodynamics of Formaldehyde Production from Methanol

The production of formaldehyde from methanol is undertaken using two different methods, dehydrogenation conducted over supported silver catalysts and oxidative dehydrogenation (ODH) over mixed metal oxides. The conditions used for each process is typically a methanol rich air-lean gas mixture using high temperatures (~600 °C) and a methanol lean (<13 %) air rich mixture between 250-400 °C respectively.

The main reactions considered with the production of formaldehyde are dehydrogenation (1.3 and 1.4), ODH (1.5) and combustion (1.6 and 1.7).¹⁷



Combustion reactions are more thermodynamically favoured for both reactions so temperature controls are chosen to limit these reactions. ODH is also favoured as an exothermic reaction although not nearly as exothermic as combustion pathways.

Dehydrogenation is endothermic which explains the higher average temperatures to force the reaction towards completion, typically higher methanol partial pressures and lower oxygen conditions are employed to facilitate the reactions the dehydrogenation reaction over silver based catalysts.¹⁸

1.2.3. Industrial Production of Formaldehyde Using Mixed Metal Oxides

The industrial production of formaldehyde using mixed metal oxides is currently conducted using the Formox™ process. It utilises the CAP™ 3.0(T) catalysts which uses an iron vanadium or iron vanadium molybdenum mixed oxide spinel structures depending on specifications required.^{16,19,20} This catalyst allows for the process to utilise a higher methanol loading (11 % MeOH feed) than previously used by mixed metal oxide catalysts without sacrificing performance.²¹ $\text{MoO}_3/\text{Fe}_2(\text{MoO}_4)_3$ is still utilised as a catalyst for the partial oxidation reaction with plants not able to utilise the CAP™ 3.0(T) catalysts.

Fig. 1.4 displays a simplified schematic of the Formox™ process, reaction gas mixture is made from the pressurised air mixed with process gas from the absorber to make the correct $\text{O}_2:\text{N}_2$ mixture prior to entering the vaporizer. Methanol is added to the vaporizer to make a gas mixture of 11:11:78 molar % of $\text{MeOH}:\text{O}_2:\text{N}_2$ although lower methanol content can be used to maintain higher catalyst life times.

Flow from the vaporizer is passed through into the multi-tubular reactor, each tube contains layers of pelletised catalyst, inert packing material and ceramic rings in alternate layers to maintain heat distribution over the catalyst beds. Mixtures of inert packing material and catalyst are used in some layers to prevent high concentrations of “hot spots” if catalyst only layers are employed due to the exothermic nature of the reaction.

Temperature is controlled by high temperature fluid (HTF) oil (biphenyl and diphenyl oxide) which enters the reactor at its boiling point, the evaporation of this causes contact areas to cool controlling the temperature. The temperature is monitored using thermocouple placed at various locations along the reactor, control of the temperature is maintained by altering the pressure of HTF. The evaporated HTF is transferred into a condenser which is fed with boiler fed water (BFW) which captures the energy formed by the condensation of the HTF forming steam in the process which can be utilised elsewhere. The condensed HTF is then pumped back into the reactor to be reutilised.

The reactor outlets flow over the vaporizer heating the methanol, this utilises waste energy cooling reactant gases in the process. This flow is directed into the absorber where process water is added to make the required concentration of formalin which can be as high as 55 % wt.

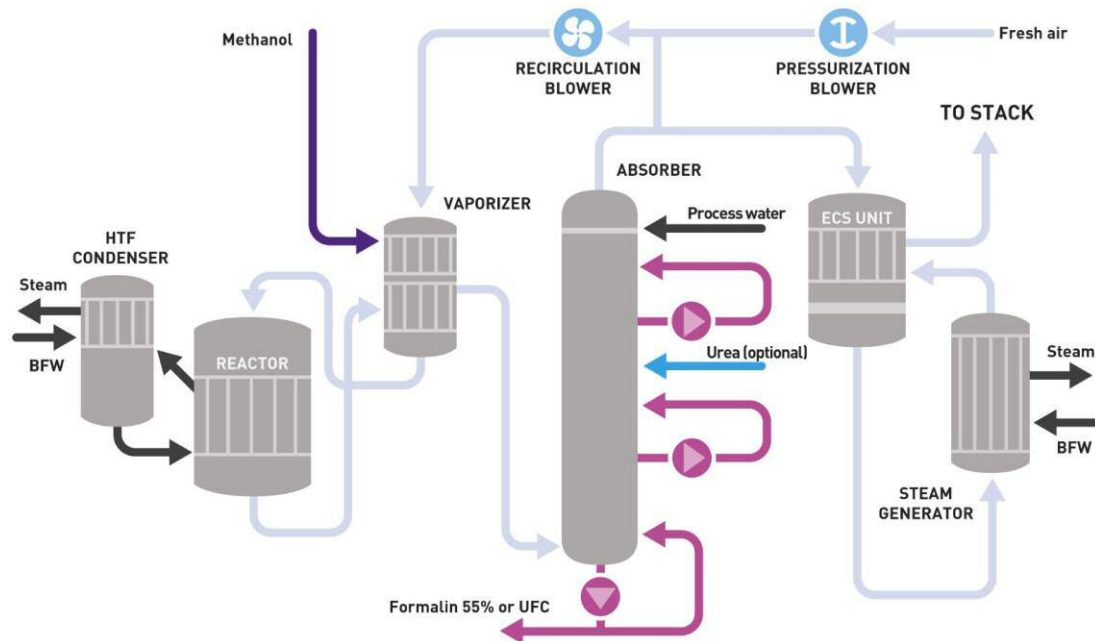


Figure 1.4 Simplified schematic of the Formox™ process for the industrial production of formalin solution or direct urea formaldehyde concentrate (UFC) from methanol.²²

The remaining gas mixture from the absorber is split with some going back into the recirculation blower. The rest is treated using a Pt catalyst to remove CO and volatile organic compounds within the environmental control system (ECS). Residual energy of the waste gases is recaptured in the steam generator which forms steam for use elsewhere.

Direct urea formaldehyde concentrate (UFC) production can be facilitated via the input of urea into the absorber forming UFC rather than formalin.²³

1.2.4. Production of Formaldehyde via Alternative Production Methods

The industrial production of formaldehyde has been shared between mixed metal oxide catalysts and supported silver systems.^{24,25} Until recently the production of formaldehyde was split equally between silver based systems and mixed metal oxides, although recently the silver system has been less utilised.

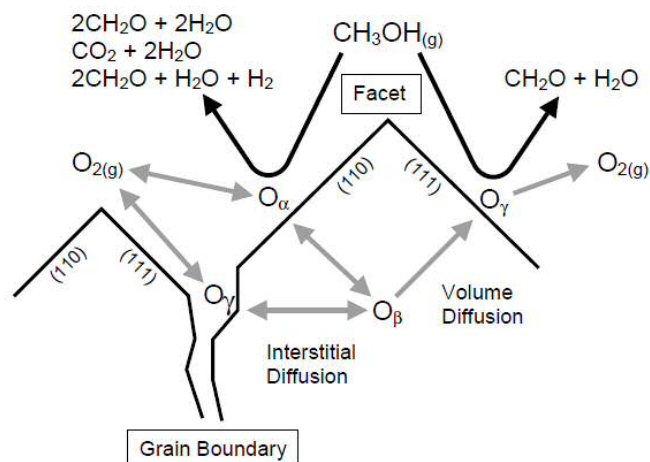


Figure 1.5 Reaction scheme showing the formation of the O_α , O_β and O_γ species from gas-phase O_2 at $650\text{ }^\circ\text{C}$, and the initial product distributions obtained during methanol oxidation on the O_α and O_γ sites.²⁶

The formaldehyde formation over silver surfaces occurs via either dehydrogenation or oxidative dehydrogenation depending on the oxygen species that the methanol encounter at the surface as shown in Fig. 1.5. The three different oxygen species have been investigated by Waterhouse *et al.*²⁷ are O_α , O_γ and O_β , they are formed by the dissociative adsorption of O_2 forming either a weakly or strongly chemisorbed surface atomic oxygen species as O_α and O_γ , respectively. O_γ is preferentially formed on the (111) like planes of the silver whereas O_α is formed on (110) planes. Neither of these species are thermally stable at operating conditions at $650\text{ }^\circ\text{C}$ and can desorb forming gaseous O_2 or diffuse into the catalyst subsurface forming O_β . At reaction conditions, the diffusion occurs in a dynamic equilibrium between the chemisorbed bulk and surface O species and the desorption of molecular O_2 .

Formaldehyde yields attained by the silver based processes are comparable to mixed metal oxide examples achieving between 85-94 % over the life time of the catalyst.²⁸⁻³⁰ The use of silver based systems rely on the high temperatures ($>600\text{ }^\circ\text{C}$) required to maintain high conversion, and methanol rich reaction stream to prevent total oxidation products formation.

Industrially, high conversion is limited using methanol and air only gas mixtures meaning subsequent recapture of unreacted methanol is required. The addition of water into the gas stream (60:40 MeOH:H₂O) in the BASF water ballast process has been utilised to complete conversion in a one pass process.³¹

Due to the high temperatures employed, issues with stabilising the catalyst have always been a challenge when using the silver based catalysts systems, with an average life span of the catalyst ranging from 4-12 months with the formation of CO₂ and formic acid becoming more prevalent over time.^{32,33}

1.3 Individual Metal Oxide Components of MoO₃/ Fe₂(MoO₄)₃ Catalysts

1.3.1. Iron Oxide

1.3.1.1. Structure and Characteristics

Iron (III) oxide exists in 8 distinct structures³⁴ with the α -Fe₂O₃ and Fe₃O₄ described in this section for their reactivity towards methanol.

α -Fe₂O₃ (Hematite) is the most common of the structures and is highly thermally stable, it forms rhombohedral structure as shown in Fig.1.6.a, a space group of R3c and unit cell parameters $a = 5.0385 \text{ \AA}$, $b = 5.0385 \text{ \AA}$ and $c = 13.7400 \text{ \AA}$.³⁵ Each iron atom is octahedrally coordinated to 6 oxygen ligands with the iron atom forming the centre of the octahedra with a combination of corner, edge and face sharing between octahedra.

Fe₃O₄ (Magnetite) has a cubic structure³⁶ with a space group of Fd3m and unit cell parameters of 8.397 \AA . It is comprised of a combination of both Fe³⁺ in octahedral geometry similar to α -Fe₂O₃ and Fe²⁺ in tetrahedral geometry. It is suggested that the Fe²⁺ and Fe³⁺ alternate along the (110) plane.

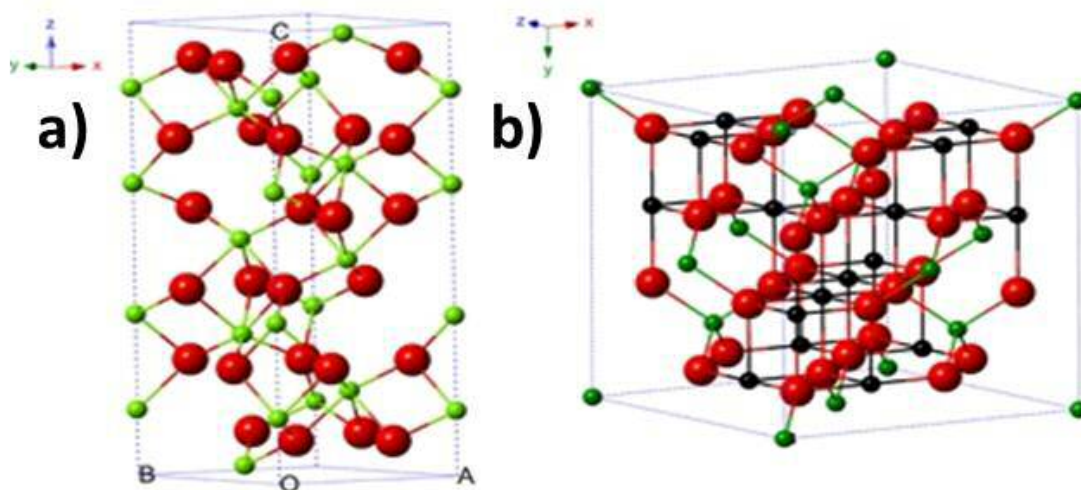


Figure 1.6 Structural representations of rhombohedral $\alpha\text{-Fe}_2\text{O}_3$ (Hematite) and b) cubic Fe_3O_4 (Magnetite).³⁴

1.3.1.2. Methanol Partial Oxidation over Bulk Iron Oxide

Bowker *et al.*¹⁷ describe the use of methanol temperature programmed desorption (TPD) experiments, displayed in Fig. 1.7, that $\alpha\text{-Fe}_2\text{O}_3$ preferentially favours dehydrogenation and combustion of methanol as the dominant products of H_2O , H_2 and CO_2 . Initially adsorption of the methanol forming water observed as a broad peak at 110 °C, this is followed by a broad desorption of hydrogen at 200 °C and a second at 290 °C. The second desorption of hydrogen corresponds with the main carbon product (CO_2) at 290 °C. Supporting pulsed-flow reactions using $\text{O}_2\text{:He}$ 3:4 mixture they found that large amounts of H_2O was produced at the onset of CO_2 and H_2 production at 300 °C suggesting that dehydrogenation and combustion were happening in tandem.

The lack of CO production suggested this mechanism progressed through the formation of a formate (HCOO) species on the acidic surface site, this was proven in a subsequent study by Bowker *et al.*³⁷ using in-situ infrared reflection-absorption spectroscopy (IRAS).

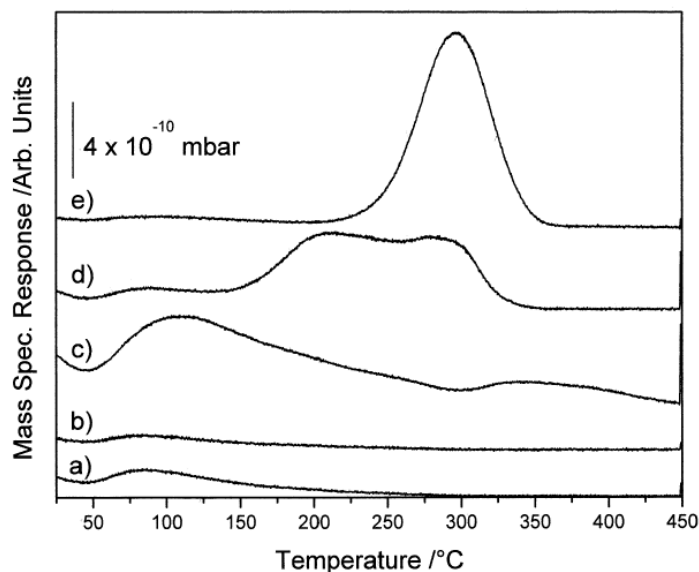
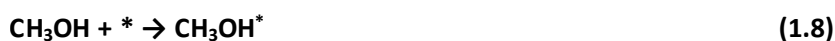


Figure 1.7 TPD from Fe_2O_3 after dosing $36 \mu\text{l}$ of methanol at 25°C . (a) 31 amu (methanol), (b) 30 amu (formaldehyde), (c) 18 amu X 0.5 (water), (d) 2 amu (hydrogen) and (e) 44 amu (carbon dioxide).¹⁷

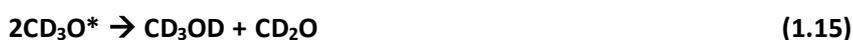
A small number of redox sites on $\alpha\text{-Fe}_2\text{O}_3$ have been shown to favour the production of dimethyl ether (DME) via dehydration of methanol, this proceeded by the mechanism suggested in methanol temperature programmed surface reaction ($\text{CH}_3\text{OH-TPSR}$) spectroscopy results indicated by Routray *et al.*³⁸:



With the “*” representing empty surface site and “X*” representing surface adsorbed species, the adsorption of methanol was observed forming methoxy (CH_3O^*) and hydroxyl (OH^*) groups on the surface of the Fe_2O_3 . Rate determining steps (rds) were determined to be the desorption of methanol off the surface and the cleavage of the $\text{CH}_3\text{-O}$ bond, rapid formation and removal of DME and water was then suggested. Reoxidation of the surface

occurs through the dissociation of gaseous oxygen shown in Equation 1.14 rather than through bulk oxygen migration, this was thought to prevent the formation of formaldehyde.

Production of deuterated formaldehyde on Fe terminated Fe_3O_4 (111) surface from deuterated methanol was reported by Li *et al.*³⁹ using methanol TPD analysis. They found the desorption of both CD_3OD and CD_2O from the surface simultaneously at 357 °C, this suggested the production of formaldehyde through a disproportionation reaction between two deuterated methoxy species by the following mechanism:



1.3.2. Molybdenum (VI) Oxide

1.3.2.1. Structure

Molybdenum (VI) trioxide is the most common form of molybdenum oxide featuring the Mo^{+6} oxidation state. This oxide is traditionally synthesised via the oxidation of molybdenite (MoS_2)^{40–42} as shown in Equation 1.16, this was traditionally undertaken for the production of molybdenum metal via the reduction of the oxide.⁴³



Other than the production of molybdenum metal, MoO_3 has received interest in the electronics industry for use in capacitors⁴⁴ and in high performance battery technology^{45–47}, antibacterial applications have also been investigated.^{48,49}

MoO_3 has two common phases, α - MoO_3 and β - MoO_3 as shown in Fig. 1.8, with α - MoO_3 being the most frequent of the two due to higher thermodynamic stability, β - MoO_3 was found to transform completely to α - MoO_3 when heat treated beyond 350 °C^{50,51}.

The structure of α - MoO_3 has been well established⁵² with an orthorhombic layered crystal structure with a Pbnm space group, the unit cell parameters were observed to be a 3.962 Å, b 13.582 Å and c 3.697 Å.⁵³ The structure comprises of MoO_6 distorted octahedra, these

are bound together in two sublayers with edge-sharing along the c-axis and corner-sharing observed along the a-axis.⁵⁴ Three oxygen positions were observed as shown in Fig. 1.10 with Mo=O (terminal position), Mo₂-O (asymmetrically bridging and corner-sharing) and Mo₃-O (bridging and edge-sharing) coordinations^{54,55}. The individual sublayers were shown to form weak van der Waals forces along the (010) direction between terminal Mo=O of other sublayers forming well organised lamellar like structures shown in Fig. 1.8.^{54,56}

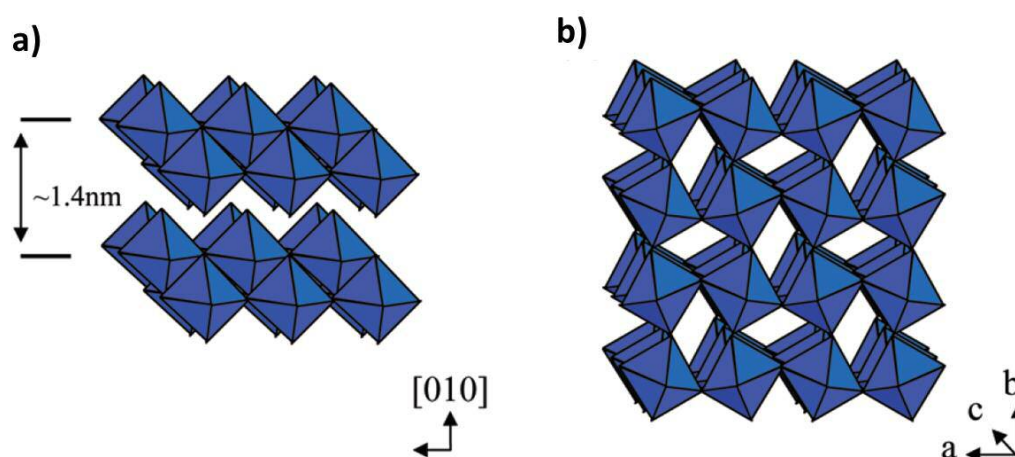


Figure 1.8 The structural representations of a) Thermodynamically stable orthorhombic α -MoO₃ and b) meta stable monoclinic β -MoO₃.⁵¹

The structure of β -MoO₃, also depicted in Fig. 1.8, has a monoclinic structure with the space group $P2_1/c$, unit cell parameters of $a = 7.122 \text{ \AA}$, $b = 5.374 \text{ \AA}$ and $c = 5.565 \text{ \AA}$ were observed.⁵⁷ The structure is comprised of corner-shared MoO₆ octahedra⁵⁰ which prevents the formation of terminal Mo=O and Mo₂O₂ units observed in Raman results of the metastable phase.^{50,58-60} It actually display greater similarity to WO₃ than α -MoO₃.⁵⁷ As a result of the loss of the terminal Mo=O, layered stacking is prevented the stacking of sublayers by weak Van der Waals forces observed in α -MoO₃.^{50,57}

1.3.2.2. Methanol Partial Oxidation Over Bulk MoO₃

A temperature programmed desorption (TPD) study by Farneth *et al.*⁶¹ on MoO₃ suggested the possible mechanism for the partial oxidation of methanol to formaldehyde occurs as

shown in Fig. 1.9. Methanol is adsorbed to the surface of the MoO_3 and much of this was thought to desorb unchanged, some coordinates as molybdenum methoxy species ($\text{Mo}-\text{OCH}_3$) at unsaturated molybdenum site (Mo^{5+}) forming $\text{Mo}-\text{OH}$ neighbouring species. At low temperatures, some H_2O was shown to desorb from the surface suggesting some loss of surface oxygen with increased adsorption of the methoxy species.

The rate determining step of the process was the cleavage of C-H bond forming adsorbed formaldehyde and H_2O which are subsequently desorbed proven by isotopic labelling study undertaken by Machiels and Sleight⁶², this yields a reduced Mo site. These sites were thought to be largely regenerated via a Mars-van Krevelen mechanism^{63,64} where by surface reoxidation was occurring via bulk oxygen migration. A gradual loss of formaldehyde production after subsequent adsorptions without reoxidation suggests a low rate of surface site regeneration from the bulk oxygen alone, this suggests gaseous oxygen to oxidise the reduced surface sites is required to achieve higher conversions.

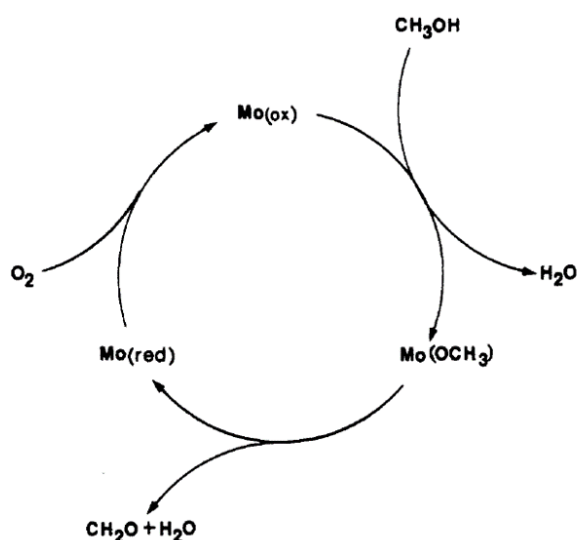


Figure 1.9 Proposed steady state reaction mechanism of methanol partial oxidation over MoO_3 .⁶¹

The active sites of MoO_3 was suggested by Chung *et al.*⁶⁵ and supported by work by Phuc *et al.*⁵⁵ and is highlighted in Fig. 1.10. Dimethyl Ether (DME), dimethoxy methane (DMM) and methyl formate (MF) and direct CO and CO_2 production was thought to require a combination of both terminal $\text{Mo}=\text{O}$ and bridging oxygen vacancies during operation by Chung *et al.*⁶⁵ Formaldehyde and CO production requires the chemisorption of a methoxy species at a terminal oxygen vacancy (Mo^{5+}) with an oxygen provided by a neighbouring terminal $\text{Mo}=\text{O}$ as proposed by Allison and Goddard.^{66,67} This suggests that methanol

partial oxidation is limited to the (010) facets which comprise of terminal Mo=O although initial vacancies were shown to be low in number requiring higher temperatures to initiate the loss of terminal oxygen.^{61,68} The amount of the (010) face has also been shown to be limited on the surface of bulk α -MoO₃ comprising of typically less than 10 %⁶⁹ further inhibiting the activity of α -MoO₃, this is due to the highly limited number of active sites.

Due to the structure of β -MoO₃, it has been suggested by Pham *et al.*⁵⁰ that the formation of oxygen vacancies is far easier due to its symmetric structure, it can be cleaved in any direction by the breaking of Mo-O bonds causing larger amounts of unsaturated molybdenum atoms compared to α . As a result of this, higher activity is expected by the β phase.

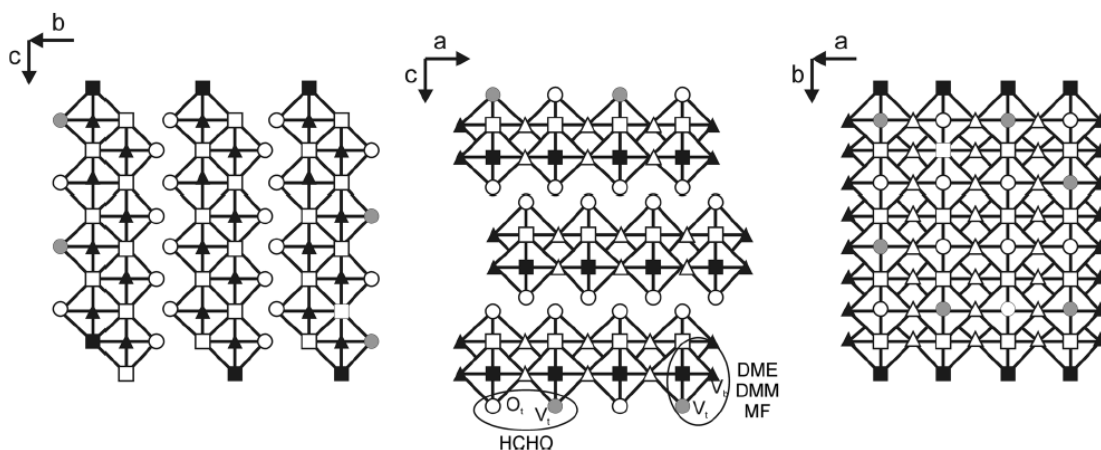


Figure 1.10 Schematic presentation of the MoO₃ structure. The three unequal oxygen atoms in Mo=O, Mo₂-O and Mo₃-O bonds are denoted as open circle, open triangle, open square, respectively. The black symbols are the available oxygen vacancies and the grey ones are the probable oxygen vacancies which are generated during reaction.⁵⁵

The results of methanol partial oxidation over bulk α -MoO₃ and β -MoO₃ are achieved by Pham *et al.*⁵⁰, shown in Fig. 1.11, displayed clear differences between the two phases. Commercial bulk α -MoO₃ displayed very low overall activity not even able to achieve 20 % methanol conversion by 350 °C which is not unsurprising due to the lack of exposed active sites. Whilst β in contrast displayed high activity by 280 °C with high conversions (>90 %) achieved prior to 320 °C. Formaldehyde selectivity was shown to increase with both samples as reaction temperatures were increased with DME selectivity was shown to decrease gradually.

Time on line analysis showed that the β phase rapidly broke down in favour of α formation at temperatures exceeding 320 °C lowering overall activity substantially consistent with

other studies^{58,60}. Further Work by Pham *et al.*⁵⁹ presented the preparation of NO doped β - MoO_3 which increased the activity at lower temperatures while not compromising formaldehyde selectivity. This allowed lower operating conditions (300 °C) perturbing the formation of the α phase maintaining the samples performance over a prolonged period of time (>30 h).

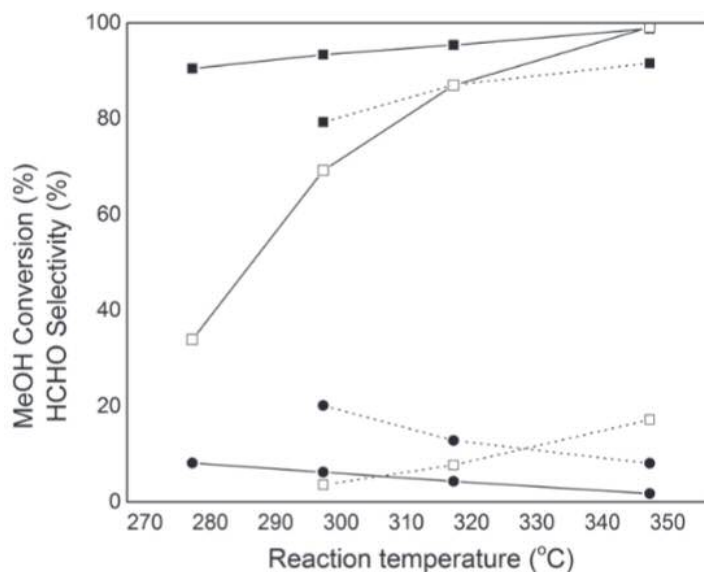


Figure 1.11 Methanol conversion (□) and selectivity of formaldehyde (■) and DME (●) over the as-prepared β - MoO_3 (solid lines) and commercial α - MoO_3 (dot lines).⁵⁰

1.3.2.3. Supported MoO_3

Supports for MoO_3 have been utilised to increase productivity of bulk MoO_3 due to the low number of active sites of the material. A summary of some of these has been compiled and shown in Table 1.1. The use of MgO as a support was found to be detrimental by Kim *et al.*⁷⁰ due to the formation of inactive MgMoO_4 proven by Raman spectroscopy. This limited the activity of the samples by inhibition of reactant access to the Mo^{6+} within the molybdena tetrahedra (MoO_4^{2-}) present within the sample.⁷¹

The silica (SiO_2) supported molybdena presented greater activity compared to MgO supported though not exceeding bulk MoO_3 , although this was tested at greater temperatures which may explain the higher activity observed. The use of 13 % wt molybdena loading by Kim *et al.*⁷⁰ caused a small increase in activity but 100 % selectivity

towards CO_x at the temperature tested. Jehng *et al.*⁷² employed higher oxygen content and lower molybdenum loading which resulted in lower activity and selectivity towards CO_x but mixed selectivity towards formaldehyde, methyl formate and dimethoxy methane with formaldehyde presented as the most dominant product. Changes in surface species has been proposed by Hu *et al.*⁷³ between both Mo₇O₂₄⁶⁻ and Mo₈O₂₆⁴⁻ in Raman results independent to molybdenum loading using hydrated conditions. This is thought to be due to the agglomeration of molybdena forming octahedral polymolybdates over the surface exposing inactive SiO₂ which may have caused the decrease in activity.

TiO₂, ZrO₂, Nb₂O₅ and Al₂O₃ were compared by Hu and Wachs⁷⁴ for the purposes of molybdena supports. Both TiO₂ and ZrO₂ presented with great similarity, high formaldehyde selectivity and activity compared to bulk MoO₃ at significantly lower temperatures unlike SiO₂ and MgO examples. The reasons for this may be due to the tetrahedral MoO₄²⁻ and Mo₇O₂₄⁶⁻ surface species observed in both examples in X-ray adsorption near-edge spectroscopy (XANES) and Raman results.⁷³ At higher molybdenum content octahedral Mo₈O₂₆⁴⁻ was also present in both examples suggesting some evidence of agglomeration, although the more active Mo₇O₂₄⁶⁻ was still the major species. This may have prevented the formation of larger, less active polymeric species similar to those observed by bulk MoO₃.³⁸ Methyl formate selectivity observed by the ZrO₂ example is thought to be due to the support which observed 86 % selectivity at similar conditions.

The Nb₂O₅ supported system by contrast displayed far lower activity compared to both TiO₂ and ZrO₂ examples with higher DME selectivity observed at all MoO₃ loadings. The lower activity was due to the formation of Mo₈O₂₆⁴⁻ even at low loadings on the surface though Mo₇O₂₄⁶⁻, this lack of isolated MoO₄²⁻ has been attributed to the lower activity as more polymeric molybdena is favoured. Higher DME selectivity was caused by the Nb₂O₅ support which showed 100 % selectivity when tested under the same conditions.

The use of Al₂O₃ presented the highest activity of all the supported samples however due to the high Lewis acidity of the Al₂O₃ support. This also resulted in very high DME production which was the dominant product. By increasing molybdena, formaldehyde selectivity was shown to increase although DME was still the dominant product. The molybdena on the surface was shown to be MoO₄²⁻ exclusively at low coverages by Hu *et al.*⁷³ but at higher coverages both Mo₇O₂₄⁶⁻ and Mo₈O₂₆⁴⁻ were present in Raman results suggesting some agglomeration.

All samples upon reaction with methanol saw a reduction in terminal Mo=O, responsible for the selective partial oxidation of methanol to formaldehyde^{55,65}, and were not recovered fully upon reoxidation using O₂/He suggesting that the supports were unable to maintain the molybdena structure on the surface, this effect was less pronounced by the TiO₂ example which presented the highest redox turnover frequency.

Table 1.1 Comparison of supported MoO₃ catalysts for the partial oxidation of methanol.

Sample	Activity (mmol/h g)	Selectivity (%)					Ref
		FA	MF	DME	DMM	CO _x	
33.6 %MoO ₃ /MgO ^a	0	-	-	-	-	-	70
13.0 %MoO ₃ /SiO ₂ ^a	3	0	0	0	0	100	70
1%MoO ₃ /SiO ₂ ^b	2.6	45	28	0	19	8	72
7 %MoO ₃ /TiO ₂ ^c	1082	90	0	6	2	2	74
7 %MoO ₃ /ZrO ₂ ^c	811	83	11	3	1	2	74
6 %MoO ₃ /Nb ₂ O ₅ ^c	351.7	80	0	18	2	0	74
20 %MoO ₃ /Al ₂ O ₃ ^c	2.6x10 ³	21	0	79	0	0	74
MoO ₃ ^d	31.7	65	0	20	15	0	38

Note. FA, MF, DME and DMM represent formaldehyde, methyl formate, dimethyl ether and dimethoxy methane respectively.

^a Reaction conditions: 225 °C, CH₃OH:O₂:N₂ = 3:15:82 (mol%)

^b Reaction conditions: 230 °C, CH₃OH:O₂:He = 4:34:62 (mol%)

^c Reaction conditions: 230 °C, CH₃OH:O₂:He = 6.9:11:82.1 (mol%)

^d Reaction conditions: 300 °C, CH₃OH:O₂:He = 6:13:81 (mol%)

1.3.3 Fe₂(MoO₄)₃

1.3.3.1. Structure and Characteristics

Iron molybdate (Fe₂(MoO₄)₃) was first synthesised for the purposes of methanol partial oxidation by Adkins *et al.*¹⁵ in 1931.

The crystal structure of Fe₂(MoO₄)₃ has been proposed to be monoclinic with a P2₁/a space group, the unit cell parameters were observed to be a = 15.707 Å, b = 9.231 Å and c =

18.204 Å with a β angle of 125.25°. ^{75,76} The unit cell is comprised of 8 unique iron atoms in a near octahedral coordinated by 6 oxygen atoms and 12 distorted tetrahedra of MoO₄ as shown in Fig. 1.12 with each oxygen bound to the FeO₆ octahedra corner-sharing with the MoO₄ tetrahedra.

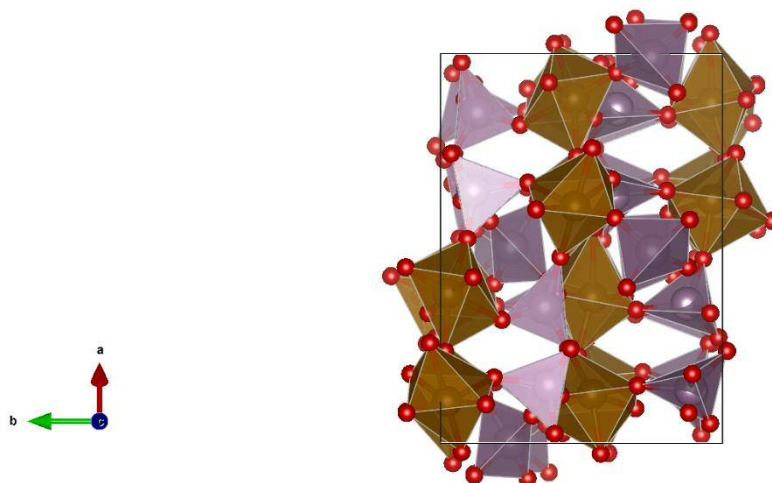


Figure 1.12 Structural representation of monoclinic Fe₂(MoO₄)₃ viewed along the (101) plane.

The non-destructive reversible phase transformation into a β orthorhombic form at 518 °C⁷⁵ with the Pbcn space group, unit cell parameters of $a = 12.8687$ Å, $b = 9.2460$ Å and $c = 9.3336$ Å⁷⁷. Bonding within the lattice was similar with the corner-sharing of oxygen atoms between the molybdenum tetrahedra and iron octahedra observed, the crystal structure of β -Fe₂(MoO₄)₃ closely resemble those observed by scandium tungstate⁷⁸.

1.3.3.2. Methanol Partial Oxidation Over Bulk Fe₂(MoO₄)₃

Partial oxidation of methanol over bulk iron molybdate (Fe:Mo 1:1.5) was shown to be similar to MoO₃ with the formation of the same intermediates by Routary *et al.*³⁸ CH₃OH-TPSR experiments over bulk Fe₂(MoO₄)₃ and MoO₃ yielded high selectivity to formaldehyde (HCHO) at comparable temperatures shown in Fig. 1.13. DME selectivity was greatly reduced for Fe₂(MoO₄)₃ due to the lack of Mo-O-Mo bonding observed by bulk MoO₃ forming the Lewis acidic site required to facilitate the dehydration reaction.^{65,79}

In-situ CH₃OH infra-red spectroscopy investigation by Routary *et al.*³⁸ found both adsorbed methanol and methoxy groups were present on the surface of Fe₂(MoO₄)₃ and MoO₃ at low temperatures consistent with findings by Bowker *et al.*^{37,80} As temperatures were increased surface methanol was shown to decrease at a greater rate compared to surface methoxy species suggesting they were directly oxidatively dehydrogenated to formaldehyde. This was supported by corresponding TPRS results shown in Fig. 1.13 which displayed only a minor desorption of unreacted methanol compared to MoO₃.

An increase in formaldehyde production by bulk Fe₂(MoO₄)₃ was thought to be due to the increase in redox site number determined to be far greater than that of bulk MoO₃ extrapolated from TPRS results.^{81–83} This is thought to be due to the isotropic nature of Fe₂(MoO₄)₃³⁸ which allows for all faces to oxidise methanol to formaldehyde unlike MoO₃.

Carbon oxide production was thought to be produced by the overoxidation of the methoxy group the formation of formate (HCOO) species on the surface by iron single and dual sites respectively elaborated further in Fig. 1.15.³⁷

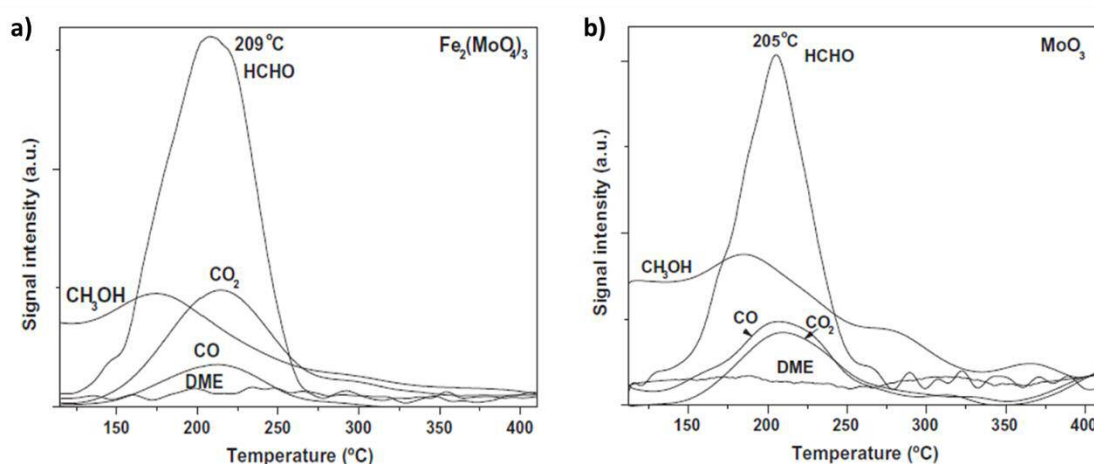


Figure 1.13 MeOH-TPSR spectra over bulk Fe₂(MoO₄)₃ (a) and bulk MoO₃ (b).³⁸

The overall mechanism for the partial oxidation over $\text{Fe}_2(\text{MoO}_4)_3$ as proposed by Routary *et al.*³⁸ proceeds as follows:



The rate determining step was determined to be both the C-H bond cleavage of adsorbed methoxy species similar to MoO_3 described previously but also the direct oxidative dehydrogenation (ODH) of adsorbed methanol.

Surface reoxidation is thought to be occurring from the lattice via a Mars-van Krevelen mechanism^{63,64} much in the same way as MoO_3 , repeated anaerobic reactions without oxidation have however shown that the surface is maintained far better by $\text{Fe}_2(\text{MoO}_4)_3$ compared to bulk MoO_3 producing only gradual change in formaldehyde yield.^{17,38}

1.4 Optimisation and Deactivation of $\text{MoO}_3/\text{Fe}_2(\text{MoO}_4)_3$

1.4.1. $\text{MoO}_3/\text{Fe}_2(\text{MoO}_4)_3$ Active Site

The identity of the active site of $\text{Fe}_2(\text{MoO}_4)_3$ and by extension $\text{MoO}_3/\text{Fe}_2(\text{MoO}_4)_3$ has been under contention in literature. $\text{Fe}_2(\text{MoO}_4)_3$ was thought to be the active phase initially⁸⁴ with Pernicone⁸⁵ suggesting the active phase to be expressed as $\text{Fe}_{2-3x}(\text{Mo}_{1+x}\text{O}_{4+1.5x})_3$ where the maximum value of x is thought to be 0.05.

The other proposed active site is thought to be a molybdenum surface excess, rather than the $\text{Fe}_2(\text{MoO}_4)_3$, due to the surface segregation observed by the iron molybdate systems. Evidence of surface-segregation of molybdenum on the surface of iron molybdate has been

well documented^{38,86–90} with recent microscopy results presenting clear evidence of this shown in Fig. 1.14.

Molybdenum surface enrichment was observed on bulk $\text{Fe}_2(\text{MoO}_4)_3$ containing the stoichiometric Fe:Mo ratio 1:1.5 in surface measurements by multiple authors^{88,91,92} such as those observed in Fig.1.14.a where MoO_3 was indicated to be a 5-10 nm amorphous surface covering, which has been suggested to be the active site⁹³.

This segregation was even observed in molybdenum lean mixtures where low surface coverings were placed over iron oxide^{38,80,87,89}, migration of molybdenum causing the bulk iron dilution forming $\text{Fe}_2(\text{MoO}_4)_3$ leaving an iron enriched surface. This is however not the case, molybdenum is the dominant species on the surface even using molybdenum lean conditions as shown in Fig.1.13.b and corresponding elemental line scans results. Even at very low molybdenum loadings tested by Brookes *et al.*⁸⁰ (0.24 monolayers of Mo on Fe_2O_3), 1:0.14 Fe:Mo surface ratio was observed using XPS surface analysis where the bulk Fe:Mo ratio was 1:0.0017 suggesting surface enrichment.

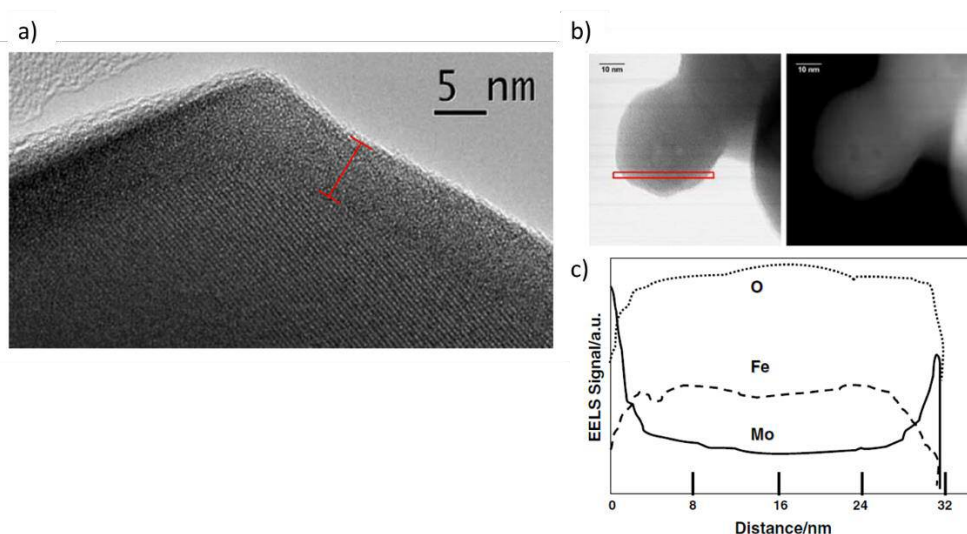


Figure 1.14 (a) HRTEM image of typical $\text{Fe}_2(\text{MoO}_4)_3$ crystal with amorphous surface layer highlighted⁹³, (b) STEM images of an iron molybdate particle in bright and dark field modes and (c) Mo, Fe and O EELS line scan results corresponding to the area highlighted in (b).

Investigation into the selective production of formaldehyde, carbon dioxide and carbon monoxide was suggested to be due to different sites as shown in Fig.1.15 proposed by Bowker *et al.*³⁷ They suggested that the active site responsible for the selective production

of formaldehyde required Mo dual sites, as suggested in prior studies. CO₂ formation, as discussed previously, requires the formation of a formate intermediate over two iron centres. CO formation was suggested to form on the isolated surface site of either molybdenum or iron from methoxy species. From the results shown by Bowker *et al.* it was unclear whether one site or both are responsible for CO production, as studies using either high or low molybdenum loading changes the selectivity towards formaldehyde and CO₂ respectively. It is difficult to isolate conditions for isolated iron or molybdenum sites respectively.

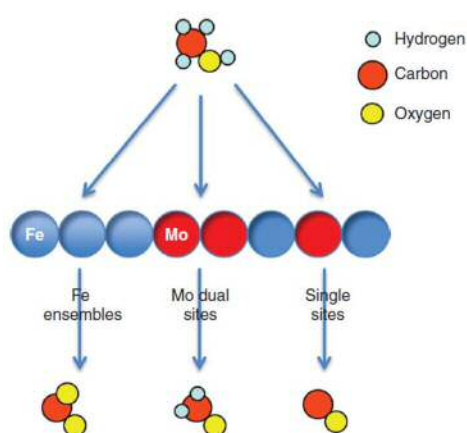


Figure 1.15 Model of the active sites on the Fe-Mo oxide materials displaying the variance of products from different sites.³⁷

The reaction mechanism of methanol partial oxidation over MoO₃/Fe₂(MoO₄)₃ was suggested to occur through an extended Mars-van Krevelen mechanism by Bowker *et al.*⁹⁴ where not just the oxygen from the lattice as it typical with a Mars-van Krevelen mechanism. Oxygen from the bulk Fe₂(MoO₄)₃ is used to regenerate the surface MoO₃ sites. The rate of formaldehyde production from methanol over these catalysts can be determined using equation 1.24 where, r = the rate of reaction, k_{rds} = first order rate constant, K_{ad} = MeOH adsorption equilibrium constant, P_{MeOH} = partial pressure of methanol and N_s = surface density of redox sites.

$$r = k_{rds}K_{ad}P_{MeOH}N_s \quad (1.24)$$

This indicated that methanol partial oxidation was independent of oxygen concentration and readily occurs under anaerobic conditions which was found in a previous study presented by House *et al.*⁹⁵ with partial oxidation occurring beyond surface reduction.

Although regeneration of the catalyst was required to maintain activity and selectivity for longer catalyst lifetimes.⁹⁵

1.4.2. $\text{MoO}_3/\text{Fe}_2(\text{MoO}_4)_3$ Deactivation Method

Many studies^{96–101} have been undertaken to analyse the deactivation of iron molybdate catalysts due to the industrial importance of maintaining catalyst life times to limit cost implications.¹⁶ All studies suggested the deactivation was caused by the sublimation of MoO_3 over time via the formation of volatile molybdena species on the surface such as those observed in Fig. 1.16.

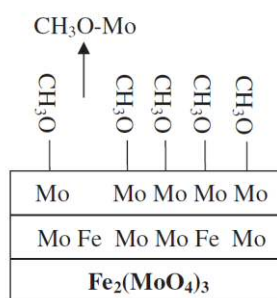


Figure 1.16 Mechanism of molybdenum loss by sublimation off a $\text{Fe}_2(\text{MoO}_4)_3$ surface.³⁸

Ivanov and Dimitrov⁹⁸ presented an industrial study of iron molybdate tested after 15 months following standard methods of operation. Their results showed little change in formaldehyde yield over the time but the composition of the catalyst was altered. Limited change in bulk Fe_2O_3 and MoO_3 content were observed along the first 40 cm of the reactor tube as shown in Fig. 1.17 but the surface saw nearly 10 % loss in MoO_3 content and 5 % increase in Fe_2O_3 at 20 cm depth along the bed. Molybdenum enrichment was then observed along the surface further down the reactor with MoO_3 in the form of needles observed which was also seen by Andersson *et al.*⁹⁷ with Fe_2O_3 showing a relative decrease. Independent methanol oxidation reactions over used catalyst samples from 20 cm reactor depth saw >60 % loss in formaldehyde selectivity caused by the increase in Fe_2O_3 surface content.

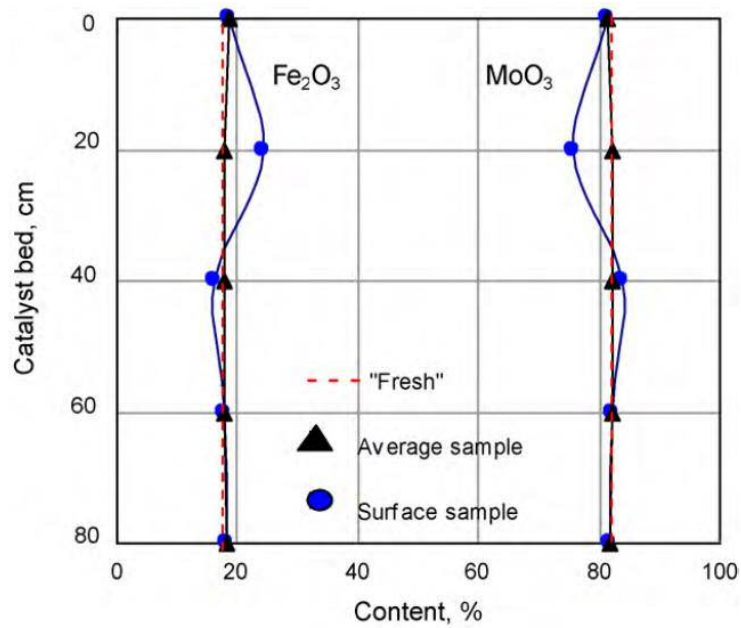
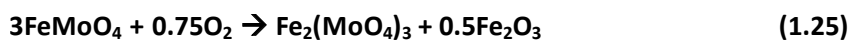


Figure 1.17 Catalyst composition along catalyst bed pre and post long term reaction looking at both the bulk and surface composition of post reaction samples.⁹⁸

It was suggested by Pernicone⁹⁹ that the reoxidation of $\text{Fe}_2(\text{MoO}_4)_3$ from FeMoO_4 under MoO_3 lean conditions causes the formation of Fe_2O_3 as shown in Equation 1.25, which as stated previously is very detrimental if exposed to the surface.³⁷



Investigations by Soares *et al.*^{96,101} presented the effect of water addition, which was increased by the introduction of water into the stream, on the deactivation of the iron molybdate catalyst. The addition of just 2 % water in the gas stream caused a 10 % reduction in initial activity over 24 h, compared to the anhydrous gas stream which saw only a 5.5 % loss over 72 h. In both cases formaldehyde was found to decrease as activity was decreased as CO selectivity was shown to increase. Lower activity was also observed by the samples tested using water in the gas stream due to the competitive inhibition toward the active site preventing methanol adsorption proposed by Pernicone *et al.*¹⁰²

1.4.3 Effect of Iron: Molybdenum Ratio

Many authors^{38,88,92,103} have investigated the use of different Fe:Mo ratios towards the production of methanol partial oxidation. Results presented by House *et al.*⁹² in Table 1.2 showed that even very small molybdenum content improves the formaldehyde yield by 4 times compared to Fe₂O₃ as molybdenum enrichment at the surface was observed.

Formaldehyde selectivity was shown to increase as molybdenum content although with decreases in activity observed thought to be due to the formation of low activity, crystalline MoO₃ on the surface of the samples which also caused a decrease in overall surface area as shown in Table 1.2.

Table 1.2 Comparison of samples prepared using various Fe:Mo ratios.⁹²

Fe:Mo	Surface area (m ² g ⁻¹)	Surface Fe:Mo Ratio	Formaldehyde Yield (% (temp °C))
1:0 (Fe₂O₃)	16.8	1:0	~2 (310)
1:0.02	34.0	1:0.098	8 (180)
1:1	16.3	1:1	50 (220)
1:1.5	7.8	1:1.6	78 (260)
1:2.2	6.7	1:2.2	85 (280)
1:4	3.6	1:2.3	86 (300)
0:1 (MoO₃)	1.0	0:1	88 (400)

Many other studies have indicated the usage of ratios between 1:1.7-1:2.2^{38,91,103} due to the combination of the increased MoO₃ surface content suggested to be the active site of the catalyst, also to limit deactivation by maintaining a reservoir of MoO₃ to replace lost MoO₃ via sublimation.

1.4.4. Effect of Calcination Temperature

In the calcination of iron molybdate catalysts numerous processes occur, at low temperatures (< 300 °C) the loss of precursor impurities such as NH₄⁺, which are removed producing the oxides¹⁰⁴. A topochemical reaction between the produced Fe₂O₃ and MoO₃ at temperatures exceeding 380 °C produces Fe₂(MoO₄)₃ with higher temperatures increasing the rate of Fe₂(MoO₄)₃ formation.¹⁰⁵

Thermal spreading of MoO_3 is also a consideration for iron molybdates.^{106,107} This is due to the relatively low sublimation temperature of MoO_3 which allows for the migration of MoO_3 within the bulk and over the surface of the samples during calcination. This has a positive effect in many cases with the gradual covering of iron centres with a surface covering of molybdenum preventing carbon oxide selectivity. Some effects are however negative, especially at higher temperatures ($> 500\text{ }^\circ\text{C}$) and using Fe:Mo ratio above the stoichiometric 1:1.5. This is shown in the example shown in Fig. 1.18 presented by Xu *et al.*¹⁰⁸ who saw the formation of large crystalline MoO_3 needle structures using a $700\text{ }^\circ\text{C}$ calcination which have been found to prevent high activity of the samples.

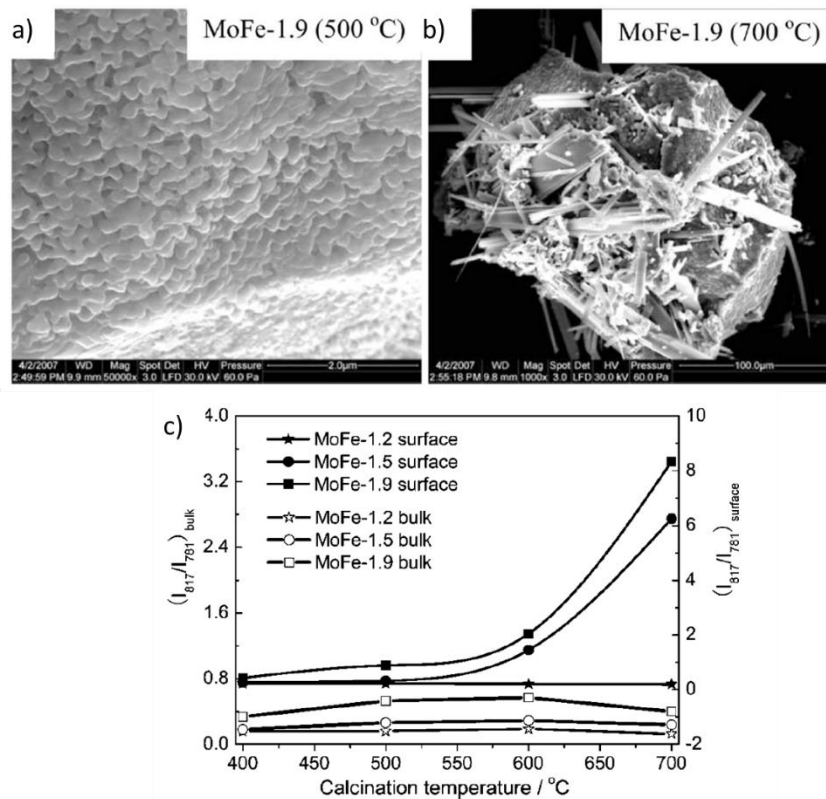


Figure 1.18 SEM micrographs of iron molybdate sample using Fe:Mo ratio 1:1.9 calcined at (a) $500\text{ }^\circ\text{C}$ and (b) $700\text{ }^\circ\text{C}$ and (c) Raman comparison of bulk and surface composition of iron molybdate samples prepared using various temperatures.¹⁰⁸

Raman results showed that the molybdenum was being removed from the bulk and migrating towards the surface, an increase in intensity observed at wavenumber 817 cm^{-1} corresponding to MoO_3 compared to 781 cm^{-1} corresponding to $\text{Fe}_2(\text{MoO}_4)_3$ shown in

Fig.1.18.c with the inverse observed in bulk results as calcination was increased beyond 500 °C.

1.5 MoO₃/Fe₂(MoO₄)₃ Preparation Methods

1.5.1 Physical Grinding and Solvent Free Systems

The use of physical grinding method for MoO₃/Fe₂(MoO₄)₃ synthesis has been proposed using ground mixture of MoO₃ and Fe₂O₃ by Huang *et al.*¹⁰⁶ and Dong *et al.*¹⁰⁹ both of whom suggested the non-uniform distribution of iron and molybdenum as shown in microscopy results presented in Fig.1.19.

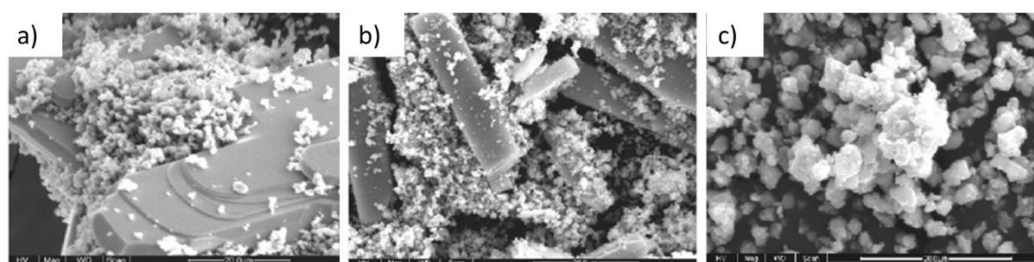


Figure 1.19 SEM micrographs of physically ground samples of Fe₂O₃ and MoO₃ uncalcined (a), calcined at 300 °C (b) and calcined at 600 °C (c).¹⁰⁶

Results by both authors concluded that the formation of Fe₂(MoO₄)₃ was not observed at calcination conditions under 470 °C. It was suggested by Huang *et al.*¹⁰⁶ that the rate of the solid-state reaction between Fe₂O₃ and MoO₃ at low temperatures is limited, although there was evidence of molybdenum migration in XPS results at low temperatures (300-400 °C) causing an encapsulation of the Fe₂O₃ grains. Calcinations at 600 °C facilitated the loss of the MoO₃ structures completely forming Fe₂(MoO₄)₃ as the molybdenum permeated into the Fe₂O₃ structures. Methanol oxidation over the samples tested by Huang *et al.*¹⁰⁶ yielded 75.3 % formaldehyde at 260 °C using a 400 °C calcination with yield decreasing as calcination temperatures were increased. Higher temperatures may yield lower formaldehyde selectivity as exposed iron centres would facilitate combustion, although these are not discussed in this study.

Changing the precursors to $\text{Fe}(\text{NO}_3)_3 \cdot 9\text{H}_2\text{O}$ and $(\text{NH}_4)_6\text{Mo}_7\text{O}_{24} \cdot 4\text{H}_2\text{O}$ used by Li *et al.*¹¹⁰ and Shaheen¹¹¹ displayed greater $\text{Fe}_2(\text{MoO}_4)_3$ production at lower temperatures (<420 °C) although when tested for methanol partial oxidation they were still found to have limited formaldehyde selectivity. Li *et al.*¹¹⁰ displayed $86.7 \pm 5.6\%$ formaldehyde yield at 280 °C which was both worse and far less consistent than equivalent samples produced using wet mixing ($94.5 \pm 0.3\%$).

Radev *et al.*¹¹² proposed the use of $\text{FeO}(\text{OH})$ rather than $\text{Fe}(\text{NO}_3)_3 \cdot 9\text{H}_2\text{O}$ and using a planetary mill produced pure $\text{Fe}_2(\text{MoO}_4)_3$ based on XRD results using a 400 °C calcination. Compared to physically ground samples of the same precursors which were unable to remove $\alpha\text{-Fe}_2\text{O}_3$ even using 600 °C calcination.

Although physically ground samples don't produce highly stable catalysts due to the limit of mixing potential, this limits the viability of the catalyst preparation method due to the over exposure of Fe_2O_3 .

1.5.2 Coprecipitation

Coprecipitation production of iron molybdate has been extensively used in the study of methanol partial oxidation and was the industrial standard used until recently.^{101,113–115} The first recorded instance of coprecipitated iron molybdate production for the partial oxidation of methanol to formaldehyde was reported by Adkins and Peterson.¹⁵

The general composition of coprecipitated iron molybdate samples are very homogeneous, excess molybdenum forms as crystallites of MoO_3 on the surface of the $\text{Fe}_2(\text{MoO}_4)_3$.^{38,93} Formaldehyde yields achieved by these samples are also high achieving between 85-93 % using Fe:Mo ratios between 1:1.7-1:3.0.

Coprecipitation methods are highly sensitive to a combination of effects discussed by Trifirò¹¹⁶, the molybdenum species in solution is varied by pH, temperature and molybdenum concentration as shown in Table 1.3.

Table 1.3. Evolution of soluble molybdenum species with the variation of pH, temperature and Mo concentration as presented by Trifirò.¹¹⁷

	Mo Species					
	<i>cis</i> -Mo ₂ ⁺	HMo ₂ O ₆ ⁺	Mo ₄ O ₁₃ ²⁻	Mo ₈ O ₂₄ ⁴⁻	Mo ₇ O ₂₄ ⁶⁻	MoO ₄ ²⁻
pH	1 → 6					
Temp.	r.t. → 100 °C					
Mo conc.	→decreasing→					

Many authors use pH 2 with aging temperatures ranging from 60-100 °C which promotes the formation of Fe₂(MoO₄)₃ while preventing large crystalline formation of MoO₃.^{38,88,92,93} Those same authors used iron nitrate and ammonium molybdate precursors which is commonly used in literature.

Industrially, iron (III) chloride and hydrochloric acid were used, replacing the nitrates which seems to have little effect on reactivity.^{113,115} Changing of the molybdenum precursor to an alkali metal based system such as sodium molybdate was found to decrease reactivity by blocking acidic sites.¹¹⁸

Due to the higher degree of homogeneity prior to calcination, lower temperatures may be employed compared to physically ground samples due to the lower requirement of MoO₃ thermal spreading to dilute iron rich areas. Higher temperature calcination can actually be detrimental as shown by Soares *et al.*⁸⁸ causing lower activity due to the formation of large inactive MoO₃ crystallites on the surface of the catalyst.

1.5.3 MoO₃ Impregnation onto Fe₂O₃

Supported MoO₃ on Fe₂O₃ was found to improve formaldehyde selectivity even at very low loading as discussed previously. Many studies^{38,80,86,87,119,120} have been undertaken recently to produce selective iron molybdate catalysts by supporting MoO₃ onto Fe₂O₃ by impregnation and subsequent annealing processes. Many of these have been employed as model catalyst surfaces for the investigation into the active site of the iron molybdate systems as discussed earlier.

Even at very small molybdenum loadings (0.24 monolayer coverage) onto bulk Fe₂O₃ there are substantial improvements in formaldehyde selectivity at low temperatures (~70 % at

160 °C) caused by the formation of a molybdenum rich surface layer which can selectively form formaldehyde, unlike the bulk Fe_2O_3 .

Increasing the molybdenum loading onto the surface of the Fe_2O_3 has been found to increase the production of $\text{Fe}_2(\text{MoO}_4)_3$ as shown in Fig. 1.20 as Fe_2O_3 was suggested to dilute in favour of $\text{Fe}_2(\text{MoO}_4)_3$.

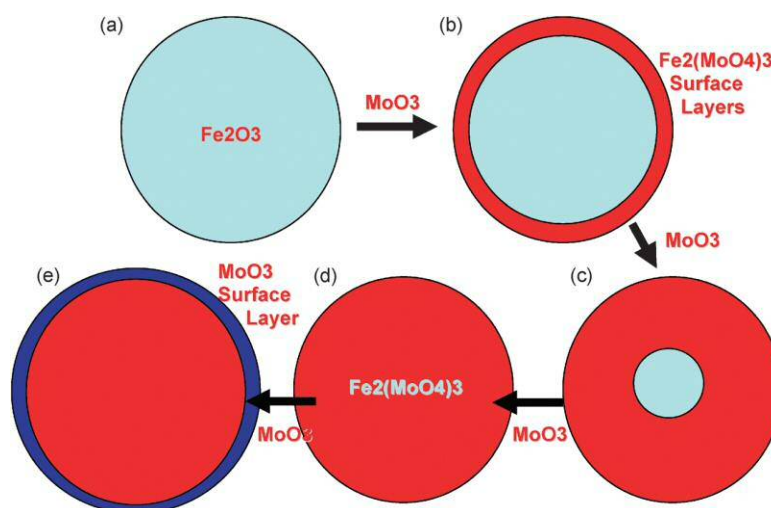


Figure 1.20 Mechanism of $\text{Fe}_2(\text{MoO}_4)_3$ production from monolayer additions onto Fe_2O_3 .

When compared to more conventional coprecipitation methods, the use of $\text{MoO}_3/\text{Fe}_2\text{O}_3$ are shown to be limited, catalytically as shown in Fig. 1.21, by Bowker *et al.*⁸⁰ The higher activity observed at lower temperatures does not translate into higher formaldehyde yield with CO selectivity shown to increase rapidly as temperatures were increased. This was improved with increased Mo monolayer coverages although even with 7.2 molybdenum monolayers on the surface of the sample, CO selectivity remained high.

Brookes *et al.*⁸⁷ suggested that higher formaldehyde selectivity could be attained using 500 °C annealing temperatures, this produced 82.8 % formaldehyde yield at 225 °C presenting a 10.8 % increase compared to similar samples annealed at 300 °C. This shows that higher annealing temperatures might be required to adequately form $\text{Fe}_2(\text{MoO}_4)_3$ similar to physically ground samples.

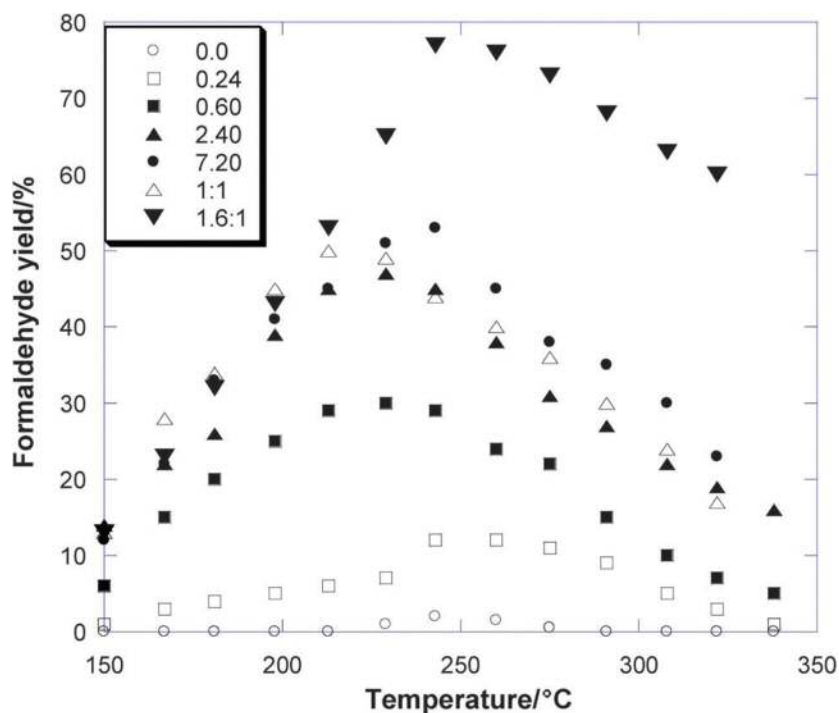


Figure 1.21 Comparison of formaldehyde yield for thin film molybdena on Fe_2O_3 catalysts with bulk preparation catalysts of sub stoichiometric ratio (1:1) and super-stoichiometric ratio (1.6:1).⁸⁰

The commercial viability of these catalysts is limited due to the over exposure of Fe_2O_3 even at higher molybdenum loadings which limits the formaldehyde yields achieved. Higher loadings would eventually negate the improved activity observed by these samples displaying the reactivity of bulk MoO_3 . Higher annealing temperatures do yield better catalytic performance but none were shown to be as stable as those produced using more traditional methods.

1.5.4 Fe_2O_3 Impregnation $\text{Fe}_2(\text{MoO}_4)_3$ onto MoO_3

The use of MoO_3 as a support for $\text{Fe}_2(\text{MoO}_4)_3$ has been studied recently for methanol partial oxidation by Jin *et al.*¹⁰³, using hydrothermally produced $\alpha\text{-MoO}_3$ nano-rod supporting material¹²¹. Impregnation of $\text{Fe}_2(\text{MoO}_4)_3$ particles onto the surface was successful forming a well dispersed structure over the surface of the support as shown in Fig.1.22.a.

The method was shown to be sensitive to Fe:Mo ratio with an excess of molybdenum crucial to maintain higher selectivity to formaldehyde with the ideal ratios shown to be

1:2.2. When compared to more traditional coprecipitation methods, the rate of formaldehyde production was increased with similar formaldehyde yields achieved by the nano-rod supported examples. This is thought to be due to the formation of small, high surface area $\text{Fe}_2(\text{MoO}_4)_3$ nanoparticles supported on a large MoO_3 reservoir allowing for the regeneration of the active catalyst.

The use of lower temperature, prolonged calcination was found to decrease the activity of the samples as MoO_3 was found to migrate by the Kirkendall effect^{122,123} over the surface engulfing iron nanoparticles forming a continuous $\text{Fe}_2(\text{MoO}_4)_3$ over layer. Similar results were observed by Wang *et al.*¹²² and Chen *et al.*¹²⁴ who suggested the migration of MoO_3 from the nano-rods towards the surface formed internal voids making the overall structure highly porous (Fig.1.22.b). These structures have however not been tested for methanol partial oxidation.

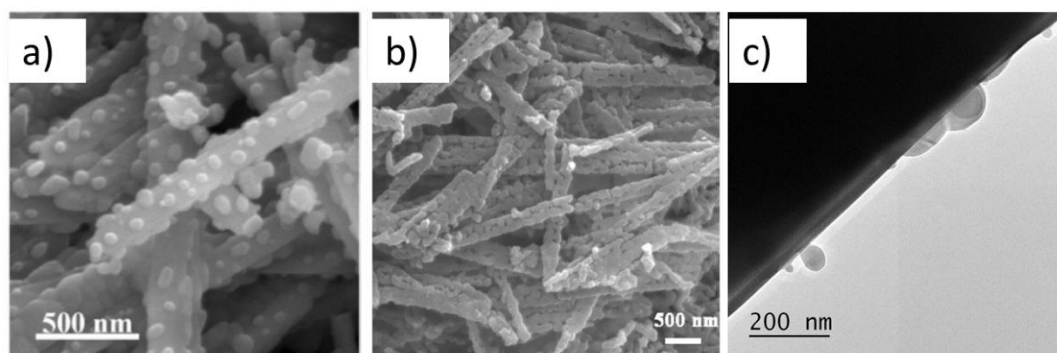


Figure 1.22 SEM micrographs of $\text{Fe}_2(\text{MoO}_4)_3/\text{MoO}_3$ nano-rod using Fe:Mo 1:2.2¹⁰³ (a) and porous iron molybdate nano-rods using Fe:Mo 1:1.6 (b), STEM micrograph of $\text{Fe}_2(\text{MoO}_4)_3/\text{MoO}_3$ bulk¹²⁵ using Fe:Mo 1:0.22 ratio(c).

Another study¹²⁵ showed that the production of these supported iron structures can occur on the surface of bulk $\alpha\text{-MoO}_3$ as shown in Fig.1.22.c. although due to the lower surface area ($1 \text{ m}^2 \text{ g}^{-1}$ for bulk, $13 \text{ m}^2 \text{ g}^{-1}$ for the nanorods) only a tenth of the iron loading was employed. Because of this, lower activity was achieved by these samples. This was due to the low $\text{Fe}_2(\text{MoO}_4)_3$ content produced which was unable to overcome the low activity of the support although formaldehyde selectivity remained high throughout.

The use of the nano-rod supported samples could be viable although the thermal stability of the samples was suggested to be limited due to the loss of nano-rod structure using higher temperature calcination ($>500 \text{ }^\circ\text{C}$). Whether deactivation via the migration of MoO_3

occurs is yet to be analysed, Jin *et al.*¹⁰³ were certain the MoO₃ reservoir from the nano-rods would prevent the loss of MoO₃ on the surface of the Fe₂(MoO₄)₃ nanoparticles.

1.5.5 Sol Gel Method

The sol-gel method proposed by Soares *et al.*^{101,114} where a mixture of iron and molybdenum precursors were dissolved in solution and prevented from precipitation by acidification using propanoic acid. Water was removed yielding a precursor gel which was subsequently calcined. Soares *et al.*^{101,114} suggested that the calcination conditions were highly important with the loss of surface Mo with the use of flowing air due to the volatility of organo-malonates. The use of static air limited this effect although XPS results showed there was reduced iron species at the surface.

X-ray diffraction (XRD) results of the samples prepared by sol-gel compared to similar coprecipitated examples display lower MoO₃ crystallinity. This is due to the formation of amorphous MoO₃ located in the Fe₂(MoO₄)₃ lattice spacings instead of forming the crystalline MoO₃ excesses observed using coprecipitation. This was thought to increase the surface area and by extension, the activity observed by the sol-gel samples towards methanol partial oxidation. Formaldehyde selectivity was however not maintained at higher temperatures and conversion. Interestingly a deactivation study conducted by Soares *et al.*^{101,114} showed that the use of sol-gel synthesis limited the deactivation and actually improved the formaldehyde selectivity over time unlike the comparison coprecipitated sample. This was thought to be due to the migration of MoO₃ from the lattice spacings towards the surface.

1.6 Research Objectives

This project set out to produce novel iron molybdate nanomaterials and this was to be achieved by an overall change in the methods employed in production. The utilisation of molten oxalic acid mixtures as solvents for iron molybdate synthesis was proposed by Oudghiri-Hassani.¹²⁶ The novel method of iron molybdate synthesis uses the decomposition of oxalates formed via the melting of precursors and oxalic acid yielded iron molybdate nanoparticles once calcined.

The first results chapter(Chapter 3) expands on work undertaken by Oudghiri-Hassani.¹²⁶

The focus of this chapter is the utilisation of an oxalate decomposition method to produce iron molybdate catalysts for the methanol partial oxidation reaction. This production method was compared to more traditional production methods, optimisation of this method is then investigated to analyse possible avenues for improvements using the oxalate decomposition method.

The second results chapter(Chapter 4) considers the use of malonic acid instead of oxalic acid as a solvent for iron molybdate synthesis. Investigating whether the alteration in solvent yields changes in morphology and composition, and to what extent that may have on methanol partial oxidation results. Further optimisation is to then be analysed to ascertain the sensitivity of the method to both Fe:Mo ratios and calcination condition.

The third results chapter(Chapter 5) studies the effect of iron precursor with the use of the malonate decomposition method replacing iron nitrate, investigating the effect of the anionic component of the iron precursor on the malonate mixtures. This is discussed with respect to surface and bulk structures and what effect this has on methanol oxidation results.

The final chapter provides a summary of the discussion of the results obtained.

1.7 References

- (1) catalyst | Definition of catalyst in English by Oxford Dictionaries
<https://en.oxforddictionaries.com/definition/catalyst> (accessed Sep 26, 2017).
- (2) Fadhel, A. Z.; Pollet, P.; Liotta, C. L.; Eckert, C. A. *Mol. Basel Switz.* **2010**, *15* (11), 8400–8424.
- (3) Ross, J. R. H. In *Heterogeneous Catalysis*; Elsevier: Amsterdam, 2012; pp 1–15.
- (4) Murzin, D. Y.; Salmi, T. In *Catalytic Kinetics (Second Edition)*; Elsevier: Amsterdam, 2016; pp 345–446.
- (5) Ross, J. R. H. In *Heterogeneous Catalysis*; Elsevier: Amsterdam, 2012; pp 17–45.
- (6) Ali, M.; Rahman, M.; Sarkar, M.; Abd Hamid, S. B. *J. Nanomater.* **2014**, *2014*, 1–23.
- (7) Myers, R. L. *The 100 Most Important Chemical Compounds: A Reference Guide*; ABC-CLIO, 2007.
- (8) Thavarajah, R.; Mudimbaimannar, V. K.; Elizabeth, J.; Rao, U. K.; Ranganathan, K. J. *Oral Maxillofac. Pathol. JOMFP* **2012**, *16* (3), 400–405.
- (9) Baekeland, L. H. *J. Ind. Eng. Chem.* **1909**, *1* (3), 149–161.
- (10) Baekeland, L. H. Method of making a plastic body. US1160362 A, November 16, 1915.
- (11) Tang, X.; Bai, Y.; Duong, A.; Smith, M. T.; Li, L.; Zhang, L. *Environ. Int.* **2009**, *35* (8), 1210–1224.

- (12) JMF_Informally_speaking 2015 for web.pdf http://www.formox.com/images-uploaded/files/JMF_Informally_speaking%202015%20for%20web.pdf (accessed Feb 20, 2017).
- (13) Bailey, G. C.; Craver, A. E. Process of producing formaldehyde. US1383059 A, June 28, 1921.
- (14) Payne, W. A. Conversion of methanol to formaldehyde combination catalysts. US2519788 A, August 22, 1950.
- (15) Adkins, H.; Peterson, W. R. *J. Am. Chem. Soc.* **1931**, *53* (4), 1512–1520.
- (16) Andersson, A.; Holmberg, J.; Häggblad, R. *Top. Catal.* **2016**, *59* (17–18), 1589–1599.
- (17) Bowker, M.; Holroyd, R.; Elliott, A.; Morrall, P.; Alouche, A.; Entwistle, C.; Toerncrona, A. *Catal. Lett.* **2002**, *83* (3–4), 165–176.
- (18) Soares, A. P. V.; Portela, M. F.; Kiennemann, A. *Catal. Rev.* **2005**, *47* (1), 125–174.
- (19) Andersson, A.; Haggblad, R. Spinel structured catalyst for aldehyde production. US9056304 B2, June 16, 2015.
- (20) Andersson, A.; HÄGGBLAD, R. Spinel structured catalyst for aldehyde production. WO2011093763 A1, August 4, 2011.
- (21) JMF_Informally_speakingFINAL160223.pdf http://www.jmprotech.com/pdfs-formox/JMF_Informally_speakingFINAL160223.pdf (accessed Aug 30, 2017).
- (22) JM Formox formaldehyde process <http://www.jmprotech.com/jm-formox-formaldehyde-process> (accessed Aug 3, 2017).
- (23) Erlandsson, O.; Magnusson, A.; Pach, J. D.; Sheldon, D. Process for the production of formaldehyde. WO2016132091 A1, August 25, 2016.
- (24) Millar, G. J.; Dam, T. Q. Crystalline silver catalysts for methanol oxidation to formaldehyde. WO2001030492 A1, May 3, 2001.
- (25) Kiser, G. L.; Hendricks, B. G. Formaldehyde manufacturing process. US4076754 A, February 28, 1978.
- (26) Waterhouse, G. I. N.; Bowmaker, G. A.; Metson, J. B. *Appl. Catal. Gen.* **2004**, *265* (1), 85–101.
- (27) Waterhouse, G. I. N.; Bowmaker, G. A.; Metson, J. B. *Appl. Surf. Sci.* **2003**, *214* (1), 36–51.
- (28) Cao, Y.; Dai, W.-L.; Deng, J.-F. *Appl. Catal. Gen.* **1997**, *158* (1), L27–L34.
- (29) Li, J.-L.; Dai, W.-L.; Dong, Y.; Deng, J.-F. *Mater. Lett.* **2000**, *44* (3), 233–236.
- (30) Dai, W.-L.; Liu, Q.; Cao, Y.; Deng, J.-F. *Appl. Catal. Gen.* **1998**, *175* (1), 83–88.
- (31) Brenk, M. Silver catalyst for formaldehyde preparation. CA2735745 A1, March 4, 2010.
- (32) Millar, G. J.; Collins, M. *Ind. Eng. Chem. Res.* **2017**, *56* (33), 9247–9265.
- (33) Qian, M.; Liauw, M. A.; Emig, G. *Appl. Catal. Gen.* **2003**, *238* (2), 211–222.
- (34) Wu, W.; Wu, Z.; Yu, T.; Jiang, C.; Kim, W.-S. *Sci. Technol. Adv. Mater.* **2015**, *16* (2), 023501.
- (35) Alpha Fe₂O₃. ICDD 01-071-5088.
- (36) Haavik, C.; Stølen, S.; Fjellvåg, H.; Hanfland, M.; Häusermann, D. *Am. Mineral.* **2000**, *85* (3–4), 514–523.
- (37) Bowker, M.; House, M.; Alshehri, A.; Brookes, C.; Gibson, E. K.; Wells, P. P. *Catal. Struct. React.* **2015**, *1* (2), 95–100.
- (38) Routray, K.; Zhou, W.; Kiely, C. J.; Grünert, W.; Wachs, I. E. *J. Catal.* **2010**, *275* (1), 84–98.
- (39) Li, Z.; Potapenko, D. V.; Rim, K. T.; Flytzani-Stephanopoulos, M.; Flynn, G. W.; Osgood, R. M.; Wen, X.-D.; Batista, E. R. *J. Phys. Chem. C* **2015**, *119* (2), 1113–1120.
- (40) Ross, S.; Sussman, A. *J. Phys. Chem.* **1955**, *59* (9), 889–892.

- (41) Ketcham, V. J.; Coltrinari, E. L.; Hazen, W. W. Pressure oxidation process for the production of molybdenum trioxide from molybdenite. US6149883 A, November 21, 2000.
- (42) Shariat, M. H.; Setoodeh, N.; Dehghan, R. A. *Miner. Eng.* **2001**, *14* (7), 815–820.
- (43) Lasheen, T. A.; El-Ahmady, M. E.; Hassib, H. B.; Helal, A. S. *Miner. Process. Extr. Metall. Rev.* **2015**, *36* (3), 145–173.
- (44) Li, T.; Beidaghi, M.; Xiao, X.; Huang, L.; Hu, Z.; Sun, W.; Chen, X.; Gogotsi, Y.; Zhou, J. *Nano Energy* **2016**, *26*, 100–107.
- (45) Ette, P. M.; Gurunathan, P.; Ramesha, K. J. *Power Sources* **2015**, *278*, 630–638.
- (46) Zhang, H.; Gao, L.; Gong, Y. *Electrochem. Commun.* **2015**, *52*, 67–70.
- (47) Li, S.; Hou, H.; Huang, Z.; Liao, H.; Qiu, X.; Ji, X. *Electrochimica Acta* **2017**, *245*, 949–956.
- (48) Zollfrank, C.; Gutbrod, K.; Wechsler, P.; Guggenbichler, J. P. *Mater. Sci. Eng. C* **2012**, *32* (1), 47–54.
- (49) Shafaei, S.; Van Opdenbosch, D.; Fey, T.; Koch, M.; Kraus, T.; Guggenbichler, J. P.; Zollfrank, C. *Mater. Sci. Eng. C* **2016**, *58*, 1064–1070.
- (50) Pham, T. T. P.; Nguyen, P. H. D.; Vo, T. T.; Nguyen, H. H. P.; Luu, C. L. *Adv. Nat. Sci. Nanosci. Nanotechnol.* **2015**, *6* (4).
- (51) Yao, D. D.; Ou, J. Z.; Latham, K.; Zhuyikov, S.; O’Mullane, A. P.; Kalantar-zadeh, K. *Cryst. Growth Des.* **2012**, *12* (4), 1865–1870.
- (52) Wooster, N. *Nature* **1931**, *127*, 93.
- (53) MoO₃ XRD. ICDD 00-005-0508.
- (54) Inzani, K.; Grande, T.; Vullum-Bruer, F.; Selbach, S. M. *J. Phys. Chem. C* **2016**, *120* (16), 8959–8968.
- (55) Phuc, N. H. H.; Phuong, P. T. T.; Tai, V. T.; Huan, N. M.; Duy, N. P. H.; Loc, L. C. *Catal. Lett.* **2016**, *146* (2), 391–397.
- (56) Peelaers, H.; Walle, C. G. V. de. *J. Phys. Condens. Matter* **2014**, *26* (30), 305502.
- (57) McCarron, E. M. *J. Chem. Soc. Chem. Commun.* **1986**, *0* (4), 336–338.
- (58) Mizushima, T.; Moriya, Y.; Phuc, N. H. H.; Ohkita, H.; Kakuta, N. *Catal. Commun.* **2011**, *13* (1), 10–13.
- (59) Pham, T. T. P.; Nguyen, P. H. D.; Vo, T. T.; Luu, C. L.; Nguyen, H. H. P. *Mater. Chem. Phys.* **2016**, *184*, 5–11.
- (60) Mizushima, T.; Fukushima, K.; Ohkita, H.; Kakuta, N. *Appl. Catal. Gen.* **2007**, *326* (1), 106–112.
- (61) Farneth, W. E.; Ohuchi, F.; Staley, R. H.; Chowdhry, U.; Sleight, A. W. *J. Phys. Chem.* **1985**, *89* (12), 2493–2497.
- (62) Machiels, C. J.; Sleight, A. W. *J. Catal.* **1982**, *76* (1), 238–239.
- (63) Doornkamp, C.; Ponec, V. J. *Mol. Catal. Chem.* **2000**, *162* (1), 19–32.
- (64) Mars, P.; van Krevelen, D. W. *Chem. Eng. Sci.* **1954**, *3*, 41–59.
- (65) Chung, J. S.; Miranda, R.; Bennett, C. O. *J. Catal.* **1988**, *114* (2), 398–410.
- (66) Allison, J. N.; Goddard, W. A. *J. Catal.* **1985**, *92* (1), 127–135.
- (67) Goddard, W. A. *Science* **1985**, *227* (4689), 917–923.
- (68) Smith, R. L.; Rohrer, G. S. *J. Catal.* **1998**, *180* (2), 270–278.
- (69) McCarron, E. M.; Sleight, A. W. *Polyhedron* **1986**, *5* (1), 129–139.
- (70) Kim, D. S.; Wachs, I. E.; Segawa, K. *J. Catal.* **1994**, *149* (2), 268–277.
- (71) Baldychev, I.; Javadekar, A.; Buttrey, D. J.; Vohs, J. M.; Gorte, R. J. *Appl. Catal. Gen.* **2011**, *394* (1), 287–293.
- (72) Jehng, J.-M.; Hu, H.; Gao, X.; Wachs, I. E. *Catal. Today* **1996**, *28* (4), 335–350.
- (73) Hu, H.; Wachs, I. E.; Bare, S. R. *J. Phys. Chem.* **1995**, *99* (27), 10897–10910.
- (74) Hu, H.; Wachs, I. E. *J. Phys. Chem.* **1995**, *99* (27), 10911–10922.

- (75) Rapposch, M. H.; Anderson, J. B.; Kostiner, E. *Inorg. Chem.* **1980**, *19* (11), 3531–3539.
- (76) Chen, H. *Mater. Res. Bull.* **1979**, *14* (12), 1583–1590.
- (77) Harrison, W. T. A. *Mater. Res. Bull.* **1995**, *30* (11), 1325–1331.
- (78) Zhou, Y.; Adams, S.; Rao, R. P.; Edwards, D. D.; Neiman, A.; Pestereva, N. *Chem. Mater.* **2008**, *20* (20), 6335–6345.
- (79) Badlani, M.; Wachs, I. E. *Catal. Lett.* **2001**, *75* (3–4), 137–149.
- (80) Bowker, M.; Brookes, C.; Carley, A. F.; House, M. P.; Kosif, M.; Sankar, G.; Wawata, I.; Wells, P. P.; Yaseneva, P. *Phys. Chem. Chem. Phys. PCCP* **2013**, *15* (29), 12056–12067.
- (81) Chowdhry, U.; Ferretti, A.; Firment, L. E.; Machiels, C. J.; Ohuchi, F.; Sleight, A. W.; Staley, R. H. *Appl. Surf. Sci.* **1984**, *19* (1), 360–372.
- (82) Briand, L. E.; Hirt, A. M.; Wachs, I. E. *J. Catal.* **2001**, *202* (2), 268–278.
- (83) Burcham, L. J.; Briand, L. E.; Wachs, I. E. *Langmuir* **2001**, *17* (20), 6175–6184.
- (84) Pernicone, N.; Lazzerin, F.; Liberti, G.; Lanzavecchia, G. *J. Catal.* **1969**, *14* (4), 293–302.
- (85) Pernicone, N. *CATTECH* **2003**, *7* (6), 196–204.
- (86) Brookes, C.; Wells, P. P.; Dimitratos, N.; Jones, W.; Gibson, E. K.; Morgan, D. J.; Cibin, G.; Nicklin, C.; Mora-Fonz, D.; Scanlon, D. O.; Catlow, C. R. A.; Bowker, M. *J. Phys. Chem. C* **2014**, *118* (45), 26155–26161.
- (87) Brookes, C.; Wells, P. P.; Cibin, G.; Dimitratos, N.; Jones, W.; Morgan, D. J.; Bowker, M. *ACS Catal.* **2014**, *4* (1), 243–250.
- (88) Soares, A. P. V.; Farinha Portela, M.; Kiennemann, A.; Hilaire, L.; Millet, J. M. M. *Appl. Catal. Gen.* **2001**, *206* (2), 221–229.
- (89) House, M. P.; Shannon, M. D.; Bowker, M. *Catal. Lett.* **2008**, *122* (3–4), 210–213.
- (90) Carbuicchio, M.; Trifirò, F. *J. Catal.* **1976**, *45* (1), 77–85.
- (91) Popov, B. I.; Pashis, A. V.; Shkuratova, L. N. *React. Kinet. Catal. Lett.* **1986**, *30* (1), 129–135.
- (92) House, M. P.; Carley, A. F.; Echeverria-Valda, R.; Bowker, M. *J. Phys. Chem. C* **2008**, *112* (11), 4333–4341.
- (93) Söderhjelm, E.; House, M. P.; Cruise, N.; Holmberg, J.; Bowker, M.; Bovin, J.-O.; Andersson, A. *Top. Catal.* **2008**, *50* (1–4), 145.
- (94) Bowker, M.; Holroyd, R.; House, M.; Bracey, R.; Bamroongwongdee, C.; Shannon, M.; Carley, A. *Top. Catal.* **2008**, *48* (1–4), 158–165.
- (95) House, M. P.; Carley, A. F.; Bowker, M. *J. Catal.* **2007**, *252* (1), 88–96.
- (96) Soares, A. P. V.; Portela, M. F.; Kiennemann, A.; Millet, J. M. M. *React. Kinet. Catal. Lett.* **2002**, *75* (1), 13–20.
- (97) Andersson, A.; Hernelind, M.; Augustsson, O. *Catal. Today* **2006**, *112* (1–4), 40–44.
- (98) Ivanov, K. I.; Dimitrov, D. Y. *Catal. Today* **2010**, *154* (3–4), 250–255.
- (99) Pernicone, N. *Catal. Today* **1991**, *11* (1), 85–91.
- (100) Ma, Y. H.; Kmiotek, S. J. *J. Catal.* **1988**, *109* (1), 132–142.
- (101) Soares, A. P. V.; Portela, M. F.; Kiennemann, A.; Hilaire, L. *Chem. Eng. Sci.* **2003**, *58* (7), 1315–1322.
- (102) Pernicone, N.; Lazzerin, F.; Lanzavecchia, G. *J. Catal.* **1968**, *10* (1), 83–84.
- (103) Jin, G.; Weng, W.; Lin, Z.; Dummer, N. F.; Taylor, S. H.; Kiely, C. J.; Bartley, J. K.; Hutchings, G. J. *J. Catal.* **2012**, *296*, 55–64.
- (104) Kovács, T. N.; Hunyadi, D.; Lucena, A. L. A. de; Szilágyi, I. M. *J. Therm. Anal. Calorim.* **2016**, *124* (2), 1013–1021.
- (105) Kostynyuk, A. O.; Gutenuar, F.; Kalashnikova, A. N.; Kalashnikov, Y. V.; Nikolenko, N. V. *Kinet. Catal.* **2014**, *55* (5), 649–655.
- (106) Huang, Y.; Cong, L.; Yu, J.; Eloy, P.; Ruiz, P. *J. Mol. Catal. Chem.* **2009**, *302* (1), 48–53.

- (107) Braun, S.; Appel, L. G.; Camorim, V. L.; Schmal, M. *J. Phys. Chem. B* **2000**, *104* (28), 6584–6590.
- (108) Xu, Q.; Jia, G.; Zhang, J.; Feng, Z.; Li, C. *J. Phys. Chem. C* **2008**, *112* (25), 9387–9393.
- (109) Dong, L.; Chen, K.; Chen, Y. *J. Solid State Chem.* **1997**, *129* (1), 30–36.
- (110) Li, J.-L.; Zhang, Y.-X.; Liu, C.-W.; Zhu, Q.-M. *Catal. Today* **1999**, *51* (1), 195–199.
- (111) Shaheen, W. M. *Mater. Sci. Eng. A* **2007**, *445–446*, 113–121.
- (112) Radeva, D. D.; Blaskov, V.; Klissurski, D.; Mitov, I.; Toneva, A. *J. Alloys Compd.* **1997**, *256* (1), 108–111.
- (113) Sten-Ake, B. Process for producing iron-molybdate catalyst for oxidation of methanol to formaldehyde. US3420783 A, January 7, 1969.
- (114) Vieira Soares, A. P.; Farinha Portela, M.; Kiennemann, A. *Stud. Surf. Sci. Catal.* **1997**, *110*, 807–816.
- (115) Eugenio, B.; Francesco, T.; Giulio, N.; Mario, B.; Remo, P.; Umberto, S. Preparation of a molybdenum oxide-iron oxide catalyst composition. US3152997 A, October 13, 1964.
- (116) Trifirò, F. *Catal. Today* **1998**, *41* (1), 21–35.
- (117) Trifirò, F.; De Vecchi, V.; Pasquon, I. *J. Catal.* **1969**, *15* (1), 8–16.
- (118) Popov, B. I.; Shkuratova, L. N.; Skorokhova, N. G. *React. Kinet. Catal. Lett.* **1975**, *3* (4), 463–469.
- (119) Bamroongwongdee, C.; Bowker, M.; F. Carley, A.; R. Davies, P.; J. Davies, R.; Edwards, D. *Faraday Discuss.* **2013**, *162* (0), 201–212.
- (120) Uhlrich, J. J.; Sainio, J.; Lei, Y.; Edwards, D.; Davies, R.; Bowker, M.; Shaikhutdinov, S.; Freund, H.-J. *Surf. Sci.* **2011**, *605* (15–16), 1550–1555.
- (121) Fang, L.; Shu, Y.; Wang, A.; Zhang, T. *J. Phys. Chem. C* **2007**, *111* (6), 2401–2408.
- (122) Wang, L.; Peng, B.; Guo, X.; Ding, W.; Chen, Y. *Chem. Commun.* **2009**, No. 12, 1565–1567.
- (123) SEQUEIRA, C. A. C.; AMARAL, L. *Trans. Nonferrous Met. Soc. China* **2014**, *24* (1), 1–11.
- (124) Chen, Y.-J.; Gao, X.-M.; Di, X.-P.; Ouyang, Q.-Y.; Gao, P.; Qi, L.-H.; Li, C.-Y.; Zhu, C.-L. *ACS Appl. Mater. Interfaces* **2013**, *5* (8), 3267–3274.
- (125) Pudge, G. J. F. Cardiff University 2013.
- (126) Oudghiri-Hassani, H. *Catal. Commun.* **2015**, *60*, 19–22.

Chapter 2 Experimental

2. 1. Introduction

In this chapter the experimental methods used in the production, characterisation and practical catalytic testing of iron molybdates synthesised during this project are explained. Production methods include a standard co-precipitation method for use as comparison¹, oxalate decomposition method (OM)² and malonate decomposition method (MM).

The characterisation methods utilised to analyse the produced samples include; Brunauer–Emmett–Teller (BET) surface area measurements, X-ray photoelectron spectroscopy (XPS), Raman mapping spectroscopy, powder X-ray diffraction (XRD), thermal gravimetric analysis (TGA) and scanning electron microscopy (SEM).

Methanol partial oxidation reactions are undertaken over the catalytic samples in a micro reactor using online reaction analysis by gas chromatography (GC). In-situ reduction studies were undertaken for samples using an in-situ XRD analysis.

2. 2. Catalyst Preparation

2.2.1. Coprecipitation

A sample of more traditional coprecipitated iron molybdate was synthesised, using an adapted method proposed by Soares *et al.*¹ using an Fe:Mo ratio of 1:2.2 as a reference for subsequent samples. Iron(III) nitrate nonahydrate ($\text{Fe}(\text{NO}_3)_3 \cdot 9\text{H}_2\text{O}$)(2.53 g) was dissolved in deionised water (100 ml). The resulting solution was added dropwise to a solution of defined concentration of ammonium heptamolybdate tetrahydrate ($(\text{NH}_4)_6\text{Mo}_7\text{O}_{24} \cdot 4\text{H}_2\text{O}$)(2.42 g) and deionised water (150 ml) which was pre-acidified to pH 2 using concentrated nitric acid which caused a colour change to occur forming a bright yellow solution. The mixture was stirred vigorously at 80 °C for 3 h where a yellow precipitate was formed. The solution was cooled to room temperature and the precipitate was filtered and washed twice with cold deionised water. The filtrate was dried for 12 h at 120 °C and

ground with a mortar and pestle before being calcined at 500 °C for 2 h using 30 ml min⁻¹ flowing air.³

2.2.2. Oxalate Decomposition Method (OM)

Initial testing of the oxalate decomposition method (OM) was undertaken using the procedure described in our recent publication² based on Oudghiri-Hassani's⁴ method using the same 1:1.5 Fe:Mo ratio of the published example. A mixture of iron (III) nitrate nonahydrate (Fe(NO₃)₃ · 9H₂O)(2.53 g), ammonium heptamolybdate tetrahydrate ((NH₄)₆Mo₇O₂₄ · 4H₂O)(1.65 g), oxalic acid dihydrate (C₂O₄H₂ · 2H₂O)(7.88 g) using a Fe:Mo:Oxalic acid ratio of 1:1.5:10 was ground together using a mortar and pestle. The resulting yellow solid was heated with constant agitation at 160 °C for 2 h at which point a dark blue solid foam was formed. The resulting foam was ground and calcined using the same method used by the coprecipitated example. An investigation into the effect of Fe:Mo was undertaken using the same OM methods varying the amount of ammonium heptamolybdate tetrahydrate used to achieve bulk Fe:Mo between 1:1.5 and 1:3.0 but keeping Fe: Oxalic acid ratio to 1:10. A summary of co-precipitated and OM samples is presented in Table 2.1.

Table 2.1 Preparation summary of samples prepared by coprecipitation and OM with varying Fe:Mo ratios.

Sample ID	Prep method	Fe:Mo Ratio	(NH ₄) ₆ Mo ₇ O ₂₄ ·4H ₂ O used (g)	Fe(NO ₃) ₃ · 9H ₂ O used (g)	C ₂ O ₄ H ₂ ·2H ₂ O used (g)
1:2.2 Coprep	Coprecipitation	1:2.2	2.42	2.53	-
1:1.5 OM	OM	1:1.5	1.65	2.53	7.88
1:1.7 OM	OM	1:1.7	1.88	2.53	7.88
1:1.9 OM	OM	1:1.9	2.10	2.53	7.88
1:2.2 OM	OM	1:2.2	2.42	2.53	7.88
1:3.0 OM	OM	1:3.0	3.31	2.53	7.88

Using the Fe:Mo:Oxalic acid ratio of 1:2.2:10 samples were prepared with the addition of water. Various volumes of water between 5-25 ml of deionised water were added to 4 g of mixture prior to heating to 100 °C under reflux for 1 h. The water was removed by heating

to 160 °C for 2 h with constant agitation, this yielded the oxalate foam which was subsequently calcined as per the other OM samples. A summary of sample preparation is displayed in Table 2.2.

Table 2.2 Preparation summary of OM samples prepared using varied addition of water.

Sample ID	Prep method	Fe:Mo Ratio	Water addition (ml)
0 ml 1:2.2 (1:2.2 OM)	OM	1:2.2	0
5 ml 1:2.2	OM	1:2.2	5
10 ml 1:2.2	OM	1:2.2	10
15 ml 1:2.2	OM	1:2.2	15
25 ml 1:2.2	OM	1:2.2	25

2.2.3. Malonate Decomposition Method (MM)

Samples produced using malonate decomposition method (MM) were prepared using a similar method described in the OM examples. Mixtures of iron (III) nitrate nonahydrate ($\text{Fe}(\text{NO}_3)_3 \cdot 9\text{H}_2\text{O}$), ammonium heptamolybdate tetrahydrate ($(\text{NH}_4)_6\text{Mo}_7\text{O}_{24} \cdot 4\text{H}_2\text{O}$) and anhydrous malonic acid ($\text{CH}_2(\text{CO}_2\text{H})_2$) in ratios corresponding to Fe:Mo:Malonic acid ratios of 1:x:10 where x ranged from 1:1.5-1:3.0, were ground together by pestle and mortar. The yellow solid was heated with constant agitation to 130 °C for 2 h where a low density, dark blue foam was formed. The foam was calcined at 500 °C 2 h producing low density, light green foam. A summary of these samples is shown in Table 2.3.

Table 2.3 Preparation summary of samples prepared by MM with varying Fe:Mo ratios.

Sample ID	Prep method	Fe:Mo Ratio	(NH ₄) ₆ Mo ₇ O ₂₄ ·4H ₂ O used (g)	Fe(NO ₃) ₃ ·9H ₂ O used (g)	CH ₂ (CO ₂ H) ₂ used (g)
1:1.5 MM	MM	1:1.5	1.65	2.53	6.50
1:1.7 MM	MM	1:1.7	1.88	2.53	6.50
1:1.9 MM	MM	1:1.9	2.10	2.53	6.50
1:2.2 MM	MM	1:2.2	2.42	2.53	6.50
1:3.0 MM	MM	1:3.0	3.31	2.53	6.50

A selection of 1:2.2 MM samples were produced using different calcination conditions. Conditions of 500 °C for 4 h and 6 h, 450 °C for 2 h, 4 h and 6 h and 600 °C for 2 h, 4 h and 6 h, these conditions were deployed using the same Fe:Mo:Maloic acid ratio 1:2.2:10 as previously. A summary of these samples is shown in Table. 2.4.

Table 2.4. Preparation summary of samples prepared using MM with varying calcination conditions.

Sample ID	Prep method	Fe:Mo Ratio	Calcination Conditions
MM 500 2 h (1:2.2 MM)	MM	1:2.2	500 °C 2 h
MM 500 4 h	MM	1:2.2	500 °C 4 h
MM 500 6 h	MM	1:2.2	500 °C 6 h
MM 450 2 h	MM	1:2.2	450 °C 2 h
MM 450 4 h	MM	1:2.2	450 °C 4 h
MM 450 6 h	MM	1:2.2	450 °C 6 h
MM 600 2 h	MM	1:2.2	600 °C 2 h
MM 600 4 h	MM	1:2.2	600 °C 4 h
MM 600 6 h	MM	1:2.2	600 °C 6 h

2.2.4. Effect of Iron Precursors on MM

All samples were produced using the same malonate decomposition method described in Section 2.2.3 keeping Fe:Mo:Malonic acid ratios to 1:2.2:10, replacing iron (III) nitrate

nonahydrate with respective iron precursors (iron(III) phosphate dihydrate, iron (III) chloride hexahydrate, iron (II) sulphate heptahydrate, anhydrous iron (III) acetate and iron (II) oxalate dihydrate). Table 2.5 presents a summary of samples produced using various iron precursors.

Table 2.5 Preparation summary of samples prepared by MM using varying iron precursors.

Sample ID	Prep method	Fe:Mo Ratio	Iron precursor used	Weight of iron precursor (g)
Nitrate MM (1:2.2 MM)	MM	1:2.2	Iron (III) nitrate nonahydrate	2.53
Phosphate MM	MM	1:2.2	Iron(III) phosphate dihydrate	1.17
Chloride MM	MM	1:2.2	Iron (III) chloride hexahydrate	1.69
Sulphate MM	MM	1:2.2	Iron (II) sulphate heptahydrate	1.72
Acetate MM	MM	1:2.2	Anhydrous iron (II) acetate	1.09
Oxalate MM	MM	1:2.2	Iron (II) oxalate dihydrate	1.13

A calcination study matching the method shown in section 2.2.2 was undertaken using Chloride MM and Oxalate MM. Table 2.6 presents a summary of the samples.

Table 2.6 Preparation summary of Chloride MM and Oxalate MM samples using various calcination conditions.

Sample ID	Iron precursor used	Calcination Conditions
Cl 500 2h (Chloride MM)	Iron (III) chloride hexahydrate	500 °C 2h
Cl 500 4h	Iron (III) chloride hexahydrate	500 °C 4h
Cl 500 6h	Iron (III) chloride hexahydrate	500 °C 6h
Cl 450 2h	Iron (III) chloride hexahydrate	450 °C 2h
Cl 450 4h	Iron (III) chloride hexahydrate	450 °C 4h
Cl 450 6h	Iron (III) chloride hexahydrate	450 °C 6h
Cl 600 2h	Iron (III) chloride hexahydrate	600 °C 2h
Cl 600 4h	Iron (III) chloride hexahydrate	600 °C 4h
Cl 600 6h	Iron (III) chloride hexahydrate	600 °C 6h
Ox 500 2h (Oxalate MM)	Iron (II) oxalate dihydrate	500 °C 2h
Ox 500 4h	Iron (II) oxalate dihydrate	500 °C 4h
Ox 500 6h	Iron (II) oxalate dihydrate	500 °C 6h
Ox 450 2h	Iron (II) oxalate dihydrate	450 °C 2h
Ox 450 4h	Iron (II) oxalate dihydrate	450 °C 4h
Ox 450 6h	Iron (II) oxalate dihydrate	450 °C 6h
Ox 600 2h	Iron (II) oxalate dihydrate	600 °C 2h
Ox 600 4h	Iron (II) oxalate dihydrate	600 °C 4h
Ox 600 6h	Iron (II) oxalate dihydrate	600 °C 6h

2. 3. Catalyst Characterisation

2. 3. 1. Brunauer–Emmett–Teller (BET)

2.3.1.1. Introduction To BET

The BET method is used extensively in surface science to determine the surface area of solids. The method uses the relationship proposed by Brunauer, Emmett and Teller⁵ suggesting the adsorption isotherm considering multi-layered adsorptions. The principle works by the bonding of gaseous molecules such as N₂ at low temperatures which form monolayers on the surface of the sample following the Langmuir isotherm. Subsequent molecule additions such as those exhibited at high pressures have the ability to physisorb

on top of the formed monolayer forming multilayers which can increase indefinitely, equation 2.1 is derived from this relationship.

$$\frac{V - V_{\text{mon}}}{V_{\text{mon}}} = \frac{p}{p^*} \quad (2.1)$$

V represents the total volume of adsorbed material, V_{mon} corresponds to the monolayer coverage volume.

z represents the relationship between the equilibrium pressure for a given surface coverage (p) and the volume pressure above a layer of adsorbate that is more than one molecule thick and resembles pure liquid (p^*).

$$z = \frac{p}{p^*} \quad (2.2)$$

c represents a constant depended on the enthalpy of both desorption and vaporisation as shown:

$$c = \frac{e^{-\Delta_{\text{des}}H^\theta / RT}}{e^{-\Delta_{\text{vap}}H^\theta / RT} - 1} \quad (2.3)$$

With $\Delta_{\text{des}}H^\theta$ representing enthalpy of desorption, $\Delta_{\text{vap}}H^\theta$ the enthalpy of vaporisation R gas constant and T is temperature.

Experimentally, nitrogen adsorption is commonly used to probe the V_{mon} of the surface when adsorbed at the boiling temperature of liquid nitrogen (-196 °C). This volume result can then be converted into the surface area of the surface surveyed due to the known size of the N_2 molecule (0.16 nm²).

2.3.1.2 BET surface area measurements procedure

BET surface areas were determined by N_2 absorption at -196 °C using a Quantachrome Quadrasorb-evo instrument. The samples (0.5-3.0 g) were prepared for analysis by removing physisorbed water at 120 °C for 2 h under a vacuum. Both the reference and sample were cooled to -196 °C and tested to attain an equilibrium measurement. Analysis was conducted at 5 different pressures along the isotherm before results were converted into surface area measurements (m² g⁻¹).

2.3.2. X-Ray Photoelectron Spectroscopy (XPS)

2.3.2.1. Theory

XPS is a highly utilised and sensitive method of characterisation extensively used in heterogeneous catalysis due to the ability to accurately determine surface elemental composition. The method relies on the quantification of electrons released from surface atoms by photoemission. Photoemission as an analytical tool was first reported by K. Siegbahn⁶ who was later awarded the Nobel prize in 1981 for the development. The process works by the Photoelectric effect, proposed by Einstein, with the interaction between photons and core electrons shown in equation 2.4:

$$(2.4)$$

Where E_k is the kinetic energy of the ionised electron, $h\nu$ is the characteristic energy of the photon and E_B representing the binding energy of the electron.

Siegbahn⁶ proposed the usage of monochromatic X-rays typically produced from either aluminium or magnesium anodes which are bombarded with high energy electrons producing X-ray photons with known energy values (1486.6 eV and 1253.6 eV respectively⁷). These photons are radiated onto the sample causing the emission of photoelectrons from atom orbitals irradiated by the photons shown in Fig.2.1.

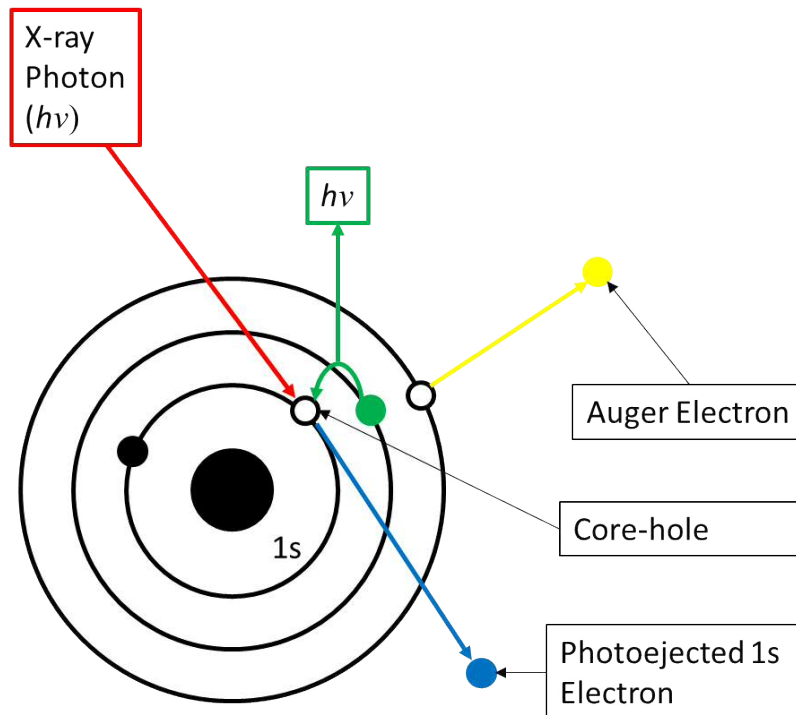


Figure 2.1. Adaptation of the photoionisation of a core shell electron ($\rightarrow \bullet$) by incident X-ray radiation (\rightarrow). X-ray photoemission fluorescence (\rightarrow) and Auger electron generation (\rightarrow) core-hole filling transitions are also presented.

These photoelectrons are collected and quantified, each electron having a kinetic energy unique to the orbitals they were emitted from due to the different binding energies due to the electrons independent proximity to the nucleus of the atoms. Each element also possess different binding energies of these orbital electron emissions which allows for accurate elemental analysis. Changes in binding energy were observed with changes in polarisability of the elements surveyed causing chemical shifts, this in turn allows for the analysis of the oxidation states of materials surveyed.

The area under the peak correspond to the number of electrons counted although due to the differing photoionisation cross-section (ionisation probability) of the elements, element sensitivity factors are used to accurately quantify the concentrations observed.

Experimentally, the photoelectric effect equation was changed introducing Φ_s corresponding to the work function of spectrometer as shown in equation 2.5 which is calibrated for the spectrometer used.

$$(2.5)$$

Once an electron is ionised a core-hole is produced as shown in Fig. 2.1, two different transitions may occur to fill the hole by the transition of an electron from a higher energy orbital. This facilitates either the production of an X-ray photon emission by fluorescence with $h\nu$ corresponding to the energy difference between the two orbitals. The second possible transition may cause the ionisation of an electron in another orbital called Auger electrons, these have kinetic energies independent to the original X-ray source, therefore appear to present with different binding energies when detected.

2.3.2.2. XPS Experimental

Elemental and atom oxidation states analysis of the calcined and uncalcined iron molybdate samples surfaces were conducted on a Thermo Scientific™ K-Alpha⁺ X-ray photoelectron spectrometer (XPS), this used a monochromatic Al radiation operating at 72 W power with a spot size of 400 μm . Dual low energy electron and Ar⁺ neutralisation was used and all results calibrated against C(1s) results where applicable. The data was analysed using CasaXPS software using Scofield sensitivity factors corrected with an energy dependence of 0.6, after application of a Shirley background.⁸

2. 3. 3. Raman Spectral Mapping

2.3.3.1. Introduction To Raman Spectroscopy

Raman spectroscopy is utilised to investigate the vibrational and rotational energy levels in materials for the purposes of identification of phases present. This is achieved by the radiation of the sample using a monochromatic source of ultra violet, visible and near infra-red light.

The Raman effect named after its discoverer Sir C.V. Raman⁹ who received the Nobel prize in Physics in 1930 for his work. He found that by irradiating molecules using monochromatic light source which caused a scattering effect, the majority of which are

scattered unchanged (Rayleigh scattering) but a small amount of the scattered radiation was found to change frequency shown by equation 2.6.

(2.6)

Where $\Delta\nu$ corresponds to the change in frequency, ν_0 represents the frequency of the incident radiation and ν_r the frequency of the reflected radiation.

Raman transitions rely on the polarisability of the sample up to virtual energy states as shown in Fig. 2.2 compared to infra-red transitions which require an induced dipole moment. Vibrational energy levels can be investigated using the inelastic scattering of the monochromatic in the form of both Stokes and Anti-Stokes scattering as shown in Fig. 2.2. Experimentally Anti-stokes are used over Stokes scattering. From the changes in frequencies (Raman shift) observed by the scattered photons, identification of vibrational and rotational energy levels can be determined and thus identification of the sample surveyed.

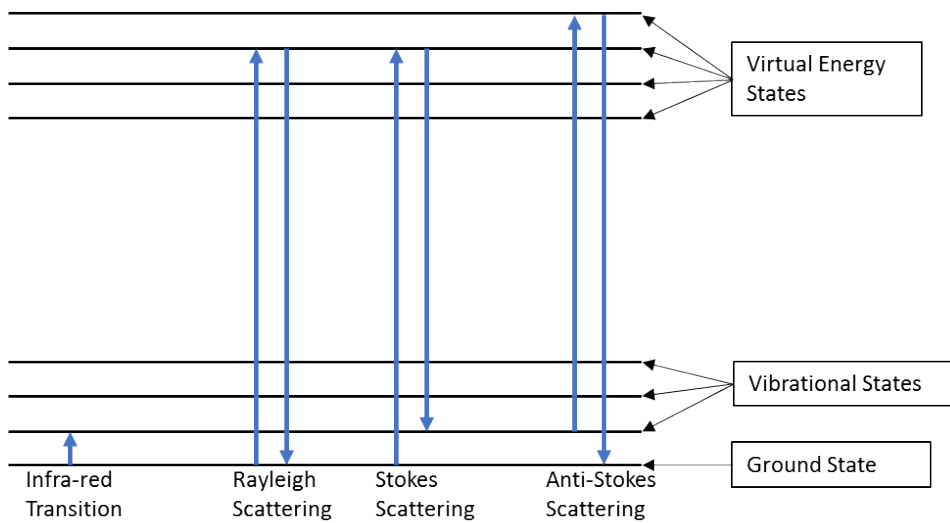


Figure 2.2. Example energy level transitions for infra-red and the three Raman transitions.

2.3.3.2. Experimental Raman Mapping

Raman mapping results were achieved using a Renishaw Ramancope, the monochromatic light source was supplied by a green Ar visible laser of wavelength 514 nm. An Olympus BH2-UMA using 20x Leica optical zoom lens was used to focus the laser light. Samples were placed onto aluminium backing plates which are mounted onto an automated stage to allow for mapping operations.

Raman mapping results were presented as shown in Fig. 2.3 where differences were observed between points surveyed. Averages were taken over the results with highlighted areas presented alongside the common points. Along with mapping, 3 random points surveyed outside of the mapping area were analysed to prove how representative the mapping results were. Due to the large crystallite sizes of the molybdates, Raman spots scans can only account for individual crystallites, as a result other characterisation methods are employed to confirm average composition of the samples (XRD and SEM).

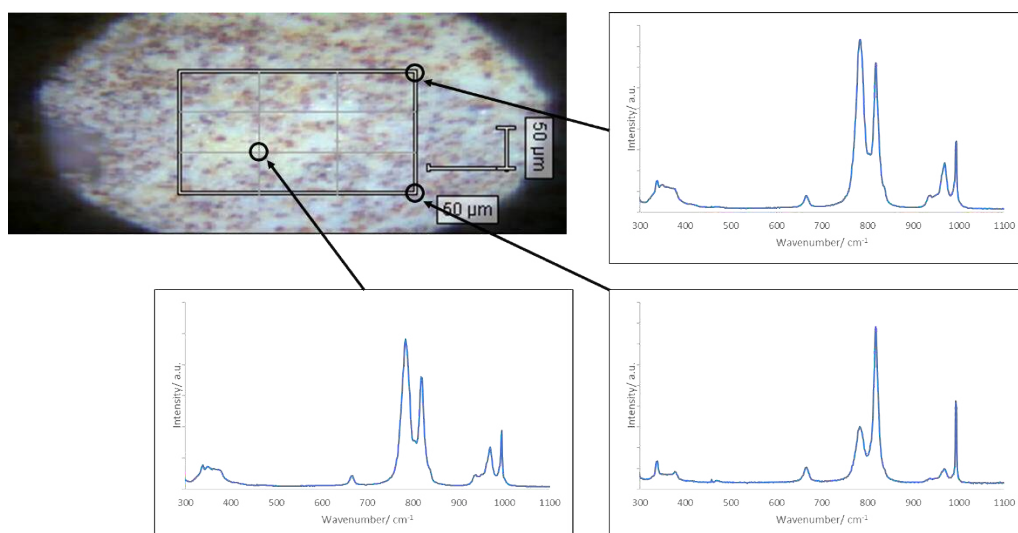


Figure 2.3. Raman mapping survey of iron molybdate sample.

2.3.4. Powder X-Ray Diffraction (XRD)

2.3.4.1. Introduction To XRD

XRD, in particular powder XRD (PXRD) is extensively used in heterogeneous catalysis as a rapid, non-destructive method of bulk phase characterisation which is able to give information on the composition of mixed systems as long as they are crystalline in nature.

The diffraction of X-rays by crystal planes was first proposed by Sir W. L. Bragg and Sir W. H. Bragg in 1913,¹⁰ and later achieving the Nobel prize in physics in 1915. They found by orientating crystal faces at certain angles to a monochromatic X-ray beam it caused elastic reflection of the X-rays off atoms within the lattice at the same angle (θ) as the incident beam as shown in Fig. 2.4.

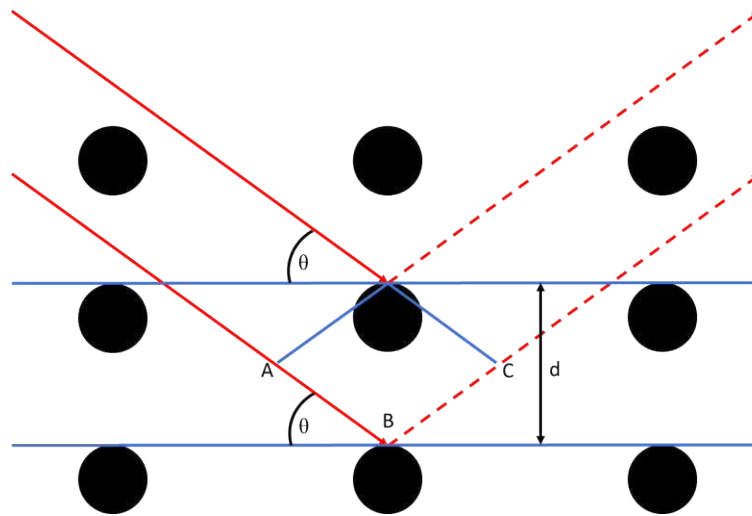


Figure 2.4. Representation of X-ray diffraction by crystalline planes following Bragg's Law.

These interactions give rise to the following equation:

$$(2.7)$$

Where:

n = positive integer

λ = X-ray Wavelength

d = inter lattice spacing between crystal layers

θ = Bragg angle (angle of diffraction)

Diffraction was found to only occur with the geometrical conditions to allow reflection on a series of lattice planes, as such constructive interference can only occur when diffracted waves run in parallel to each other presenting a path difference equating to $AB+BC$ of $\lambda(2\pi)$ otherwise destructive interference will occur preventing detection.¹¹

From the results acquired, accurate d spacing between lattice planes can be established and therefore the base unit cell of the phase in question and by extension the overall structure of the material within the crystal lattice.

Considerations for XRD are that the materials are required to be crystalline with regular lattice planes for the diffraction so materials with little to no long-range order cannot be quantified. XRD is also a bulk analysis tool and therefore not surface sensitive due to the need for long range ordered structure.

Two different methods of XRD analysis are commonly employed, single crystal and powder XRD variants. Single crystal XRD relies on the diffraction of X-rays using large, well ordered crystals whereas powder XRD does not. From diffraction patterns produced from XRD experiments, phase identification may be identified by comparison with prior results. Relative quantification of different phases may also be undertaken based on the intensity observed by the different crystalline phases based on their individual relative intensity ratio (RIR).

Shown in Fig. 2.5 is the simplified schematic of powder X-ray diffractometer where both the X-ray source and detector are able to move along an axis allowing for full range of θ measurements. A spinning stage is employed to promote the exposure of all crystal planes present in the sample.

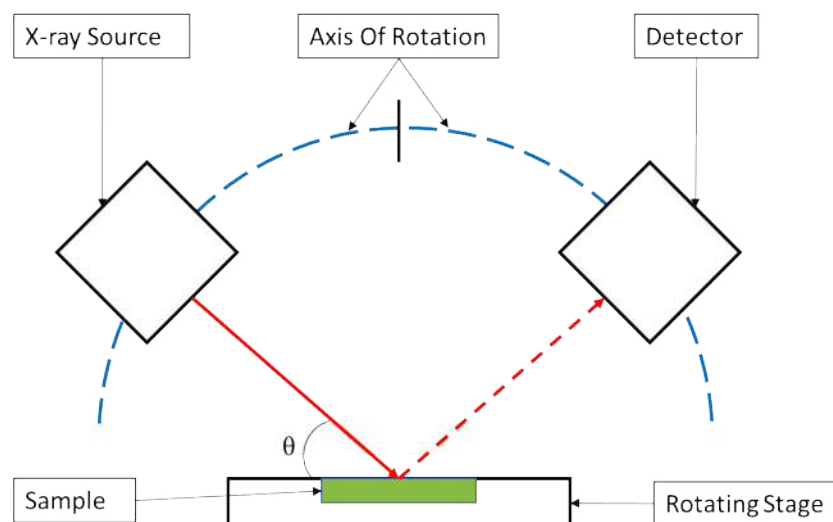


Figure 2.5. Experimental powder XRD setup schematic. (Key: incident X-ray (\rightarrow) and diffracted X-ray ($--\rightarrow$))

2.3.4.2. Powder X-ray Diffraction Experimental

XRD measurements were obtained with a Panalytical X'pert Pro diffractometer using Cu K α X-ray source operating with an accelerator voltage 40 kV and 40 mA current. X-ray patterns were recorded between 2θ 10-80 $^\circ$, all patterns produced were compared to reference patterns supplied by the international centre for diffraction data (ICDD).

2.3.5. Thermalgravimetric Analysis (TGA)

2.3.5.1. Introduction To TGA

Thermal gravimetric analysis (TGA) is a useful method for the determination of decomposition products and phase transitions commonly observed in the production of catalysts. This in turn can give information as to the likely species present during the calcination or heat treatment. The first thermobalance was developed by K. Honda in 1915^{12,13} with a similar principle followed in current methods.

TGA operates by the measurements of weight changes in the loaded sample compared to a reference vessel. Changes in weight correspond to losses of volatile products or gains caused by oxidation of samples. Derivatives of these results (DTG) present conditions where peak changes are observed which aid identification of decomposition products.

2.3.5.2 TGA Experimental Procedure

All TGA experiments were undertaken using a Perkin Elmer TGA 4000 with autosampler. 10-20 mg of sample were loaded into preweighed calcination boats and were heated 30-800 $^\circ\text{C}$ at a rate of 5 $^\circ\text{C min}^{-1}$. Both flowing air and nitrogen atmospheres were used where applicable using a flow rate of 30 ml min^{-1} .

2.3.6. Scanning Electron Microscopy (SEM)

2.3.6.1. Introduction To SEM

Morphological, topochemical and compositional surface information of samples can be determined using scanning electron microscopy (SEM). As shown in the schematic shown in Fig. 2.6 illumination of the sample is achieved using a high energy electron beam produced initially by the thermionic emission of electrons from a heated (2400 °C) tungsten filament located in the gun. This beam is channelled by the gun align coil which forces the beam towards the sample, a combination of apertures and electromagnetic lenses focuses the beam to a spot, the size of which dictates the resolution observed by the technique. A high vacuum is used in all sections to prevent unnecessary scattering of electrons due to interactions with atmospheric atomic species preserving higher resolution.

A combination of three different detectors collect different aspects of information from the sample. Secondary electrons (SE) are generated via the inelastic collision between the incident electron from the beam and an electron from the conduction or valence band of an atom as shown in Fig.2.7.a. Secondary electrons are low energy and easily collected using a positive charge making 50-100 % of the interactions observed. The results from this produces the topochemical, 3D mapping images displayed by SEM.

Back scattered electrons (BSE) are produced by the elastic interactions between incident electrons and atom nuclei. Once sufficient elastic interactions have occurred to the electrons some deviate towards the surface and the BSE detector located near the final lens. Due to the low frequency of the BSE(1/50), resolution is lower than SE so wider i-probes must be used resulting in lower resolution. Heavier atoms cause greater BSE due to the increased electron-nuclei interaction causing a raise in intensity observed.

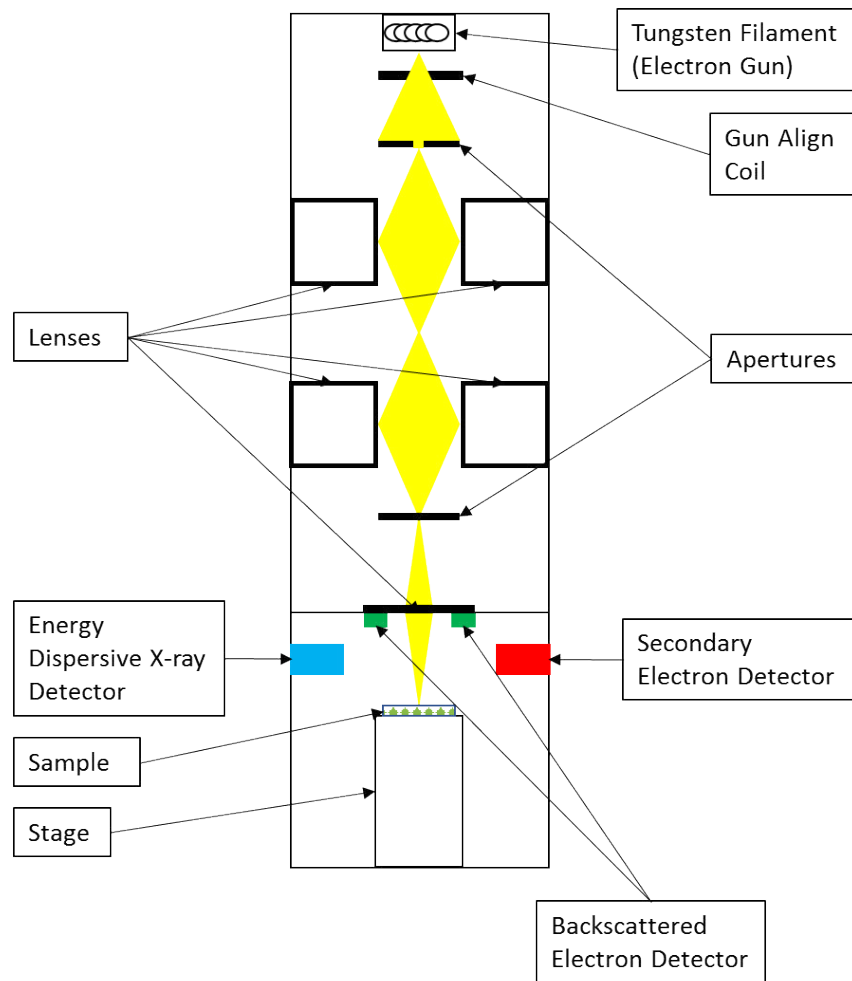


Figure 2.6. Scanning electron microscope experimental schematic.

Energy dispersive X-rays are a form of microanalysis which allows elemental analysis of surfaces corresponding to SE and BSE results. These are generated by the ionisation of inner shell electrons by the inelastic collision of a primary electron as shown in Fig.2.7.b. X-rays are generated by the transition of an electron from a higher energy orbital filling the electron hole left by the ionisation of the inner shell electron releasing an X-ray in the process. These X-rays have different wavelengths depending on the element that produced them due to the differing energy levels of inner and outer core electron transitions allowing for accurate elemental analysis.

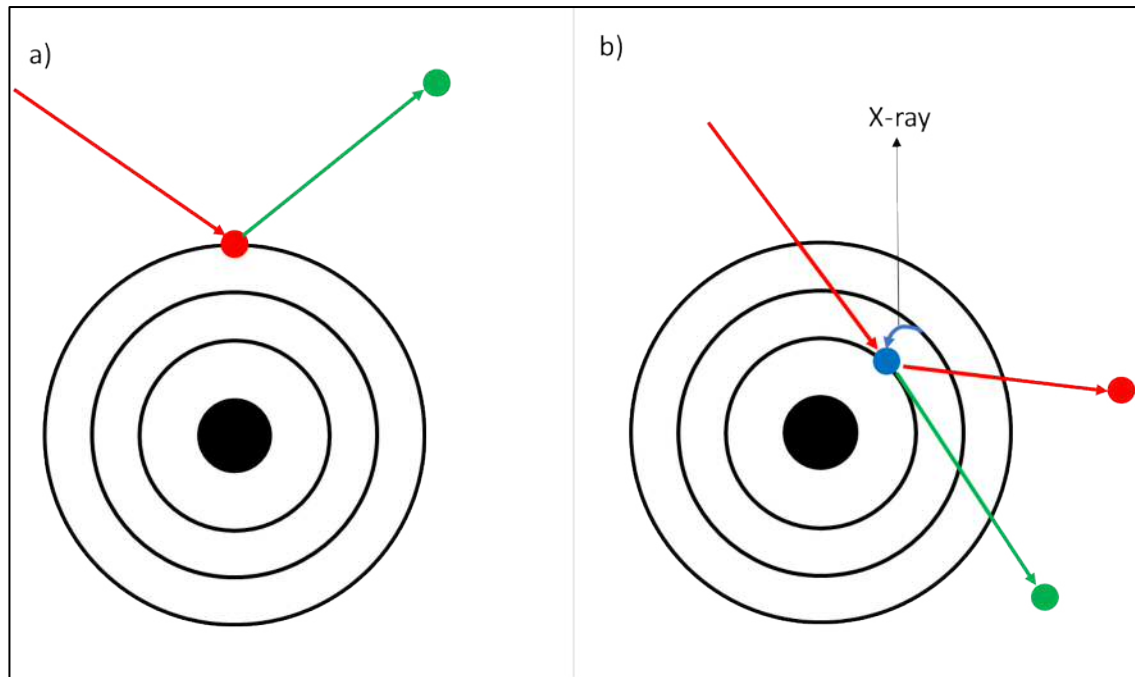


Figure 2.7. a) Secondary electron generation by an incident electron ($\rightarrow \bullet$) releasing an ionised electron ($\rightarrow \bullet$), b) EDX generation.

2.3.6.2 SEM Experimental Procedure

The analysis using SEM was undertaken using the Hitachi TM3030 fitted with secondary electron (SE), back scattered electron (BSE) and energy dispersive X-ray(EDX) detectors. BSE was not used due to lack of observed contrast between iron and molybdenum at high magnification. SEM was primarily used for SE and corresponding EDX mapping which were undertaken using accelerating voltages of 15 keV and 30 keV respectively. Both mapping and spot EDX analysis were undertaken to highlight any differences observed between the samples. All specimens were mounted on carbon adhesive disks which in turn were mounted on aluminium studs in order to limit charging observed in the samples caused by the electron beam.

2. 4. Gas Phase Reaction

2.4.1. Introduction to Online Reaction Monitoring and Gas Chromatography

The use of online reaction monitoring gives an active view of reactions where a form of characterisation is placed normally post reactor to analyse products of the reaction in question. Many different methods of characterisation are used in the investigation of catalytic processes dependent on circumstances of the reaction and products formed. In the case of gas phase reactions such as methanol partial oxidation gas chromatography (GC) is common practice.^{1,4-6}

Gas chromatography like all chromatography relies on the separation of the analyte by differing elution of different products by control of the interaction between the analyte, stationary phase (column media) and mobile phase (carrier gas).

Typically, absorption chromatography is used where a sample of the analyte is injected and passed through a column containing the adsorptive media stationary phase, separation of products occurs by the adsorption/desorption interactions between the media and the molecules in question. The adsorption media can be chosen depending on the requirement to increase or decrease analyte/media interactions to separate the desired products. Both flow rate and column temperatures can aid the resolution of products facilitating the desorption of certain products using different carrier gas flows and temperature ramp rates during operation. Separated products are detected using a variety of different methods depending on reaction products and conditions.

2.4.2. Methanol Oxidation Gas Phase Reaction Setup

The reaction setup shown in Fig. 2.8 comprises of a 9 mm diameter plug flow quartz reactor similar to those used by other authors^{3,15} where a catalytic sample (0.3 g) is supported between two plugs of quartz wool. The samples are pressed and sieved to a size between 400-600 μm prior to usage to improve gas flow through the catalyst bed by preventing

blockages caused by powder clumping. The reactor tube was placed in a tubular furnace (Carbolite) using an independent temperature controller, a thermocouple was placed in the centre of the catalyst bed to accurately monitor the catalyst temperature during reaction.

A constant flow of helium was passed through a saturator containing methanol (99.5 % Sigma-Aldrich) which was held in a water bath held at 5.2 °C to maintain 5 % composition of methanol in the gas mixture.^{15,17,18} Oxygen was introduced to the methanol helium gas mixture in series making a total flow of 60 ml min⁻¹ comprising of MeOH:O₂:He 5:10:85. Flows of helium and oxygen (both supplied by BOC Ltd., ≥ 99.5 % purity) were controlled by mass flow controllers(MFC) (Bronkhorst). The flow was passed over the catalyst sample at a variety of temperatures monitored using thermocouple. Both inlet and outlet lines to the reactor were heated to 130 °C to prevent condensation of reactants and products. Flow from the reactor was sampled online using an Agilent 7820A GC.

Each sample were analysed at 100 °C where methanol conversion is negligible as a baseline for the total counts which were compared to prior reactions to monitor for unexplained loss in counts (reactor leaks or contamination). At each increase in temperature, the reactor was stabilised for 20 min prior to first injection. At each reaction temperature 3 injections were conducted to attain an average and limit anomalous results before subsequent increases.

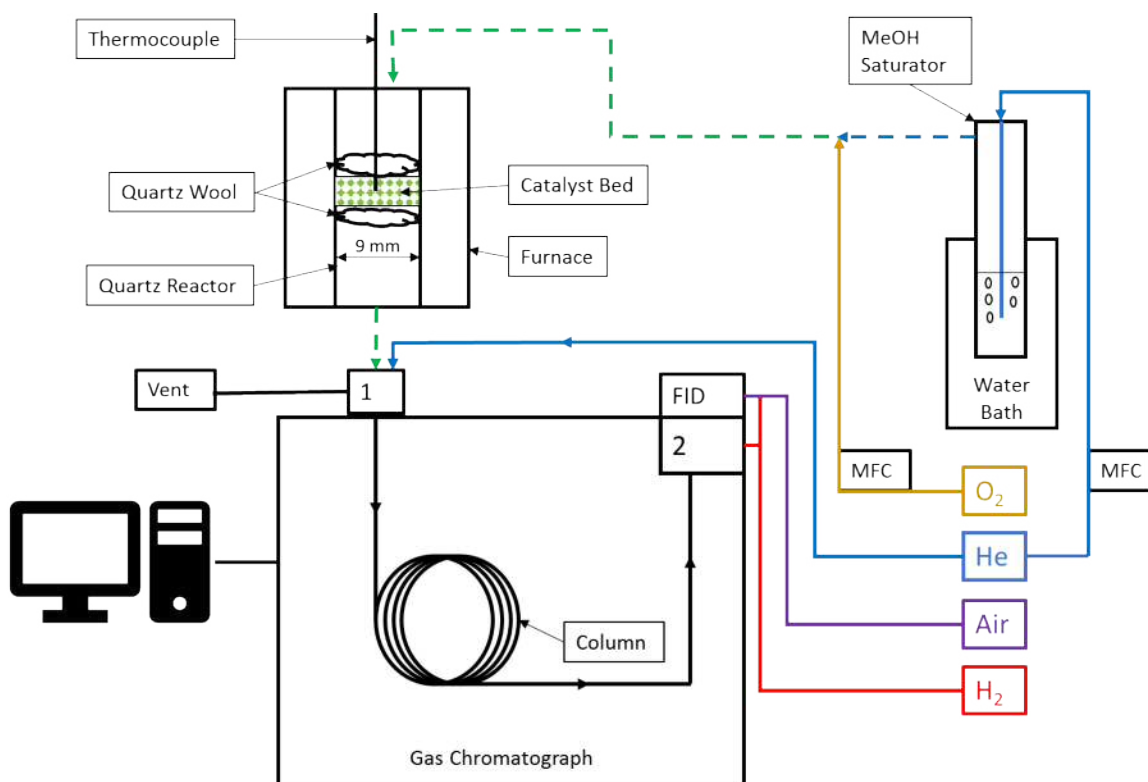


Figure 2.8 Experimental methanol partial oxidation reactor with online GC schematic. (Key: He flow (\rightarrow), MeOH/He flow ($--\rightarrow$), O₂ Flow (\rightarrow), MeOH/O₂/He flow ($--\rightarrow$), H₂ flow (\rightarrow) and compressed air flow (\rightarrow)).

2.4.3. GC Setup and Gas Sampling

The product analysis of the methanol oxidation reactor was conducted using an online Agilent 7820A GC. The 6-port valve positions of the GC are shown in Fig. 2.9, position a) has the outlet from the reactor feeding the sample loop through to the vent. A constant helium carrier gas flow (60 ml min^{-1}) was passed over the Porapak™ Q packed column (1 m 80/100 mesh) using styrene/ethyl vinylbenzene adsorbents with a surface area of between $500\text{--}600 \text{ m}^2 \text{ g}^{-1}$.¹⁹ The 6-port valve assembly was kept at a constant $130 \text{ }^\circ\text{C}$ to prevent condensation of products.

Upon injection, 6-port assembly was switched to position b) where helium carrier gas was passed through the sample loop back flushing collected sample onto the column for 2 s where it was switched back to position “a)”. The sample was then passed with the carrier gas through the Porapak™ Q column and held in the GC oven at a temperature which was maintained at a constant $120 \text{ }^\circ\text{C}$ at all times. Separated products were passed over a

methaniser which comprises of a Ni/Al₂O₃ catalyst bed held at 350 °C fed by a H₂ flow (30 ml min⁻¹) (supplied by H₂ generators) converting all carbon products to methane.²⁰ The separated methane products were detected using a flame ionisation detector (FID) fed by a supplementary H₂ (10 ml min⁻¹ + residual from methaniser making total ~ 40 ml min⁻¹) and compressed air (400 ml min⁻¹).

Investigation into the retention factors of products were conducted by injections and gas sampling of likely products and calibration of methaniser and FID conducted using CO₂, methane and methanol.

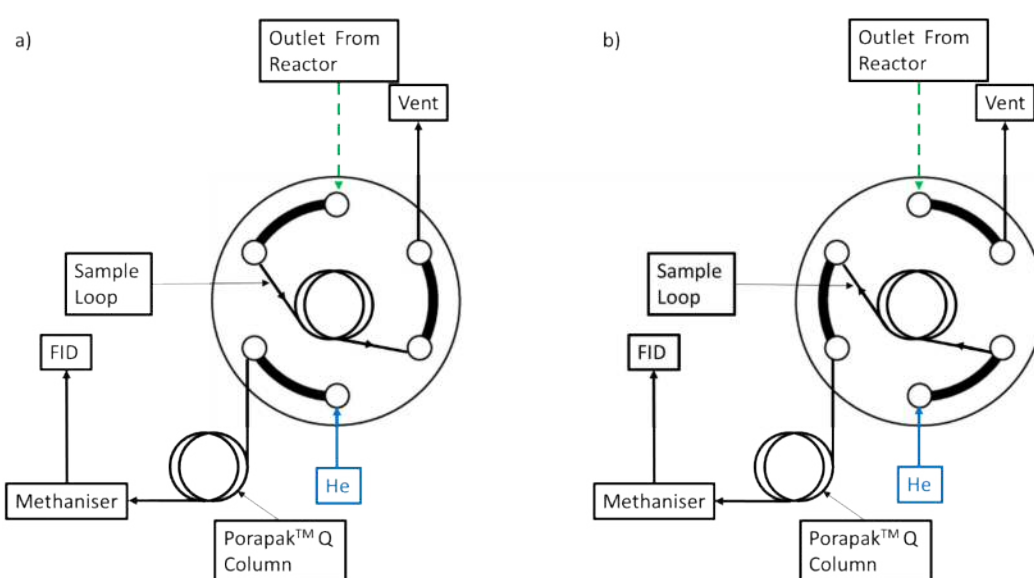


Figure 2.9. 6-port valve positions for sample loop filling and post injection (a) and samples injection (b).

Due to the complete conversion of all carbon products to methane, all carbon products have a relative response factor of 1 with the exception of dimethyl ether and methyl formate (2) and dimethoxy methane (3) due to their higher carbon number. As a result of this conversion of methanol calculated directly from FID counts as such:

$$\text{Conv MeOH} = (\text{MeOH counts} / \text{Total counts}) \times 100$$

Selectivity towards products was calculated by % carbon conversion selectivity towards the selected product (X):

$$\text{Selec. X} = (\text{X counts} / (\text{Total counts} - \text{MeOH counts})) \times 100$$

2. 5. In-Situ XRD Reactions

2. 5. 1. Introduction to In-situ Experiments

In-situ experiments are used to analyse materials during reactions, this is especially useful for heterogeneous catalysis where the identity of the active site of catalysts are hard to determine compared to heterogenous catalysts. Many of techniques are employed to analysed reactions during operation with most adapted from characterisation techniques used on the same materials as to analyse any possible changes. From in-situ results possible phase changes, transition states and possible reaction intermediates can be postulated.

2. 5. 2. In-situ XRD reduction

The experimental set up of the in-situ XRD reduction is shown in Fig. 2.10. 0.3 g of sieved and pressed sample was placed in the XRK 900 sample chamber fitted with special beryllium windows to allow for XRD penetration. A flow of 10:90 H₂:N₂ mixture was managed by computer controlled MFCs(Brokhurst) running in parallel which led into a third MFC which maintained total flow to 30 ml min⁻¹ into the temperature controlled chamber. The gas flow was passed through the sample as shown, through the holder and out to the vent.

The sample was heated to 450 °C at a rate of 10 °C min⁻¹ and held for 5 min, during operation the chamber was kept at 450 °C by temperature controls monitored by the thermocouple, the temperatures were chosen to facilitate adequate reduction rate based on experimental observations.²¹ XRD measurements between 2θ 10-80 ° every 9 minutes for 5 h were undertaken using Panalytical X'pert Pro diffractometer using Cu Kα X-ray source operating using accelerator voltage 40 kV and 40 mA current. X-ray patterns were taken at 50 °C at both beginning and the end of experiments for use as reference. All patterns produced were compared to reference patterns supplied by the international centre for diffraction data (ICDD).

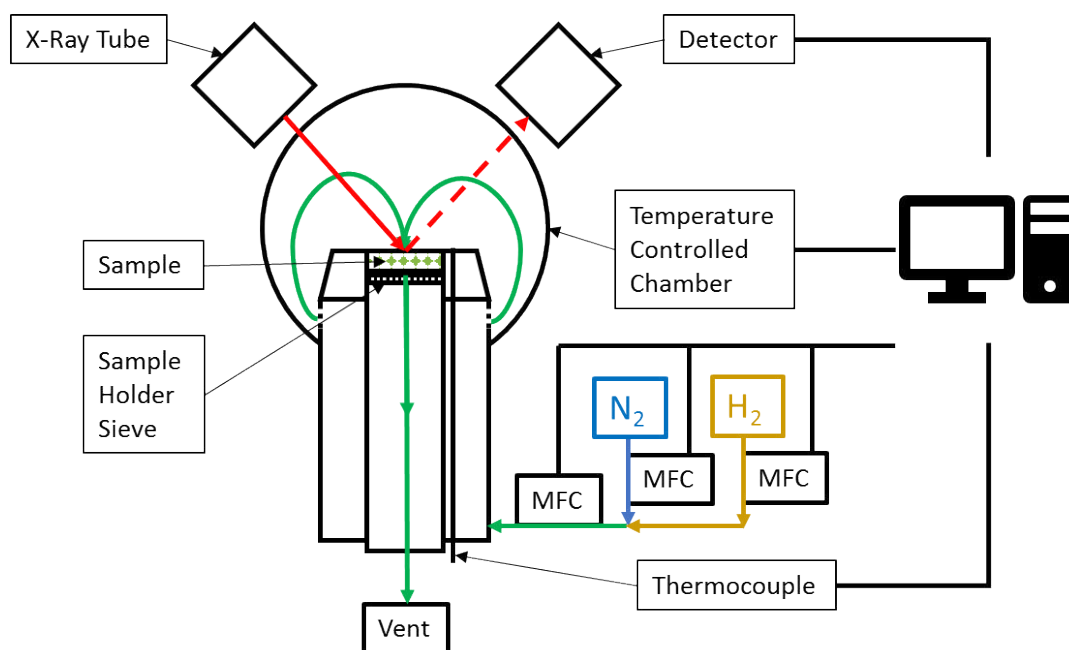


Figure 2.10. Experimental in-situ XRD reduction setup schematic. (Key: N₂ flow (→), H₂ Flow (→), mixed flow (→) incident X-ray (→) and diffracted X-ray (- ->))

2.6. References

- (1) Soares, A. P. V.; Farinha Portela, M.; Kiennemann, A.; Hilaire, L.; Millet, J. M. M. *Appl. Catal. Gen.* **2001**, *206* (2), 221–229.
- (2) Yeo, B. R.; Pudge, G. J. F.; Bugler, K. G.; Rushby, A. V.; Kondrat, S.; Bartley, J.; Golunski, S.; Taylor, S. H.; Gibson, E.; Wells, P. P.; Brookes, C.; Bowker, M.; Hutchings, G. J. *Surf. Sci.* **2016**, *648*, 163–169.
- (3) Jin, G.; Weng, W.; Lin, Z.; Dummer, N. F.; Taylor, S. H.; Kiely, C. J.; Bartley, J. K.; Hutchings, G. J. *J. Catal.* **2012**, *296*, 55–64.
- (4) Oudghiri-Hassani, H. *Catal. Commun.* **2015**, *60*, 19–22.
- (5) Brunauer, S.; Emmett, P. H.; Teller, E. *J. Am. Chem. Soc.* **1938**, *60* (2), 309–319.
- (6) Siegbahn, K. *ESCA. Atomic, Molecular and Solid State Structure Studied by Means of Electron Spectroscopy*; 1967.
- (7) X-ray Generation in XPS http://xpssimplified.com/xray_generation.php (accessed Aug 22, 2017).
- (8) Repoux, M. *Surf. Interface Anal.* **1992**, *18* (7), 567–570.
- (9) Raman, S. C. V. *Molecular diffraction of light*; University of Calcutta, 1922.
- (10) Bragg, W. H.; Bragg, W. L. *Proc. R. Soc. Lond. Math. Phys. Eng. Sci.* **1913**, *88* (605), 428–438.
- (11) Kellner, R. *Analytical Chemistry*; John Wiley & Sons Australia, Limited, 2004.
- (12) Saito, Y.; Morikawa, J. *J. Therm. Anal. Calorim.* **2013**, *113* (3), 1157–1168.
- (13) HONDA, K. *Sci. Rep. Tohoku Imp. Univ.* **1915**, *4*, Fig. 1-4.
- (14) Soares, A. P. V.; Portela, M. F.; Kiennemann, A.; Hilaire, L. *Chem. Eng. Sci.* **2003**, *58* (7), 1315–1322.
- (15) Beale, A. M.; Jacques, S. D. M.; Sacaliuc-Parvalescu, E.; O'Brien, M. G.; Barnes, P.; Weckhuysen, B. M. *Appl. Catal. Gen.* **2009**, *363* (1–2), 143–152.
- (16) Routray, K.; Briand, L. E.; Wachs, I. E. *J. Catal.* **2008**, *256* (1), 145–153.
- (17) Miller, G. A. *J. Chem. Eng. Data* **1964**, *9* (3), 418–420.

- (18) Kretschmer, C. B.; Wiebe, R. *J. Am. Chem. Soc.* **1954**, 76 (9), 2579–2583.
- (19) Agilent | Packed GC Columns <http://www.agilent.com/en-us/products/gas-chromatography/gc-columns/packed/packed-gc-columns> (accessed Aug 21, 2017).
- (20) Kruissink, E. C.; Reijen, L. L. van; Ross, J. R. H. *J. Chem. Soc. Faraday Trans. 1 Phys. Chem. Condens. Phases* **1981**, 77 (3), 649–663.
- (21) Zhang, H.; Shen, J.; Ge, X. *J. Solid State Chem.* **1995**, 117 (1), 127–135.

Chapter 3

The Use of Oxalate Decomposition Method (OM) For Iron Molybdate Synthesis

3.1. Introduction

3.1.1. Oxalic Acid Synthesis and Uses

Oxalic acid is the simplest of the organic dicarboxylic acids comprised of a two-carbon chain with carboxylic acid functional groups at both ends and it is highly acidic (pK_{a1} 1.28, pK_{a2} 4.27¹) compared to simple organic acids such as acetic acid (pK_a 4.76²). It is known to be a reducing agent and the conjugate base $C_2O_4^{2-}$ is a well-established chelating ligand for metal cations readily forming bidentate bonds with cationic centres^{3,4}.

The traditional production method of oxalic acid proceeded via oxidation of sugars such as dextrose using concentrated nitric acid^{5,6}. Subsequent neutralisation forms potassium acid saccharate which undergoes oxidation using V_2O_5 and concentrated nitric acid yielding oxalic acid from their potassium salts. Biochemical approaches have been investigated with high yields attained from the fermentation of sucrose using *Aspergillus Niger*⁷.

Oxalic acid has many uses, due to its relatively high acidity and reductive abilities it is extensively used in domestic and industrial cleaning⁸⁻¹⁰ and bleaching^{11,12}. It is also used in the dissolution of metals due to its high acidity and chelating effect of the oxalate anion in both removal of unwanted metal contaminants^{13,14} and selective leaching metals from raw materials¹⁵. The formation of iron and molybdenum oxalates and the subsequent decomposition of the materials forming metal oxides are investigated in this chapter for the synthesis of iron molybdate catalysts for the partial oxidation of methanol to formaldehyde.

3.1.2. Iron Oxalate

Iron readily forms complexes with oxalic acid in two distinct iron oxidation states $\text{Fe}^{\text{(II)}}(\text{C}_2\text{O}_4) \cdot 2\text{H}_2\text{O}$ and $\text{Fe}_2^{\text{(III)}}(\text{C}_2\text{O}_4)_3 \cdot 4\text{H}_2\text{O}$. Iron (II) oxalate dihydrate is the most common complex of iron oxalate and like most 2+ transitional metal dihydrated oxalates has α and β forms¹⁶. Due to the higher thermal stability of the α polymorph, β rapidly transforms irreversibly during heat treatment into the α species.

The structure of $\text{Fe}(\text{C}_2\text{O}_4) \cdot 2\text{H}_2\text{O}$ is shown in Fig. 3.1 where the oxalate anion is tetravalently bounded to each iron centre forming infinite chain arrangements with water molecules coordinated to form a distorted octahedral geometry as shown.

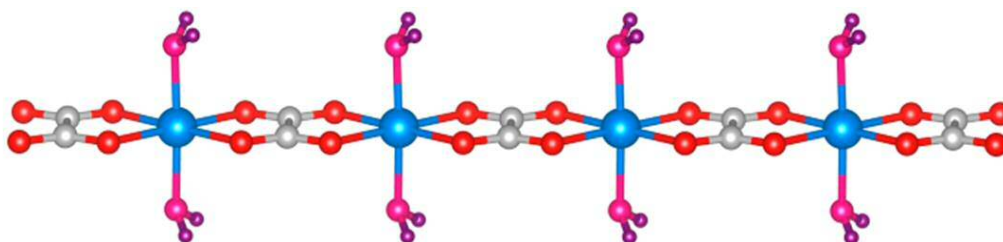


Figure 3.1 $\text{Fe}^{\text{(II)}}(\text{C}_2\text{O}_4) \cdot 2\text{H}_2\text{O}$ displayed as an infinite chain structure¹⁷. (Key: Iron = blue, carbon = grey, oxygen (oxalate) = red, oxygen (water) = pink and hydrogen = purple)

Fig. 3.2 displays the coordinated infinite chain structure of $\text{Fe}_2(\text{C}_2\text{O}_4)_3 \cdot 4\text{H}_2\text{O}$ with the hydrogen bonded water molecules removed for clarity. Similarities in the structure of both iron oxalates are observed with the same tetradentate bonding of oxalate observed in both examples, bridging between the iron centres. However, in $\text{Fe}_2(\text{C}_2\text{O}_4)_3 \cdot 4\text{H}_2\text{O}$ one of the coordinated water molecules is replaced by a monodentate oxalate ligand causing the distortion of the structure observed, preventing the formation of planar chain structures along the oxalate axis seen for $\text{Fe}(\text{C}_2\text{O}_4) \cdot 2\text{H}_2\text{O}$. The monodentately bound oxalate has been found to bridge between other $\text{Fe}_2(\text{C}_2\text{O}_4)_3 \cdot 4\text{H}_2\text{O}$ chains resulting in larger conglomerated structures¹⁷.

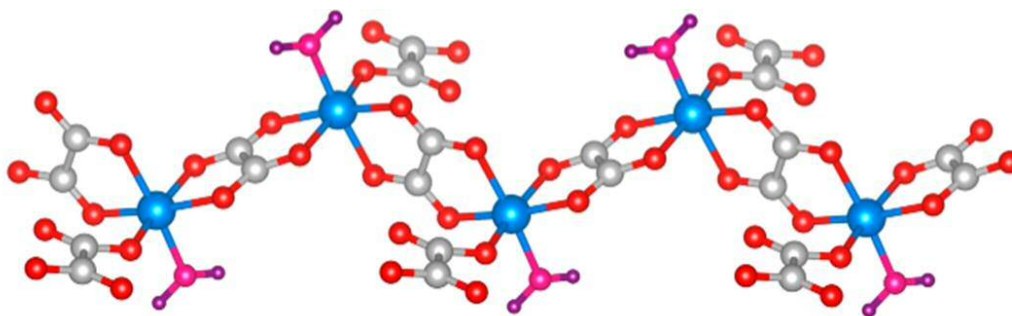


Figure 3.2 $\text{Fe}_2^{(\text{III})}(\text{C}_2\text{O}_4)_3 \cdot 4\text{H}_2\text{O}$ displayed as an infinite chain structure¹⁷. (Key: Iron = blue, carbon = grey, oxygen (oxalate) = red, oxygen (water) = pink and hydrogen = purple)

Thermal decomposition of iron(II) oxalate dihydrate in air is thought to occur by the following mechanism¹⁸:



The initial endothermic dehydration step observed in equation 3.1 is achieved between 130-160 °C removing octahedrally coordinated water molecules¹⁹⁻²². Oxidation of anhydrous $\text{Fe}(\text{C}_2\text{O}_4)$ occurs between 190-250 °C in a highly exothermic decomposition followed by the oxidation steps 3.2-3.5 which are thought to happen simultaneously forming Fe_2O_3 as the final product of the decomposition^{18,19}.

Iron (III) oxalate is thought to decompose through a similar initial dehydration step followed by an endothermic removal of oxalate at 180 °C which occurs even in oxygen free gas streams^{23,24}. This in turn forms the $\text{Fe}(\text{C}_2\text{O}_4)$ intermediate which subsequently decomposes via equations 3.2-3.5.

Other studies have found that^{20,25} $\text{Fe}(\text{C}_2\text{O}_4)$ decomposition yields an Fe_3O_4 intermediate which aids the activation of other oxalates in close proximity. This is due to the highly exothermic catalytic oxidation of produced CO to CO_2 over the Fe_3O_4 (Equation 3.6) and the oxidation of Fe_3O_4 to Fe_2O_3 (Equation 3.5).



The localised high temperatures around these decompositions have been found to activate neighbouring oxalate species.

3.1.3. Molybdenum Oxalate

Molybdenum has also been shown to complex with oxalate in two distinct oxidation states^{26,27}. Mo^V and Mo^{VI} oxidation states have been found to be prevalent based on Mo₂O₄ and Mo_nO_{2n+1} centres respectively.

The structure shown in Fig. 3.3 depicts the Mo^V [$\{\text{Mo}_2\text{O}_4((\text{C}_2\text{O}_4)_2)_2(\text{C}_2\text{O}_4)\}^{6-}$] anion featuring the Mo₂O₄ dimer unit suggested by Modéc *et al.*²⁷ following single crystal XRD analysis. It was shown that two [Mo₂O₄]²⁺ units were held together by a bridging oxalate ion. The observed Mo-Mo bond is 2.5655 Å which agrees with metal-metal single bonds. Each metal centre is also bound to a bidentate oxalate ligand, which show some bending towards the bridging oxalate ion in an umbrella-like formation, suggesting some shielding of the bridging oxalate.

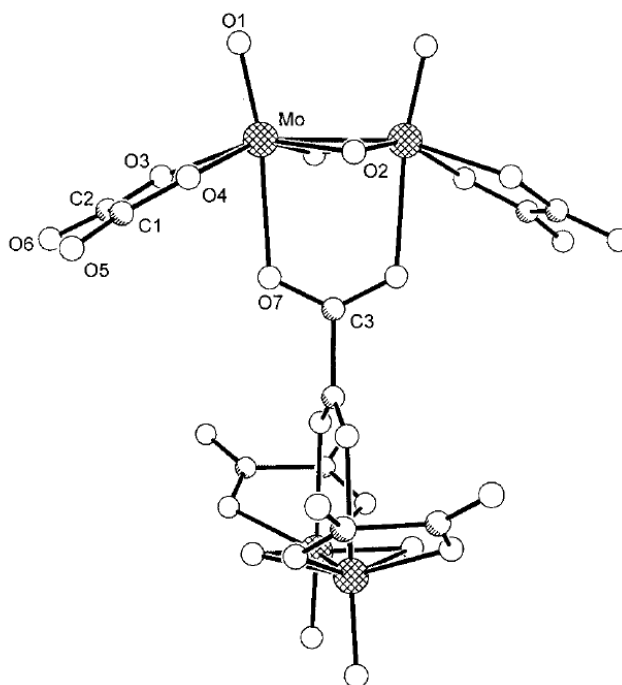


Figure 3.3. Structural representation of Mo^V [$\{\text{Mo}_2\text{O}_4((\text{C}_2\text{O}_4)_2)_2(\text{C}_2\text{O}_4)\}^{6-}$] anion²⁷.

The Mo^{VI} oxalate structure presented by Cindrić *et al.*²⁶ is shown in Fig. 3.4 and depicts the polymeric $\{[\text{MoO}_3(\text{C}_2\text{O}_4)]^{2-}\}_n$ anion. Unlike Mo^V which shows Mo-Mo bonding with oxalate bridging between Mo₂O₄ subunits, Mo^{VI} is bound via Mo-O-Mo linear chain structures. The oxalate ions are bidentate bound to each Mo centre with similar Mo-O bond lengths between oxalate (Mo-O3 and Mo-O2) and molybdenum centre (Mo-O4).

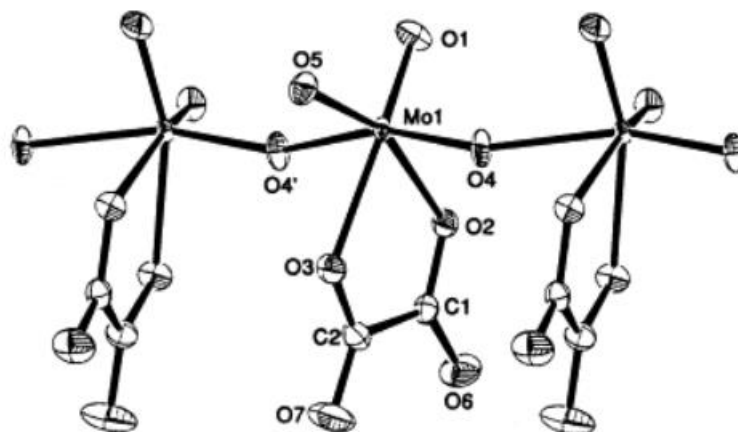
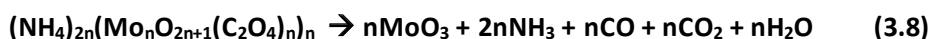


Figure 3.4 Structural representation of $\{[\text{MoO}_3(\text{C}_2\text{O}_4)]^{2-}\}_n$ anion depicted as chain structure²⁶.

Decomposition of ammonium molybdenum oxalate species is thought to decomposed via a single exothermic step peaking at 240 °C summarised in the following equation^{28–30}:



Decomposition of the oxalate to CO and CO₂ occurs simultaneously with ammonia evolution to form polymeric MoO₃. Due to the reducing atmosphere produced by CO and NH₃ evolution, it has been suggested that Mo^V is formed as an intermediate with Mo^{VI} reduced before subsequent oxidation to MoO₃²⁹. Exothermic decomposition of molybdenum oxalate is unaffected by the use of an inert atmosphere instead of flowing air, iron oxalates were stable up to 330 °C in inert atmospheres³¹. This phenomena is not exclusive to molybdenum with copper³², zinc³³ and silver³⁴ all displaying exothermic decompositions possibly caused by the autocatalytic decomposition of the oxalate ions²⁸.

3.1.4. Iron Molybdenum Oxalate

The formation of and subsequent decompositions of mixed oxalates of both molybdenum and iron were used to form iron molybdate $\text{Fe}_2(\text{MoO}_4)_3$ nanoparticles by Oudghiri-Hassani³⁵. One of the main benefits of this method is the lack of solvent used to produce the molten precursor and oxalic acid mixture which limits the need for both pH and concentration controls of solutions during production. The TEM micrographs of the sample produced by Oudghiri-Hassani (Fig. 3.5)³⁵ show the size of the nanoparticles ranges from between 50-200 nm in size with XRD analysis of the sample showing high $\text{Fe}_2(\text{MoO}_4)_3$ purity. This is thought to be achieved is through the homogeneous mixing of the oxalates in solid solution, which when decomposed yield highly dispersed iron and molybdenum mixed oxide nanoparticles.

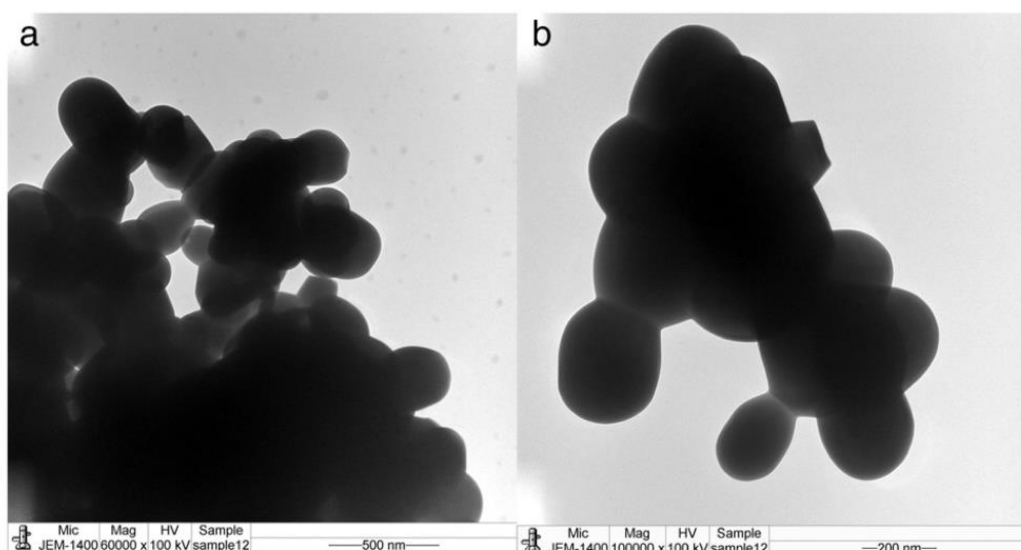


Figure 3.5 TEM Micrographs of $\text{Fe}_2(\text{MoO}_4)_3$ nanoparticles formed by method described by Oudghiri-Hassani³⁵.

3.2. Oxalic Acid Used as a Solvent For Iron Molybdate Synthesis

3.2.1. Introduction

Iron molybdate catalysts were synthesised using the oxalate decomposition method (OM) for the partial oxidation of methanol to formaldehyde. A comparison of OM and a sample of more traditional coprecipitation method were analysed to ascertain what differences in morphology may cause in methanol oxidation results between production methods.

3.2.2. Characterisation

3.2.2.1. BET Surface Area and XPS Elemental Surface Analysis

Understanding of catalyst surface areas and surface species is highly important to analyse any possible reaction results. The active surface area of iron molybdate samples have been displayed to be one of the most important factors for methanol partial oxidation³⁶.

Another important aspect would be the Fe:Mo surface ratios, as described in Chapter 1, the active site of iron molybdate catalyst is a α -MoO₃ surface layer over an Fe₂(MoO₄)₃ bulk³⁷⁻⁴¹ so a molybdenum excess on the surface would be expected for a selective catalyst.

Displayed in Table 3.1 is a BET surface area and XPS Fe:Mo surface ratio comparison of both 1:2.2 Coprep and 1:1.5 OM samples.

Table 3.1 BET surface area and XPS surface ratio comparison for 1:2.2 Coprep and 1:1.5 OM samples.

Sample	BET Surface Area/ m ² g ⁻¹	XPS Surface Ratios	Rel. Surface Mo Excess/ %
		Fe:Mo	
1:2.2 Coprep	3.9 ± 0.1	1:3.0	36.4
1:1.5 OM	4.4 ± 0.2	1:2.2	46.7

The surface area results show that both samples were similar with the differences between them within experimental error.

Both samples present with higher molybdenum surface content than their predicted bulk content which suggested surface Mo enrichment, this same trend was observed in literature with the formation of a MoO₃ surface layer.⁴⁰ The relative surface molybdenum surface enrichment was calculated from the maximum molybdenum content of the precursor mixtures corresponding to the Mo bulk content relative to iron as follows:

$$\text{Rel. Surface Mo Excess} = ((\text{XPS Mo} - \text{Bulk Mo}) / \text{Bulk Mo}) \times 100 \quad (3.9)$$

The relative Mo excess based on XPS results showed that Mo surface enrichment was more pronounced on 1:1.5 OM compared to 1:2.2 Coprep, this same trend was observed by House *et al.*⁴⁰ who saw relative molybdenum surface enrichment increase with higher Fe bulk content.

3.2.2.2. Powder XRD Crystallography

The XRD patterns of both samples (Fig. 3.6) showed a combination of 3 phases all interpreted from published standards. α -Fe₂(MoO₄)₃ (ICDD: 01-083-1701), α -MoO₃ (ICDD: 00-005-0508) and α -Fe₂O₃ (ICDD: 01-071-5088) relative content was quantised based on reference intensity ratio (RIR) of the different phases. 1:1.5 OM displayed a majority Fe₂(MoO₄)₃ (85.7 %) composition with a small amount of MoO₃ (13.5 %) and minor quantities of Fe₂O₃ (0.8 %) were observed in the XRD pattern. Due to the stoichiometric Fe:Mo ratio used by 1:1.5 OM, all molybdenum and iron should be incorporated into the Fe₂(MoO₄)₃ and should display no MoO₃ or Fe₂O₃ phase. The presence of both MoO₃ and Fe₂O₃ phases could indicate segregation caused either due to inadequate mixing prior to calcination or by thermal conglomeration of MoO₃ during calcination.

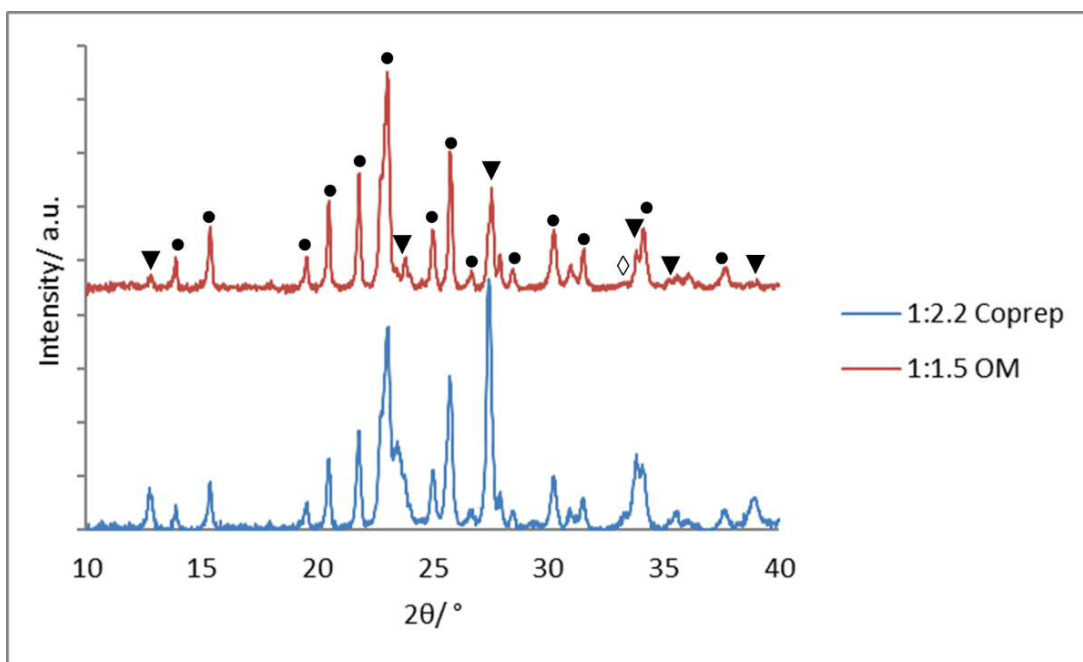


Figure 3.6. Powder XRD patterns of the 1:2.2 Coprep and 1:1.5 OM samples. (Key: ▼ MoO_3 , ● $\text{Fe}_2(\text{MoO}_4)_3$ and ◊ Fe_2O_3).

The 1:2.2 Coprep sample displayed relatively less $\text{Fe}_2(\text{MoO}_4)_3$ phase (65.3 %) with a larger MoO_3 (33.2 %) and Fe_2O_3 (1.5 %) compared to 1:1.5 OM. The relative phase composition of 1:2.2 Coprep was more like the theoretical $\text{Fe}_2(\text{MoO}_4)_3$ (68.2 %) and MoO_3 (31.8 %) content that should be observed by the Fe:Mo ratio used compared to 1:1.5 OM.

3.2.2.3. Raman Spectral Mapping

The Raman spectral mapping results exhibited in Fig. 3.7 further supported the findings from the XRD data, the 1:1.5 OM sample contained of relatively large amounts of $\text{Fe}_2(\text{MoO}_4)_3$ with a very strong peak at 784 cm^{-1} indicating the asymmetric O-Mo-O bond stretch⁴². Peaks at 937, 970 and a broad peak at 990 cm^{-1} has also been associated with symmetric Mo=O from isolated MoO_4 present in $\text{Fe}_2(\text{MoO}_4)_3$ ⁴². 3.7.d displays a minor amount MoO_3 which is similar to observations in XRD results with strong sharp peaks at 821 and 997 cm^{-1} due to the asymmetric Mo-O-Mo and symmetric terminal Mo=O stretch^{43,44} and to a lesser extent a peak at 666 cm^{-1} from the Mo-O-Mo bridging deformation.

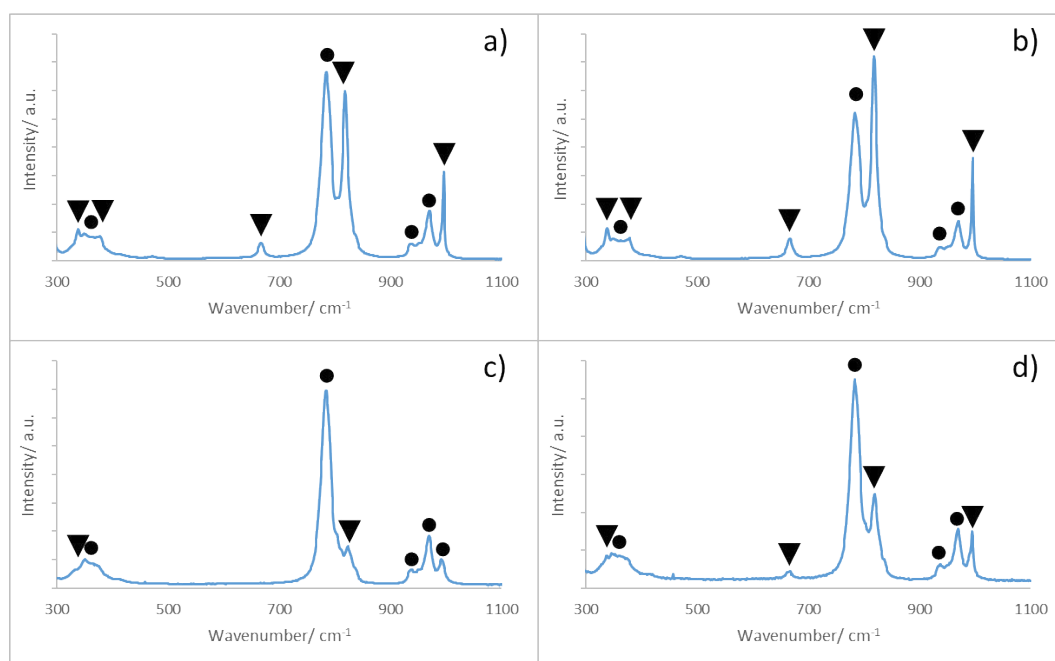


Figure 3.7. Raman spectra of (a,b) 1:2.2 Coprep and (c,d) 1:1.5 OM samples. (Key: ▼ MoO₃ and ● Fe₂(MoO₄)₃).

The Raman spectra of the 1:2.2 Coprep sample displays a substantial amount of Fe₂(MoO₄)₃ with a larger MoO₃ content compared to 1:1.5 OM, again supporting results shown by XRD results (Fig. 3.6), this is expected using the higher Fe:Mo ratio and is shared by House *et al.*⁴⁰ using coprecipitation methods.

One factor to note was the differences between the points surveyed with different phase amounts observed in both samples. This gives an indication of homogeneity with less discrepancy between Raman spectra suggesting higher homogeneity of the sample in question. Both 1:1.5 OM and 1:2.2 Coprep displayed comparable homogeneity with small changes in MoO₃ and Fe₂(MoO₄)₃ content between points.

3.2.2.4. Electron Microscopy and Elemental Mapping

Microscopy results (Fig. 3.8) present clear differences in morphology between the two samples. 1:2.2 Coprep displayed large block formations with smaller particles observed on the surface. EDX mapping results of the corresponding micrographs suggested the surface was highly homogeneous Fe:Mo distribution. Crystallites (1-3 μm) were also presented on

the surface which were found to be molybdenum enriched as highlighted indicating MoO_3 formation on the surface.

1:1.5 OM exhibited varying size, irregular particles of $\text{Fe}_2(\text{MoO}_4)_3$, these particles were significantly larger than the proposed $\text{Fe}_2(\text{MoO}_4)_3$ nanoclusters observed by Oudghiri-Hassani.³⁵ Near iron exclusive areas in 2 μm diameter pits along the surface were also observed which have been suggested to lead to higher total oxidation selectivity when exposed to the surface.^{37–39,45,46} MoO_3 exclusive areas were also observed which could indicate less homogeneous surface composition of the 1:1.5 OM sample compared to the 1:2.2 Coprep sample.

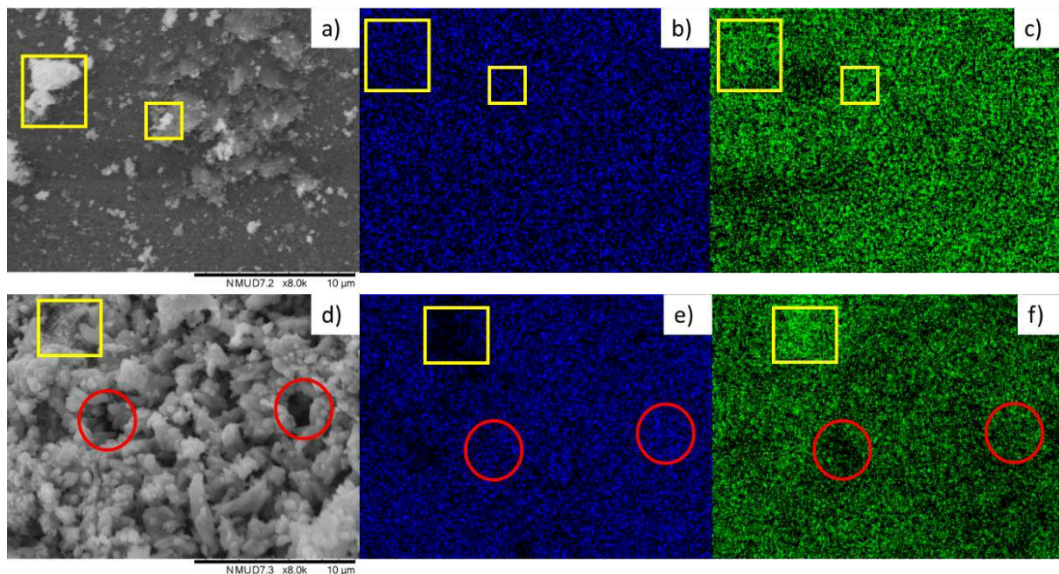


Figure 3.8. SEM micrograph and EDX elemental mapping comparison of 1:2.2 Coprep and 1:1.5 OM samples. (a) SEM image of 1:2.2 Coprep, (b) EDX map showing Fe content of 1:2.2 Coprep, (c) EDX map showing Mo content of 1:2.2 Coprep, (d) SEM image of 1:1.5 OM, (e) EDX map showing Fe content of 1:1.5 OM and (f) EDX map showing Mo content of 1:1.5 OM. Highlighted Fe rich (red circles) and Mo rich (yellow squares).

3.2.3. Methanol Partial Oxidation and Discussion

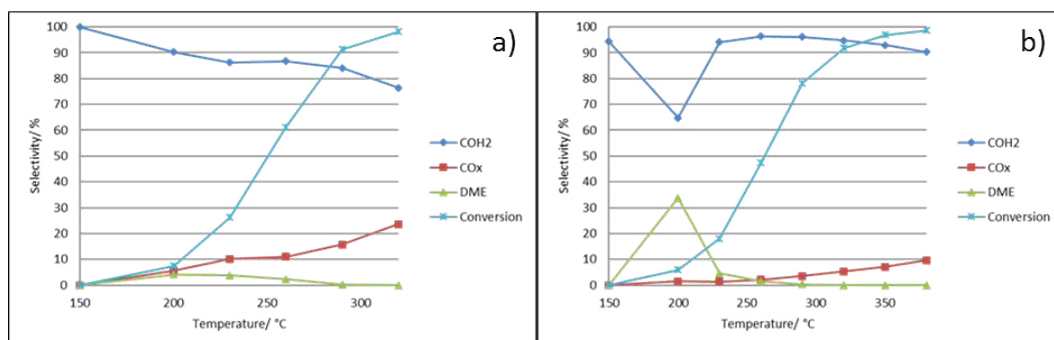


Figure 3.9. Methanol partial oxidation reaction profiles for (a) 1:1.5 OM and (b) 1:2.2 Coprep samples.

The 1:1.5 OM and 1:2.2 Coprep samples were tested as catalysts for methanol partial oxidation over a range of temperatures (Fig. 3.9). Both samples displayed a mixture of products throughout the reaction initially showing high formaldehyde (COH₂) selectivity before a significant increase in dimethyl ether (DME) selectivity at low temperatures and low conversions. Increasing the temperature raised the conversion and formaldehyde selectivity with a decrease in DME observed for both samples. At high temperatures (>290 °C) over 90 % conversion was observed where selectivity towards formaldehyde decreased favouring total oxidation products.

The 1:2.2 Coprep sample displays superior formaldehyde selectivity at high conversions which were achieved at increased temperatures. The 1:1.5 OM sample in contrast showed a significant drop in formaldehyde selectivity at 260 °C decreasing below 70 % at 320 °C. Higher conversions (>90%) were only achieved by 1:2.2 Coprep at temperatures exceeding 320 °C whereas 1:1.5 OM achieved these high conversions before 290 °C.

This higher conversion at lower temperatures and lower selectivity towards formaldehyde of 1:1.5 OM can be attributed to the formation of Fe₂O₃ on the surface, these were found in microscopy results and are suggested to decrease selectivity and increase the low temperature activity.^{37–39,45} The areas of Fe₂O₃ in question as well as crystallites of MoO₃, which would not contribute to overall catalytic results at the temperature range due to their substantially lower activity,^{38,40,47} lead to the 1:2.2 Coprep sample displaying superior maximum formaldehyde yield overall, 90 % compared to 76.8%.

3.3. Effect of Fe:Mo Ratio on Samples Formed Using Oxalate Decomposition Method (OM)

3.3.1. Introduction

In an attempt to improve on the low formaldehyde selectivity produced by the 1:1.5 OM sample a range of materials with different Fe:Mo ratios were synthesised, in a similar manner to previous work undertaken using coprecipitated catalysts^{37,40,48}. This focused on a region of small Mo excess (1:1.7-1:2.2 Fe:Mo) to ascertain what effect this might have on the overall structure and reactivity.

3.3.2. Characterisation

3.3.2.1. BET Surface Area and XPS Surface Analysis

The results from BET the surface areas (Table 3.2) of the iron molybdates synthesised using OM were largely unchanged between Fe:Mo ratios 1:1.5-1:2.2 with the differences between the samples within experimental error. A sharp rise in surface area was observed for 1:3.0 OM sample which is contrary to trends observed by House *et al.*⁴⁰ who saw a reduction in surface area as molybdenum content was raised with the formation of low surface area MoO₃. This rise was however observed by Soares *et al.*⁴⁹ using a sol-gel method attributed to sponge-like MoO₃ morphologies using similar Fe:Mo ratios.

Table 3.2 BET surface area and XPS surface ratio comparison for 1:2.2 Coprep and samples prepared by OM using various Fe:Mo ratios.

Sample	BET Surface Area/ m ² g ⁻¹	XPS Surface Ratios	Rel. Surface Mo Excess/ %
		Fe:Mo	
1:2.2 Coprep	3.9 ± 0.1	1:3.0	36.4
1:1.5 OM	4.4 ± 0.2	1:2.2	46.7
1:1.7 OM	4.3 ± 0.2	1:2.9	70.1
1:1.9 OM	4.5 ± 0.4	1:3.8	100.0
1:2.2 OM	4.6 ± 0.2	1:3.6	63.6
1:3.0 OM	7.0 ± 0.6	1:3.6	20.0

The XPS results of the same samples (Table 3.2) showed a molybdenum excess on the surface of every sample compared to the bulk content. A gradual increase in surface Mo content was observed as Mo bulk content was increased from 1:1.5-1:1.9 to a point where 1:1.9 OM displayed a 100 % Mo excess relative to bulk content on the surface. At higher Mo bulk content (Fe:Mo 1:2.2 and 1:3.0) no increases were observed, this was similar to results shown by House *et al.*⁴⁰ who actually saw a reduction in Mo surface content at Fe:Mo ratios above 1:2.2.

3.3.2.2. Powder XRD Crystallography

Powder XRD results shown in Fig. 3.10 and summarised in Table 3.3 displayed significant changes as Fe:Mo ratios were altered using OM. The highest relative Fe₂(MoO₄)₃ content was observed by both 1:1.5 OM and 1:1.7 OM samples which were comparable to one another. Increased Mo content saw a decrease in Fe₂(MoO₄)₃ content with both 1:2.2 OM and 1:1.9 OM both displaying comparable Fe₂(MoO₄)₃ content (≈70 %). Further Mo addition lowers relative Fe₂(MoO₄)₃ content to below 50 % as MoO₃ content increased.

Significantly lower $\text{Fe}_2(\text{MoO}_4)_3$ content was observed by 1:1.9 OM compared to the theoretical composition which might be due the inhibition of $\text{Fe}_2(\text{MoO}_4)_3$ crystal growth caused by MoO_3 as reported by Borsov *et al.*⁵⁰, this same phenomena was also observed more recently by Soares *et al.* using a sol-gel preparation method.⁴⁹ Due to the sensitivity limit of XRD, any amorphous $\text{Fe}_2(\text{MoO}_4)_3$ produced could not be detected.

The Fe_2O_3 content was highest in the 1:1.9 OM and 1:3.0 OM samples followed by the 1:2.2 Coprep sample. The lowest Fe_2O_3 content was observed by the 1:2.2 OM, 1:1.7 OM and 1:1.5 OM samples. The higher Fe_2O_3 content of the 1:1.9 OM and 1:3.0 OM samples is contrary to results shown in other studies^{37,40,48} as the Fe_2O_3 should be removed with the formation of $\text{Fe}_2(\text{MoO}_4)_3$ by the solid-state reaction with MoO_3 , which for both examples was in excess. This may indicate inadequate mixing of the iron and molybdenum either prior to calcination or caused by the decomposition of the oxalate precursors forming larger areas of Fe_2O_3 .

Table 3.3 Relative phase composition of OM samples produced using various Fe:Mo ratios corresponding to XRD results shown in Fig. 3.10

Sample	Relative % Phase Based On Powder XRD Results			Ideal Theoretical % Phase Composition	
	$\text{Fe}_2(\text{MoO}_4)_3$	MoO_3	Fe_2O_3	$\text{Fe}_2(\text{MoO}_4)_3$	MoO_3
1:2.2 Coprep	65.3	33.2	1.5	68.2	31.8
1:1.5 OM	85.7	13.5	0.8	100.0	0.0
1:1.7 OM	86.0	13.1	0.9	88.2	11.8
1:1.9 OM	69.6	28.5	2.0	78.9	21.1
1:2.2 OM	71.0	27.9	1.1	68.2	31.8
1:3.0 OM	48.4	49.5	2.1	50	50

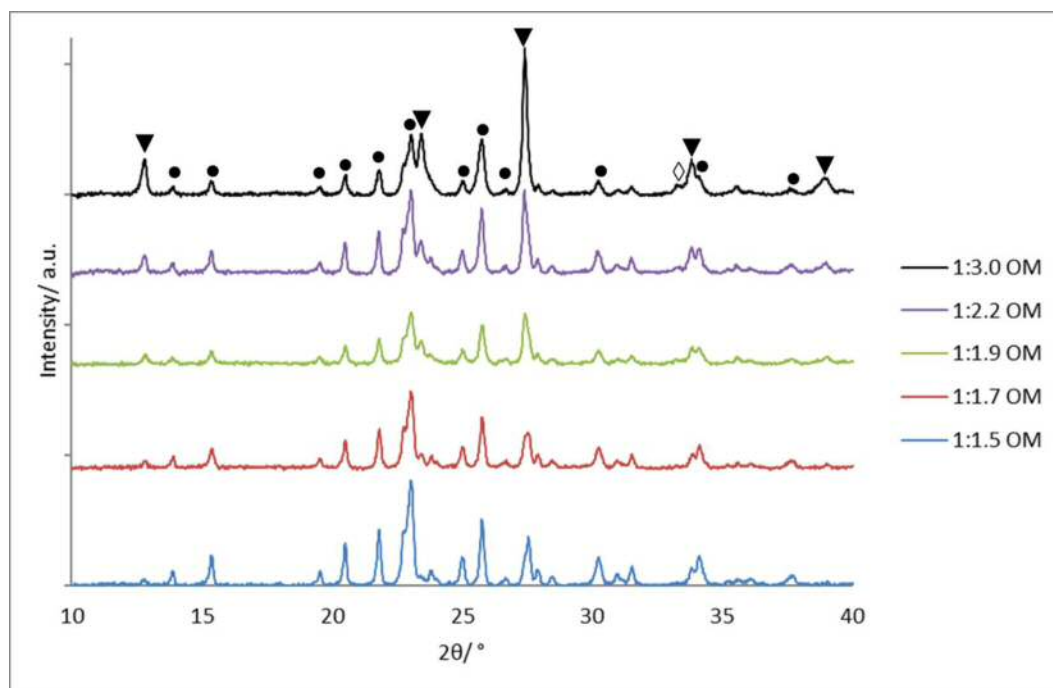


Figure 3.10 Powder XRD patterns of samples prepared using OM using various Fe:Mo ratios. (Key: ▼ MoO₃, ● Fe₂(MoO₄)₃ and ◊ Fe₂O₃).

3.3.2.3. Raman Spectral Mapping

Raman spectral mapping results of OM samples prepared using various Fe:Mo ratios are shown in Fig. 3.11. The most common spectra for each sample is represented as 3.11.a, 3.11.d, 3.11.g, 3.11.j and 3.11.m for 1:1.5 OM, 1:1.7 OM, 1:1.9 OM, 1:2.2 OM and 1:3.0 OM respectively.

The 1:1.5 OM displayed the most Fe₂(MoO₄)₃ content overall with most of points displaying only minor amounts of MoO₃. 1:1.7 OM-1:2.2 OM samples showed similarity between the majority of their points surveyed, these results matched those obtained by House *et al.*⁴⁰ using 1:2.2 Fe:Mo ratio sample produced using coprecipitation methods. The 1:3.0 OM presented with far higher MoO₃ content than the other samples with Fe₂(MoO₄)₃ only present in small amounts.

The homogeneity of the samples varied as Fe:Mo ratios were altered, 1:1.5 OM, 1:2.2 OM and 1:3.0 OM displayed the highest homogeneity with little change observed between the points surveyed. 1:1.7 OM presented a number of areas of near Fe₂(MoO₄)₃ exclusivity similar to results shown by 1:1.5 OM although these areas were rarely observed. The 1:1.9 OM sample was the least homogeneous based on Raman spectral results with a range of

different points observed with higher MoO₃ content, some areas had near MoO₃ exclusive content (3.11.h) very similar to 1:3.0 OM samples.

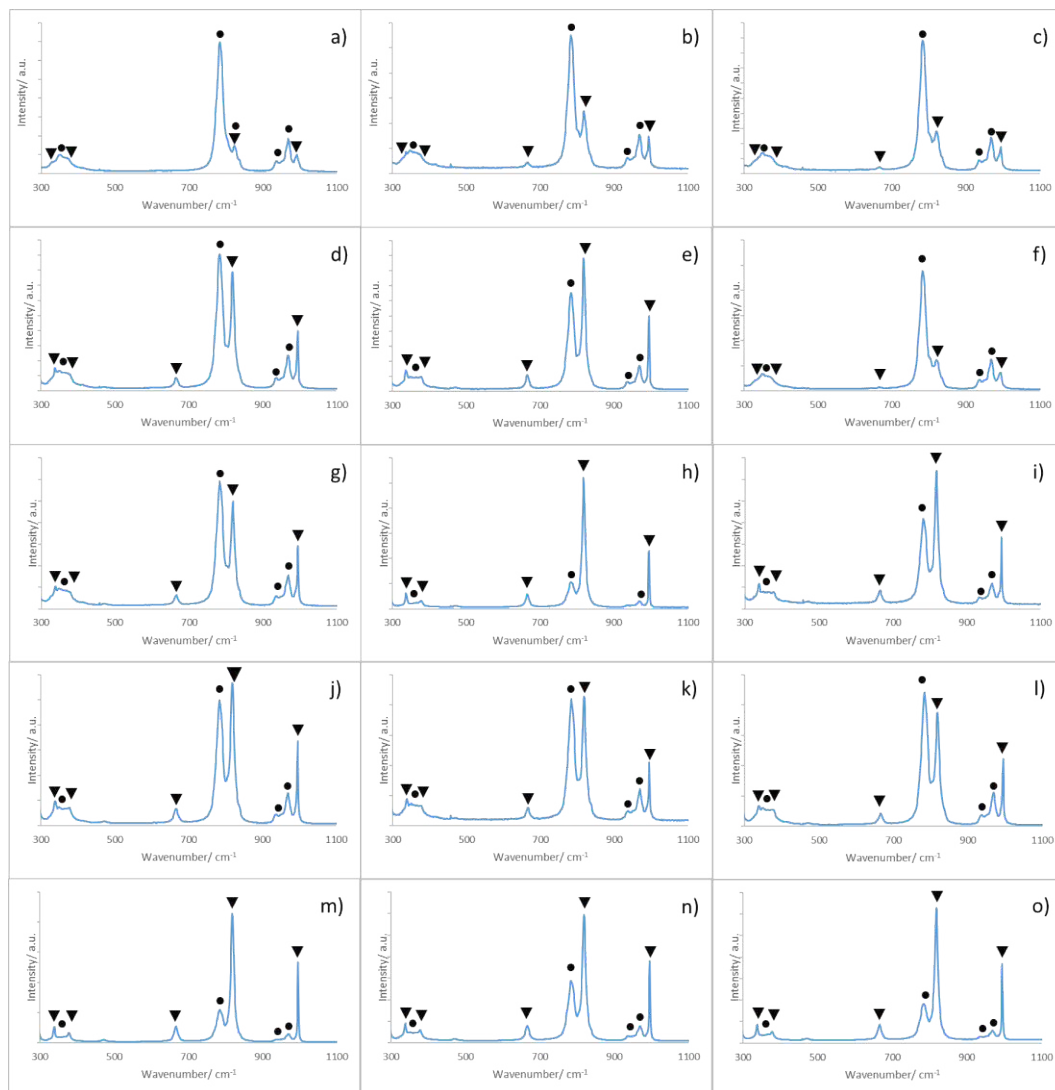


Figure 3.11. Raman spectral mapping of (a-c)1:1.5 OM, (d-f)1:1.7 OM, (g-i)1:1.9 OM, (j-l)1:2.2 OM and (m-o)1:3.0 OM samples. (Key: ▼ MoO₃ and ● Fe₂(MoO₄)₃).

3.3.2.4. SEM Imaging and EDX Surface Mapping

The microscopy results shown in Fig. 3.12 display dramatic changes in morphology as Fe:Mo ratios were altered. Both 1:1.5 OM and 1:1.7 OM both presented large variably sized compact particles. The 1:1.9 OM sample displayed what looked like the agglomeration of the particles observed in the previous examples forming a lamellar like structure broken up by 2 μm diameter holes. The 1:2.2 OM sample presented further changes in morphology forming sponge-like structures similar to those observed by Soares *et al.*^{49,51} formed using a sol-gel method. The 1:3.0 OM catalyst presented with a lamellar like structure broken up with large concentrations of holes similar to 1:1.9 OM.

EDX mapping of the corresponding images suggested that both 1:2.2 OM and 1:1.7 OM were the most homogeneous with iron and molybdenum evenly distributed over the surface. Some areas of iron and molybdenum enrichment were observed for both samples but neither of these were found to be elementally exclusive.

Both 1:1.9 OM and 1:3.0 OM presented with large areas of near molybdenum exclusivity as highlighted suggesting MoO_3 production. The holes observed in both examples were found to be highly iron rich suggesting the formation of Fe_2O_3 possibly caused by the decomposition of isolated iron oxalate. 1:1.5 OM as stated previously contained a combination of Fe and Mo exclusive areas suggesting Fe_2O_3 and MoO_3 formation on the surface of the catalyst.

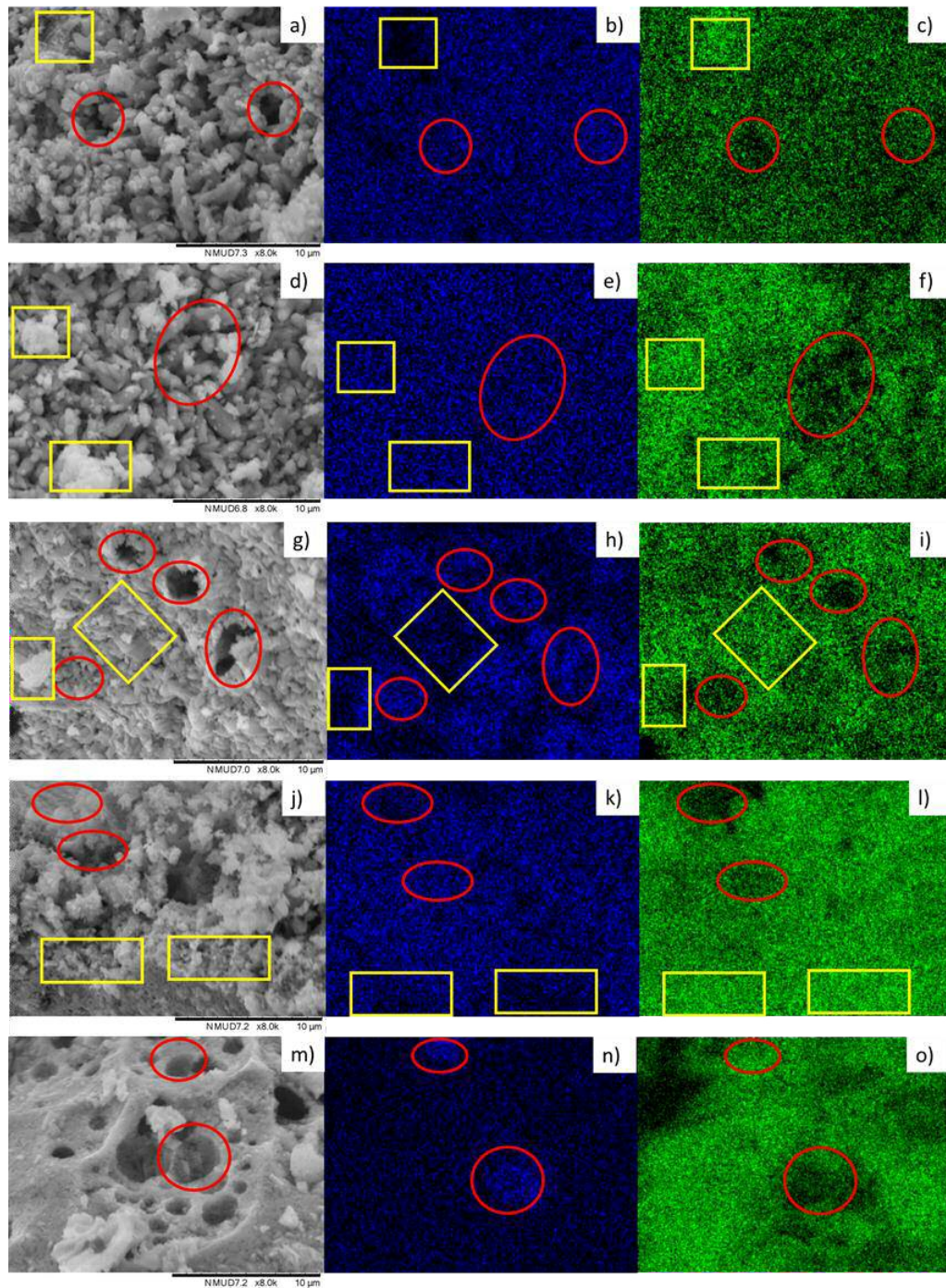


Figure 3.12. SEM and EDX elemental mapping comparison of OM samples prepared using a variety of Fe:Mo ratios. (a) SEM image of 1:1.5 OM, (b) EDX map showing Fe content of 1:1.5 OM, (c) EDX map showing Mo content of 1:1.5 OM, (d) SEM image of 1:1.7 OM, (e) EDX map showing Fe content of 1:1.7 OM, (f) EDX map showing Mo content of 1:1.7 OM, (g) SEM image of 1:1.9 OM, (h) EDX map showing Fe content of 1:1.9 OM, (i) EDX map showing Mo content of 1:1.9 OM, (j) SEM image of 1:2.2 OM, (k) EDX map showing Fe content of 1:2.2 OM, (l) EDX map showing Mo content of 1:2.2 OM, (m) SEM image of 1:3.0 OM, (n) EDX map showing Fe content of 1:3.0 OM and (o) EDX map showing Mo content of 1:3.0 OM. Highlighted Fe rich (red circles) and Mo rich (yellow squares).

3.3.3. Methanol Partial Oxidation Study

The methanol partial oxidation results of the OM samples prepared using different Fe:Mo ratios (Fig. 3.13) displayed some significant differences between samples.

The activity of the samples was shown to decrease in the order 1:3.0 OM > 1:1.5 OM > 1:2.2 OM > 1:1.7 OM > 1:1.9 OM > 1:2.2 Coprep. All OM samples were more active than 1:2.2 Coprep throughout which was only able to attain high conversion (>95 %) at 350 °C. At 290 °C the difference between conversions all the OM samples was small (9 %), all attaining over 85 % conversion at this temperature. High methanol conversions (>95 %) were attained by all OM samples by 320 °C.

The formaldehyde selectivity for all but 1:1.9 OM was highest at 260 °C with significant variation between the Fe:Mo ratios used decreasing in the order 1:2.2 Coprep \approx 1:2.2 OM > 1:1.7 OM > 1:3.0 OM > 1:1.9 OM > 1:1.5 OM. At 290 °C formaldehyde selectivity decreased rapidly for 1:3.0 OM and 1:1.5 OM catalyst in favour of CO_x products. Formaldehyde selectivity was shown to decrease gradually as reaction temperatures were raised for the other samples maintaining over 90 % selectivity up to 350 °C.

Table 3.4 Maximum formaldehyde yield summary of 1:2.2 Coprep and OM samples prepared using different Fe:Mo ratios.

Sample	Maximum Formaldehyde Yield/ %	Temperature / °C
1:2.2 Coprep	90.0	350
1:1.5 OM	76.8	290
1:1.7 OM	91.2	320
1:1.9 OM	89.3	335
1:2.2 OM	92.6	320
1:3.0 OM	87.1	320

The effect these had on the maximum formaldehyde yield attained by the samples is shown in Table 3.4. The highest yields were attained by 1:2.2 OM closely followed by 1:1.7 OM both surpassing the 1:2.2 Coprep comparison sample at significantly lower

temperature(320 °C). The next best catalyst was 1:1.9 OM which produced a 89.3 % formaldehyde yield at the higher temperature of 335 °C due to the lower activity and selectivity of the sample. The 1:3.0 OM samples presented a further decline in formaldehyde yield with CO_x selectivity increased throughout. The worst formaldehyde yield was attained by 1:1.5 OM which presented the highest CO_x selectivity even at low temperatures.

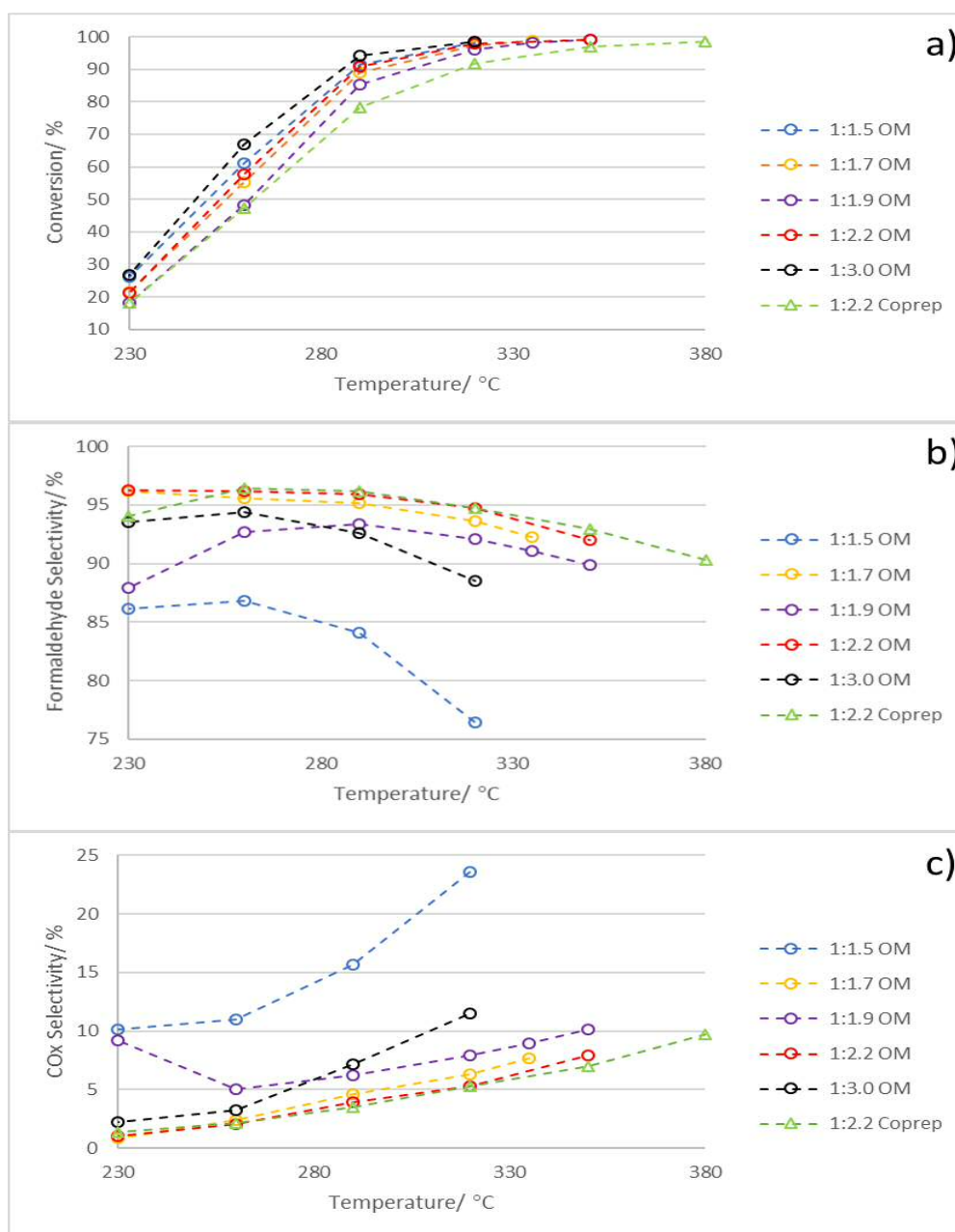


Figure 3.13. MeOH partial oxidation reaction summary of samples synthesised using OM method with different Fe:Mo ratios compared to 1:2.2 Coprep sample showing variations in a) Conversion, b) formaldehyde selectivity and c) CO_x selectivity over a range of temperatures.

3.3.4. Precalcination study

3.3.4.1. XPS of Uncalcined Oxalate Mixtures

As described in section 3.1.3. oxomolybdate oxalate comes in two distinct forms with the formation of both Mo^V dimer complexes through $[\text{Mo}_2\text{O}_4]^{2-}$ central metal units complexed with oxalic acid²⁷. Mo^{VI} was found to form $\{[\text{MoO}_3(\text{C}_2\text{O}_4)]^{2-}\}_n$ ²⁶ which could promote the formation of polymeric MoO₃ through the Mo-O-Mo bond present between complexed units, this could be detrimental if formed in large volumes causing isolation from iron cations.

XPS analysis of Mo could give good indication as to the species that may have formed during the melting that occurs in the initial heat treatment step. This is due to Mo^{IV}, Mo^V and Mo^{VI} having clearly defined binding energies for Mo 3d_{5/2}-Mo 3d_{3/2} doublets of 229.9 eV and 233.0 eV, 231.2 eV and 234.3 eV also 232.5 eV and 235.6 eV respectively⁵². Using standard coprecipitation methods resulted in the formation of only Mo^{VI} species as expected due to the precipitation of both Fe₂(MoO₄)₃ and MoO₃ prior to calcination.

All OM samples presented with varying quantities of both Mo^V and Mo^{VI}. Both 1:1.9 OM and 1:3.0 OM samples presented the lowest amounts of Mo^V which may be the reason why 1:1.9 OM displayed relatively high amounts of MoO₃ and the limited of Fe₂(MoO₄)₃ production. The formation of Mo^{VI} polymeric species may dominate which, together with the lack of iron within the reaction mixture, could result in the crystalline MoO₃ production observed in characterisation results in Section 3.3.2. 1:3.0 OM which also presented with very high MoO₃ content(49.5 %) though this may be explained by far higher Mo excess in production.

Large amounts of Mo^V are also present in the 1:1.5 OM, 1:1.7 OM and 1:2.2 OM samples which may have caused the intermixing of Fe and Mo oxalates prior to calcination rather than Mo^{VI} species. The formation of molybdenum (V) oxalate could prevent the formation of polymeric molybdena species during the melting step which could increase the surface exposed to iron prior to decomposition. This may have caused the lower quantities of inactive MoO₃ present in 1:1.7 OM and 1:2.2 OM compared to 1:2.2 Coprep.

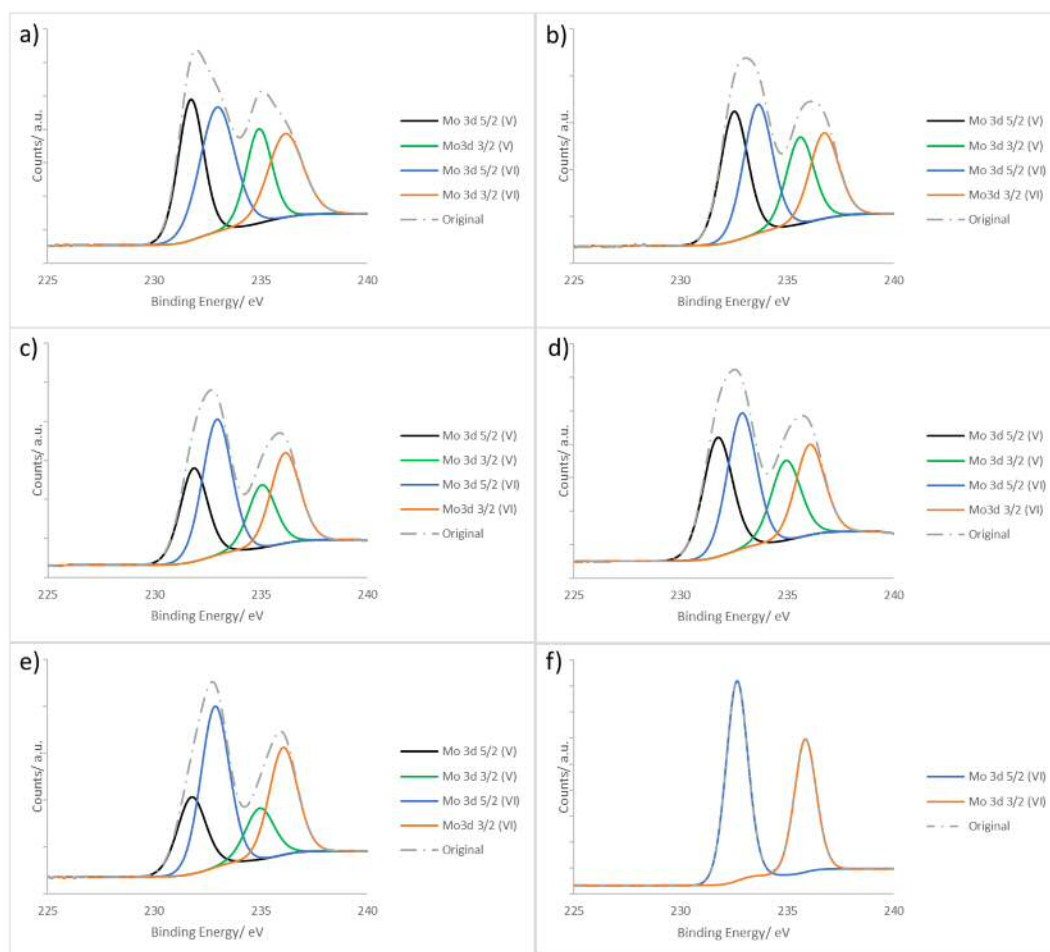


Figure 3.14 XPS spectra of Mo 3d region of uncalcined OM and Coprep samples. (a) 1:1.5 OM, b) 1:1.7 OM, c) 1:1.9 OM, d) 1:2.2 OM, e) 1:3 OM and f) 1:2.2 Coprep)

3.3.4.2 Thermalgravimetric Analysis

The DTG of the OM samples shown in Fig. 3.15 and corresponding TGA results presented in Table 3.5 displayed two large regions of mass loss for all OM samples. Initial losses at 140-200 °C which corresponded to iron oxalate decomposition in air as observed previously.^{18,19} The second major feature was between 230-290 °C which was suggested to be the decomposition of oxomolybdate oxalate which is again supported by literature examples.²⁸⁻³⁰ Mass loss between 325-350 °C was thought to be due to the decomposition of ammonium molybdate species to form crystalline MoO₃.⁵³ Another minor change observed at 350-400 °C was attributed to the formation of Fe₂(MoO₄)₃ during a solid phase reaction between Fe₂O₃ and MoO₃ species.⁵⁴

In all examples there was an overlap between the iron and molybdenum oxalate decompositions between 200-230 °C, this may be a secondary catalytic decarboxylation of oxomolybdate oxalate similar to results shown by Majumdar *et al.*²⁰ Their findings using $\text{FeC}_2\text{O}_4 \cdot 2\text{H}_2\text{O}$ and $\text{ZnC}_2\text{O}_4 \cdot 2\text{H}_2\text{O}$ mixtures saw significant decrease of zinc oxalate decomposition temperatures, this was achieved by the exothermic catalytic oxidation of CO to CO_2 over Fe_3O_4 and the oxidation of Fe_3O_4 to Fe_2O_3 as shown in Equation 3.6 and 3.4 respectively. This caused localised high temperatures around these decomposition centres causing the activation of neighbouring carboxylate species. Increases in this overlapped region may give an indication of mixing of the oxalates and possibly the overall homogeneity of the material produced post calcination.

The quantity of isolated iron oxalate (140-200 °C) was shown to decrease in the order 1:1.5 OM > 1:1.7 OM > 1:3.0 OM > 1:2.2 OM > 1:1.9 OM. The high iron oxalate content observed for both 1:1.5 OM and 1:1.7 OM could be caused by the higher Fe content of the samples, 1:3.0 OM however could suggest inadequate mixing of the oxalates due to the higher molybdenum content so should be more diluted in the oxalate mixture.

Molybdenum oxalate decomposition (230-290 °C) was a significant part of the TGA results for all samples decreasing in significance in the order, 1:1.9 OM > 1:3.0 OM > 1:1.7 OM > 1:2.2 OM > 1:1.5 OM. Both 1:1.9 OM and 1:3.0 OM presented substantially higher isolated molybdenum oxalate content based on TGA results which may indicate why both samples contained large areas of isolated MoO_3 post calcination.

The overlap between the two oxalate species (200-230 °C) indicating a possible activation of the molybdenum oxalate by neighbouring exothermic decomposition of iron oxalate was shown to decrease in significance in the order, 1:2.2 OM > 1:1.5 OM > 1:1.7 OM > 1:1.9 OM > 1:3.0 OM.

The final decomposition between 325-350 °C indicating the loss of ammonia from ammonium molybdate was highest for 1:1.5 OM possibly indicating some uncomplexed ammonium molybdate in the oxalate mixture. The other samples presented similar mass losses in this region (1.9-2.6 %).

Based on the DTG/TGA results the 1:2.2 OM sample presented the highest mixing of the oxalates based on the overlapping region between the two oxalates. It also contained the second lowest quantities of isolated iron and molybdenum oxalate based on TGA mass loss.

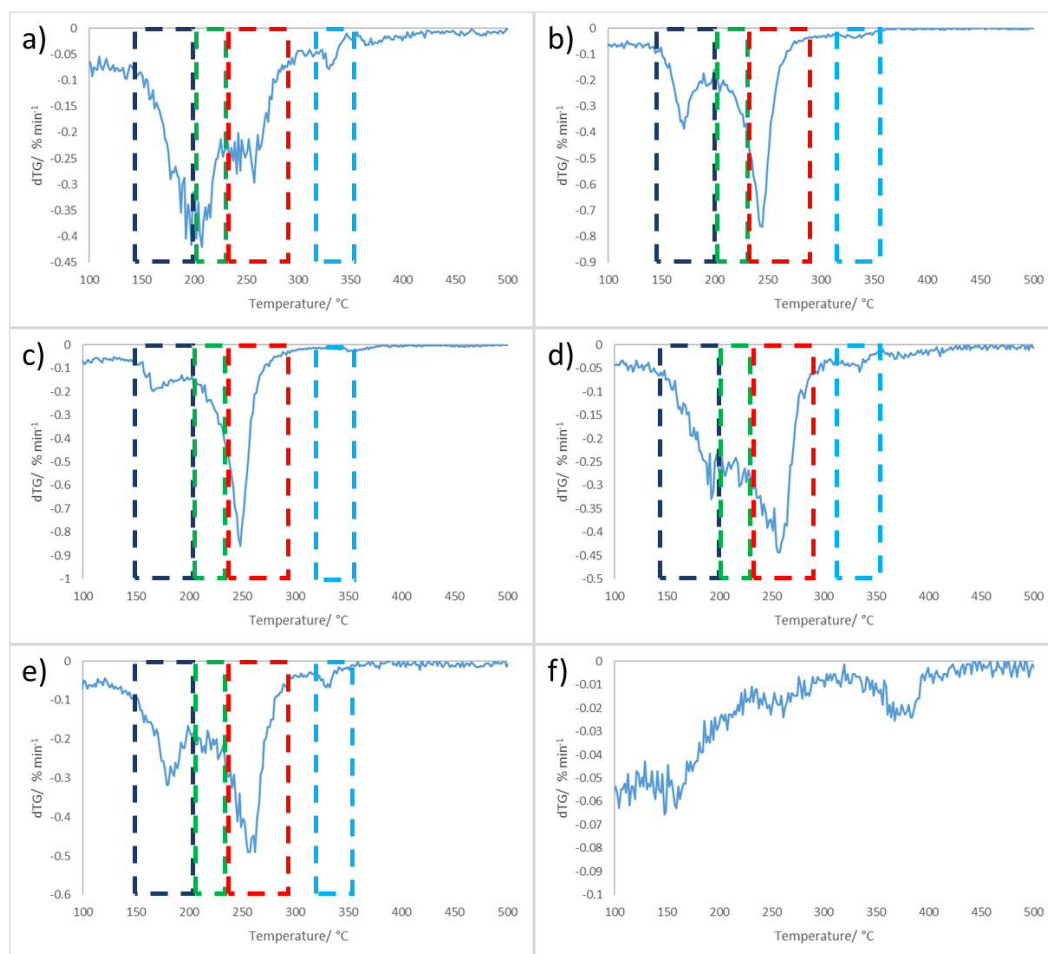


Figure 3.15 DTG Analysis of uncalcined samples of both OM and Coprep samples ranging from 100-500 °C using a ramp rate of 5 °C min⁻¹ (a) 1:1.5 OM, b) 1:1.7 OM, c) 1:1.9 OM, d) 1:2.2 OM, e) 1:3.0 OM and f) 1:2.2 Coprep)

Table 3.5 TGA comparison of OM samples prepared using various Fe:Mo ratios corresponding to regions highlighted in DTG results in Fig. 3.15.

TGA Temperature Range/ °C	Percentage Weight Loss/ %				
	1:1.5 OM	1:1.7 OM	1:1.9 OM	1:2.2 OM	1:3.0 OM
140-200	12.8	12.6	8.6	10.5	12.5
200-230	10.4	8.3	7.7	13.2	6.3
230-290	11.2	17.2	20.6	14.0	18.8
325-350	4.0	2.2	1.9	2.6	2.5

3.3.5. Discussion of the Effect of the Fe:Mo Ratio for the Oxalate Decomposition Method Samples

Based on the catalytic performance of the OM samples, it seems that the oxalate decomposition method is highly sensitive to changes in Fe:Mo ratios. Overall all the OM samples were more active than the comparison 1:2.2 Coprep sample possibly due to the different morphologies created out of the decomposition of the oxalate precursors.

The best samples based on catalytic performance were 1:2.2 OM and 1:1.7 OM which produced 92.6 % and 91.2 % formaldehyde yield respectively at 320 °C. Possible reasons for the improved performance may be due to the increase in overall iron and molybdenum distribution, leading to high $\text{Fe}_2(\text{MoO}_4)_3$ production as observed in XRD and minimal elemental enrichment observed in EDX mapping results.

The 1:1.9 OM sample was next best achieving a maximum yield of 89.3 % at 335 °C. Lower activity was observed throughout possibly due to the surface distribution of molybdena, the highest Mo content observed in XPS results which were then shown to be forming the bulk of the exposed surface in Microscopy and EDX results. Bulk observations also indicated the second highest MoO_3 content in XRD and isolated areas of near exclusive MoO_3 content in Raman spectral mapping. The crystalline MoO_3 does not contribute significantly at low temperatures due to the low number of active sites compared to more amorphous MoO_3 over $\text{Fe}_2(\text{MoO}_4)_3$.^{37,46} Lower formaldehyde selectivity could be explained by a rise in Fe_2O_3 content XRD which were found to be localised to void structures observed over the surface in microscopy results, Fe_2O_3 has been proven to favour CO_x products.^{38,41,55} This may also account for the lack of surface area change observed with increased MoO_3 production which has been found to decrease with increase MoO_3 content presented in other studies.^{37,40}

The catalytic performance of 1:3.0 OM presented further reduction in formaldehyde yield (87.1 % at 320 °C), this is due to the same heterogeneous composition observed in 1:1.9 OM results but to a greater extent. MoO_3 was the dominant species in all characterisation results and was shown to make up the majority of the surface in microscopy results. Fe_2O_3 was also presented in larger quantities in XRD which, like 1:1.9 OM, was observed to be

isolated to void structures on the surface although these voids were localised into concentrated areas.

The worst catalytic performance was achieved by 1:1.5 OM which produced significant CO_x amounts even at low temperatures. This caused only a maximum formaldehyde yield of 76.8 % at 290 °C. This is thought to be due to the formation of Fe₂O₃ and MoO₃ on the surface of the catalyst as observed in microscopy results. Similar yields have been presented by other authors using Fe:Mo ratios of 1:1.5 using other synthesis methods.^{40,48}

The differences between these samples is thought to be due to the mixing of the oxalates prior to calcination, higher mixing was determined by DTG/TGA with larger quantities of isolated iron oxalate, molybdenum oxalate and ammonium molybdate. An indication of better mixing was suggested with better overlap between the two oxalate decomposition, this suggested possible activation of molybdenum oxalate by the exothermic decomposition iron oxalate and secondary catalytic reaction suggested by Majumdar *et al.*²⁰ This method relies on close proximity of the two oxalates for the activation to occur.

Based on these observations, 1:2.2 OM had the best mixing of the oxalates with the largest overlap and second lowest amounts of both isolated oxalates. The 1:1.7 OM sample was the next best with significantly higher quantities of isolated oxalates observed. The 1:1.9 OM sample presented the highest molybdenum oxalate content but also significant decrease in iron oxalate but due to the inadequate mixing, the iron oxalate was shown to decompose forming large Fe₂O₃ voids observed in microscopy results. Similar observations were also presented by the 1:3.0 OM sample to a greater extent with localised areas of iron oxalate decomposing to form groups of these void structures. The highest isolated iron oxalate and ammonium molybdate content was present in the 1:1.5 OM sample, even though a significant overlap was observed between iron and molybdenum oxalate, the oxalate decomposition method was shown to be unable to adequately mix the precursors required to prevent Fe₂O₃ formation on the surface.

Improvements in oxalate mixing observed in 1:2.2 OM and 1:1.7 OM may be due to the increased formation of Mo^V oxalate²⁷, this was thought to prevent the formation of polymeric molybdenum oxalate species by preventing the formation of Mo-O-Mo bonding between molybdenum centres.²⁶ Mo^{VI} was the dominant molybdenum oxidation state of both 1:1.9 OM and 1:3.0 OM samples, both of which had high isolated molybdenum oxalate prior to calcination and which translated into MoO₃ dominating the composition of both samples post calcination.

3.4. Effect of Water Addition into Oxalate Mixtures

3.4.1 Introduction

The solubility effect of oxalic acid concentrations have been investigated for both molybdenum⁵⁶ and iron⁵⁷ finding that both are highly sensitive to the pH and oxalate concentration changes associated with dilution.

In this section effect of varying solvation of the iron, molybdenum and oxalic acid mixture was investigated and what effect this had on the mixing potential of the method. A possibility for this change may be due to a different mechanism for phase formation would occur such as those observed in coprecipitation methods described previously. Introducing varying amounts of water to the 1:2.2 OM mixture before refluxing at 100 °C for 2 h prior to evaporation and standard calcination was investigated.

1:2.2 OM was added as comparison and discussed in detail in Section 3.3 therefore not in this section.

3.4.2. Characterisation

3.4.2.1. BET and XPS surface analysis

The surface area of the OM samples was shown to alter substantially with differing water content in the initial precursor mixtures as exhibited in Table 3.5. 15 ml 1:2.2 displayed the lowest surface area with both 1:2.2 OM and 25 ml 1:2.2 displaying a 24 % and 27 % increase respectively. 5 ml and 10 ml 1:2.2 samples displayed the highest surface area which presented over double that observed by 15 ml 1:2.2.

The XPS surface analysis shown in Table 3.5 displays a trend as various water contents were added to the OM mixtures. The 1:2.2 OM samples displays a substantial excess of molybdenum on the surface compared to bulk content. Addition of small amounts of water (5 ml and 10 ml) the surface excess nearly doubled. Further addition of water caused a

decrease in surface molybdenum content and by extension molybdenum surface excess dropping below the surface content displayed by 1:2.2 OM once 25 ml of water was added.

Table 3.6 BET surface area and XPS surface ratio comparison for OM samples produced using varying volumes of water addition to OM mixture.

Sample	BET Surface Area/ m^2g^{-1}	XPS Surface Ratios	Rel. Surface Mo Excess/ %
		Fe:Mo	
1:2.2 OM	4.6 ± 0.2	1:3.6	63.6
5 ml 1:2.2	7.5 ± 0.6	1:4.8	118.2
10 ml 1:2.2	8.4 ± 0.9	1:4.8	118.2
15 ml 1:2.2	3.7 ± 0.4	1:3.8	72.7
25 ml 1:2.2	4.8 ± 0.2	1:3.2	45.5

3.4.2.2. Powder XRD Crystallography

The bulk composition of 1:2.2 OM samples was shown to change depending on water added to the precursor mixtures as shown in XRD results in Fig. 3.16 and the corresponding results displayed in Table. 3.6. All samples displayed a combination of $\text{Fe}_2(\text{MoO}_4)_3$, MoO_3 and Fe_2O_3 phases. The relative $\text{Fe}_2(\text{MoO}_4)_3$ content increased in the following order 10 ml 1:2.2 > 5 ml 1:2.2 > 15 ml 1:2.2 > 1:2.2 OM > 25 ml 1:2.2, MoO_3 content decreased in the same order.

Fe_2O_3 content for all samples remained below 3.5 % for all samples, the content decreased in the following order 15 ml 1:2.2 > 10 ml 1:2.2 > 5 ml 1:2.2 > 25 ml 1:2.2 > 1:2.2 OM.

Addition of water seemed to have no effect on crystal size with little change observed with peak width remaining unchanged as water was added in the post calcined samples.

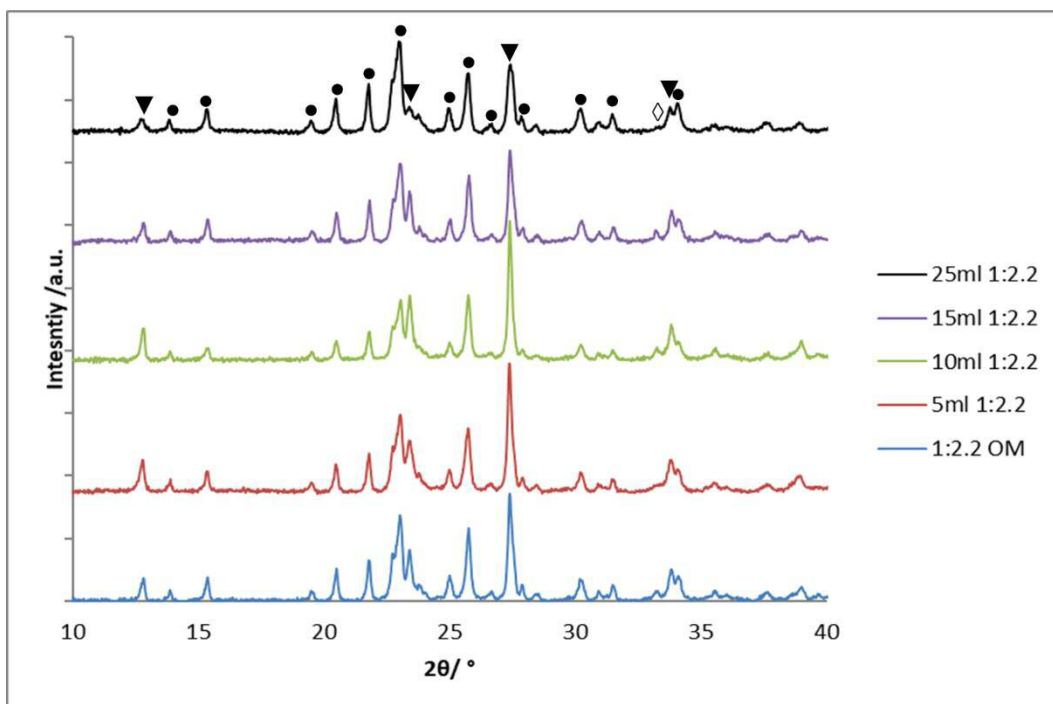


Figure 3.16 Powder XRD patterns of samples prepared using OM using varying additions of water to OM mixture. (Key: ▼ MoO_3 , ● $\text{Fe}_2(\text{MoO}_4)_3$ and ◇ Fe_2O_3).

Table 3.7 Relative phase composition of 1:2.2 OM samples produced using various water additions to the oxalate mixture corresponding to XRD results shown in Fig. 3.16.

Sample	Relative % Phase Based On Powder XRD Results		
	$\text{Fe}_2(\text{MoO}_4)_3$	MoO_3	Fe_2O_3
1:2.2 OM	71.0	27.9	1.1
5 ml 1:2.2	54.6	43.1	2.3
10 ml 1:2.2	50.0	47.6	2.4
15 ml 1:2.2	66.7	30.1	3.2
25 ml 1:2.2	75.6	22.9	1.5

3.4.2.3. Raman Spectral Mapping

Raman spectral mapping shown in Fig. 3.17. presents significant changes in composition as water was added to the OM mixture. The most common points for each sample are shown as 3.17.a, 3.17.d, 3.17.j and 3.17.m for 1:2.2 OM, 5 ml 1:2.2, 15 ml 1:2.2 and 25 ml 1:2.2 respectively.

The 1:2.2 OM, 5 ml 1:2.2 and 25 ml 1:2.2 samples were nearly identical with a mixture of $\text{Fe}_2(\text{MoO}_4)_3$ and MoO_3 similar to results shown by House *et al.*⁴⁰ utilising the same Fe:Mo ratio. The 15 ml 1:2.2 displayed near exclusive $\text{Fe}_2(\text{MoO}_4)_3$ content in the majority of the points surveyed similar to 1:1.5 OM presented in Section 3.2.2.3.

The 5 ml 1:2.2 and 15 ml 1:2.2 samples indicated low homogeneity with some regions of higher MoO_3 content, a small number of areas with near exclusive MoO_3 content were also observed. The 0 ml 1:2.2 and 25 ml 1:2.2 samples exhibited very little change between points surveyed which indicated a more homogeneous distribution of iron and molybdenum in the calcined samples.

10 ml 1:2.2 did not have a single common composition, instead a mixture of results with near exclusive areas of $\text{Fe}_2(\text{MoO}_4)_3$ (3.17.g) and MoO_3 (3.17.h and 3.17.i) observed over the survey with little results in between. Small quantities of Fe_2O_3 were seen in areas of more iron enrichment (3.17.g) not typically observed due to its low Raman sensitivity relative to molybdates with small peaks observed at 600 cm^{-1} and 410 cm^{-1} .^{37,40}

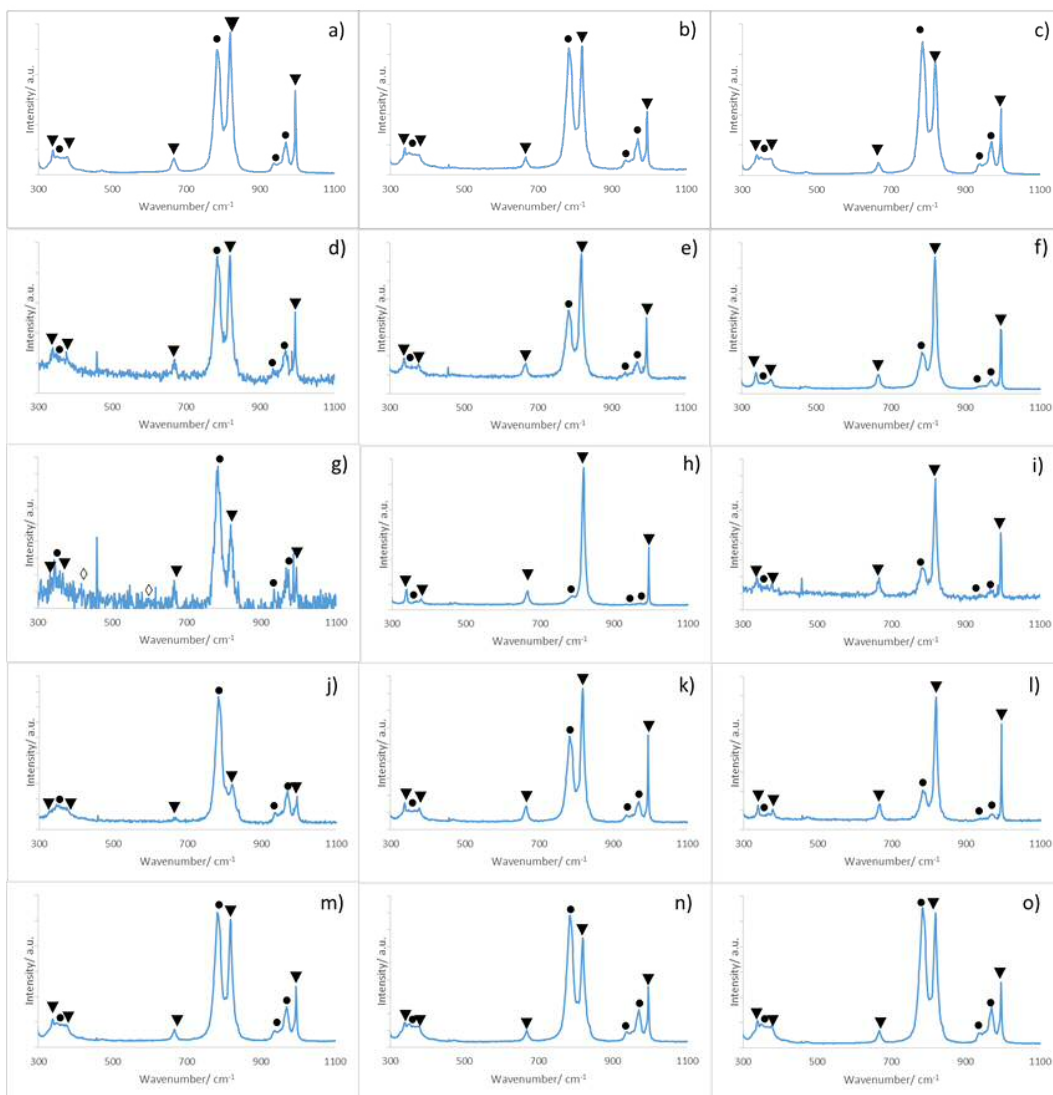


Figure 3.17 Raman spectral mapping of (a-c) 1:2.2 OM, (d-f) 5 ml 1:2.2, (g-i) 10 ml 1:2.2, (j-l) 15 ml 1:2.2 and (m-o) 25 ml 1:2.2 samples. (Key: ▼ MoO₃, ● Fe₂(MoO₄)₃ and ◇ Fe₂O₃)

3.4.2.4. SEM and EDX Surface Elemental Mapping

Microscopy results (Fig. 3.18) presented clear differences between samples produced using OM with varying water additions into the precursor mixtures.

Sponge-like morphologies were observed of the 0 ml 1:2.2 sample similar to those observed by Soares *et al.*^{49,51} Both 5 ml and 10 ml 1:2.2 samples were composed of irregular block formations areas of sponge-like morphology observed along the surface. Crystallite formations were also observed on the surface of 5 ml 1:2.2. The 15 ml 1:2.2 sample displayed a mixture of large agglomerated particle formations and rounded crystallites. Morphology very similar to 1:2.2 Coprep presented in Section 3.2.2.4 were observed by the 25 ml 1:2.2 with the formation of regular large block structures with crystallites formed on the surface, void (1-2 μm) structures were also observed over the surface similar to other OM samples.

Corresponding EDX mapping results of the micrographs suggested that the surfaces of both 1:2.2 OM and 25 ml 1:2.2 displayed even distribution of iron and molybdenum. Some areas of both iron and molybdenum enrichment were observed as highlighted but none were elementally exclusive.

The 5 ml and 15 ml 1:2.2 samples displayed less iron and molybdenum distribution over the surface with many areas of both iron and molybdenum enrichment. The crystallites observed in both samples were found to be molybdenum exclusive suggesting MoO_3 production. The 10 ml 1:2.2 displayed the greatest separation with very large areas of near molybdenum and iron exclusivity in the highlighted areas.

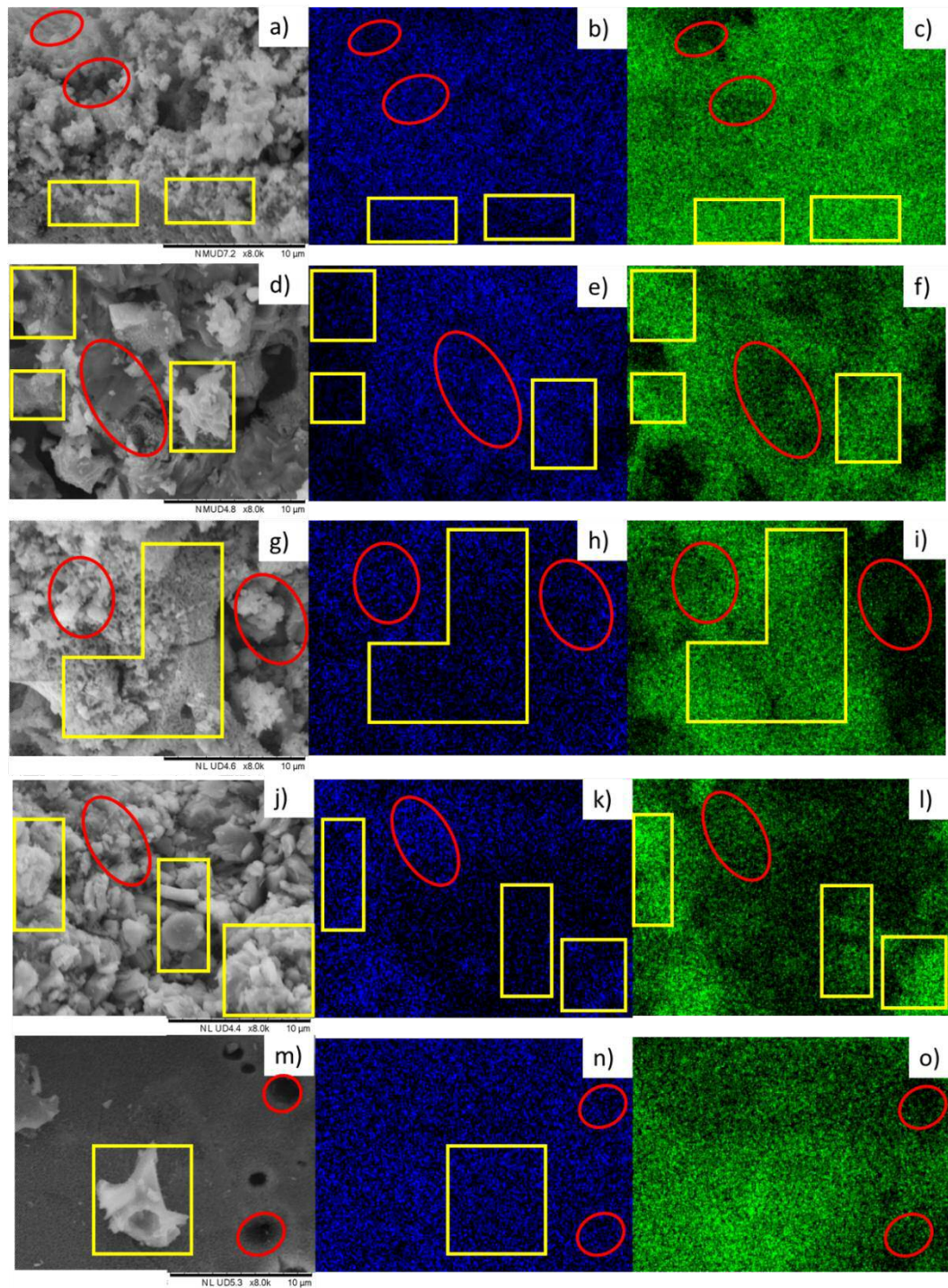


Figure 3.18 SEM micrograph and EDX elemental mapping comparison of samples prepared using various amounts of water addition into 1:2.2 OM precursor mixtures. (a) SEM image of 1:2.2 OM, (b) EDX map showing Fe content of 1:2.2 OM, (c) EDX map showing Mo content of 1:2.2 OM, (d) SEM image of 5 ml 1:2.2, (e) EDX map showing Fe content of 5 ml 1:2.2, (f) EDX map showing Mo content of 5 ml 1:2.2, (g) SEM image of 10 ml 1:2.2, (h) EDX map showing Fe content of 10 ml 1:2.2, (i) EDX map showing Mo content of 10 ml 1:2.2, (j) SEM image of 15 ml 1:2.2, (k) EDX map showing Fe content of 15 ml 1:2.2, (l) EDX map showing Mo content of 15 ml 1:2.2 (m) SEM image of 25 ml 1:2.2, (n) EDX map showing Fe content of 25 ml 1:2.2 and (o) EDX map showing Mo content of 25 ml 1:2.2. Highlighted Fe rich (red circles) and Mo rich (yellow squares).

3.4.3. Methanol Partial Oxidation

Methanol partial oxidation results presented in Fig. 3.19 present significant differences between samples prepared using a variety of water contents added to the OM mixtures.

All samples displayed gradual increase in conversion as temperatures were increased from 200 °C, up until 260 °C the activity of the samples ordered from lowest 15 ml, 1:2.2 OM, 5 ml, 25 ml and 10 ml 1:2.2 observed the highest. At 290 °C the order was altered with 1:2.2 OM, 10 ml and 25 ml 1:2.2 displaying comparable conversions all exceeding 90 %. Both 5 ml and 15 ml 1:2.2 samples did not exceed 90 % conversion until temperatures beyond 300 °C. High conversion (>95 %) were achieved by all samples at 320 °C.

Formaldehyde selectivity from 200-260 °C was highest for 1:2.2 OM, 25 ml and 5 ml 1:2.2 samples which all exhibited over 93 % selectivity. Both 15 ml and 10 ml 1:2.2 formaldehyde selectivity was limited to under 90 % and 85 % respectively, this was due higher CO_x selectivity exhibited by these samples at lower temperatures.

As temperatures were increased to 290 °C, 5 ml 1:2.2 and 10 ml 1:2.2 exhibited a rapid decrease in formaldehyde selectivity in favour of CO_x production. The 15 ml 1:2.2 catalyst in contrast presented an increase in formaldehyde selectivity (91.2 %) due to the loss of DME selectivity which was produced at lower temperatures, both 0 ml and 25 ml 1:2.2 remained largely unchanged.

Table 3.8 Maximum formaldehyde comparison of 1:2.2 OM samples prepared using various water additions.

Sample	Maximum Formaldehyde Yield/ %	Temperature / °C
1:2.2 Coprep	90.0	350
1:2.2 OM	92.6	320
5 ml 1:2.2	82.8	320
10 ml 1:2.2	67.3	290
15 ml 1:2.2	88.0	335
25 ml 1:2.2	90.0	320

Further increases in temperature saw a reduction of formaldehyde selectivity for all samples with an increase in CO_x selectivity. Both 1:2.2 OM and 25 ml 1:2.2 presented

formaldehyde selectivity above 90 % at temperatures exceeding 320 °C unlike the other water addition samples which exhibited further reduction in favour of CO_x.

The effects these changes had on overall formaldehyde yield are summarised in Table 3.8, both the 1:2.2 OM and 25 ml 1:2.2 produced the highest formaldehyde yields of the catalysts tested with the high yields largely maintained over a range of temperatures (305-350 °C). This was due to the superior formaldehyde selectivity observed for both samples. The 15 ml 1:2.2 was the next best achieving a small reduction in formaldehyde yield but unlike the two previous samples, these yields were not maintained and were attained at higher temperatures.

Further reduction in formaldehyde yield was observed for both 5 ml 1:2.2 and 10 ml 1:2.2 with the latter presenting the lowest yield of the water addition samples. This was due to the lower formaldehyde selectivity expressed throughout by both catalysts.

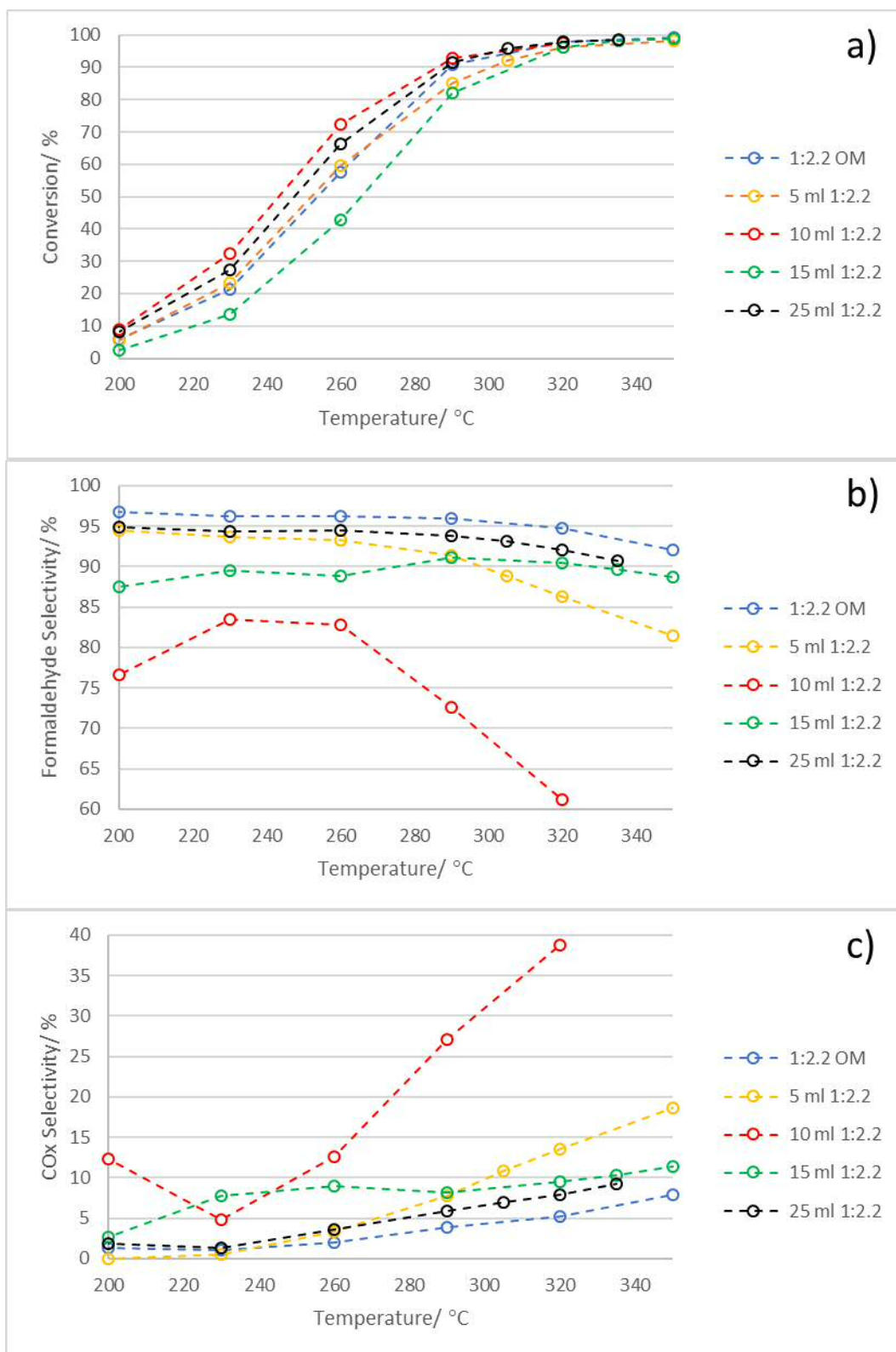


Figure 3.19 MeOH partial oxidation reaction summary of 1:2.2 OM samples synthesised various water additions to the oxalate mixtures presenting variations in a) Conversion, b) formaldehyde selectivity and c) CO_x selectivity over a range of temperatures.

3.4.4. Precalcination Study

3.4.4.1 XPS of Uncalcined Mixtures

XPS comparison shown in Table 3.9 presents the surface Mo^V:Mo^{VI} ratios of uncalcined water addition samples, 1:2.2 OM presented a mixture of both molybdenum oxidation states which was suggested to improve the mixing of the oxalates with the limitation of polymeric molybdenum species prior to calcination.

The addition of water into the mixture presented a drop of Mo^V content with Mo^{VI} becoming the dominant oxidation state which continued as more water was added. The 25 ml 1:2.2 sample displayed only Mo^{VI} content.

Mo^{VI} as stated previously was responsible for the formation of polymeric molybdenum oxalate species which up until now have been shown to be detrimental using the OM method. The Mo^{VI} oxidation state is also present in both MoO₃ and Fe₂(MoO₄)₃ which are typically only observed in the calcined samples but it observed in large quantities in higher water addition samples.

Table 3.9 XPS comparison of Mo 3d region of uncalcined OM using various water additions.

Sample	XPS Surface Ratios
	Mo ^V :Mo ^{VI}
1:2.2 OM	1:1.12
5 ml 1:2.2	1:1.58
10 ml 1:2.2	1:6.71
15 ml 1:2.2	1:12.36
25 ml 1:2.2	0:1

3.4.4.2. Raman Spectroscopy

Raman comparison of uncalcined water addition OM samples are shown in Fig. 3.21 looking at key identification region between 600-1100 cm^{-1} for molybdenum oxide and molybdate species.

The 0-10 ml water addition samples presented no significant species in the Raman results except for some very broad regions covering the entire expanse between 700-1000 cm^{-1} which could suggest some Mo-O-Mo bonding.⁴² This may suggest that polymeric MoO_3 and $\text{Fe}_2(\text{MoO}_4)_3$ formation was limited by possible formation of oxomolybdate(VI) oxalate prior to calcination.

The 15 ml water addition caused large changes as shown in the Raman results with many peaks displayed in molybdenum oxide region. The broad peak observed at 857 cm^{-1} was suggested to be caused by ν O-O stretch, peaks at 920 cm^{-1} and 955 cm^{-1} was thought to be caused by ν Mo=O all of which present by peroxymolybdate oxalate ($[\text{MoO}(\text{O}_2)_2(\text{C}_2\text{O}_4)]^{2-}$) structures similar to those shown in Fig. 3.20 suggested by Dengel *et al.*⁵⁸ This may have prevented the formation of large MoO_3 exclusive areas like those observed in 10ml 1:2.2 OM samples. This is due to the inhibition of Mo-O-Mo coupling prior to calcination allowing for greater mixing and a more homogeneous sample post calcination. The broad peak at 751 cm^{-1} was thought to be caused by MoO_4 tetrahedra from unconventional iron molybdate structures such as those observed in $\text{Fe}_2(\text{MoO}_4)_3$ thin films suggested by Uhlrich *et al.*⁵⁹

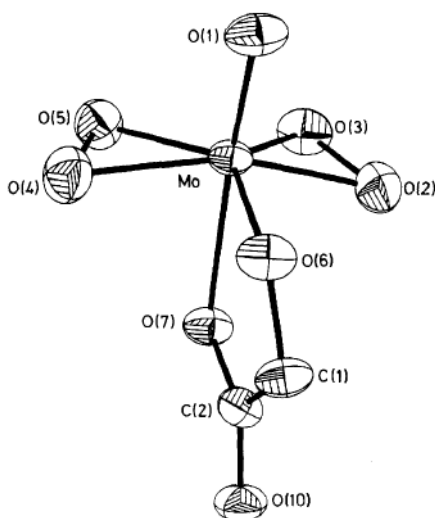


Figure 3.20 Structure of the $[\text{MoO}(\text{O}_2)_2(\text{glyc})]^{2-}$ anion complex suggested by Dengel *et al.*⁵⁸

Further water addition saw the ν O-O stretch remain but asymmetric O-Mo-O peak of $\text{Fe}_2(\text{MoO}_4)_3$ at 784 cm^{-1} was presented as well as possible peak at 984 cm^{-1} suggesting the Mo=O stretch of the same structure. MoO_3 may also be present in the uncalcined sample with a broadening of the peaks between 784 and 857 cm^{-1} suggesting the asymmetric Mo-O-Mo but little to no peak suggesting the terminal Mo=O stretch at 997 cm^{-1} . The ν O-O stretch was still present suggesting that the peroxymolybdate oxalate species was maintained with the higher water content in conjunction to the formation of $\text{Fe}_2(\text{MoO}_4)_3$.

These Raman spectra may indicate that coprecipitation like formation was occurring with higher water additions with the formation of $\text{Fe}_2(\text{MoO}_4)_3$ and MoO_3 prior to calcination. This was similar to results obtained by Nikolenko *et al.*⁶⁰ who saw the direct precipitation of $\text{Fe}_2(\text{MoO}_4)_3$ from concentrated solutions of iron and molybdenum salts in an acidic media. The outcome of which may be the cause of the formation of the larger, crystalline $\text{Fe}_2(\text{MoO}_4)_3$ formations post calcination similar to 1:2.2 Coprep.

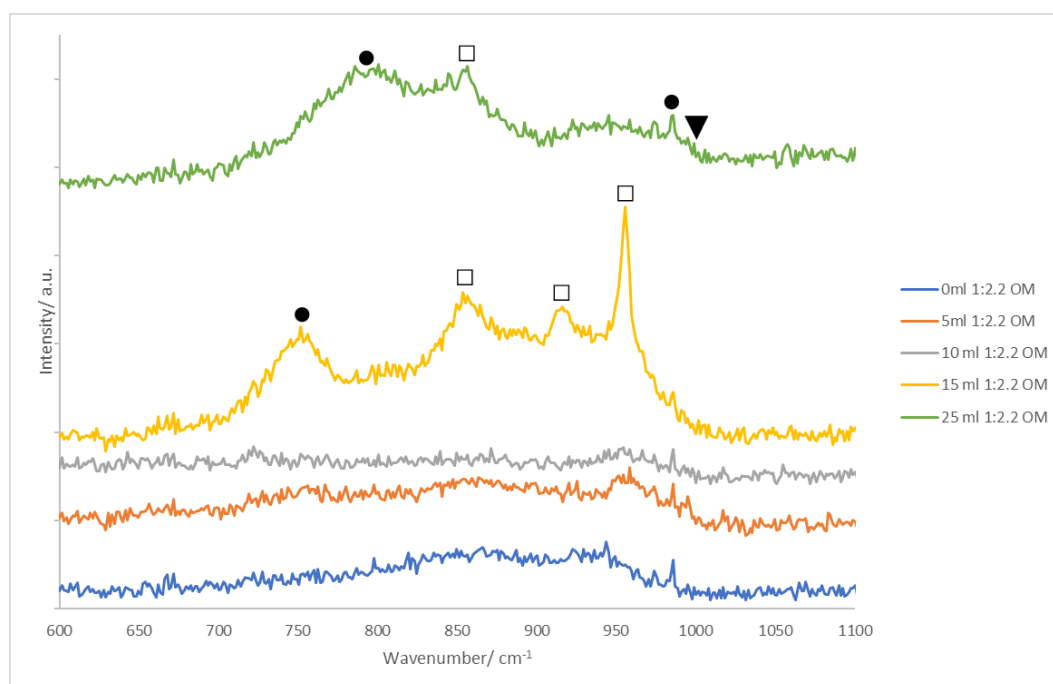


Figure 3.21 Raman spectral comparison of samples produced using varying volumes of water addition into OM mixtures. (Key: ▼ MoO_3 , ● $\text{Fe}_2(\text{MoO}_4)_3$ and □ $[\text{MoO}(\text{O}_2)_2(\text{C}_2\text{O}_4)]^{2-}$).

3.4.4.3. Thermogravimetric Analysis

The DTG comparison of water addition samples shown in Fig. 3.22 and corresponding TG results (Table 3.11), the decomposition steps were interpreted as those observed in Section 3.3.4.2.

The amount of isolated iron oxalate decomposition (140-200 °C) was shown to decrease in significance as follows, 5 ml 1:2.2 > 15 ml 1:2.2 > 1:2.2 OM > 10 ml 1:2.2 > 25 ml 1:2.2. The 25 ml 1:2.2 samples presented half the amount of isolated iron oxalate of lower water addition samples.

Molybdenum oxalate decomposition step (230-290 °C) was most significant for both 15 ml 1:2.2 and 25 ml 1:2.2 samples (17.8-17.9 % weight reduction) where it was the dominant product. Both the 1:2.2 OM and 5 ml 1:2.2 were comparable and presented a small reduction in mass loss by molybdenum oxalate decomposition. 10 ml 1:2.2 presented half the molybdenum oxalate content of the other samples.

The decomposition step between the iron and molybdenum oxalates (200-230 °C) was most significantly presented by 1:2.2 OM. Both the 5 ml 1:2.2 and 10 ml 1:2.2 samples also displayed significant mass reductions in TGA results. Unlike the other examples, the area between 200-230 °C for 10 ml 1:2.2 looked like a continuation of the iron oxalate decomposition rather than an overlap between the two oxalates in DTG results. The lowest weight loss in this region was observed by 15 ml 1:2.2 and 25 ml 1:2.2.

The final decomposition between 325-350 °C indicating the loss of ammonia from ammonium molybdate⁶¹ was considerably higher for both 10 ml 1:2.2 and 15 ml 1:2.2 compared to the other samples. The other water addition samples presented between 2.4-2.8 % mass loss in this region.

Due to the comparatively low iron oxalate quantities observed in 25 ml 1:2.2 results it may suggest much of the iron content had been precipitated as $\text{Fe}_2(\text{MoO}_4)_3$ as suggested in Raman results. 15 ml 1:2.2 presented with relatively large quantities of isolated iron oxalate with minimal overlap between the two oxalate species produced suggesting inadequate mixing prior to calcination.

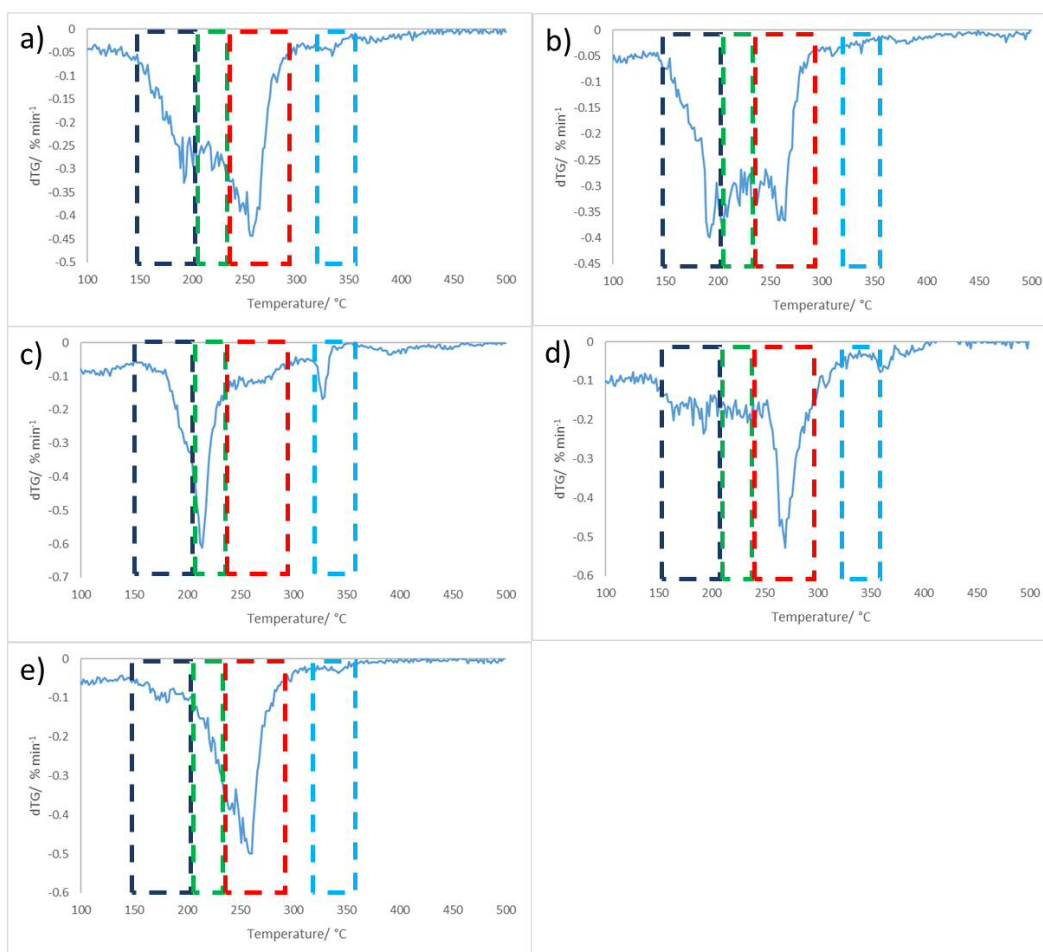


Figure 3.22 DTG Analysis of uncalcined samples of OM water addition samples ranging from 100-500 °C using a ramp rate of 5 °C min⁻¹ (a) 0ml OM 1:2.2, b) 5ml OM 1:2.2, c) 10ml OM 1:2.2, d) 15ml OM 1:2.2 and e) 25ml OM 1:2.2).

Table 3.11 TGA comparison of 1:2.2 OM samples prepared using various water additions into the oxalate mixtures corresponding to regions highlighted in DTG results in Fig. 3.22.

TGA Temperature Range/ °C	Percentage Weight Loss/ %				
	1:2.2 OM	5 ml 1:2.2	10 ml 1:2.2	15 ml 1:2.2	25 ml 1:2.2
140-200	10.5	11.2	9.0	11.0	5.5
200-230	13.2	9.6	10.1	5.5	5.5
230-290	14.0	15.2	7.7	17.8	17.9
325-350	2.6	2.8	4.4	3.2	2.4

3.4.5. Effect of water addition on OM Samples Discussion

Investigations into the use of water additions to OM have found that the oxalate decomposition method was highly sensitive to water additions.

The 0 ml 1:2.2 showed the best performance achieving 92.6 % yield at 320 °C which was due to high $\text{Fe}_2(\text{MoO}_4)_3$ content and well dispersed MoO_3 preventing exposure of Fe_2O_3 and isolated crystalline MoO_3 . This was formed out of the homogeneous composition of the oxalate mixture prior to calcination as indicated in DTG/TGA results.

The next best was 25 ml 1:2.2 which presented similar performance achieving 90.0 % yield at 320 °C. Possible reasons for the decrease in formaldehyde yield may be due to the non-homogeneous surface composition of the catalyst observed in microscopy results. Large MoO_3 crystallites were observed similar to 1:2.2 Coprep which have been shown to be inactive at lower temperatures.^{37,40,55} These structures may have been formed by chemical precipitation out of solution similar to results shown by Nikolenko *et al.*⁶⁰ Some evidence of iron enrichment was also observed formed possibly out of the decomposition of some isolated iron oxalate which could contribute an increase in CO_x selectivity.^{38,41}

The 15 ml 1:2.2 sample had the lowest activity of water addition catalysts as well as presenting significant CO_x selectivity at low temperatures. This caused a maximum formaldehyde yield of 88.0 % at the higher temperature of 335 °C. Possible reasons for the lower activity could be due to the increase in crystalline MoO_3 observed in XRD and microscopy results. Lower formaldehyde selectivity especially at lower temperatures may be due to exposed Fe_2O_3 observed in XRD and microscopy results which as stated in section 3.3, is very active but favours CO_x products throughout.^{37,38,40,41,55} This lack of $\text{Fe}_2(\text{MoO}_4)_3$ production may have been caused by the non-homogenous mixing prior to calcination by the partial precipitation of iron molybdate as suggested in uncalcined Raman results, this left relatively large quantities of poorly mixed oxalates and isolated ammonium molybdate as suggested by DTG/TGA.

The 5 ml 1:2.2 and 10 ml 1:2.2 catalysts displayed the worst catalytic performance, this may be due to the low $\text{Fe}_2(\text{MoO}_4)_3$ production with both MoO_3 and Fe_2O_3 observed in larger quantities in XRD and Raman spectral mapping. This was especially prevalent for 10 ml 1:2.2 which produced the highest CO_x quantities throughout which may be explained by large amount of Fe_2O_3 exposed to the surface. The reasons for this increase in Fe_2O_3 content could be the rise in isolated iron oxalate as observed in DTG/TGA results, both

samples presenting the decomposition of iron oxalate as a significant product suggesting inadequate mixing prior to calcination.

3.5. Oxalate Decomposition Method Conclusion

The oxalate decomposition method has been tested extensively for the production of $\text{Fe}_2(\text{MoO}_4)_3$ as a catalyst for formaldehyde synthesis from the partial oxidation of methanol. Testing of stoichiometric Fe:Mo ratio of 1:1.5 for $\text{Fe}_2(\text{MoO}_4)_3$ formed a $\text{Fe}_2(\text{MoO}_4)_3$ rich catalyst with some phase separation observed in the form of both Fe_2O_3 and MoO_3 which suggests non homogeneous mixing. As a result, significantly lower formaldehyde yield was observed compared to the coprecipitated sample it was tested against although it was much more active displaying high conversions below 300 °C unlike the 1:2.2 Coprep sample.

The oxalate decomposition method was found to be highly sensitive to the Fe:Mo ratio as a small increase in Mo content from 1:1.5 to 1:1.7 dramatically improved formaldehyde selectivity caused by Fe_2O_3 content reduction. High activity was maintained surpassing the 90.0 % formaldehyde yield at 350 °C achieved by 1:2.2 Coprep achieving 91.2 % yield at 320 °C. Further Mo addition to 1:1.9 Fe:Mo limited the mixing of the oxalate precursors prior to calcination which produced Fe_2O_3 voids to be exposed to the surface, the result of which causes a drop in formaldehyde yield to 89.3 % at 335 °C.

The highest performing OM sample tested was 1:2.2 OM, dilution of the iron voids seen in 1:1.9 OM yielded a sponge-like homogeneous structure causing a formaldehyde yield of 92.6 % at 320 °C, a substantial improvement on 1:2.2 Coprep. Further Mo addition to 1:3.0 caused less homogenous mixing of the solid solution and a conglomeration of large iron rich hole and large MoO_3 areas causing a lower overall yield at the same temperature.

OM mixtures have also displayed high sensitivity to water addition with initial dilutions causing limited mixing of iron and molybdenum prior to calcination, which gave Fe_2O_3 and MoO_3 in the calcined samples. This resulted in lower formaldehyde yields (82.8 % and 67.3 % for 5ml 1:2.2 and 10ml 1:2.2 respectively) as Fe_2O_3 selectivity towards total oxidation increased carbon oxides yield. Further water additions presented changes in morphology forming more homogeneous $\text{Fe}_2(\text{MoO}_4)_3$ crystalline structures caused in part by the

formation of peroxyomolybdate(VI) oxalate instead of the polymeric oxomolybdate(VI) oxalate. Larger additions yielded $\text{Fe}_2(\text{MoO}_4)_3$ formation prior to calcination unlike other OM samples suggesting possible chemical precipitation of $\text{Fe}_2(\text{MoO}_4)_3$, void structures were still formed from the decomposition of the oxalate precursors which could have caused higher activity observed by 25 ml 1:2.2 compared to 1:2.2 Coprep allowing for the same yield (90.0 %) at lower temperature.

3.6 References

- (1) Gelb, R. I. *Anal. Chem.* **1971**, *43* (8), 1110–1113.
- (2) Domínguez de María, P.; Fernández-Álvaro, E.; ten Kate, A.; Bargeman, G. J. *Mol. Catal. B Enzym.* **2009**, *59* (1–3), 220–224.
- (3) Deb, N. J. *Anal. Appl. Pyrolysis* **2007**, *78* (1), 24–31.
- (4) Thuéry, P.; Rivière, E. *Dalton Trans.* **2013**, *42* (29), 10551–10558.
- (5) Mehlretter, C. L.; Rist, C. E. *J. Agric. Food Chem.* **1953**, *1* (12), 779–783.
- (6) Gürü, M.; Bilgesü, A. Y.; Pamuk, V. *Bioresour. Technol.* **2001**, *77* (1), 81–86.
- (7) Cameselle, C.; Bohlmann, J. T.; Núñez, M. J.; Lema, J. M. *Bioprocess Eng.* **1998**, *19* (4), 247–252.
- (8) Li, Y.-S.; Shi, L.-C.; Gao, X.-F.; Huang, J.-G. *Desalination* **2016**, *390*, 62–71.
- (9) Poirier, M. R.; Hay, M. S.; Herman, D. T.; Crapse, K. P.; Thaxton, G. D.; Fink, S. D. *Sep. Sci. Technol.* **2010**, *45* (12–13), 1858–1875.
- (10) Solbes-García, Á.; Miranda-Vidales, J. M.; Nieto-Villena, A.; Hernández, L. S.; Narváez, L. *J. Cult. Herit.* **2017**, *25*, 127–134.
- (11) Komkova, K. G.; Malyshev, L. N.; Khovryakov, S. Y.; Kubaenko, T. M. **1980**.
- (12) Hong, F.; Reimann, A.; Jönsson, L.-J.; Nilvebrant, N.-O. *Linchan Huaxue Yu Gongye Chemistry Ind. For. Prod.* **2005**, *25* (1), 23–28.
- (13) Vegliò, F.; Passariello, B.; Abbruzzese, C. *Ind. Eng. Chem. Res.* **1999**, *38* (11), 4443–4448.
- (14) Ash, C.; Tejnecký, V.; Borůvka, L.; Drábek, O. *J. Contam. Hydrol.* **2016**, *187*, 18–30.
- (15) Hu, P.; Zhang, Y.; Liu, T.; Huang, J.; Yuan, Y.; Zheng, Q. *J. Ind. Eng. Chem.* **2017**, *45*, 241–247.
- (16) D’Antonio, M. C.; Wladimirsky, A.; Palacios, D.; Coggiolaa, L.; González-Baró, A. C.; Baran, E. J.; Mercader, R. C. *J. Braz. Chem. Soc.* **2009**, *20* (3), 445–450.
- (17) Ahouari, H.; Rouse, G.; Rodríguez-Carvajal, J.; Sougrati, M.-T.; Saubanère, M.; Courty, M.; Recham, N.; Tarascon, J.-M. *Chem. Mater.* **2015**, *27* (5), 1631–1639.
- (18) Boyanov, B.; Khadzhiev, D.; Vasilev, V. *Thermochim. Acta* **1985**, *93*, 89–92.
- (19) Diefallah, E.-H. M.; Mousa, M. A.; El-Bellihi, A. A.; El-Mossalamy, E.-H.; El-Sayed, G. A.; Gabal, M. A. *J. Anal. Appl. Pyrolysis* **2002**, *62* (2), 205–214.
- (20) Majumdar, R.; Sarkar, P.; Ray, U.; Roy Mukhopadhyay, M. *Thermochim. Acta* **1999**, *335* (1–2), 43–53.
- (21) Rane, K. S.; Nikumbh, A. K.; Mukhedkar, A. J. *J. Mater. Sci.* **1981**, *16* (9), 2387–2397.
- (22) Hermanek, M.; Zboril, R.; Mashlan, M.; Machala, L.; Schneeweiss, O. *J. Mater. Chem.* **2006**, *16* (13), 1273–1280.
- (23) Basahel, S. N.; El-Bellihi, A. A.; Gabal, M.; Diefallah, E.-H. M. *Thermochim. Acta* **1995**, *256* (2), 339–346.

- (24) Hermankova, P.; Hermanek, M.; Zboril, R. *Eur. J. Inorg. Chem.* **2010**, 2010 (7), 1110–1118.
- (25) Gabal, M. A.; El-Bellihi, A. A.; El-Bahnasawy, H. H. *Mater. Chem. Phys.* **2003**, 81 (1), 174–182.
- (26) Cindrić, M.; Strukan, N.; Vrdoljak, V.; Devčić, M.; Veksli, Z.; Kamenar, B. *Inorganica Chim. Acta* **2000**, 304 (2), 260–267.
- (27) Modec, B.; Brenčić, J. V.; Koller, J. *Eur. J. Inorg. Chem.* **2004**, 2004 (8), 1611–1620.
- (28) Diaz-Guemes, M. I.; Bhatti, A. S.; Dollimore, D. *Thermochim. Acta* **1986**, 106, 125–132.
- (29) Gopalakrishnan, J.; Viswanathan, B.; Srinivasan, V. *J. Inorg. Nucl. Chem.* **1970**, 32 (8), 2565–2568.
- (30) Goel, S. P.; Mehrotra, P. N. *Thermochim. Acta* **1983**, 70 (1), 201–209.
- (31) Brown, R. A.; Bevan, S. C. *J. Inorg. Nucl. Chem.* **1966**, 28 (2), 387–391.
- (32) Lamprecht, E.; Watkins, G. M.; Brown, M. E. *Thermochim. Acta* **2006**, 446 (1–2), 91–100.
- (33) Mikhail, R. S.; Guindy, N. M.; Ali, I. T. *J. Appl. Chem. Biotechnol.* **1974**, 24 (10), 583–594.
- (34) Dollimore, D.; Evans, T. A. *Thermochim. Acta* **1991**, 178, 263–271.
- (35) Oudghiri-Hassani, H. *Catal. Commun.* **2015**, 60, 19–22.
- (36) Beale, A. M.; Jacques, S. D. M.; Sacaliuc-Parvalescu, E.; O'Brien, M. G.; Barnes, P.; Weckhuysen, B. M. *Appl. Catal. Gen.* **2009**, 363 (1–2), 143–152.
- (37) Routray, K.; Zhou, W.; Kiely, C. J.; Grünert, W.; Wachs, I. E. *J. Catal.* **2010**, 275 (1), 84–98.
- (38) Bowker, M.; Brookes, C.; Carley, A. F.; House, M. P.; Kosif, M.; Sankar, G.; Wawata, I.; Wells, P. P.; Yaseneva, P. *Phys. Chem. Chem. Phys. PCCP* **2013**, 15 (29), 12056–12067.
- (39) House, M. P.; Shannon, M. D.; Bowker, M. *Catal. Lett.* **2008**, 122 (3–4), 210–213.
- (40) House, M. P.; Carley, A. F.; Echeverria-Valda, R.; Bowker, M. *J. Phys. Chem. C* **2008**, 112 (11), 4333–4341.
- (41) Bowker, M.; House, M.; Alshehri, A.; Brookes, C.; Gibson, E. K.; Wells, P. P. *Catal. Struct. React.* **2015**, 1 (2), 95–100.
- (42) Tian, H.; Wachs, I. E.; Briand, L. E. *J. Phys. Chem. B* **2005**, 109 (49), 23491–23499.
- (43) Briand, L. E.; Hirt, A. M.; Wachs, I. E. *J. Catal.* **2001**, 202 (2), 268–278.
- (44) Hardcastle, F. D.; Wachs, I. E. *J. Raman Spectrosc.* **1990**, 21 (10), 683–691.
- (45) Brookes, C.; Bowker, M.; Wells, P. P. *Catalysts* **2016**, 6 (7), 92.
- (46) Söderhjelm, E.; House, M. P.; Cruise, N.; Holmberg, J.; Bowker, M.; Bovin, J.-O.; Andersson, A. *Top. Catal.* **2008**, 50 (1–4), 145.
- (47) Jin, G.; Weng, W.; Lin, Z.; Dummer, N. F.; Taylor, S. H.; Kiely, C. J.; Bartley, J. K.; Hutchings, G. J. *J. Catal.* **2012**, 296, 55–64.
- (48) Soares, A. P. V.; Farinha Portela, M.; Kiennemann, A.; Hilaire, L.; Millet, J. M. M. *Appl. Catal. Gen.* **2001**, 206 (2), 221–229.
- (49) Soares, A. P. V.; Portela, M. F.; Kiennemann, A.; Hilaire, L. *Chem. Eng. Sci.* **2003**, 58 (7), 1315–1322.
- (50) Boreskov, G. K.; Kolovertnov, G. D.; Kefeli, L. M.; Plyasova, L. M.; Karakchiev, L. G.; Mastikhin, V. N.; Popov, V. I.; Dzis'Ko, V. A.; Tarasova, D. V. *Kinet Catal Engl Transl* **1965**, 7 (1), 125.
- (51) Vieira Soares, A. P.; Farinha Portela, M.; Kiennemann, A. *Stud. Surf. Sci. Catal.* **1997**, 110, 807–816.
- (52) Choi, J.-G.; Thompson, L. T. *Appl. Surf. Sci.* **1996**, 93 (2), 143–149.
- (53) Shaheen, W. M. *Mater. Sci. Eng. A* **2007**, 445–446, 113–121.

- (54) Kostynyuk, A. O.; Gutenuar, F.; Kalashnikova, A. N.; Kalashnikov, Y. V.; Nikolenko, N. V. *Kinet. Catal.* **2014**, *55* (5), 649–655.
- (55) Bowker, M.; Holroyd, R.; Elliott, A.; Morrall, P.; Alouche, A.; Entwistle, C.; Toerncrona, A. *Catal. Lett.* **2002**, *83* (3–4), 165–176.
- (56) Liu, J.; Qiu, Z.; Yang, J.; Cao, L.; Zhang, W. *Hydrometallurgy* **2016**, *164*, 64–70.
- (57) Lee, S. O.; Tran, T.; Jung, B. H.; Kim, S. J.; Kim, M. J. *Hydrometallurgy* **2007**, *87* (3–4), 91–99.
- (58) Dengel, A. C.; Griffith, W. P.; Powell, R. D.; Skapski, A. C. *J. Chem. Soc. Dalton Trans.* **1987**, No. 5, 991–995.
- (59) Uhlrich, J. J.; Sainio, J.; Lei, Y.; Edwards, D.; Davies, R.; Bowker, M.; Shaikhutdinov, S.; Freund, H.-J. *Surf. Sci.* **2011**, *605* (15–16), 1550–1555.
- (60) Nikolenko, M. V.; Kostynyuk, A. O.; Goutenoire, F.; Kalashnikov, Y. V. *Inorg. Mater.* **2014**, *50* (11), 1140–1145.
- (61) Kovács, T. N.; Hunyadi, D.; Lucena, A. L. A. de; Szilágyi, I. M. *J. Therm. Anal. Calorim.* **2016**, *124* (2), 1013–1021.

Chapter 4

The Use of Malonate Decomposition Method(MM) for Iron Molybdate Synthesis

4.1 Introduction

4.1.1. Malonic Acid Applications and Production

Malonic acid otherwise known as 1,3 propanedioic acid comprises of a 3 C hydrocarbon chain featuring carboxylic acid groups at each end, lower acidity compared to oxalic with pKa of 2.83 and 5.69 for each group respectively¹. Unlike oxalic acid, malonic is not used as a bulk chemical for cleaning even though it has similar chelating and chemical properties. Its uses are more specialised with applications including starting material for production of specialty polyesters², crosslinking applications for bioplastic synthesis³, manufacture of barbiturates⁴ and coatings for alloys⁵.

Production of malonic acid is achieved commercially by the hydrolysis of malonate diesters, these are manufactured from sodium cyanoacetate via hydrolysis and esterification yielding malonate diesters⁶. Recent developments have suggested the direct formation via the fermentation of sugars using modified yeast strains with the prospect to avoid the use of cyanide-based process⁷.

4.1.2. Iron Malonate

The properties of iron malonate has been investigated in recent studies for the ability to preferentially form γ -Fe₂O₃ nanoparticles upon decomposition^{8,9} and photocatalytic degradation of organic dyes.¹⁰ Two distinct malonate complexes of iron have been suggested Fe(CH₂C₂O₄)·2H₂O^{9,11,12} and Fe₂(CH₂C₂O₄)₃^{13,14} corresponding to Fe^{II} and Fe^{III} metallic centres.

$\text{Fe}^{\text{II}}\text{CH}_2\text{C}_2\text{O}_4 \cdot \text{H}_2\text{O}$ shown in Fig. 4.1 found great similarity with iron (II) oxalate dihydrate compounds displayed in Section 3.1. It was found to form planar structure with respect to two bidentate bound malonates which in turn can form polymeric iron malonate chains which are distorted by the malonate alkyl group, water ligands occupy terminal octahedral positions as shown similar to oxalate examples.

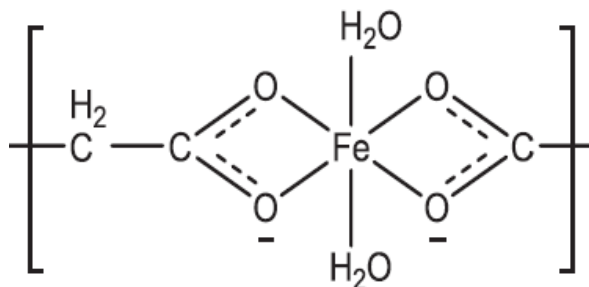


Figure 4.1. Representative structure of $\text{Fe}^{\text{II}}\text{CH}_2\text{C}_2\text{O}_4 \cdot 2\text{H}_2\text{O}$ monomer.⁸

Unlike the previous example $\text{Fe}^{\text{III}}(\text{CH}_2\text{C}_2\text{O}_4)_3$ presents with the formation of 3 chelated bidentate malonate ligands in an octahedral geometry as shown in Fig. 4.2. Some evidence of monochelates between iron centres has been discussed similar to Fe^{II} examples suggesting possible chain structures.^{8,15}

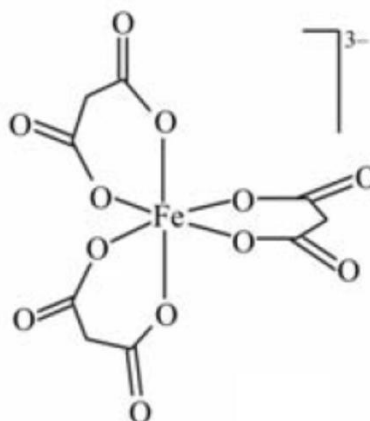


Figure 4.2. Representative structure of the $[\text{Fe}^{\text{III}}(\text{CH}_2\text{C}_2\text{O}_4)_3]^{3-}$ anion^{13,14}.

Thermal decomposition of iron malonates has been well investigated with both Fe^{II} and Fe^{III} shared great similarities beyond the initial dehydration steps, this is in contrast to iron

oxalate examples which displayed clear differences between the two iron oxidation state complexes.

The thermal decomposition of iron (II) malonate dihydrate proceeds via a multi-step process,^{9,11,12} initial dehydration of the complex occurs between 128-265 °C peaking at 230 °C suggesting the loss of the ionically bound water. Between 220-379 °C CO, CO₂ and H₂O were observed with a peak rate of loss observed in DTG results at 265 °C, this suggests the decarboxylation of anhydrous iron(II) malonate forming poorly crystalline Fe₂O₃.

Iron (III) malonate dihydrate presented differences initially with the dehydration occurring between 60-117 °C peaking at 101 °C suggesting the loss of water from the crystal lattices, this contrasts with ionically bound as Fe^{II} examples. Decomposition of the anhydrous malonate occurs between 233-414 °C peaking at 267 °C forming CO, CO₂ and H₂O forming Fe₂O₃.

Both anhydrous malonates were found to decompose autocatalytically with the spontaneous initiation of the reaction occurring regardless of atmosphere^{8,11} unlike oxalate examples which displayed greater thermal stability in anaerobic conditions.

4.1.3. Molybdenum Malonate

The study of molybdenum malonate complexes has received far less attention than equivalent oxalate complexes though those studies yield similarities between the two carboxylates. Mo^V complex described by Modéc *et al.*¹⁶ displayed in Fig. 4.3. presented the same Mo₂O₄ dimer at its centre. Two bidentate bound malonate ligands were complexed in an umbrella like form shielding the monodentate bonds between the third malonate. Due to the distortion caused by the alkyl group of the third malonate prevented the bridging between Mo₂O₄ dimers like those seen in the oxalate example¹⁷.

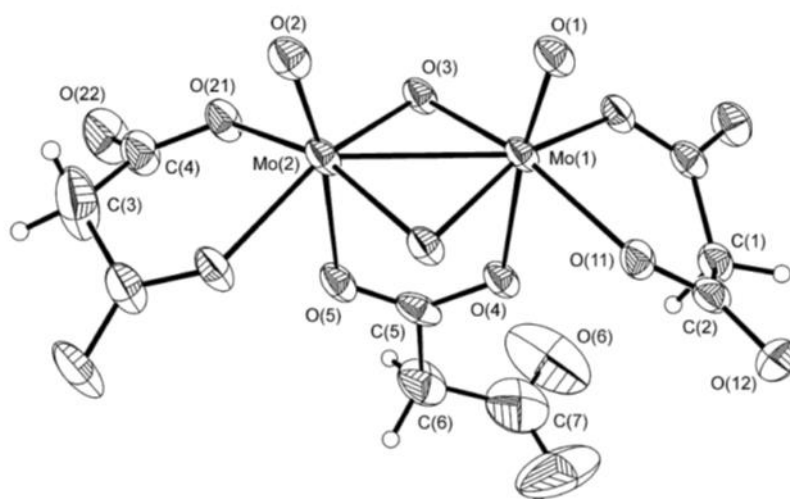


Figure 4.3. Structural representation of the $[\text{Mo}_2\text{O}_4(\text{CH}_2\text{C}_2\text{O}_4)_3]^{3-}$ anion.¹⁶

The Mo^{VI} malonate complexes have been shown to be polymeric with respect to molybdenum similar to the oxalate precursors discussed previously¹⁸. The complex described by Wang *et al.*¹⁹ shown in Fig. 4.4. presents edge-sharing octahedral MoO_6 cage structure with bidentate malonate ligands bound to the molybdenum ions. Beltrán-Porter *et al.*²⁰ suggested the formation of $[\text{Mo}_2\text{O}_5(\text{OH})_2(\text{C}_3\text{O}_4\text{H}_2)_2]^{4-}$ which featured the dimer unit similar to the Mo^{V} unit described previously, although featuring Mo-O-Mo bonding exclusively preventing the Mo-Mo bonding observed. These units were found to polymerise forming heptamolybdate species if malonate concentrations were low in solution.

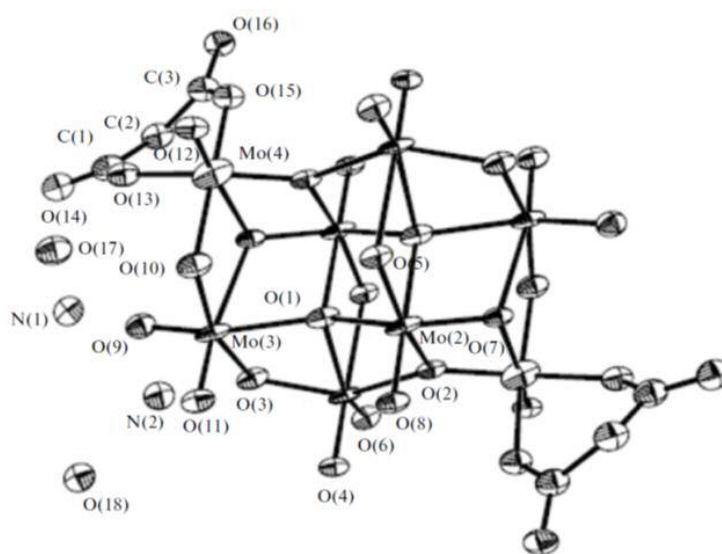


Figure 4.4. Structural representation of the $[\text{Mo}_8\text{O}_{24}(\text{CH}_2\text{C}_2\text{O}_4)_2]^{4-}$ anion.¹⁹

The thermal decomposition of molybdenum malonate has been studied by Brown *et al.*²¹ using potassium peroxomolybdate malonate. They found the rapid, highly exothermic decomposition via an autocatalytic decarboxylation of the malonate was onset at 191 °C peaking at 193 °C and finishing by 210 °C yielding K_2MoO_4 .

The use of ammonium heptamolybdate malonate was investigated using the method described in section 2.2.3. and was found to produce a mixture of both Mo^V and Mo^{VI} in XPS results prior to calcination. DTG results presented in Fig. 4.5 share similarities with results acquired by Brown *et al.*²¹ Rapid onset of decomposition was observed between 176 °C and 214 °C with a peak observed at 191 °C in flowing air forming MoO_3 .

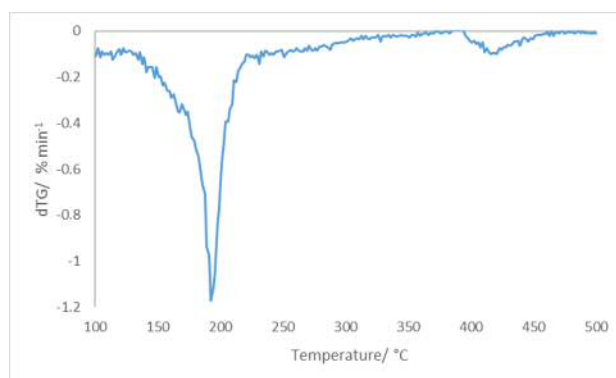


Figure 4.5. DTG analysis of $(NH_4)_6Mo_7O_{24}$ and malonic acid mixtures using flowing air atmospheres ranging from 100-500 °C using a ramp rate of 5 °C min⁻¹.

4.1.4. Malonate Decomposition for Mixed Metal Oxide Production

Due to the ability for malonate decomposition to yield nanoparticles of metal oxides⁸ it has recently been under investigation for the production of mixed metal oxides to increase component mixing in these systems²².

In this chapter, the investigation into the use of malonate decomposition to produce iron molybdate was investigated. This was to ascertain whether the production of metal oxide nanoparticles and subsequent mixed metal oxides was possible, also to analyse their performance for the production of formaldehyde from methanol.

All samples described in this chapter were prepared as described in Section 2.2.3.

4.2 Malonic acid Usage as a Solvent for Iron Molybdate Synthesis

4.2.1. Introduction

In Section 4.2, the use of the malonate decomposition method (MM) was employed to synthesize iron molybdate for use in the catalytic partial oxidation of methanol to formaldehyde. The malonate decomposition method itself was similar to oxalate decomposition method (OM) described previously. It relied on the formation and subsequent decomposition of carboxylates formed in molten dicarboxylic acid mixtures.

To ascertain the effects MM had on the samples, a comparison between similar OM and coprecipitated examples was undertaken taken from results from Chapter 3. The use of a 1:2.2 Fe:Mo ratio was employed due to the superior formaldehyde selectivity displayed in previous results shared by other studies^{23,24}.

4.2.2. Characterisation

4.2.2.1. BET Surface Area and XPS Elemental Surface Analysis

The BET surface areas results shown in Table 4.1 show that Fe:Mo 1:2.2 sample produced by malonate decomposition method (MM) had the lowest surface area when compared to equivalent samples produced by coprecipitated and oxalate decomposition methodologies (OM). The 1:2.2 MM presented a 21 % and 33 % reduction in surface area compared to 1:2.2 Coprep and 1:2.2 OM respectively.

XPS elemental surface analysis of the same samples showed that 1:2.2 Coprep had the lowest Fe:Mo ratio at the surface (1:3.0), this is followed by 1:2.2 MM (1:3.3) and 1:2.2 OM (1:3.6) displaying the highest molybdenum surface content and by extension the highest relative molybdenum surface excess compared to the bulk.

Table 4.1. BET surface area and XPS surface ratio comparison for Fe:Mo 1:2.2 samples produced using coprecipitation, OM and MM.

Sample	BET Surface Area/ m ² g ⁻¹	XPS Surface Ratios	Rel. Surface Mo Excess/ %
		Fe:Mo	
1:2.2 Coprep	3.9 ± 0.1	1:3.0	36.4
1:2.2 OM	4.6 ± 0.2	1:3.6	63.7
1:2.2 MM	3.1 ± 0.2	1:3.3	50.0

4.2.2.2. Powder XRD Crystallography

The powder XRD comparison of the three 1:2.2 samples presented in Fig. 4.6 showed all three displayed a combination of Fe₂(MoO₄)₃, α-MoO₃ and α-Fe₂O₃ with no other phases present. These phases vary in content between production methods and differ from the theoretical Fe₂(MoO₄)₃ (68.2 %) and MoO₃ (31.8 %) amounts.

Fe₂(MoO₄)₃ content was highest in the 1:2.2 OM sample (71.0 %), closely followed by 1:2.2 MM (68.8 %) and 1:2.2 Coprep (65.3 %) observed the lowest. α-MoO₃ amounts also varied with 1:2.2 Coprep displaying the highest content (33.2 %), both MM and OM samples were very similar presenting 27.9 % and 28.7 % respectively. α-Fe₂O₃ content was highest in 1:2.2 MM (2.5 %) with Coprep and OM samples presenting 1.5 % and 1.1 % respectively.

1:2.2 MM and 1:2.2 OM should present with higher activity compared to 1:2.2 Coprep due to the formation of more Fe₂(MoO₄)₃ and presenting less crystalline MoO₃, this has been found to decrease activity due to limited active surface area of bulk MoO₃.^{25,26}

The broadening of the peaks was shown to be unchanged as the methods were altered which suggests the crystallite sizes were unaffected. The only difference was observed by the sharpening of the peak at 2θ 23.3 ° corresponding to the (110) plane of α-MoO₃ seen in 1:2.2 MM results.

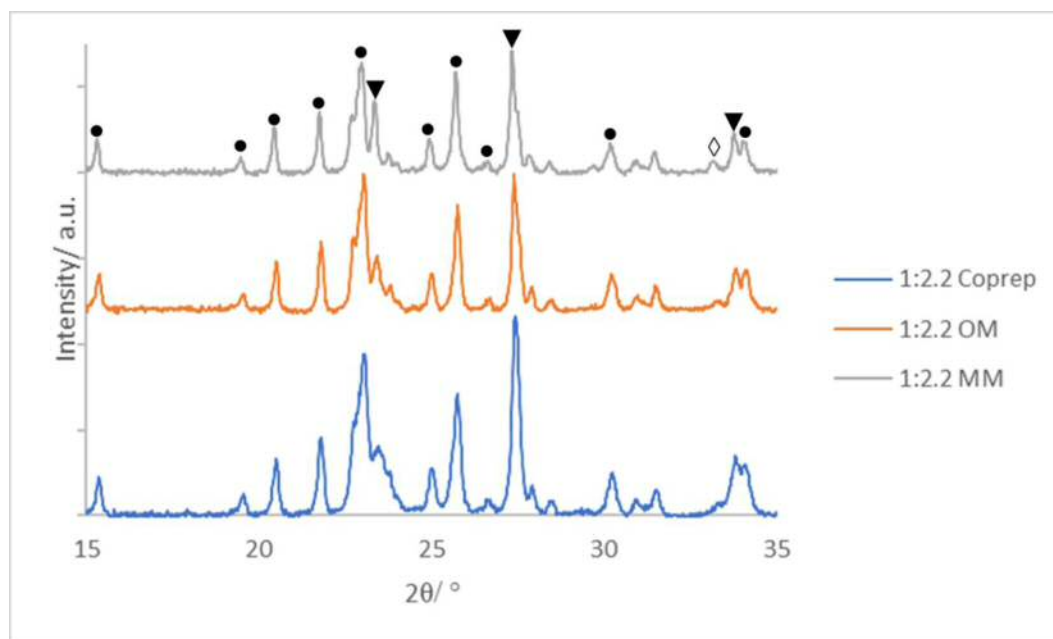


Figure 4.6. Powder XRD patterns of 1:2.2 Coprep, 1:2.2 OM and 1:2.2 MM samples. (Key: ▼ MoO_3 , ● $\text{Fe}_2(\text{MoO}_4)_3$ and ◇ Fe_2O_3).

4.3.2.3. Raman Spectral Mapping

The Raman mapping results (Fig.4.7) presented peaks corresponding to MoO_3 and $\text{Fe}_2(\text{MoO}_4)_3$ phases in all points surveyed. The most common composition of the three samples are shown in Figures 4.7.a, 4.7.d and 4.7.g for 1:2.2 MM, 1:2.2 OM and 1:2.2 Coprep respectively.

All three samples display similar ratios of $\text{Fe}_2(\text{MoO}_4)_3$ and MoO_3 supporting the XRD results. The highest MoO_3 content on average was displayed by the 1:2.2 MM sample which is contrary to XRD results which suggested 1:2.2 Coprep contained the highest amount of MoO_3 . This may indicate an increase in amorphous or nanoparticulate MoO_3 production using MM due to the increase sensitivity of Raman for less crystalline materials.

The differences in $\text{Fe}_2(\text{MoO}_4)_3$: MoO_3 ratio between points gave an indication of homogeneity of the samples. 1:2.2 Coprep displayed the greatest variance between points followed closely by 1:2.2 OM, 1:2.2 MM was the most homogeneous with little change between the points surveyed.

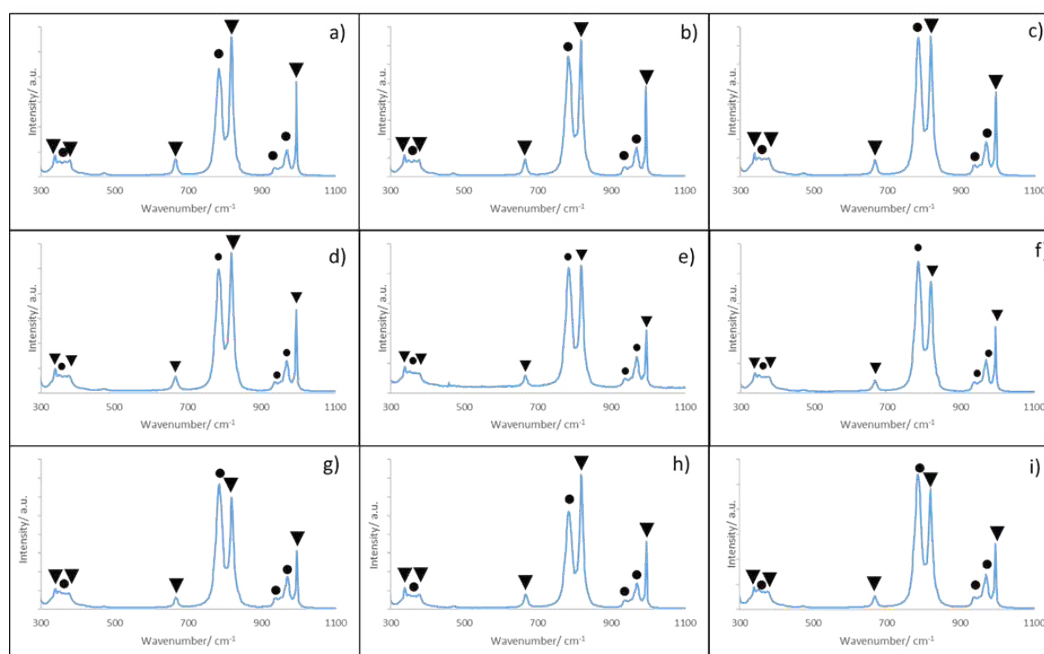


Figure 4.7. Raman spectral mapping of 1:2.2 MM(a-c), 1:2.2 OM {d-f) and 1.2.2 Coprep(g-i) samples. (Key: ▼ MoO₃ and ● Fe₂(MoO₄)₃).

4.3.2.4. SEM and EDX Elemental Mapping

Microscopy results (Fig. 4.8) presented similarities between decomposition methods. Both OM and MM displayed a sponge like morphology similar to those observed by Soares *et al.*^{27,28} utilising a sol-gel method. 1:2.2 Coprep as stated in Section 3.2 presented with large ordered block structures with MoO₃ in the form of crystallites (2-3 μm) shown on the surface.

EDX mapping and spot analysis of the corresponding micrographs showed that Mo content was highest over the 1:2.2 MM sample surface which was also distributed evenly over the area surveyed. Although this is contrary to XPS results which showed 1:2.2 OM having the highest Mo surface content, this may be localised to MoO₃ areas like those highlighted in EDX results.

Some areas of Mo enrichment in the form of possible MoO₃ crystallites (1-2 μm) were observed for 1:2.2 MM although these areas were rarely observed. Likewise, Fe distribution over the surface of 1:2.2 MM was also homogeneous except some areas of

variation although unlike both the Coprep and OM samples, these areas were also limited in number and none displayed elemental exclusivity.

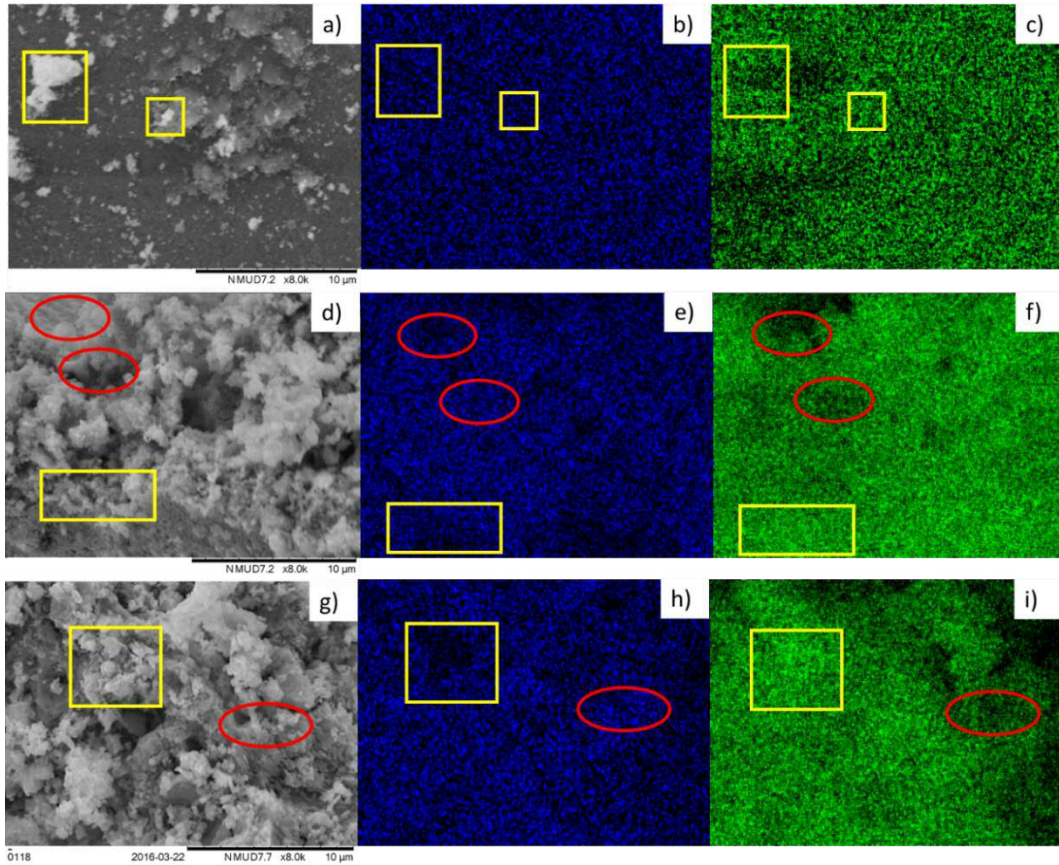


Figure 4.8. SEM and EDX elemental mapping of iron molybdate samples with Fe:Mo 1:2.2 prepared using coprecipitation, OM and MM. (a) SEM image of 1:2.2 Coprep, (b) EDX map showing Fe content of 1:2.2 Coprep, (c) EDX map showing Mo content of 1:2.2 Coprep, (d) SEM image of 1:2.2 OM, (e) EDX map showing Fe content of 1:2.2 OM, (f) EDX map showing Mo content of 1:2.2 OM, (g) SEM image of 1:2.2 MM, (h) EDX map showing Fe content of 1:2.2 MM and (i) EDX map showing Mo content of 1:2.2 MM. Highlighted Fe rich (red circles) and Mo rich (yellow squares).

4.2.3. Methanol Partial Oxidation

The methanol partial oxidation results of 1:2.2 MM displayed substantial improvements over the other 1:2.2 samples displayed in Fig. 4.9.

The formaldehyde selectivity displayed by MM closely resembles Coprep initially with high selectivity observed at 150 °C which decreased at 200 °C as DME was produced consistent with $\text{Fe}_2(\text{MoO}_4)_3$ catalysts.²³ DME selectivity rapidly decreased by 260 °C where over 96 % formaldehyde selectivity was achieved matching other 1:2.2 samples at the same temperature. This high selectivity was maintained up to 290 °C where a gradual drop was observed in favour of CO_x products.

This loss of formaldehyde selectivity was far more gradual for 1:2.2 MM compared to other 1:2.2 samples. Between 290 °C and 350 °C saw 1:2.2 MM maintain 96.7 % and 94.2 % formaldehyde selectivity, in contrast OM attained 95.9 % and 92.0 % and Coprep 96.1 % and 93.0 % over the same temperature ranges. That meant a 2.3 % loss of formaldehyde selectivity over the range for MM compared to 3.9 % and 3.1 % for OM and Coprep samples respectively.

The MM samples presented with the lowest methanol conversion initially (<260 °C) before a rapid increase was observed at 290 °C achieving 83.8 % conversion surpassing 1:2.2 Coprep which achieved 78.2 % at the same temperature, 1:2.2 OM achieved over 90 % conversion at this same temperature which was not matched by 1:2.2 MM till beyond 300 °C. Beyond this point however both OM and MM display similar activity achieving 97.7 % and 97.3 % at 320 °C and both attaining 99.2 % conversion by 350 °C.

The overall effect these changes had on formaldehyde yield saw 1:2.2 MM achieving the highest of those tested achieving 93.9 % at 335 °C, 1.3 % increase compared to 1:2.2 OM though at a higher temperature and 3.9 % rise compared to 1:2.2 Coprep achieved at 350 °C. In conjunction to higher observed yield, greater catalytic stability was attained with little change in formaldehyde yield over the highlighted temperature range not observed by the other samples.

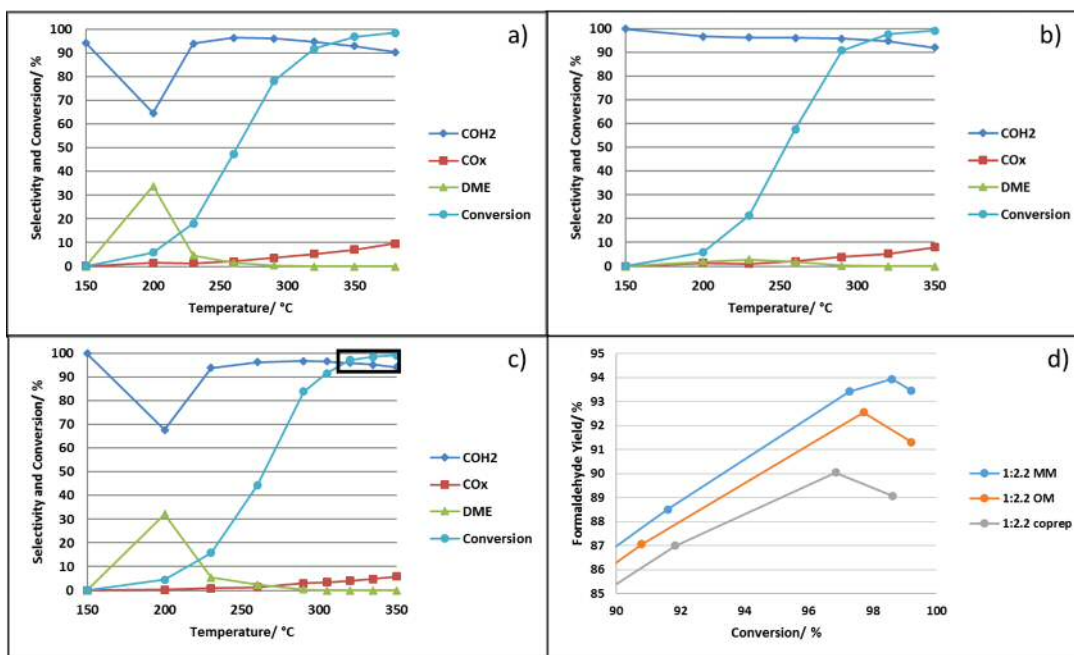


Figure 4.9 MeOH partial oxidation reaction summary of iron molybdate samples synthesised using various methods. (a) 1:2.2 Coprep, b) 1:2.2 OM, c) 1:2.2 MM and d) formaldehyde yield vs conversion comparison).

4.2.4. Discussion of Malonic Acid Usage as a Solvent for Iron Molybdate Synthesis

Malonic acid decomposition method displayed significant improvement in formaldehyde yield compared to both oxalic acid decomposition and coprecipitation methods due to superior formaldehyde selectivity maintained at higher temperatures.

The possible reason for the increase in formaldehyde selectivity may be due to an increase in overall Fe:Mo distribution which was observed to be homogeneous in the MM example suggested by both Raman mapping and microscopy studies. Rather than crystalline MoO₃ observed in the Coprep sample, this MoO₃ was suggested to be amorphous with the combination of low XRD content for the bulk ratio used (28.7 %) and relatively large quantities in both Raman and surface analysis. This could have prevented the formation of areas of iron enrichment at the surface which as stated previously can lead to the formation of more COx products at higher conversions.^{25,26,29–32} OM and Coprep samples in contrast displayed iron rich areas and MoO₃ crystallite formation respectively suggesting some phase separation along the surface in conjunction to lower overall homogeneity, the effect this has could be the lower formaldehyde selectivity observed by both the OM and Coprep samples.

The lower activity of MM over the other samples at lower temperatures may be due to the formation of more MoO_3 on the surface of the sample, this is suggested both EDX and XPS mapping with the formation of less isolated and Raman spectral mapping results although in an amorphous form due to the lower presence in XRD results. This could have caused lower iron exposure which has been indicated to be more active towards methanol at an increased rate compared to molybdena species at lower temperatures^{25,26,29–32}.

MM displayed greater activity at temperatures exceeding 260 °C than Coprep which presented increased MoO_3 crystallite formation suggested in both XRD and microscopy results. The synergy of amorphous MoO_3 and $\text{Fe}_2(\text{MoO}_4)_3$ ^{26,29,32} has been shown to display higher activity than the crystalline formations of MoO_3 observed on the surface of 1:2.2 Coprep.

This increase in activity matching OM samples at raised temperatures may also be due to the sponge like morphology similarities observed in SEM results compared to the block like morphologies observed by Coprep. This high activity was achieved with the lowest BET surface area displayed by the three samples, the reduction in surface area may be due to the lower exposure of iron rich species which present higher surface areas compared to molybdena examples.³³

When the formaldehyde yield was normalised against surface area 1:2.2 MM was shown to outperform the other two samples beyond 230 °C as shown in Fig. 4.10. This may suggest a higher concentration of Mo dual sites which were proposed to be selective site for formaldehyde production³⁴ on the surface of 1:2.2 MM compared to the other samples.

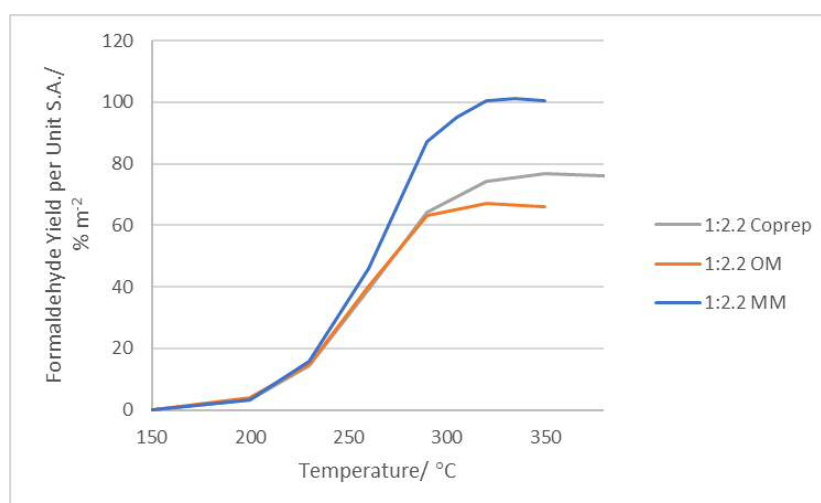


Figure 4.10 Formaldehyde yield normalised against surface area comparison of 1:2.2 MM, 1:2.2 OM and 1:2.2 Coprep samples.

4.3. Effect of Fe:Mo Ratio on Samples Synthesised Using Malonate Decomposition Method (MM)

4.3.1 Introduction

The Fe:Mo ratio was shown by OM to be highly important with large changes observed in both morphology and reactivity. Unlike other iron molybdate production methods which displayed small changes as the Fe:Mo ratio was altered between 1:1.5-1:3.0^{23,24}, OM displayed far greater changes due to the changes in mixing of the oxalates prior to calcination.

Changes in Fe:Mo were investigated for MM using the same ratios used by OM to ascertain the sensitivity of MM to these changes. Close attention was placed between 1:1.5-1:2.2 to investigate the effect of small changes in molybdenum content beyond the stoichiometric similar to OM examples.

4.3.2 Characterisation

4.3.2.1. BET Surface Area and XPS Surface Analysis

The BET surface area results shown in Table 4.2 displayed changes as the Fe:Mo ratio was changed using MM, surface area increased in the following order from the lowest 1:1.5 MM, 1:1.9 MM, 1:2.2 MM, 1:3.0 MM and 1:1.7 MM presenting the highest. Increased Mo content from 1:1.5 MM causing increased surface area is contrary to results shown by other authors^{23,26,35} using coprecipitation method. Changes between 1:1.7 MM, 1:1.9 MM, 1:2.2 MM and 1:3.0 MM were small and within error which may indicate larger molybdenum content has limited effect on surface area changes.

XPS surface results of the same sample displayed an increase in Mo surface content as the Fe:Mo ratio was increased from 1:1.5-1:2.2 before plateauing. Percentage Mo surface

enrichment relative to the bulk was also shown to increase until 1:3.0 from 33 %, 35 %, 42 %, 50 % and 10 % displayed by 1:1.5 MM – 1:3.0 MM, this may indicate a preference for surface migration from the bulk with the use of the MM method.

The 1:3.0 MM sample displayed limited surface enrichment compared to the other samples, this is supported by findings shown by House *et al.*²³ who saw samples using Mo bulk far in excess of the stoichiometric 1:1.5 Fe:Mo ratio showed a reduction in Mo surface content relative to the bulk due to surface saturation.

Table 4.2. BET surface area and XPS surface ratio comparison for MM samples produced using various Fe:Mo ratios with relative surface Mo excess compared to theoretical bulk content.

Sample	BET Surface Area/ m ² g ⁻¹	XPS Surface Ratios	Rel. Surface Mo Excess/ %
		Fe:Mo	
1:1.5 MM	2.2 ± 0.3	1:2.0	33.3
1:1.7 MM	3.6 ± 0.1	1:2.3	35.3
1:1.9 MM	3.0 ± 0.2	1:2.7	42.1
1:2.2 MM	3.1 ± 0.2	1:3.3	50.0
1:3.0 MM	3.4 ± 0.1	1:3.3	10.0

4.3.2.2. Powder XRD Crystallography

The XRD comparison of MM samples produced using various Fe:Mo ratios (Fig. 4.10) displayed a combination of Fe₂(MoO₄)₃, α-MoO₃ and α-Fe₂O₃ with no other phases present, the relative phase composition is presented in Table 4.3. The relative Fe₂(MoO₄)₃ content decreased as α-MoO₃ content increase when the Fe:Mo ratio was changed as follows 1:1.5, 1:1.7, 1:2.2, 1:1.9 and 1:3.0. The low Fe₂(MoO₄)₃ content observed using Fe:Mo ratio 1:1.9 was also observed in the OM examples and attributed to the formation of crystalline MoO₃ which has been found to prevent the crystallisation of Fe₂(MoO₄)₃³⁶.

Similar to OM samples tested in Section 3.3, Fe₂O₃ content was shown to increase as Fe:Mo ratio was increased from 1:1.5-1:3.0 (0.8 %, 1.4 %, 2.4 %, 2.5 % and 3.9 %). This observation is contrary to other studies,^{24,32,35} due to greater proportion of Fe₂O₃ that should be diluted with increased molybdenum content forming Fe₂(MoO₄)₃ via the solid state reaction³⁷.

Crystallite sizes remain unchanged as Fe:Mo ratios are changed with no significant broadening in peak width presented.

Table 4.3. Relative phase composition of MM samples produced using various Fe:Mo ratios corresponding to XRD results shown in Fig. 4.11.

Sample	Relative % Phase Based On Powder XRD Results		
	$\text{Fe}_2(\text{MoO}_4)_3$	MoO_3	Fe_2O_3
1:1.5 MM	88.8	10.4	0.8
1:1.7 MM	80.6	18.0	1.4
1:1.9 MM	66.7	30.8	2.5
1:2.2 MM	68.8	28.7	2.5
1:3.0 MM	49.0	47.1	3.9

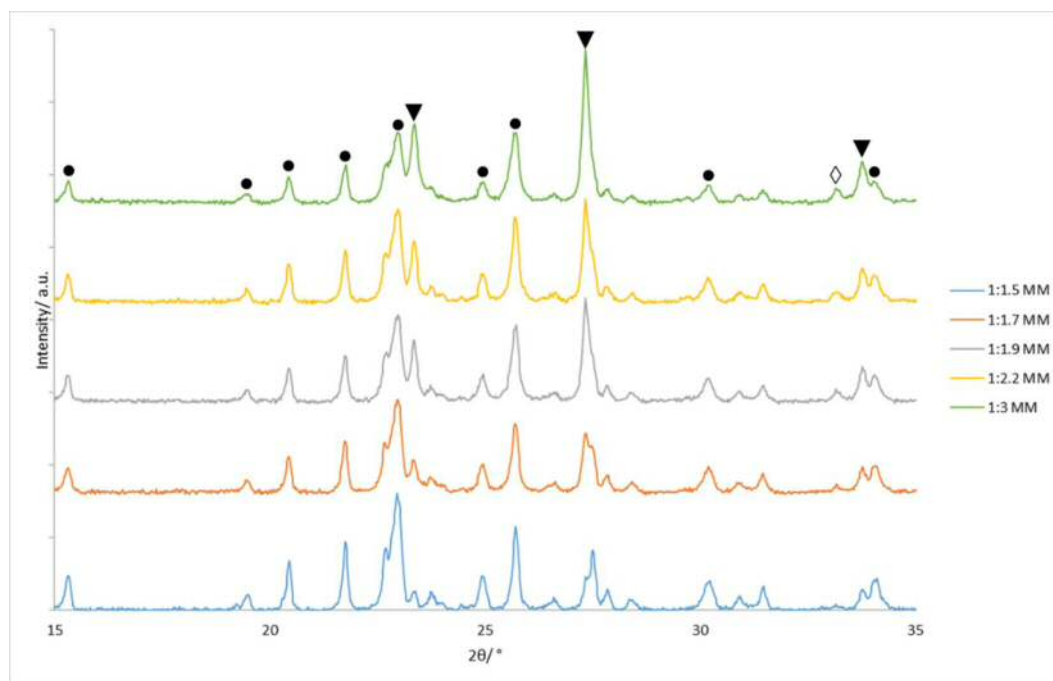


Figure 4.11. Powder XRD patterns of samples prepared using MM using various Fe:Mo ratios. (Key: ▼ MoO_3 , ● $\text{Fe}_2(\text{MoO}_4)_3$ and ◊ Fe_2O_3).

4.3.2.3. Raman Spectral Mapping

The Raman spectral mapping comparison of MM samples prepared using various Fe:Mo ratios is presented in Fig. 4.12 with all spectra displaying differing amounts of $\text{Fe}_2(\text{MoO}_4)_3$ and MoO_3 . The most representative points for 1:1.5 MM, 1:1.7 MM, 1:1.9 MM, 1:2.2 MM and 1:3.0 MM are shown in 4.12.a, d, g, j and m respectively.

As Fe:Mo ratios are increased from 1:1.5-1:3.0, MoO_3 content was shown to rise relative to $\text{Fe}_2(\text{MoO}_4)_3$. This is contrary with XRD results which showed a MoO_3 content was higher in 1:1.9 MM than 1:2.2 MM which could suggest the formation of amorphous $\text{Fe}_2(\text{MoO}_4)_3$ due to the higher sensitivity of Raman towards less crystalline materials.

The consistency over the points surveyed for each sample showed that 1:2.2 MM was the most homogeneous of those tested with little change observed between spectra. This was followed by 1:3.0 MM and 1:1.5 MM which displayed small changes in MoO_3 content. Both 1:1.9 MM and 1:1.7 MM displayed the greatest variance from the average results presenting larger MoO_3 contents in many of their points.

The higher MoO_3 contents observed in both 1:1.5 MM and 1:1.7 MM examples could be detrimental. This is due to the possible exposure of Fe_2O_3 as both have Fe:Mo ratios closest to the stoichiometric ratio for $\text{Fe}_2(\text{MoO}_4)_3$ and should be incorporated into the mixed metal oxide.

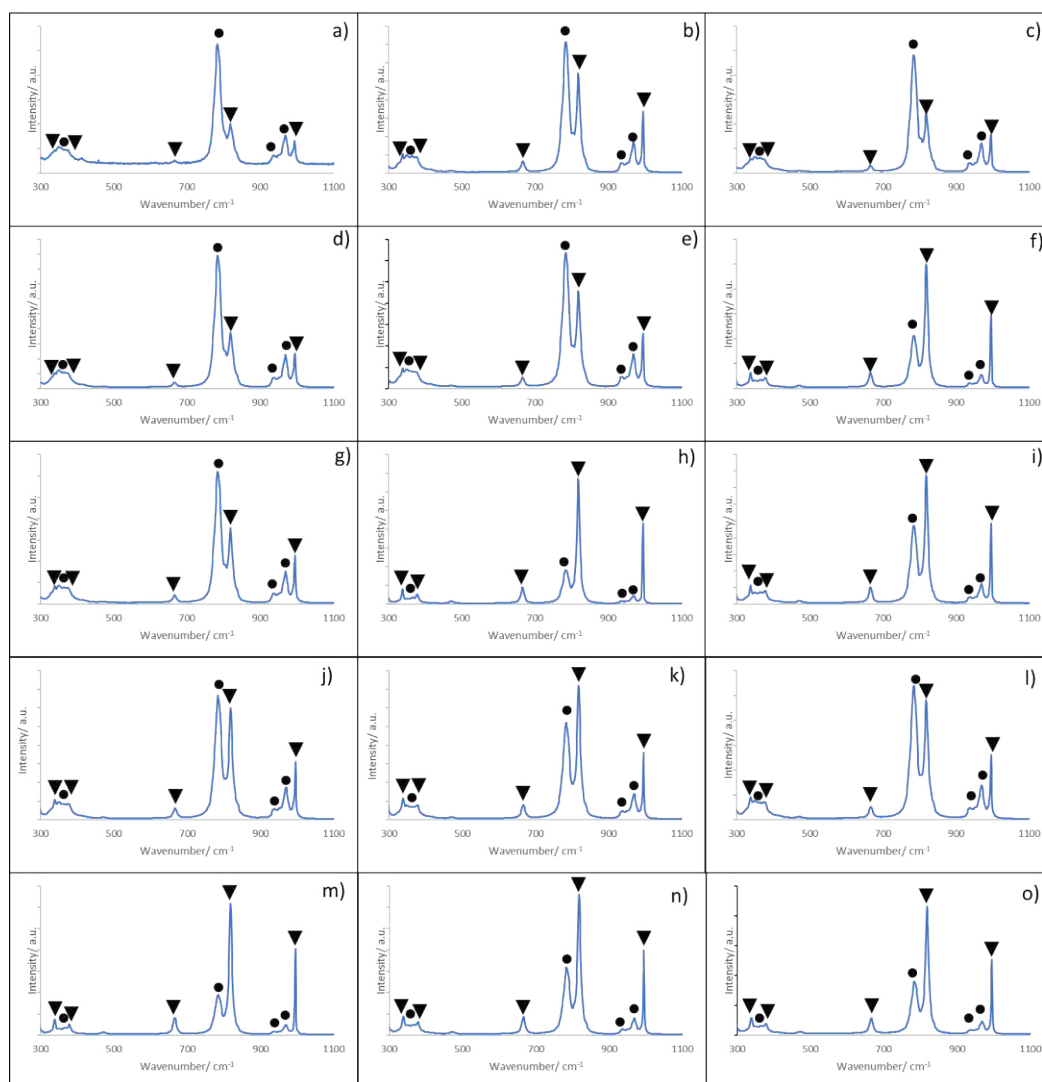


Figure 4.12. Raman spectral mapping of (a-c)1:1.5 MM, (d-f)1:1.7 MM, (g-i)1:1.9 MM, (j-k) 1:2.2 MM and (m-o) 1:3.0 MM samples. (Key: ▼ MoO₃ and ● Fe₂(MoO₄)₃).

4.3.2.4. SEM and EDX Mapping Comparison

SEM and EDX mapping of MM samples prepared using various Fe:Mo ratios displayed significant morphological changes as the ratios were altered (Fig. 4.13).

1:1.5 MM presented with big block structures with large voids (4-5 μm diameter) formed over the surface, using Fe:Mo ratios 1:1.7-1:2.2 caused the loss of the ordered block structures replaced by the sponge like morphology pitted with smaller holes (1 μm) on the surface. Increasing Mo content further to Fe:Mo 1:3.0 resulted in a further change in

morphology, regular lamellar plate structures were observed surrounding void structures (2-3 μm).

EDX mapping of the corresponding micrographs showed evidence of iron enrichment in all samples as highlighted. These areas were most frequent in 1:1.7 MM and 1:1.9 MM samples with 1:1.7 MM displaying areas of near iron exclusivity. 1:1.5 MM void structures displayed iron enrichment, with evidence of molybdenum migration into these structures possibly caused by MoO_3 migration from the bulk during the calcination, the rest of the surface surveyed displaying even Fe:Mo distribution.

1:3.0 MM void structures also displayed iron enrichment in and around these centres. The lamellar structures highlighted were found to be nearly molybdenum exclusive in some areas, this may indicate the formation of MoO_3 with the regular crystalline plate structures similar to observations by Routary *et al.*²⁶

Only 1:2.2 MM and 1:3.0 MM displayed any significant molybdenum enrichment at the surface with all samples displaying homogenous Fe:Mo distribution in the areas not highlighted.

Evidence from microscopy indicates that the worst sample surveyed was 1:1.7 with the formation of areas of near iron exclusivity observed suggesting Fe_2O_3 exposed to the surface. 1:1.9 MM and 1:3.0 MM also showed evidence of segregation although neither produced iron exclusive regions. 1:1.5 MM and 1:2.2 MM displayed iron enrichment in some areas but no areas of elemental exclusivity were observed in either example.

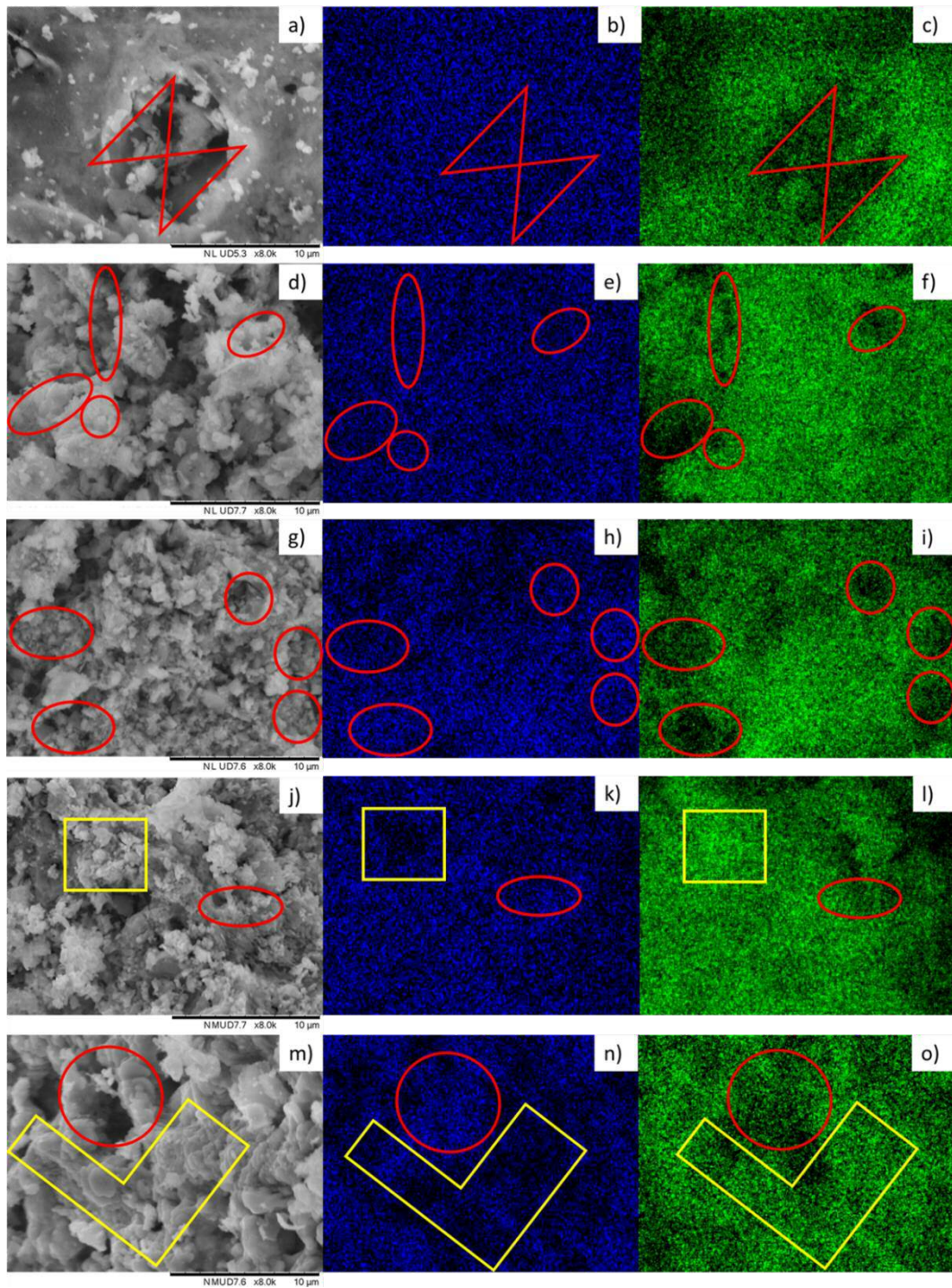


Figure 4.13 SEM and EDX elemental mapping comparison of MM samples prepared using a variety of Fe:Mo ratios. (a) SEM image of 1:1.5 MM, (b) EDX map showing Fe content of 1:1.5 MM, (c) EDX map showing Mo content of 1:1.5 MM, (d) SEM image of 1:1.7 MM, (e) EDX map showing Fe content of 1:1.7 MM, (f) EDX map showing Mo content of 1:1.7 MM, (g) SEM image of 1:1.9 MM, (h) EDX map showing Fe content of 1:1.9 MM, (i) EDX map showing Mo content of 1:1.9 MM, (j) SEM image of 1:2.2 MM, (k) EDX map showing Fe content of 1:2.2 MM, (l) EDX map showing Mo content of 1:2.2 MM, (m) SEM image of 1:3.0 MM, (n) EDX map showing Fe content of 1:3.0 MM and (o) EDX map showing Mo content of 1:3.0 MM. Highlighted Fe rich (red circles) and Mo rich (yellow squares).

4.3.3. Methanol Partial Oxidation

Methanol partial oxidation results presented in Fig. 4.14 displays a comparison of MM samples produced using various Fe:Mo ratios.

The activity of the samples seemed to vary depending on the Fe:Mo ratio used in the production of the MM samples. At low temperatures (<260 °C) no sample exceeded 30 % methanol conversion, from 260 °C onwards all except 1:1.5 MM displayed a rapid increase in conversion. 1:1.7 MM displayed the greatest activity with 58.6 % and 88.5 % conversion attained at 260 °C and 290 °C respectively, high conversions (94.3 %) was achieved at 305 °C. 1:1.9 MM, 1:2.2 MM and 1:3.0 MM samples displayed very similar activity at all temperatures tested although none of them exceeded 1:1.7 MM only achieving high conversion (> 94 %) at 320 °C. 1:1.5 MM displayed the lowest activity of all MM samples tested achieving high conversions at temperatures exceeding 320 °C.

All MM samples were selective towards formaldehyde production at temperatures exceeding 260 °C with the following order 1:1.5 MM(97.2 %), 1:1.9 MM(97.0 %), 1:2.2 MM(96.3 %), 1:3.0 MM(95.9 %) and 1:1.7 MM(93.3 %). Gradual loss of formaldehyde selectivity was observed in favour of CO_x production as temperatures were increased in all samples. Formaldehyde selectivity was largely maintained by 1:1.5 MM and 1:2.2 MM up until 350 °C presenting a loss of 1.6 % and 2.1 % respectively over the temperature range. 1:3.0 MM and 1:1.9 MM were not able to maintain formaldehyde selectivity to the same extent achieving a 3.0 % and 3.5 % respectively. 1:1.7 MM unable to maintain formaldehyde selectivity like the other MM samples decreasing below 91 % at 320 °C.

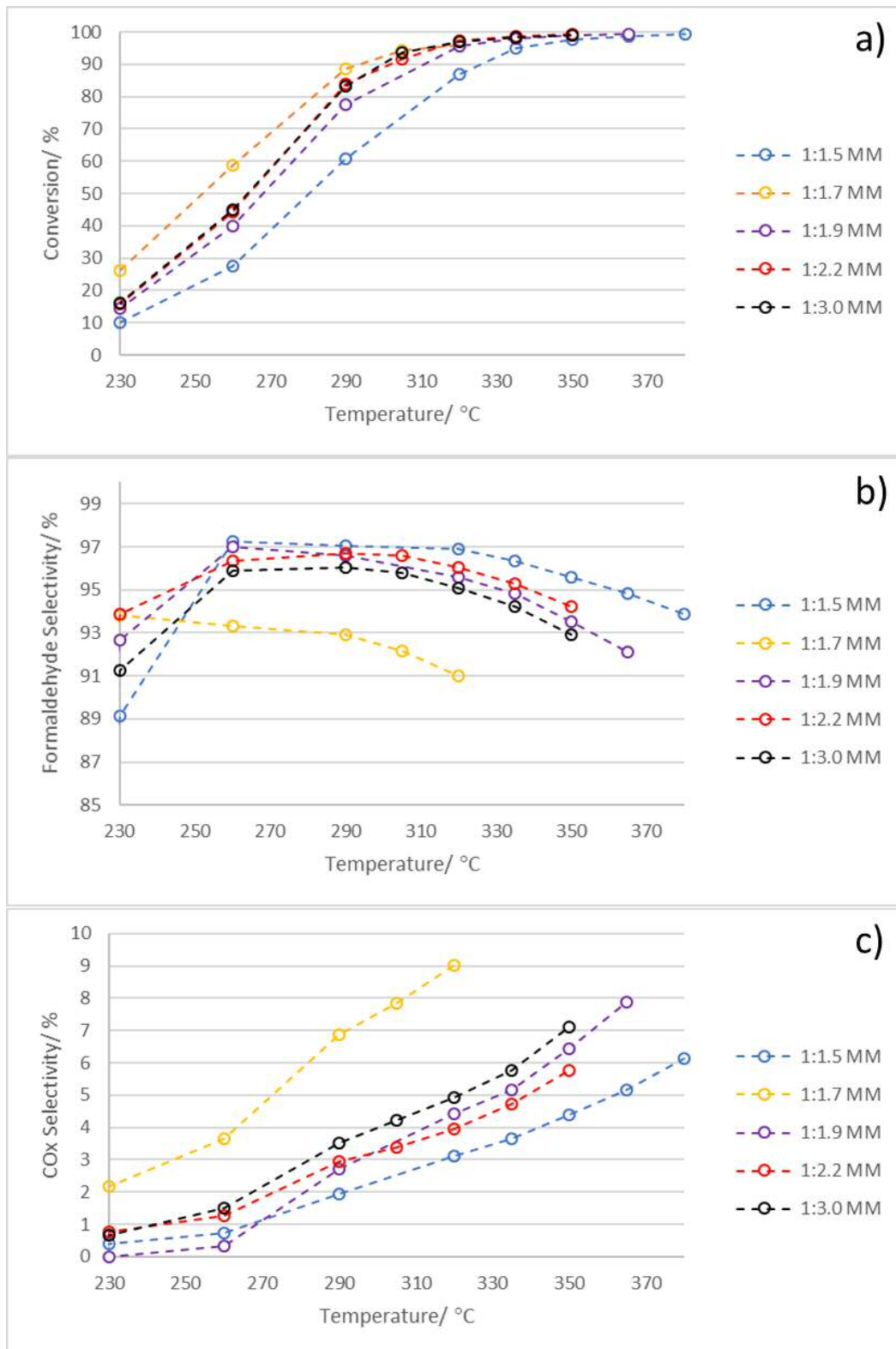


Figure 4.14. MeOH partial oxidation reaction summary of samples synthesised using MM with various Fe:Mo ratios using a variety of reaction temperatures; (a) Methanol conversion, (b) Formaldehyde Selectivity and (c) CO_x selectivity.

The effect these had on maximum formaldehyde yield is displayed in Table 4.4 where all MM samples except 1:1.7 MM produced over 92.7 % yield surpassing all samples tested previously. Unlike similar OM samples, all except 1:1.7 MM achieved their formaldehyde production maxima at temperatures exceeding 320 °C. This was due to the lower activity displayed by all MM samples compared to OM examples of the same Fe:Mo ratio. This difference in maximum formaldehyde yield temperatures is observed clearest between 1:1.5 OM and MM samples which displayed a 75 °C difference between maximums attained.

Along with higher overall formaldehyde yields by MM samples, all except 1:1.7 MM displayed areas of very high formaldehyde yield (>91 %) highlighted in Fig. 4.14. These extended operation temperature ranges were not observed by OM or Coprep samples, this suggests an increase in stability by MM samples over other iron molybdate production methods.

Table 4.4. Maximum formaldehyde yield comparison of both OM and MM samples using various Fe:Mo ratios.

Fe:Mo Bulk Ratio	OM		MM	
	Maximum Formaldehyde Yield/ %	Temperature/ °C	Maximum Formaldehyde Yield/ %	Temperature/ °C
1:1.5	76.8	290	93.6	365
1:1.7	91.2	320	87.3	320
1:1.9	89.3	335	92.9	335
1:2.2	92.6	320	93.9	335
1:3.0	87.1	320	92.7	335

4.3.4. Precalcination study

4.3.4.1. XPS of Uncalcined Mixtures

As with oxalate decomposition method, malonate decomposition method presented a similar relationship between carboxylate complexes of Mo^V and Mo^{VI}. Malonate complexes with Mo^{VI} have been shown to form polymeric molybdena malonates as shown in Fig. 4.4.

Mo^V malonate was complexes comprising of centres of individual Mo₂O₄ units (Fig. 4.3.) unlike oxalate which produced pairs of dimers connected by a bridging oxalate ligand (Fig. 3.3.). This in turn could result in further mixing of the iron and molybdenum by limiting the localised formation of molybdenum centres, thus preventing the formation of large volumes MoO₃ during the initial steps of the decomposition.

XPS surface analysis of uncalcined MM samples presented in Table 4.5 displayed clear changes between 1:1.7 MM and the other examples. 1:1.7 MM was observed to contain the highest concentrations of Mo^{VI}, this may have caused the formation of MoO₃ observed in Raman mapping results which could indicate the phase separation.

1:1.5, 1:1.9 and 1:3.0 MM all presented with very similar Mo^V content which may indicate the similar overall performance of all three samples. 1:1.9 and 1:3.0 MM were particularly close and both performed near identically. The increase in Mo^V content for all three samples may have caused the superior homogeneity observed in characterisation results due to the formation of less polymeric molybdenum species prior to calcination. 1:3.0 MM did however present with large volumes of MoO₃ post calcination which is unsurprising due to the high molybdenum content of the sample. 1:2.2 MM presented the highest Mo^V content almost matching Mo^{VI} which may have caused the superior mixing of iron and molybdenum prior to calcination.

Table 4.5. XPS comparison of Mo 3d region of uncalcined MM using various Fe:Mo ratios.

Sample	XPS Surface Ratios
	Mo ^V :Mo ^{VI}
1:1.5 MM	1:2.7
1:1.7 MM	1:3.4
1:1.9 MM	1:2.6
1:2.2 MM	1:1.5
1:3.0 MM	1:2.4

4.3.4.2 Thermogravimetric Analysis

DTG and corresponding TGA results presented in Fig. 4.15 and Table 4.6 respectively display possible evidence for the homogeneous mixing of the iron and molybdenum shown in characterisation results. As stated previously, malonates of both molybdenum and iron displayed decompositions between 176-214 °C (peak 191 °C) and 220-358 °C (peak 267 °C) respectively with the loss of malonate in the form of CO₂ and H₂O.

All MM samples presented an intense decomposition highlighted in blue between 168-210 °C peaking between 191-196 °C indicating the decomposition of molybdenum malonate. These decompositions were seen to diminish in significance as Fe:Mo content was increased as 1:1.5 MM presented the highest reduction in weight of 40.6 % during this decomposition. 37.4 % and 31.8 % weight reductions were achieved at the same conditions by 1:1.7 MM and 1:1.9 MM, 1:2.2 MM and 1:3.0 MM presented the least isolated molybdenum malonate decomposition with the loss of only 23.3 % and 27.1 % respectively.

Unlike the result of ammonium molybdate malonate mixture presented in Fig. 4.5, significant broadening was observed which looked like the formation of another species in the form of a shoulder. This second species decomposition highlighted in green between 210-263 °C was observed to peak between 220-225 °C which corresponds with the beginning of iron malonate decomposition which was observed to peak at 267 °C.

This may suggest that a similar phenomenon occurred like OM samples where highly exothermic decomposition of the molybdenum malonate causing the activation of

neighbouring malonates. This is similar to results obtained by using different mixed metal malonate mixtures, the activation of malonates was facilitated by the exothermic decomposition of neighbouring malonates.²²

This broadening is observed clearest by 1:2.2 MM corresponding to 26.3 % weight reduction which is the most significant decomposition step observed by the sample. 1:3.0 MM presented similar broadening to a lesser extent corresponding to a 25.5 % weight loss in TGA results. Between 1:1.5-1:1.9 Fe:Mo ratios this region was shown to increase gradually as molybdenum content was increased presenting 20.0 %, 21.2 % and 22.5 % weight reductions.

What this may indicate is that more homogeneous mixing of 1:2.2 and 1:3.0 MM samples prior to calcination compared to others, the molybdenum malonate to have greater access to neighbouring iron malonate thus facilitating the autocatalytic decarboxylation more rapidly at lower temperatures.

In all cases another decomposition was observed between 263-358 °C highlighted in red which may indicate isolated iron malonate which is shown to fluctuate as Fe:Mo ratio was altered. 1:1.7 MM (11.2 %) and 1:1.9 MM (9.2 %) presented the highest amounts of decomposition in TGA results in this region closely followed by 1:3.0 MM (8 %). 1:2.2 MM (7.4 %) and 1:1.5 MM (7.1 %) presented the lowest.

Unlike isolated iron oxalate which was linked to Fe₂O₃ production in OM, decomposition of iron malonate has been shown to produce γ -Fe₂O₃ nanoparticles by Stefanescu and Stefanescu⁸. This might have aided the formation of more homogeneous distribution by preventing the formation of large isolated areas of iron enrichment observed on the surface, although larger volumes of isolated iron malonate could be detrimental if not dispersed leading to localised high iron concentrations. Some areas of enrichment were observed especially in 1:1.5-1:1.9 MM and 1:3.0 MM samples, none of these areas were elementally exclusive however unlike the OM samples.

Between 400-460 °C further loss was observed suggesting the formation of Fe₂(MoO₄)₃ from Fe₂O₃ and MoO₃ via the solid state reaction³⁷.

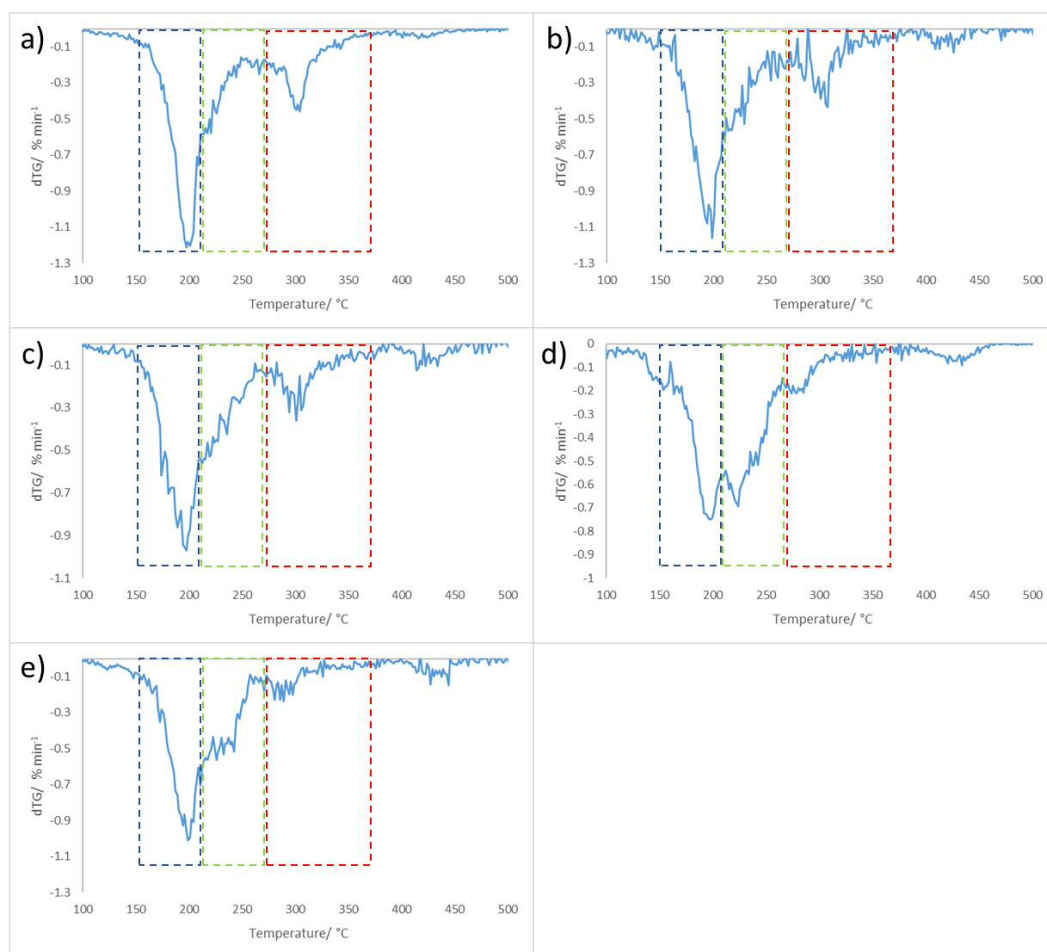


Figure 4.15. DTG Analysis of uncalcined samples of MM samples using various Fe:Mo ratios ranging from 100-500 °C using a ramp rate of 5 °C min⁻¹ (a) 1:1.5 MM, b) 1:1.7 MM, c) 1:1.9 MM, d) 1:2.2 MM and e) 1:3.0 MM)

Table 4.6. TGA summary of samples produced using MM with varying Fe:Mo ratios corresponding to DTG highlighted regions in Fig. 4.15.

TGA Temperature Range/ °C	Percentage Weight Loss/ %				
	1:1.5	1:1.7	1:1.9	1:2.2	1:3.0
168-210	40.6	37.4	31.8	23.3	27.1
210-263	20.0	21.2	22.5	26.3	25.5
263-358	7.1	11.2	9.2	7.4	8.0

4.3.5. Effect of Fe:Mo Ratio on Malonate Decomposition Method Samples Discussion

The use of MM for iron molybdate synthesis has been shown to be highly advantageous for selective methanol oxidation compared to more traditional production methods and OM tested previously. Higher formaldehyde yields (> 92.6 %) were attained by many of the samples tested with very high formaldehyde yield maintained over a range of temperatures not observed by other iron molybdate samples production methods tested.

The change in Fe:Mo ratio had far less of an effect as samples produced using OM and results shown in other studies^{23,35}. The MM samples higher yields were attained at increased temperatures than the comparison examples due to the homogeneously distributed, high molybdenum surface content which prevented the formation of iron rich centres.

Only 1:1.7 MM presented yields lower than 90 % though still exceeding many samples produced by OM. The reasons for this might be due to the change in overall morphology between block structures observed by 1:1.5 MM and the sponge like formations observed by 1:1.9 MM, this could have caused the exposure of more Fe towards the surface both increasing activity and lowering formaldehyde selectivity at lower temperatures. Similar significant transitions were observed by OM with large changes displayed between 1:1.7 OM and 1:1.9 OM samples.

The possible reasons for the higher iron and molybdenum distribution observed by samples may be due to the mixing of the precursors prior to decomposition. All but 1:1.7 MM produced large amounts of Mo^V suggesting the formation of individual Mo₂O₄ centred malonate dimers¹⁶ preventing larger Mo^{VI} polymeric molybdenum species¹⁹ prior to calcination. This could have promoted more homogeneous mixing of both iron and molybdenum by preventing isolated concentrations of either malonate.

Thermal gravimetric analysis promoted a different decomposition method compared to OM, malonate examples proceed by the initial decomposition of molybdenum malonate followed closely by an overlap thought to be iron malonate. Due to the extent of the overlapping species even at the stoichiometric Fe:Mo ratio, which equivalent OM sample produced the lowest formaldehyde yield of the Fe:Mo OM study, displayed greater distribution of iron and molybdenum after calcination. This may indicate superior mixing of

the precursors prior to decomposition as proximity to neighbouring carboxylates is essential for the autocatalytic decarboxylation reaction to occur in the acid mixture.

This second decomposition was especially prevalent in 1:2.2 MM which presented the most homogeneous distribution of both iron and molybdenum of all MM samples post calcination, as a result the highest formaldehyde yield was also produced. In all MM cases some iron malonate was isolated, the decompositions of which cause possible γ -Fe₂O₃ nanoparticle formation.⁸ Little evidence of any detrimental effect caused by this formation however and were possibly covered by migrating amorphous MoO₃ during calcination.^{38,39}

4.4. Effects of Calcination Conditions on Samples Prepared using the Malonate Decomposition Method

4.4.1. Introduction

A combination of calcination conditions were investigated to ascertain the stability of MM towards calcination conditions. The MM samples were investigated using 450 °C, 500 °C and 600 °C with the latter used to investigate the mobility of molybdenum species over the surface of the sample.^{40,41}

A combination of times was also employed to investigate changes in possible morphology caused by the different temperatures, whether these structures were temporary or were altered as calcination lengths were extended.

4.4.2. Characterisation

4.4.2.1. BET Surface Area and XPS Surface Analysis

Surface area and XPS surface ratio comparison of 1:2.2 MM samples calcined using a variety of conditions is shown in Table 4.7. Both surface area and Fe:Mo surface ratio were shown to change as calcination conditions were altered.

The surface area was shown to decrease in the following order, 450 2 h MM > 500 6 h MM > 450 6 h MM > 500 2 h MM > 500 4 h MM > 450 4 h MM > 600 2 h MM > 600 4 h MM > 600 6 h MM.

The difference between the highest surface area presented by 450 2 h MM and the lowest 600 6 h MM is a 57 % reduction in surface area. All samples produced relatively low surface area with reported values using coprecipitation methods reporting between 5-8 m² g⁻¹.

23,26,35

Molybdenum surface enrichment was observed in XPS results in all samples with the highest enrichment observed by 600 2 h MM, 500 4 h MM, 500 6 h MM, 450 2 h MM and 450 6 h MM samples. The 600 2 h MM sample presented the highest molybdenum surface content, over double the theoretical bulk content (Fe:Mo 1:2.2) possibly indicating significant molybdenum migration towards the surface from the bulk. Lower molybdenum surface content was observed for the 600 6 h MM, 500 2 h MM, 600 4 h MM and 450 4 h MM examples.

Table 4.7 BET surface area and XPS surface analysis of samples prepared via MM using Fe:Mo ratio of 1:2.2 calcined using various conditions.

Sample	BET Surface Area/ m ² g ⁻¹	XPS Surface Ratios	Rel. Surface Mo Excess/ %
		Fe:Mo	
500 2 h MM	3.1 ± 0.2	1:3.3	50.0
500 4 h MM	2.7 ± 0.1	1:3.9	77.3
500 6 h MM	3.4 ± 0.1	1:3.9	77.3
450 2 h MM	4.2 ± 0.3	1:3.9	77.3
450 4 h MM	2.5 ± 0.1	1:3.0	36.3
450 6 h MM	3.2 ± 0.1	1:3.6	63.6
600 2 h MM	2.2 ± 0.2	1:4.7	113.6
600 4 h MM	2.0 ± 0.2	1:3.2	45.5
600 6 h MM	1.8 ± 0.2	1:3.4	54.5

4.4.2.2. Powder XRD Crystallography

The bulk composition as shown in XRD results shown in Fig. 4.17 and corresponding results in Table 4.8 shows that the composition of the samples produced using MM vary with calcination condition. $\text{Fe}_2(\text{MoO}_4)_3$ content was shown to decrease relative to MoO_3 in the following order, 500 2 h MM > 450 4 h MM = 600 6 h MM > 450 6 h MM > 600 4 h MM > 500 6 h MM > 600 2 h MM > 500 4 h MM > 450 2 h MM.

All samples produced significantly less $\text{Fe}_2(\text{MoO}_4)_3$ relative to MoO_3 with changes in calcination conditions,

Fe_2O_3 content was highest in 450 4 h MM(3.7 %) and 600 MM samples(3.1-3.4 %) with the other samples displaying between 2.2-2.8 % content.

Significant peak broadening was observed by the three 450 MM and 600 4 h MM samples indicating a decrease in crystallite size of the samples.

Table 4.8 Relative phase composition of 1:2.2 MM samples produced using various calcination conditions corresponding to XRD results shown in Fig. 4.16.

Sample	Relative % Phase Based On Powder XRD Results		
	$\text{Fe}_2(\text{MoO}_4)_3$	MoO_3	Fe_2O_3
500 2 h MM	68.8	28.7	2.5
500 4 h MM	57.1	40.1	2.8
500 6 h MM	58.3	39.6	2.2
450 2 h MM	54.5	43.4	2.2
450 4 h MM	61.7	34.6	3.7
450 6 h MM	60.1	37.1	2.8
600 2 h MM	58.1	38.7	3.2
600 4 h MM	60.0	36.8	3.1
600 6 h MM	61.7	34.9	3.4

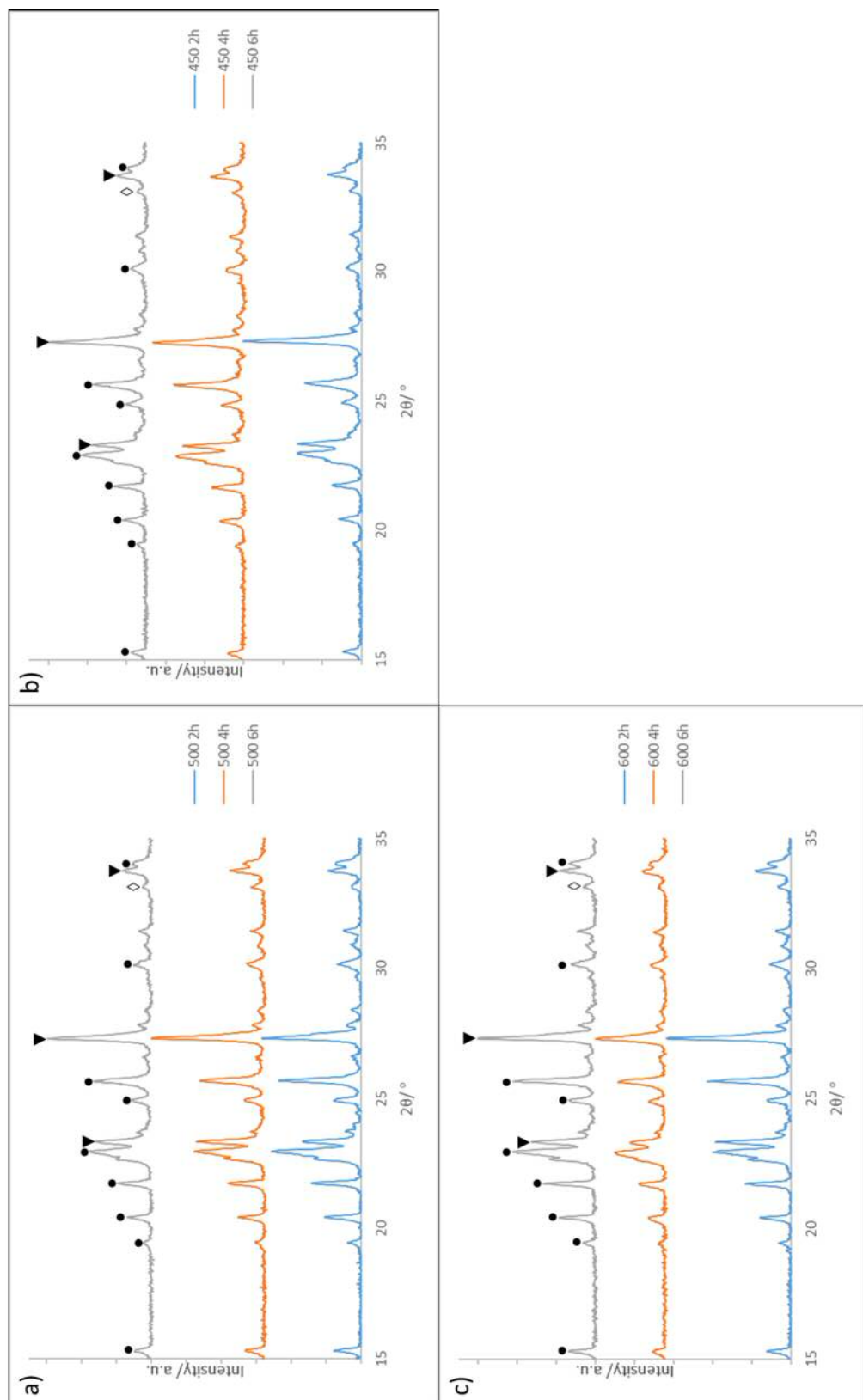


Figure 4.16 Powder XRD patterns of MM samples produced using different calcination lengths and temperature, (a) 500 °C, (b) 450 °C and (c) 600 °C. (Key: \blacktriangledown MoO_3 , \bullet $\text{Fe}_2(\text{MoO}_4)_3$ and \blacklozenge Fe_2O_3).

4.4.2.3. Raman Mapping Comparison

The Raman spectral mapping results shown in Figures 4.17, 4.18 and 4.19 display the comparison between MM samples calcined at 500 °C, 450 °C and 600 °C respectively.

Samples calcined at 500 °C all display a combination of $\text{Fe}_2(\text{MoO}_4)_3$ and MoO_3 which varied as calcinations were extended. The most common composition of the samples shown in 4.17.a, 4.17.d and 4.17.g indicated that $\text{Fe}_2(\text{MoO}_4)_3$ content was highest in the 500 2 h MM sample, 500 6 h was second with 500 4 h MM presenting the highest MoO_3 average content compared to $\text{Fe}_2(\text{MoO}_4)_3$. This supports XRD results shown in Section 4.4.2.2. which also saw a sharp rise in MoO_3 content with samples calcined at 500 °C for extended durations.

The high homogeneity observed by 500 2 h MM was reduced as calcination duration as increased, areas of higher and near exclusive $\text{Fe}_2(\text{MoO}_4)_3$ content were observed in 500 4 h MM results. 500 6 h MM by contrast displayed areas of higher MoO_3 content in some points such as 4.17.i.

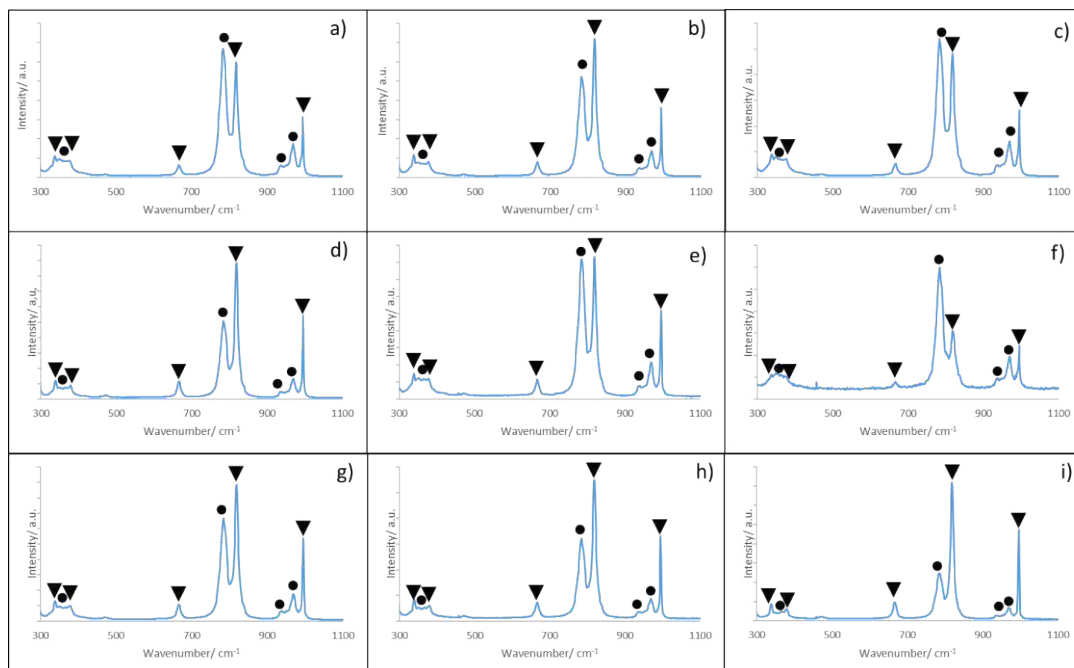


Figure 4.17 Raman spectral mapping of (a-c)500 2 h MM, (d-f)500 4 h MM and (g-i) 500 6 h MM samples. (Key: ▼ MoO_3 and ● $\text{Fe}_2(\text{MoO}_4)_3$).

The most common Raman spectra points surveyed of 450 2 h MM, 450 4 h MM and 450 6 h MM as shown in Figures 4.18.a, 4.18.d and 4.18.g respectively. Relative $\text{Fe}_2(\text{MoO}_4)_3$ content was lowest in the 450 2 h MM followed closely by 450 6 h MM, 450 4 h MM presented the highest $\text{Fe}_2(\text{MoO}_4)_3$ content on average. This support findings in XRD results of the same samples.

As calcinations were lengthened at 450 °C consistency between points increased suggesting greater homogeneity as the calcination was extended. In general, 450 2 h MM presents more MoO_3 in all the points surveyed compared to the other two samples with areas of near MoO_3 exclusivity observed. This is improved at 4 h with less areas of MoO_3 exclusive areas observed although some do remain, but many of the points do contain more $\text{Fe}_2(\text{MoO}_4)_3$ content. Only minor changes in $\text{Fe}_2(\text{MoO}_4)_3/\text{MoO}_3$ content were observed in 450 6 h MM except a small number of MoO_3 enriched areas.

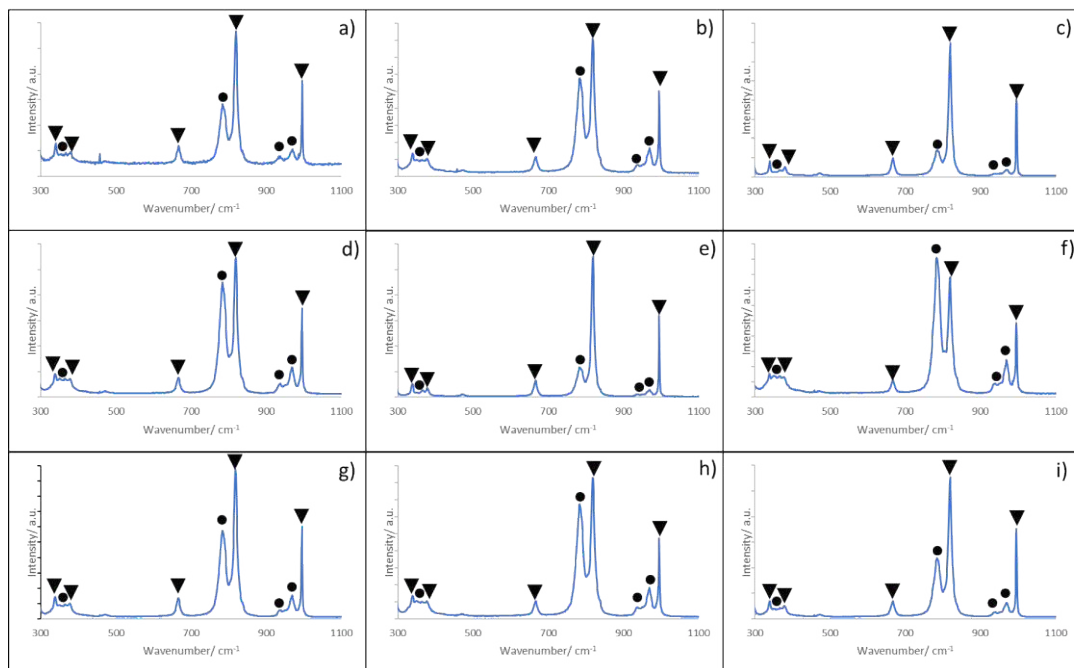


Figure 4.18 Raman spectra mapping of (a-c)450 2 h MM, (d-f) 450 4 h MM and (g-i) 450 6 h MM samples. (Key: ▼ MoO_3 and ● $\text{Fe}_2(\text{MoO}_4)_3$).

The 600 MM samples on average displayed the highest relative $\text{Fe}_2(\text{MoO}_4)_3$ content in their most common points surveyed, shown in Figs. 4.19.a, 4.19.d and 4.19.g for 600 2 h MM, 600 4 h MM and 600 6 h MM respectively, compared to the other MM samples. Both 600 2

h MM and 600 6 h MM were comparable with 600 4 h MM displaying the highest $\text{Fe}_2(\text{MoO}_4)_3$ content.

Less homogeneity was observed by all 600 MM samples with areas of MoO_3 exclusivity observed in all samples. $\text{Fe}_2(\text{MoO}_4)_3$ exclusive areas were also observed in 600 4 h MM and 600 6 h MM samples further supporting a lack of homogeneity.

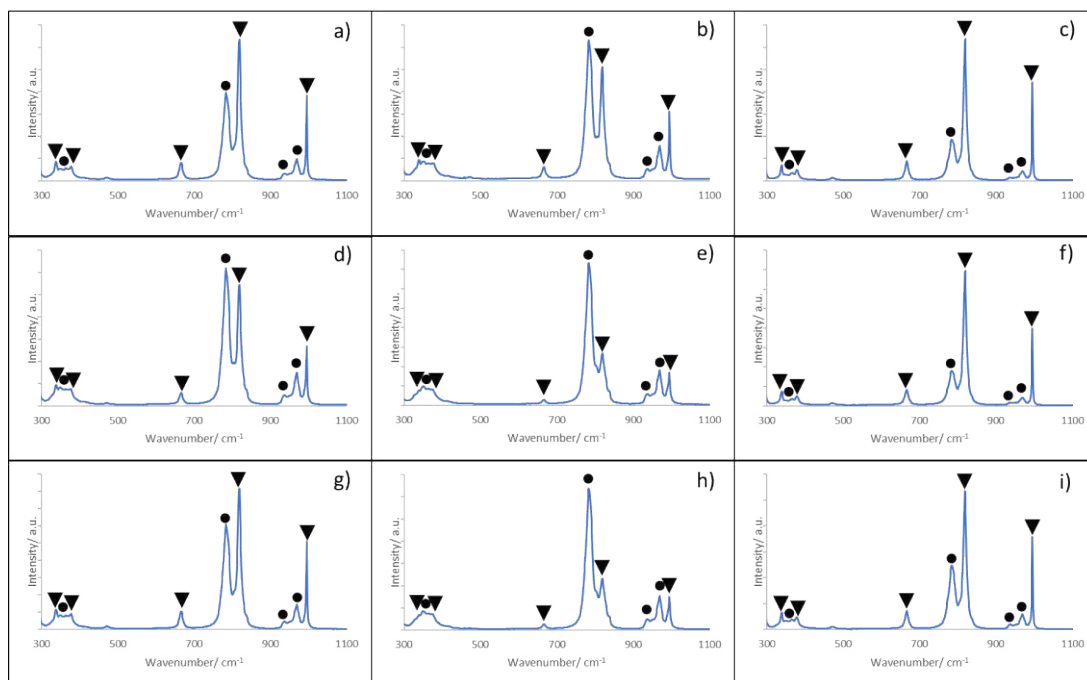


Figure 4.19 Raman spectral mapping of (a-c)600 2 h MM, (d-f)600 4 h MM and (g-i) 600 6 h MM samples. (Key: ▼ MoO_3 and ● $\text{Fe}_2(\text{MoO}_4)_3$).

4.4.2.4. SEM and EDX Elemental Mapping

SEM and EDX mapping of 500 MM samples is presented in Fig. 4.20. 500 2 h MM, as described previously (1:2.2 MM), displayed a sponge like morphology containing a high distribution of both iron and molybdenum with only minor enrichment of either.

Further calcination at 500 °C caused a dramatic change in morphology with the formation of large crystallites (5 μm diameter) with large particles forming on the borders of these structures. EDX mapping of these areas showed near exclusive molybdenum content for the plate formations. Areas of iron enrichment were also highlighted bordering the large plate structures suggesting phase separation at the surface.

500 6 h MM displayed a reduction in molybdenum rich crystallite size ($2\ \mu\text{m}$) although they were still present on the surface, the surface appears to be largely made up of agglomerates of compact particles similar to those seen by Xu *et al.*⁴¹ using similar calcination temperatures. These agglomerates were observed to be largely homogenous in corresponding EDX mapping but iron enrichment was seen in larger particles similar to 500 4 h MM as highlighted.

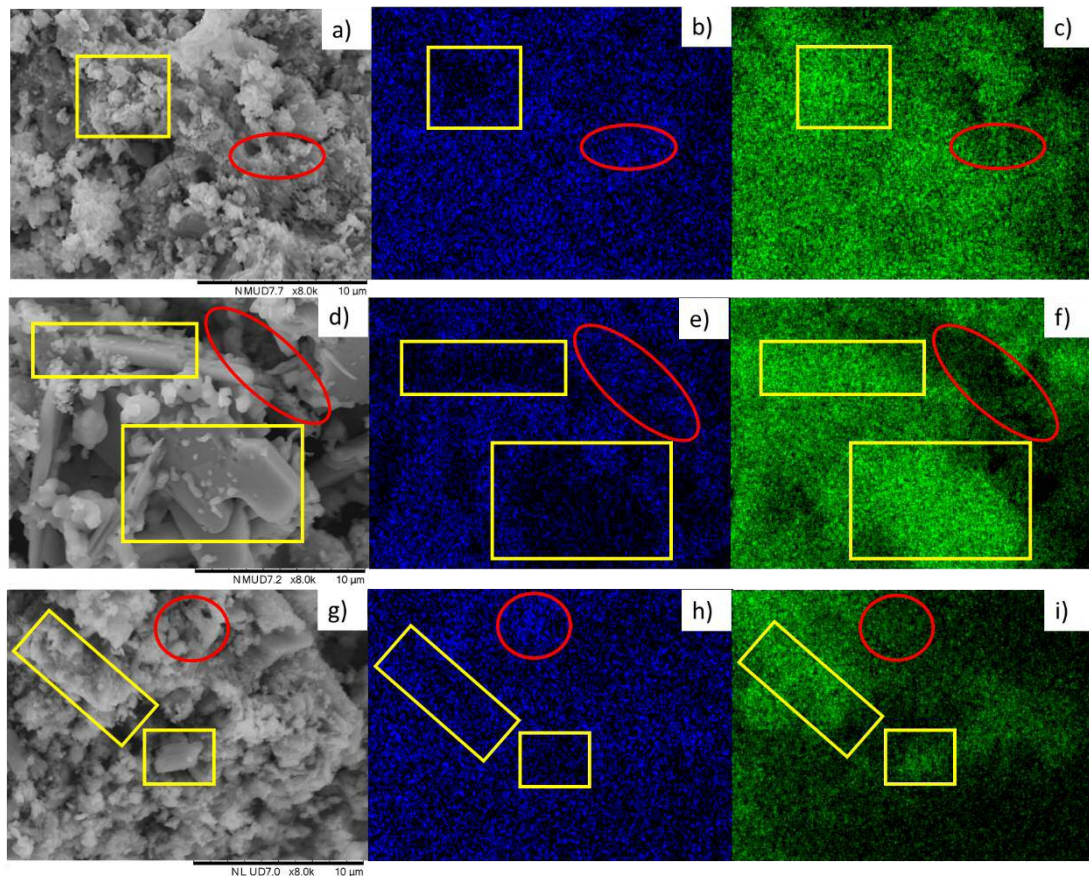


Figure 4.20 SEM and EDX elemental mapping comparison of 1:2.2 MM samples calcined at $500\ \text{°C}$ for a variety of different times. (a) SEM image of 500 2 h MM, (b) EDX map showing Fe content of 500 2 h MM, (c) EDX map showing Mo content of 500 2 h MM, (d) SEM image of 500 4 h MM, (e) EDX map showing Fe content of 500 4 h MM, (f) EDX map showing Mo content of 500 4 h MM, (g) SEM image of 500 6 h MM, (h) EDX map showing Fe content of 500 6 h MM and (i) EDX map showing Mo content of 500 6 h MM. Highlighted Fe rich (red circles) and Mo rich (yellow squares).

The 450 MM samples presented different morphologies in SEM and EDX mapping results (Fig. 4.21), 450 2 h MM presented large block structures which were broken up with shallow voids ($2\ \mu\text{m}$ diameter) along with sponge-like areas. EDX mapping suggested that

both the voids and the sponge-like areas were iron enriched although neither were elementally exclusive with some molybdenum content present in both.

The 450 4 h MM presents with a sponge-like morphology matching 500 2 h MM, some crystallites were also observed over the surface which were found to be molybdenum rich indicating possible MoO_3 production. The void structures observed by 450 2 h MM were still present but EDX results suggests significant molybdenum migration lowering iron enrichment highlighted in orange. No change in morphology was observed by the 450 6 h MM sample but a general molybdenum enrichment was observed over the surface in EDX results supporting XPS results.

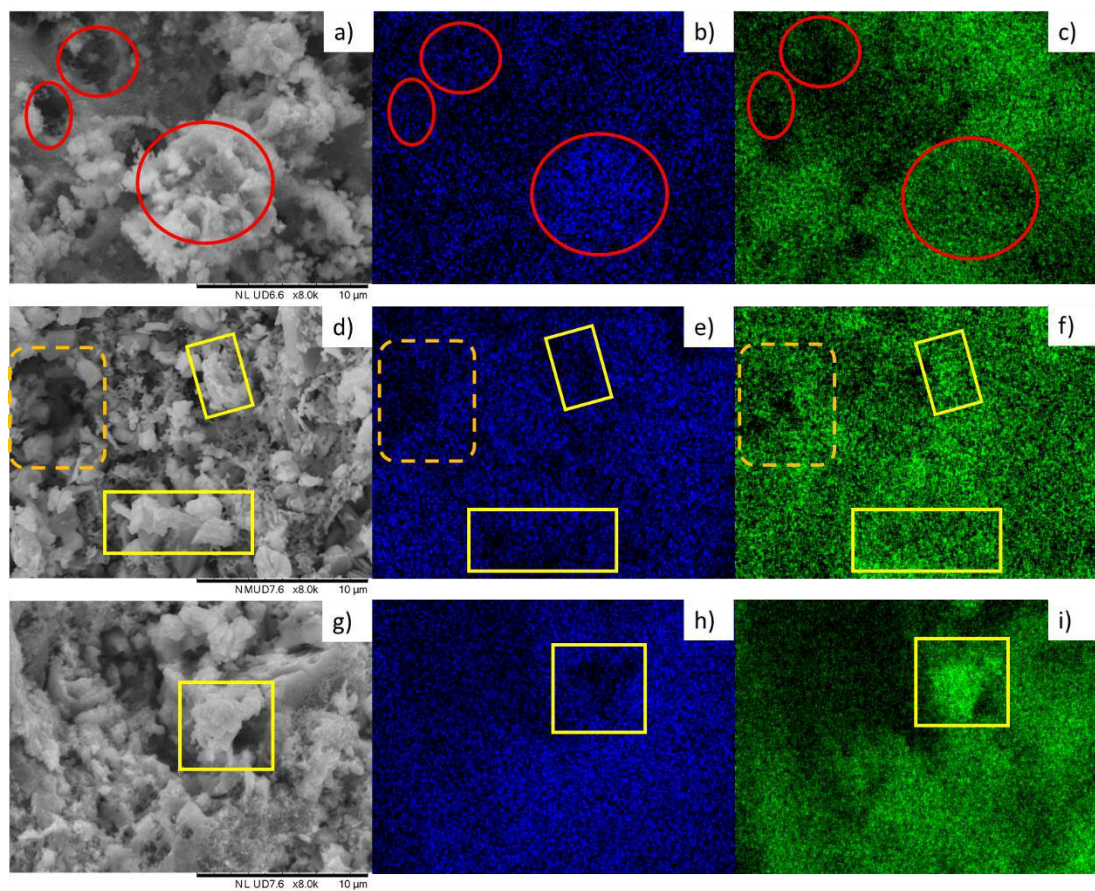


Figure 4.21 SEM and EDX elemental mapping comparison of 1:2.2 MM samples calcined at 450 °C for a variety of different times. (a) SEM image of 450 2 h MM, (b) EDX map showing Fe content of 450 2 h MM, (c) EDX map showing Mo content of 450 2 h MM, (d) SEM image of 450 4 h MM, (e) EDX map showing Fe content of 450 4 h MM, (f) EDX map showing Mo content of 450 4 h MM, (g) SEM image of 450 6 h MM, (h) EDX map showing Fe content of 450 6 h MM and (i) EDX map showing Mo content of 450 6 h MM. Highlighted Fe rich (red circles) and Mo rich (yellow squares).

The 600 2 h MM sample shared similarities with 500 6 h MM sample with the formation of large agglomerated particles, larger molybdenum rich crystallites were observed over the surface as highlighted.

As the calcination was extended to 4 h, particle size was shown to increase and become more uniform, overall elemental composition was shown to increase in homogeneity with a few areas of molybdenum enrichment in the form of MoO_3 crystallites on the surface.

The 600 6 h MM samples saw the formation of agglomerates of the particles observed of the 600 4 h MM example. Large void structures (2 μm diameter) were observed and were found to be iron rich in corresponding EDX analysis possibly indicating Fe_2O_3 formation. Larger, more frequent Mo enriched areas over the surface were also observed suggesting MoO_3 formation.

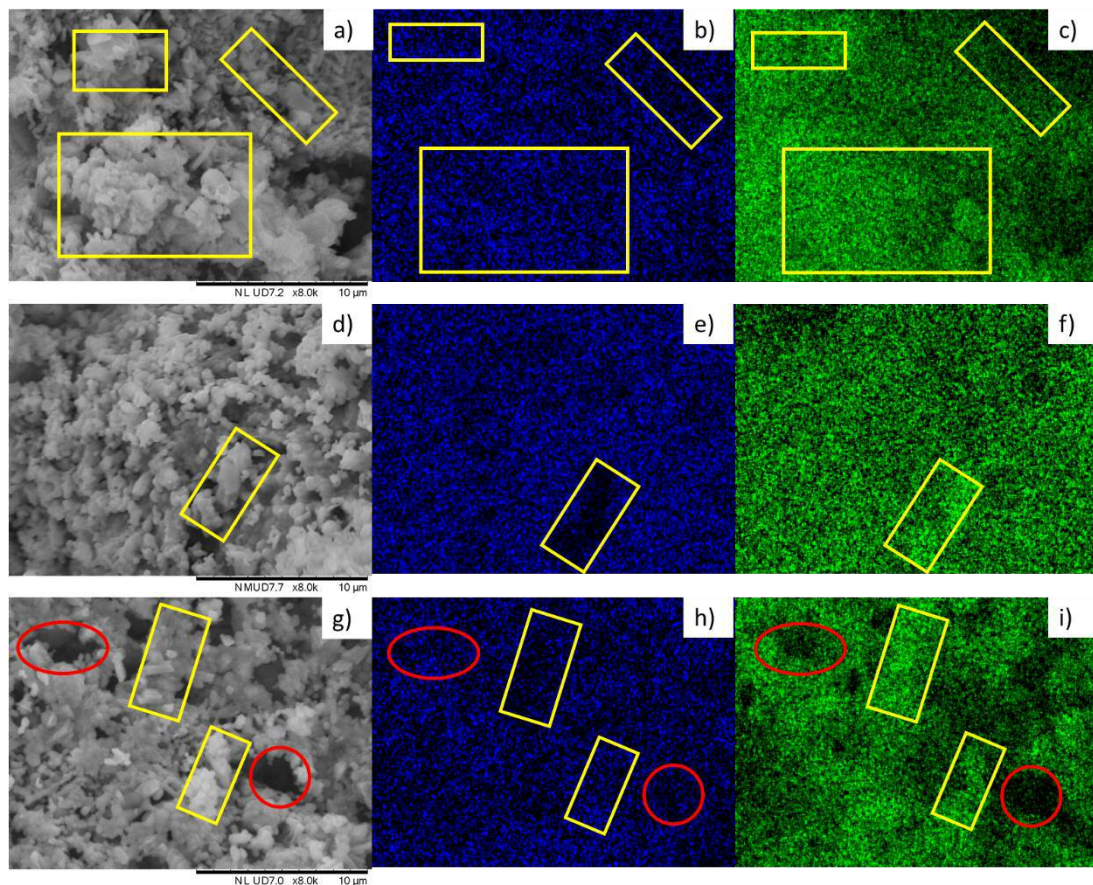


Figure 4.22 SEM and EDX elemental mapping comparison of 1:2.2 MM samples calcined at 600 °C for a variety of different times. (a) SEM image of 600 2 h MM, (b) EDX map showing Fe content of 600 2 h MM, (c) EDX map showing Mo content of 600 2 h MM, (d) SEM image of 600 4 h MM, (e) EDX map showing Fe content of 600 4 h MM, (f) EDX map showing Mo content of 600 4 h MM, (g) SEM image of 600 6 h MM, (h) EDX map showing Fe content of 600 6 h MM and (i) EDX map showing Mo content of 600 6 h MM. Highlighted Fe rich (red circles) and Mo rich (yellow squares).

4.4.3. Methanol Oxidation

Methanol partial oxidation results over 1:2.2 MM samples were shown to vary considerably depending on the calcination conditions used in production as shown in Fig. 4.22.

A wide range (29-62 %) of conversions were displayed at 260 °C with the following order from highest to lowest: 450 2 h MM > 500 6 h MM > 450 6 h MM > 500 4 h MM > 500 2 h MM > 600 2 h MM > 600 4 h MM > 600 6 h MM > 450 4 h MM. This same order is maintained throughout but the difference between the samples was decreased as temperatures were raised. Over 90 % conversion was achieved at 305 °C by all catalysts except 450 4 h MM and the 600 MM samples which achieved the same conversion at 320 °C.

Formaldehyde and CO_x selectivities were also shown to vary with changes in calcination conditions as shown in Figs. 4.22.a and 4.22.b respectively. All samples presented over 95 % formaldehyde selectivity at 260 °C. High formaldehyde selectivity was maintained by the samples over the temperature range in the following order from worst to best: 500 4 h MM, 450 2 h MM, 450 6 h MM, 500 6 h MM, 600 6 h MM, 500 2 h MM, 600 2 h MM, 600 4 h MM and 450 4 h MM.

The selectivity towards formaldehyde is not maintained by 500 4 h MM which saw a rapid decrease in favour of CO_x formation dropping below 90 % by 320 °C. 450 2 h MM, 450 6 h MM and 500 6 h MM were also unable to maintain high formaldehyde selectivity over the temperature range with a gradual drop in formaldehyde selectivity observed as temperatures were raised from 260 °C.

High formaldehyde selectivity (>96 %) was maintained by 500 2 h MM, 450 4 h MM and the three 600 MM samples up until 320 °C where 600 6 h MM rapidly dropped in favour of CO_x products. A gradual loss of formaldehyde selectivity as reaction temperatures were increased was observed by the other samples.

Table 4.9 Formaldehyde yield comparison of 1:2.2 MM samples calcined using a variety of different conditions and the temperature these yields were achieved.

Sample	Maximum Formaldehyde Yield/%	Temperature / °C
500 2 h MM	93.9	335
500 4 h MM	86.2	320
500 6 h MM	89.5	320
450 2 h MM	88.9	320
450 4 h MM	94.3	350
450 6 h MM	89.2	320
600 2 h MM	90.3	365
600 4 h MM	94.0	350
600 6 h MM	88.1	335

Because of the differing reaction results between samples, formaldehyde yields also varied as shown in Table 4.9. The highest yields were attained by 450 4 h MM, 600 4 h MM and 500 2 h MM achieving over 93.5 % yield over a selection of temperatures between 320-365 °C. 600 2 h MM displayed over 90 % yield over a short temperature range (350-365 °C) but due to the low activity of the sample, high yields were limited to very high temperatures(365 °C). 500 6 h MM, 450 2 h MM and 450 6 h MM were comparable achieving between 88.9-89.5 % at 320 °C, although they were more active than the previous samples they were unable to maintain formaldehyde selectivity with increased conversions. 500 4 h MM displayed the lowest formaldehyde yield at a similar 320 °C temperature due to the inability to maintain formaldehyde selectivity beyond 260 °C.

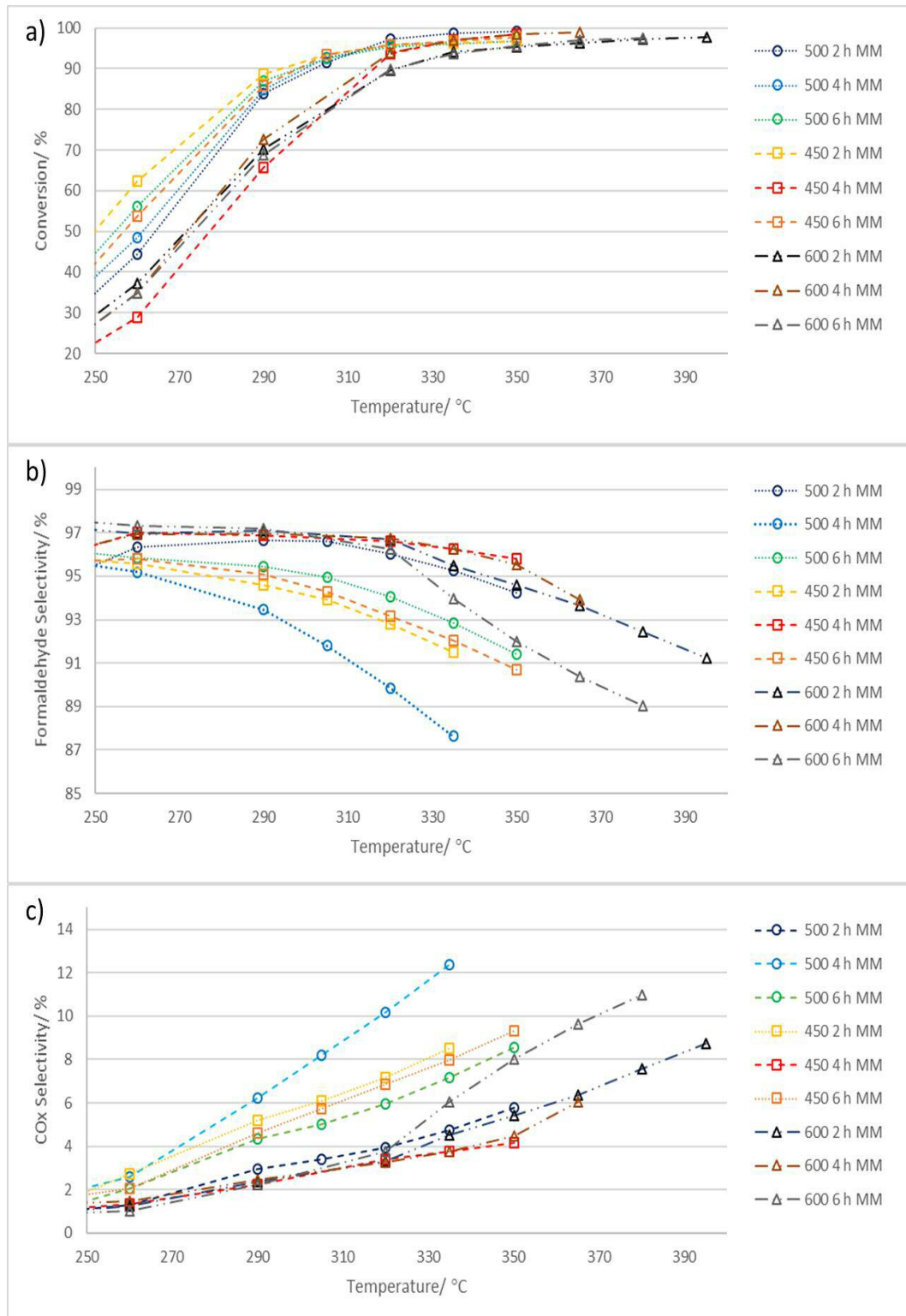


Figure 4.22 Methanol partial oxidation reaction comparison of 1:2.2 MM samples prepared using various calcination conditions; a) Methanol conversion, b) Formaldehyde selectivity and c) CO_x selectivity.

4.4.4. Effect of Calcination Conditions on Malonate Decomposition Method Discussion

The iron molybdate samples synthesised using malonate decomposition method were found to be highly sensitive to changes in calcination conditions. There was no clear trends observed as calcination conditions were changed with variation observed between temperatures and calcination time.

Of the 500 MM samples, 500 2 h MM produced the highest yields of formaldehyde (93.9 %). This could be due to the largest $\text{Fe}_2(\text{MoO}_4)_3$ content in both XRD and Raman results and most homogeneous iron and molybdenum distribution observed in microscopy and Raman mapping.

The 500 4 h MM sample displayed the lowest formaldehyde yield (86.2 %) of the calcination study, the composition of the sample displayed the second largest MoO_3 content in XRD and significantly lower $\text{Fe}_2(\text{MoO}_4)_3$ content. This is thought to be due to molybdena migration towards the surface with a sharp rise in surface molybdenum content in XPS and EDX mapping observed as large crystallites of MoO_3 on the surface. Fe_2O_3 was also observed over the surface of the sample in the form of large particles which may have caused an increase in CO_x selectivity throughout.^{25,26,30,32} These results were similar to those observed by Xu *et al.*⁴¹ who saw a sharp decrease in molybdenum bulk content which migrated towards the surface. This was thought to be due to the formation of crystalline MoO_3 on the surface by the sublimation of amorphous MoO_3 present in interstitial spaces of the $\text{Fe}_2(\text{MoO}_4)_3$ lattice.

Further calcination caused a small rise in formaldehyde yield, this may be due to the reduction in MoO_3 content in favour of $\text{Fe}_2(\text{MoO}_4)_3$ as observed in XRD and Raman spectral mapping caused by solid-state reaction between MoO_3 and Fe_2O_3 .³⁷ This may have caused the decrease in MoO_3 crystallite size and the decrease in Fe_2O_3 area particles observed in microscopy results.

Of the samples 1:2.2 MM samples calcined at 450 °C, 4 h calcination produced the highest formaldehyde yield (94.3 %). This could be due to the highest $\text{Fe}_2(\text{MoO}_4)_3$ content of the 450 MM samples tested as observed in XRD and Raman spectral mapping results. This could have been due to a combination of both thermal spreading of MoO_3 across the surface covering iron enriched areas which could limit the formation of CO_x .

Both 450 2 h MM and 450 6 h MM presented comparable methanol oxidation results with both samples presenting lower $\text{Fe}_2(\text{MoO}_4)_3$ content in XRD and Raman spectral mapping compared to 450 4 h MM. Mo surface excess based on XPS was double that observed by 450 4 h MM. 450 2 h MM presented the lowest $\text{Fe}_2(\text{MoO}_4)_3$ content of the 1:2.2 MM samples in all characterisation results possibly due to the low rate of $\text{Fe}_2(\text{MoO}_4)_3$ production at 450 °C by the solid-state reaction.³⁷ Some authors actually suggested that significant $\text{Fe}_2(\text{MoO}_4)_3$ production was not obtained until temperatures exceeding 470 °C.^{40,42} 450 6 h MM also presented high MoO_3 content which was formed on the surface in the form of larger MoO_3 crystallites, this may suggest significant MoO_3 migration towards the surface over time with limited $\text{Fe}_2(\text{MoO}_4)_3$ production at this temperature. Similar observations using lower temperatures (400 °C) were found by Jin *et al.*²⁴ using iron supported on MoO_3 nanorods, they saw that even at very long calcination time (48 h) isolated Fe_2O_3 exclusive regions were not removed with the formation of $\text{Fe}_2(\text{MoO}_4)_3$. Instead a continuous MoO_3 surface covering was observed suggesting higher temperature calcination (> 500 °C) were required.

The catalytic performance of the 600 MM samples varied significantly as the calcination length was changed, the highest formaldehyde yield was attained by 600 4 h MM (94.0 %) followed by 600 2 h MM (90.3 %) with 600 6 h MM (88.1 %) producing the lowest. All three samples were presented the lowest activity possibly due to the lower surface area of the sample. The reduction in surface area could be due to the change in morphology forming large compact particle structures. Of the 600 MM samples, the lowest activity was presented by 600 2 h MM which may be due to the high MoO_3 content observed on the surface of the sample in both EDX and XPS. MoO_3 content was also highest in both Raman spectral mapping and XRD. 600 4 h MM presented a significant decrease in molybdenum surface content in both microscopy and XPS with less MoO_3 crystallites presented on the surface. Raman spectral mapping and XRD also saw a reduction in MoO_3 content in favour of $\text{Fe}_2(\text{MoO}_4)_3$ production. The 600 6 h MM presented further increase in $\text{Fe}_2(\text{MoO}_4)_3$ bulk content but also an increase in Fe_2O_3 in XRD as MoO_3 was reduced, the surface composition shown in microscopy also showed significant changes. Far less homogeneous with areas of Fe_2O_3 and MoO_3 present on the surface which may account for the higher CO_x selectivity observed.

Possible reasons for these changes could be due to the high mobility of MoO_3 within the sample similar to results shown by Xu *et al.*⁴¹ Molybdena rapidly migrating towards the surface from the bulk at 600 °C causing the high Mo surface content presented by 600 2 h

MM. Longer heat treatment may cause the loss of molybdena from the surface via sublimation at this temperature from the surface leaving behind a surface of higher iron content as observed in both 600 4 h MM and 600 6 h MM.^{43,44} Further sublimation may have caused significant iron enrichment in the bulk of the sample as more of the MoO_3 was removed.

4.5. Malonate Decomposition Method (MM) Conclusion

The malonate decomposition method (MM) has been thoroughly tested for the synthesis of iron molybdate to produce formaldehyde from methanol via partial oxidation. Compared to more traditional coprecipitation and oxalate decomposition methodologies described in Chapter 3, MM produced Fe:Mo 1:2.2 iron molybdate samples outperformed the comparison samples attaining 93.9 % formaldehyde yield at 335 °C. Although lower activity at lower temperatures compared to the other samples, formaldehyde selectivity was superior especially at higher conversions. This was due to the increased homogeneous mixing of the iron and molybdenum which prevented the formation of areas of phase separation observed in the comparison samples.

Investigation into the effect of change of Fe:Mo ratio on MM was also tested and it was found that the method was far more stable to changes in the ratio. All except Fe:Mo 1:1.7 attained yields of formaldehyde above 92.6 %. This was due to the limitation of exposure of iron rich areas by the migration of molybdenum over these areas during calcination along with an overall improvement of homogeneity. The cause of this improvement was thought to be due to the homogeneous mixing of the iron and molybdenum malonates prior to calcination with the close proximity of the mixed metal malonates suggested by DTG/TGA results.

Calcination study of 1:2.2 MM yielded significant changes in both morphology and reactivity with the sample displaying a high sensitivity to both temperature and duration of the calcination. Highly mobile MoO_3 species were observed using 4 h calcination at 500 °C causing the formation of large MoO_3 crystallite formation, this prevented $\text{Fe}_2(\text{MoO}_4)_3$ formation which caused lower formaldehyde yields. As the calcination was extended MoO_3 content decreased increasing $\text{Fe}_2(\text{MoO}_4)_3$ formation which caused an increase in formaldehyde yield, although not reaching the same level observed using the shorter calcination length.

Lower temperature calcination caused the preservation of structures formed during the decomposition of the malonate although as calcination was extended, greater amounts of $\text{Fe}_2(\text{MoO}_4)_3$ were formed possibly due to the increased time for the solid-state reaction between MoO_3 and Fe_2O_3 to occur.³⁷ Agglomeration of MoO_3 was also observed forming crystallites on the surface over time which may have caused a decrease in relative $\text{Fe}_2(\text{MoO}_4)_3$ content observed causing lower formaldehyde yields. 450 °C 4 h calcination caused an increase in overall formaldehyde yield as the combination of higher $\text{Fe}_2(\text{MoO}_4)_3$ formation and MoO_3 migration over the surface to prevent the formation of exposed Fe_2O_3 . Further calcination at 450 °C did however cause an increase in crystalline MoO_3 content on the surface limiting the formaldehyde yield.

Higher temperature calcination caused molybdenum migration towards the surface which lowered activity with the formation of large MoO_3 crystallites on the surface. Both 600 2 h MM and 600 4 h MM samples were highly selective towards formaldehyde possibly due to the higher MoO_3 surface content. Possible MoO_3 sublimation may have caused a decrease in molybdenum surface content as calcinations were extended which left areas of Fe_2O_3 on the surface of the 600 6 h MM sample.

4.6. References

- (1) Nachod, F. C. (Frederick C.; Braude, E. A. (Ernest A. *Determination of organic structures by physical methods / editors, E.A. Braude, F.C. Nachod*; Academic Press: New York, 1955.
- (2) Duh, B. Method for production of a high molecular weight polyester prepared from a prepolymer polyester having an optimal carboxyl content. US4238593 A, December 9, 1980.
- (3) Ghosh Dastidar, T.; Netravali, A. N. *Carbohydr. Polym.* **2012**, *90* (4), 1620–1628.
- (4) López-Muñoz, F.; Ucha-Udabe, R.; Alamo, C. *Neuropsychiatr. Dis. Treat.* **2005**, *1* (4), 329–343.
- (5) Ma, X.; Chakraborty, P.; Henz, B. J.; Zachariah, M. R. *Phys. Chem. Chem. Phys.* **2011**, *13* (20), 9374–9384.
- (6) Britton, E. C.; Ezra, M. Production of malonic acid. US2373011 A, April 3, 1945.
- (7) Bomgardner, M. M. Lygos gets funding for malonic acid | Chemical & Engineering News <http://cen.acs.org/articles/95/i1/Lygos-funding-malonic-acid.html?type=paidArticleContent> (accessed Jul 26, 2017).
- (8) Stefanescu, O.; Stefanescu, M. *J. Organomet. Chem.* **2013**, *740*, 50–55.
- (9) Rahman, M. M.; Mukhedkar, V. A.; Venkataraman, A.; Nikumbh, A. K.; Kulkarni, S. B.; Mukhedkar, A. J. *Thermochim. Acta* **1988**, *125*, 173–190.
- (10) Xiao, D.; Guo, Y.; Lou, X.; Fang, C.; Wang, Z.; Liu, J. *Chemosphere* **2014**, *103*, 354–358.

- (11) Muraishi, K.; Takano, T.; Nagase, K.; Tanaka, N. *J. Inorg. Nucl. Chem.* **1981**, *43* (10), 2293–2297.
- (12) Kwiatkowski, A. *J. Inorg. Nucl. Chem.* **1972**, *34* (5), 1589–1598.
- (13) Prasad, R.; Sulaxna; Kumar, A. *J. Therm. Anal. Calorim.* **2005**, *81* (2), 441–450.
- (14) Salvadó, V.; Ribas, X.; Zelano, V.; Ostacoli, G.; Valiente, M. *Polyhedron* **1989**, *8* (6), 813–818.
- (15) Cavasino, F. P.; Dio, E. D. *J. Chem. Soc. Inorg. Phys. Theor.* **1971**, *0* (0), 3176–3180.
- (16) Modec, B.; Dolenc, D.; Brenčič, J. V. *Inorganica Chim. Acta* **2007**, *360* (2), 663–678.
- (17) Modec, B.; Brenčič, J. V.; Koller, J. *Eur. J. Inorg. Chem.* **2004**, *2004* (8), 1611–1620.
- (18) Cindrić, M.; Strukan, N.; Vrdoljak, V.; Devčić, M.; Veksli, Z.; Kamenar, B. *Inorganica Chim. Acta* **2000**, *304* (2), 260–267.
- (19) Wang, S.; Mo, S.; Liu, Z.-G. *Russ. J. Inorg. Chem.* **2012**, *57* (3), 430–433.
- (20) Beltrán-Porter, A.; Cervilla, A.; Caturla, F.; Segura, B. *Transit. Met. Chem.* **1983**, *8* (4), 222–225.
- (21) Brown, M. E.; Bhengu, T. T.; Sanyal, D. K. *Thermochim. Acta* **1994**, *242*, 141–152.
- (22) Stefanescu, M.; Bozdog, M.; Muntean, C.; Stefanescu, O.; Vlase, T. *J. Magn. Magn. Mater.* **2015**, *393*, 92–98.
- (23) House, M. P.; Carley, A. F.; Echeverria-Valda, R.; Bowker, M. *J. Phys. Chem. C* **2008**, *112* (11), 4333–4341.
- (24) Jin, G.; Weng, W.; Lin, Z.; Dummer, N. F.; Taylor, S. H.; Kiely, C. J.; Bartley, J. K.; Hutchings, G. J. *J. Catal.* **2012**, *296*, 55–64.
- (25) Bowker, M.; Holroyd, R.; Elliott, A.; Morrall, P.; Alouche, A.; Entwistle, C.; Toerncrona, A. *Catal. Lett.* **2002**, *83* (3–4), 165–176.
- (26) Routray, K.; Zhou, W.; Kiely, C. J.; Grünert, W.; Wachs, I. E. *J. Catal.* **2010**, *275* (1), 84–98.
- (27) Vieira Soares, A. P.; Farinha Portela, M.; Kiennemann, A. *Stud. Surf. Sci. Catal.* **1997**, *110*, 807–816.
- (28) Soares, A. P. V.; Portela, M. F.; Kiennemann, A.; Hilaire, L. *Chem. Eng. Sci.* **2003**, *58* (7), 1315–1322.
- (29) Söderhjelm, E.; House, M. P.; Cruise, N.; Holmberg, J.; Bowker, M.; Bovin, J.-O.; Andersson, A. *Top. Catal.* **2008**, *50* (1–4), 145.
- (30) Bowker, M.; Brookes, C.; Carley, A. F.; House, M. P.; Kosif, M.; Sankar, G.; Wawata, I.; Wells, P. P.; Yaseneva, P. *Phys. Chem. Chem. Phys.* **2013**, *15* (29), 12056–12067.
- (31) Brookes, C.; Bowker, M.; Wells, P. P. *Catalysts* **2016**, *6* (7), 92.
- (32) House, M. P.; Shannon, M. D.; Bowker, M. *Catal. Lett.* **2008**, *122* (3–4), 210–213.
- (33) Wu, W.; He, Q.; Jiang, C. *Nanoscale Res. Lett.* **2008**, *3* (11), 397–415.
- (34) Bowker, M.; House, M.; Alshehri, A.; Brookes, C.; Gibson, E. K.; Wells, P. P. *Catal. Struct. React.* **2015**, *1* (2), 95–100.
- (35) Soares, A. P. V.; Farinha Portela, M.; Kiennemann, A.; Hilaire, L.; Millet, J. M. M. *Appl. Catal. Gen.* **2001**, *206* (2), 221–229.
- (36) Boreskov, G. K.; Kolovertnov, G. D.; Kefeli, L. M.; Plyasova, L. M.; Karakchiev, L. G.; Mastikhin, V. N.; Popov, V. I.; Dzis'ko, V. A.; Tarasova, D. V. *Kinet Catal Engl Transl* **1965**, *7* (1), 125.
- (37) Kostynyuk, A. O.; Gutenuar, F.; Kalashnikova, A. N.; Kalashnikov, Y. V.; Nikolenko, N. V. *Kinet. Catal.* **2014**, *55* (5), 649–655.
- (38) Braun, S.; Appel, L. G.; Camorim, V. L.; Schmal, M. *J. Phys. Chem. B* **2000**, *104* (28), 6584–6590.
- (39) Wang, C.-B.; Cai, Y.; Wachs, I. E. *Langmuir* **1999**, *15* (4), 1223–1235.
- (40) Huang, Y.; Cong, L.; Yu, J.; Eloy, P.; Ruiz, P. *J. Mol. Catal. Chem.* **2009**, *302* (1), 48–53.
- (41) Xu, Q.; Jia, G.; Zhang, J.; Feng, Z.; Li, C. *J. Phys. Chem. C* **2008**, *112* (25), 9387–9393.
- (42) Dong, L.; Chen, K.; Chen, Y. *J. Solid State Chem.* **1997**, *129* (1), 30–36.

- (43) Atuchin, V. V.; Gavrilova, T. A.; Grigorieva, T. I.; Kuratieva, N. V.; Okotrub, K. A.; Pervukhina, N. V.; Surovtsev, N. V. *J. Cryst. Growth* **2011**, *318* (1), 987–990.
- (44) Wirtz, G. P.; Sis, L. B.; Wheeler, J. S. *J. Catal.* **1975**, *38* (1), 196–205.

Chapter 5

Iron Precursor effect on Molten Malonic Acid Method for Iron Molybdate Synthesis

5.1. Introduction

5.1.1. Industrial Considerations For Nitrate Use

The industrial use of nitrate has been under scrutiny due to a combination of factors. The environmental impact of high nitrate concentrations in water courses has been well studied including the negative effect it has on aquatic ecosystems¹. However the toxicological effect was not limited to aquatic life, with very strict guidelines on nitrate levels for drinking water of under 50 mg L⁻¹ suggested by the World Health Organisation to prevent the onset of methemoglobinemia².

NO₂ release to the air from the decomposition of nitrates is also tightly controlled with overall levels of NO_x in European Countries to be maintained below 40 µg m⁻³, whilst industrial considerations of a maximum of 200 µg m⁻³ h⁻¹ allowed to prevent respiratory inflammation diseases and acid rain³. The treatment of both nitrate and gaseous NO_x can be highly costly in both resources and energy prior to discharge⁴.

The safety implications of using nitrates, due to their high oxidising potential, have also been well documented.⁵ Industrial accidents are avoided through strict controls otherwise risking dangerous repercussions.

5.1.2. Alternate Iron Precursors Used For Iron Molybdate Synthesis

The use of varying iron precursors to produce iron molybdate to negate the use of iron nitrate using the MM method was investigated. A study by Soares *et al.* proposed the use of chloride, sulphate, phosphate, pyrophosphate as well as nitrate iron precursors to produce supported iron molybdate catalysts⁶. It was found that the use of phosphate and pyrophosphate may have a positive impact on MoO₃ with possible phosphate migration

promoting overall activity. The lack of removal of the phosphate however caused the iron to be inactive using the Soares *et al.* method. Chloride facilitated the production of the greatest amounts of $\text{Fe}_2(\text{MoO}_4)_3$ possibly caused by the prevention of polymeric MoO_3 production by forming chloromolybdate species preventing Mo-O-Mo bonding.⁷ Sulphate and nitrate were then comparable in this study producing similar sample compositions and reactivity.

Iron (III) chloride which has been well documented in other studies, in conjunction with ammonium molybdate for use in traditional coprecipitation methods.^{8,9} Iron (II) sulphate in contrast has only recently been suggested for coprecipitation, a method using a molybdo ferrate(II) intermediate to produce iron molybdate by Nikolenko *et al.*¹⁰ displayed some success for formaldehyde production, evidence of sulphate retention post calcination was observed similar to results found by Soares *et al.*⁶

As already stated in Chapter 3 using OM, iron oxalate was produced during the initial heat treatment and was found to be beneficial towards the overall mixing in calcined samples due to the formation of carboxylate solutions. The use of other iron carboxylates has not been studied in detail directly for iron molybdate production though many are used as intermediates during sol-gel production methods¹¹⁻¹³.

The use of iron (III) phosphate, iron (III) chloride, iron (II) sulphate, iron (II) oxalate and iron (III) acetate were investigated to replace the use of iron (III) nitrate. This was to ascertain whether comparable formaldehyde production was possible and what effect on overall morphology changing the anionic species would have using the malonate decomposition method (MM).

5.2. Effect of Different Iron Precursor on Iron Molybdate Synthesis Using Malonate Decomposition Method

5.2.1. Characterisation

5.2.1.1. BET Surface Area and XPS Surface Analysis

BET surface area measurements shown in Table 5.1 present clear differences as the iron precursors were altered using MM.

The surface area of the calcined iron molybdate samples was shown to decrease in the following order Oxalate MM > Acetate MM > Sulphate MM = Nitrate MM > Chloride MM > Phosphate MM. The Oxalate MM and Acetate MM presented a significant change compared to the other samples which both displayed over double the surface area of the other materials. Phosphate MM and Chloride MM displayed the opposite trend displaying a large reduction in surface area compared to both Nitrate MM and Sulphate MM (53 % and 31 % reduction respectively).

XPS surface analysis shows large differences between the iron and molybdenum surface content between the materials analysed. Molybdenum surface content was shown to decrease in the following order Sulphate MM > Phosphate MM > Nitrate MM > Acetate MM > Chloride MM > Oxalate MM. The difference between Acetate MM, Chloride MM and Oxalate MM were within experimental error, all three presented a small molybdenum surface excess compared to theoretical bulk content. Both Sulphate MM and Phosphate MM samples displayed dominant molybdenum content with both presenting very large surface molybdenum excess relative to the bulk 1:2.2 Fe:Mo ratio.

Only small molybdenum surface excesses were displayed by Oxalate MM, Chloride MM and Acetate MM samples, the differences between which were within experimental error, possibly suggesting limited molybdenum migration towards the surface from the bulk with the use of these precursors.

XPS surface analysis was also employed to analyse the surface content of residual anionic components from the iron precursors. The Phosphate MM sample displayed a surface

phosphorus enrichment beyond the stoichiometric Fe:P ratio for the FePO₄. Sulphate MM also maintained some sulphur on the surface of the sample although it was greatly reduced from the stoichiometric 1:1 Fe:S ratio for FeSO₄. The other samples displayed no residual anionic species after calcination in XPS results.

Table 5.1. BET surface area and XPS surface ratio comparison for MM samples prepared using various iron precursors.

Sample	BET Surface Area/ m ² g ⁻¹	XPS Surface Ratios		Rel. Surface Mo Excess/ %
		Fe:Mo	Fe:X	
Nitrate MM	3.2 ± 0.2	1:3.3	-	50.0
Phosphate MM	1.5 ± 0.1	1:4.3	1:1.73	95.5
Chloride MM	2.2 ± 0.1	1:2.6	-	18.2
Sulphate MM	3.2 ± 0.2	1:5.7	1:0.11	159.1
Acetate MM	7.2 ± 0.3	1:2.7	-	22.7
Oxalate MM	7.7 ± 0.5	1:2.4	-	9.1

5.2.1.2. Powder XRD Crystallography

Powder XRD analysis of samples produced using MM using different iron precursors exhibited in Fig. 5.1 and summarised in Table 5.2.

Most of the MM samples displayed a mixture of Fe₂(MoO₄)₃ and MoO₃ with the Fe₂(MoO₄)₃ content decreasing in the order Chloride MM > Nitrate MM > Oxalate MM > Acetate MM > Phosphate MM > Sulphate MM. Fe₂O₃ content was low (0.8-2.6 %) for all samples except Sulphate MM which displayed 5.5 %.

The Fe₂(MoO₄)₃ content was significantly higher for Chloride MM compared to the other samples with MoO₃ content around a third of the next nearest sample. This does not take into account any amorphous MoO₃ formation.

Crystalline FePO₄^{14,15} was present in the Phosphate MM example, although its principle reflections were only observed as a shoulder off MoO₃ peak at 2θ 25.5 ° and a second peak at 2θ 20.5 ° indicating the (102) and (100) plane respectively. This accounted for 18.8 % of the composition of the Phosphate MM sample.

Based on XRD results iron (II) sulphate and iron (III) phosphate are poor precursors for iron molybdate synthesis using MM, Phosphate MM presented with only 3.1 % $\text{Fe}_2(\text{MoO}_4)_3$ content with the majority of the sample composed of MoO_3 (75.5 %) and FePO_4 (18.8 %). Sulphate MM sample contained no $\text{Fe}_2(\text{MoO}_4)_3$, instead it was composed of MoO_3 (94.5 %) and Fe_2O_3 (5.5 %). Iron (II) sulphate may still be present but was suggested to be amorphous by Sklute *et al.*¹⁶ and therefore undetectable using XRD.

Crystallite size was largely unchanged with different iron precursors with similar peak widths observed in all samples except Acetate MM which presented with significant peak broadening for all phases suggesting lower overall crystallinity.

Table 5.2. Relative phase content of samples prepared using MM with different iron precursors based on powder XRD results shown in Fig. 5.1.

Sample	Relative % Phase Based On Powder XRD Results			
	$\text{Fe}_2(\text{MoO}_4)_3$	MoO_3	Fe_2O_3	FePO_4
Nitrate MM	68.8	28.7	2.5	-
Phosphate MM	3.1	75.5	2.6	18.8
Chloride MM	88.1	11.1	0.8	-
Sulphate MM	0.0	94.5	5.5	-
Acetate MM	58.7	39.6	1.7	-
Oxalate MM	62.2	35.6	2.2	-

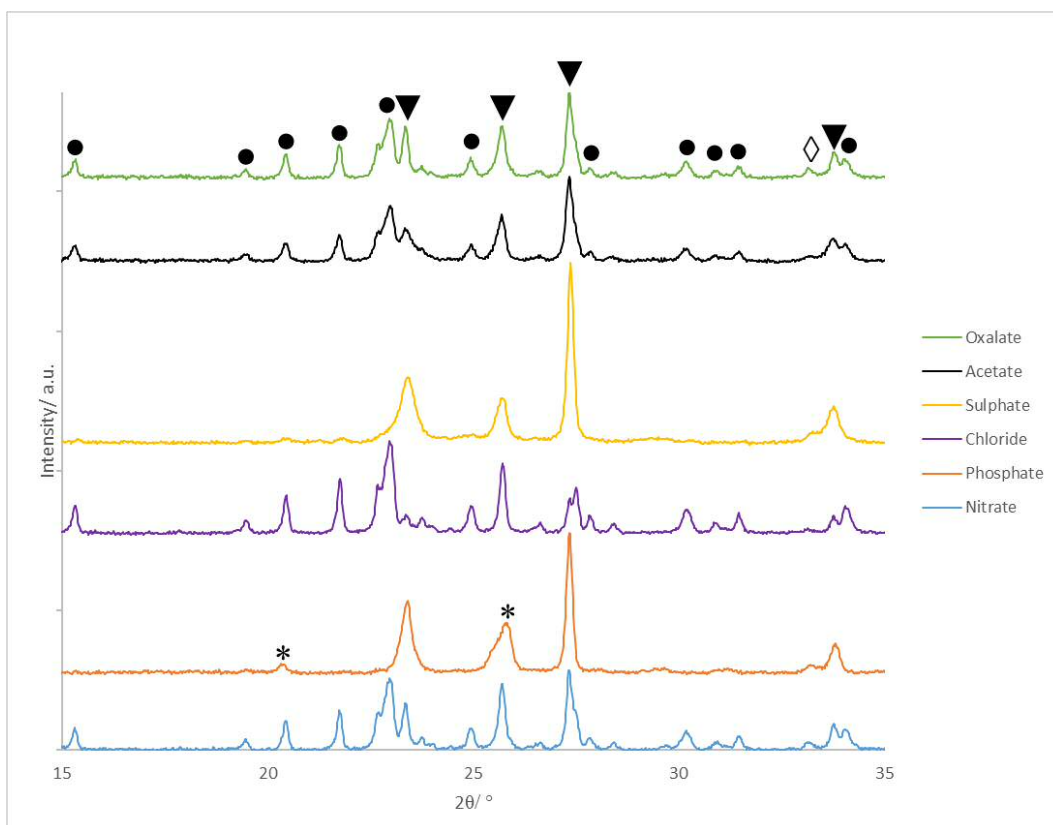


Figure 5.1 Powder XRD comparison between MM samples produced using various iron precursor. (Key: ▼ MoO_3 , ● $\text{Fe}_2(\text{MoO}_4)_3$, ◊ Fe_2O_3 and * FePO_4).

5.2.1.3. Raman Spectral Mapping

The Raman spectral mapping presented in Fig. 5.2 show clear differences between the MM samples produced using different iron precursors. All the samples display various quantities of both $\text{Fe}_2(\text{MoO}_4)_3$ and MoO_3 .

The general composition of the MM samples is shown in 5.2.a, 5.2.d, 5.2.g, 5.2.j, 5.2.m and 5.2.p for Nitrate MM, Phosphate MM, Chloride MM, Sulphate MM, Acetate MM and Oxalate MM respectively. $\text{Fe}_2(\text{MoO}_4)_3$ content decreased between these points in the following order Chloride MM > Oxalate MM > Nitrate MM > Acetate MM > Phosphate MM = Sulphate MM. MoO_3 was the dominant species in Acetate MM, Phosphate MM and Sulphate MM spectra throughout with low $\text{Fe}_2(\text{MoO}_4)_3$ content observed in all points.

Iron phosphate was present in the Phosphate MM sample in the form of FePO_4 with a peak at 1009 cm^{-1} suggesting the symmetric stretching of PO_4 and to a lesser extent peaks between $200\text{-}600\text{ cm}^{-1}$ suggesting network stretching.¹⁷ In more iron rich points such as 5.2.e,

$\text{Fe}_2(\text{MoO}_4)_3$ was present in larger amounts as well as increased FePO_4 content. $\text{Fe}_3(\text{PO}_4)_2$ was also present with peaks at 970 and 927 cm^{-1} as well as smaller peaks at 550 and 478 cm^{-1} suggesting the symmetric PO_4 stretch and network bending respectively.¹⁷ These iron rich areas were rare with MoO_3 dominating the sample composition in the majority of points surveyed.

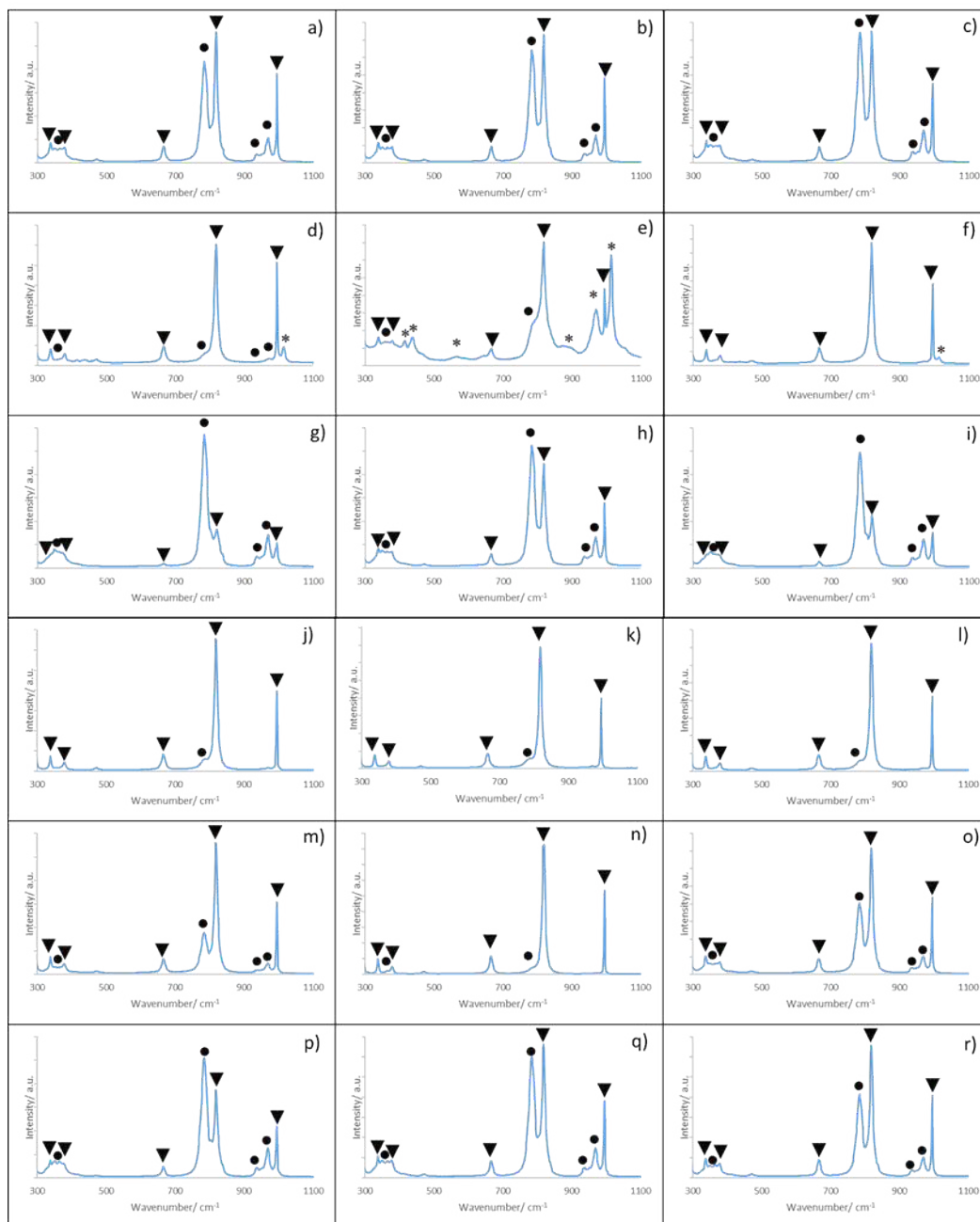


Figure 5.2 Raman spectral mapping comparison of (a-c) Nitrate MM, (d-f) Phosphate MM, (g-i) Chloride MM, (j-l) Sulphate MM, (m-o) Acetate MM and (p-r) Oxalate MM samples. (Key: ▼ MoO_3 , ● $\text{Fe}_2(\text{MoO}_4)_3$ and * FePO_4)

5.2.1.4. Microscopy and EDX Elemental Mapping

The morphology was shown to vary significantly as iron precursors were altered in SEM and EDX mapping results (Fig. 5.3). Sponge-like morphologies were observed by both Nitrate MM and Oxalate MM samples. The Oxalate MM samples displayed large void structures (2 μm diameter) which were shown to be iron exclusive in corresponding EDX mapping similar to OM samples discussed in Section 3.3 suggesting Fe_2O_3 formation.

Sulphate MM and Chloride MM presented with collections of agglomerated irregular sized crystalline plates arranged into a lamellar like arrangements. EDX analysis suggests that large areas of iron and molybdenum exclusivity were observed by Sulphate MM suggesting isolated Fe_2O_3 and MoO_3 production. The Chloride MM sample was more homogeneous with areas of iron enrichment as highlighted but none were exclusively iron. A small number of molybdenum exclusive areas were also displayed suggesting MoO_3 crystallite formation.

The Acetate MM sample was composed of a mixture of small agglomerated particles and small irregular crystalline plate structures, a small number of large globular particles were also observed. The crystalline plates were found to be molybdenum rich as highlighted possibly indicating MoO_3 . Large areas of iron enrichment and near exclusivity may indicate Fe_2O_3 present on the surface.

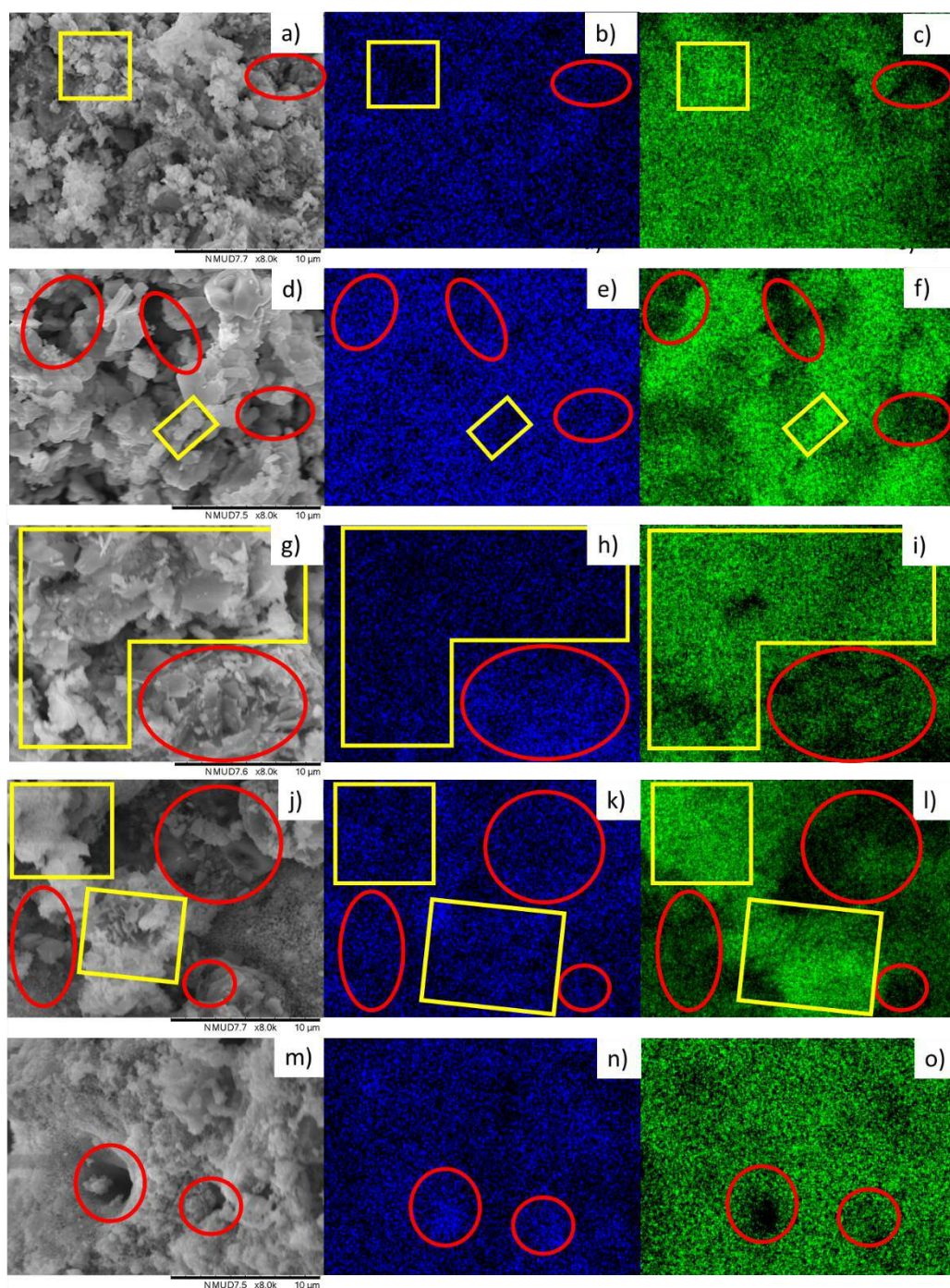


Figure 5.3 SEM and EDX elemental mapping comparison of MM samples prepared using different iron precursors. (a) SEM image of Nitrate MM, (b) EDX map showing Fe content of Nitrate MM, (c) EDX map showing Mo content of Nitrate MM, (d) SEM image of Chloride MM, (e) EDX map showing Fe content of Chloride MM, (f) EDX map showing Mo content of Chloride MM, (g) SEM image of Sulphate MM, (h) EDX map showing Fe content of Sulphate MM, (i) EDX map showing Mo content of Sulphate MM, (j) SEM image of Acetate MM, (k) EDX map showing Fe content of Acetate MM, (l) EDX map showing Mo content of Acetate MM, (m) SEM image of Oxalate MM, (n) EDX map showing Fe content of Oxalate MM and (o) EDX map showing Mo content of Oxalate MM. Highlighted Fe rich (red circles) and Mo rich (yellow squares).

Phosphate MM (Fig. 5.4) displayed large crystalline plates which were observed to be nearly molybdenum exclusive which is consistent with MoO_3 formations.¹⁸ Smaller lamellar like structures highlighted in purple were also observed over the surface of the sample, these structures were found to contain a combination of iron, molybdenum and phosphorus in corresponding EDX mapping. Smaller needle like structures were observed highlighted in blue, these were found to be iron and phosphorous exclusive. The majority of phosphorus was present in iron rich areas, this could limit the formation of Fe_2O_3 on the surface which would otherwise cause lower formaldehyde selectivity.

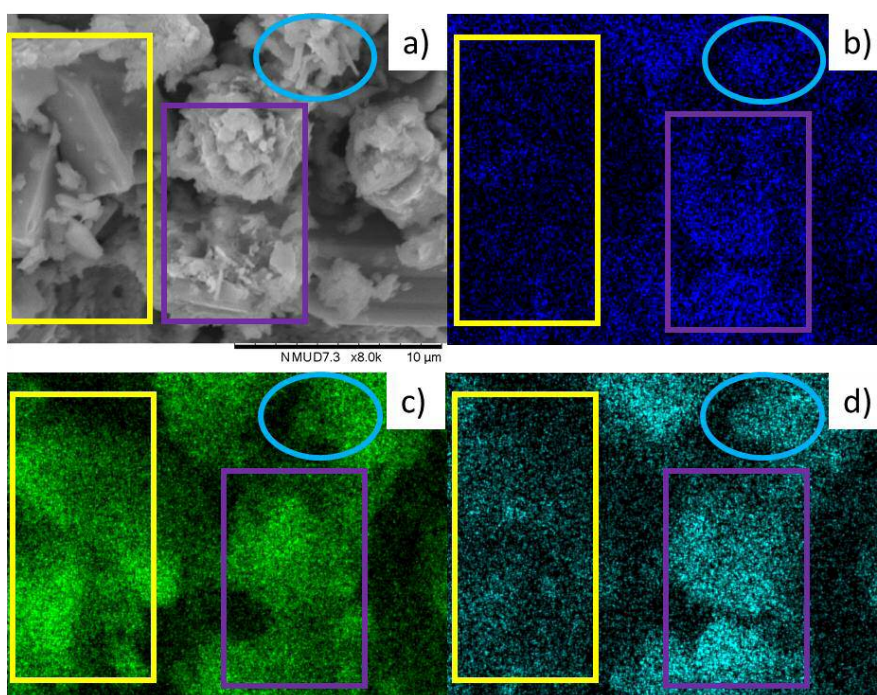


Figure 5.4. SEM micrograph and EDX elemental mapping of Phosphate MM. SEM micrograph (a) and EDX elemental mapping of Fe (b), Mo (c) and P (d). Highlighted areas of Mo rich (yellow squares), Fe Mo P mixture (purple square) and Fe P mixture (blue circle).

5.2.2. Methanol Partial Oxidation

The methanol oxidation results shown in Fig. 5.5 presents the substantial differences between MM samples prepared using different iron precursors.

The activity displayed by the MM samples decreased in the following order Acetate MM > Oxalate MM > Nitrate MM > Chloride MM > Sulphate MM > Phosphate MM. Acetate MM and Oxalate MM achieve close to 90 % conversion by 290 °C, Nitrate MM achieved similar

conversion at 305 °C. Chloride MM and Sulphate MM were unable to surpass 90 % conversion until reaction temperatures of 335 °C and 350 °C respectively, this same conversion was achieved by Phosphate MM at the limits of the reactor at 410 °C.

Formaldehyde selectivity varied as temperatures were increased from 200 °C, all samples presented under 70 % selectivity but as temperature was raised formaldehyde selectivity increased rapidly as DME selectivity decreased. Formaldehyde selectivity was lowest for Acetate MM and Sulphate MM samples which presented high CO_x selectivity throughout.

High formaldehyde selectivity at 260 °C was presented by Chloride MM(97.2 %), Nitrate MM (96.3 %), Phosphate MM (95.5 %) and Oxalate MM (94.2 %) which was shown to decrease gradually in favour of CO_x production as temperatures were increased. The high formaldehyde selectivity was maintained best by Chloride MM and Phosphate MM samples throughout with little change observed even at high temperatures (>350 °C), Nitrate MM was comparable until 320 °C where formaldehyde selectivity was shown to decrease in favour of CO_x. Oxalate MM was unable to maintain the high formaldehyde selectivity with CO_x selectivity increased from 290 °C onwards.

Table 5.3 Maximum formaldehyde yield comparison of MM samples prepared using different iron precursors.

Sample	Maximum Formaldehyde Yield/ %	Temperature/ °C
Nitrate MM	93.9	335
Phosphate MM	87.3	410
Chloride MM	94.2	365
Sulphate MM	87.0	350
Acetate MM	83.9	305
Oxalate MM	89.5	320

The effect these changes in iron precursors caused on overall formaldehyde yield is summarised in Table 5.3. The highest yields were achieved by Chloride MM and Nitrate MM, although due to the lower activity, Chloride MM achieved this high yield at significantly higher temperature. Both samples displayed over 93 % yield over an extended temperature range (320-350 °C Nitrate MM and 350-380 °C Chloride MM) which was not observed for the other samples.

The other sample attained maximum formaldehyde yield in the order Oxalate MM > Phosphate MM > Sulphate MM > Acetate MM. Due to the higher activity of the Acetate MM and Oxalate MM samples, maximum formaldehyde yield was attained at significantly lower temperatures although formaldehyde selectivity could not be maintained limiting performance. Phosphate MM formaldehyde yield was limited due to low activity with conversion limited by reactor limitations. The Sulphate MM sample presented with both low activity and low selectivity throughout causing lower yields achieved at higher temperatures.

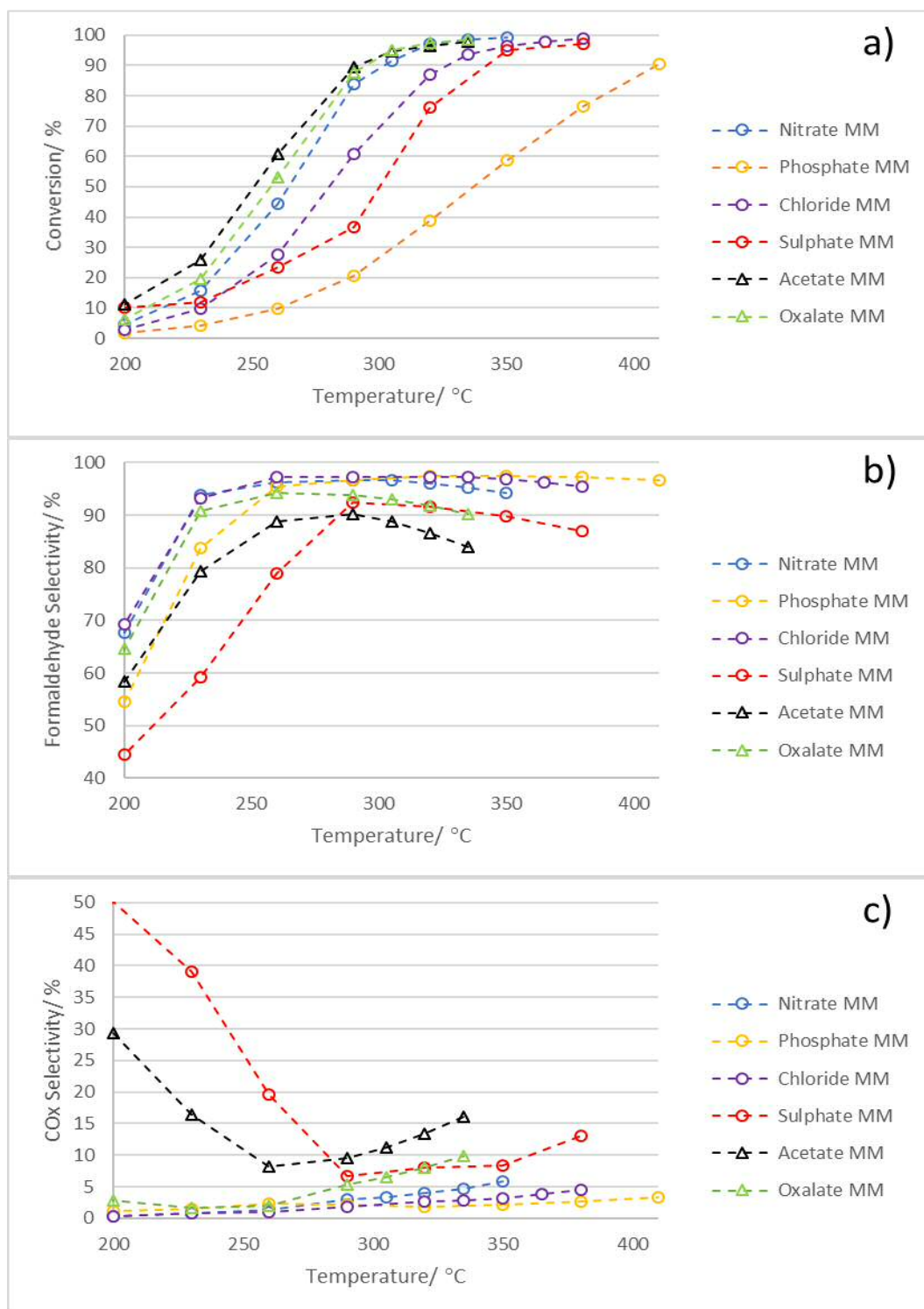


Figure 5.5. Methanol partial oxidation reaction summary of samples synthesised using MM method with different iron precursors comparing (a) Methanol conversion, (b) Formaldehyde selectivity and (c) CO_x selectivity at various reaction temperatures.

5.2.3. Precalcination Study

5.2.3.1. XPS Comparison of Uncalcined Samples

XPS characterisation of MM samples using different iron precursors was summarised in Table 5.4. Phosphate MM, Chloride MM and Sulphate MM displayed evidence of the iron precursors corresponding anionic species in XPS results prior to calcination. Phosphorous, chlorine and sulphur in quantities corresponding to the stoichiometric ratios for FePO_4 , FeCl_3 and FeSO_4 respectively were observed. All of the chlorine and most of the sulphur were removed after the calcination but the phosphorous remained.

As with previous MM examples both Mo^{V} and Mo^{VI} oxidation states are produced corresponding to the formation of dimeric and polymeric complexes of molybdenum with malonate respectively. The relative Mo^{V} content was shown to decrease dependent on iron precursor used in the following order, Sulphate MM > Chloride MM > Nitrate MM > Acetate MM > Phosphate MM > Oxalate MM.

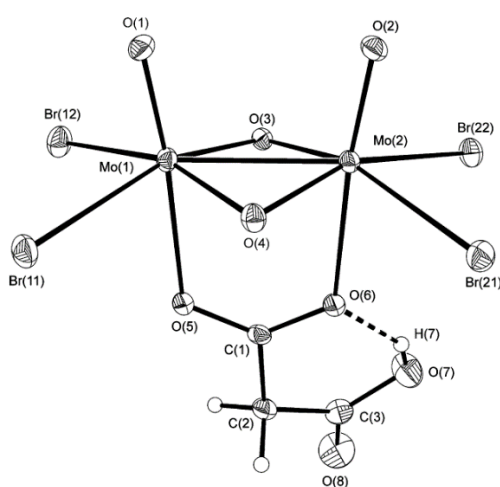
The high Mo^{V} content observed in Sulphate MM may be due to iron (II) sulphate acting as a reducing agent similar to results shown by Qin *et al.*¹⁹ for the reduction of Cr^{VI} to Cr^{III} in solution, although there was no significant evidence of iron sulphate oxidation in XPS results.

Phosphate MM and Oxalate MM presented Mo^{VI} dominance with both presenting only minor Mo^{V} content which would suggest the polymeric molybdenum malonate complex was favoured.

Table 5.4 XPS surface comparison of various MM samples pre and post calcination compared against 1:2.2 Coprep. (X⁻ representing anionic species such as Chloride MM = Cl⁻).

Sample	Pre Calcination		Post Calcination
	Mo ^V :Mo ^{VI}	Fe:X ⁻	Fe:X ⁻
1:2.2 Coprep	0:1	-	-
Nitrate MM	1:2.30	-	-
Phosphate MM	1:5.39	1:1.15	1:1.73
Chloride MM	1:0.76	1:3.65	1:0
Sulphate MM	1:0.65	1:1.01	1:0.11
Acetate MM	1:2.90	-	-
Oxalate MM	1:6.76	-	-

The Chloride MM also displays high quantities of Mo^V, which unlike other examples which comprise of the $[\text{Mo}_2\text{O}_4(\text{CH}_2\text{C}_2\text{O}_4)_3]^{3-}$ as suggested by Modéc *et al.*²⁰ Chloride examples may form complexes similar to the bromide malonate example shown in Fig. 5.6. Importantly the chloride complex was thought to prevent the formation of hydrogen bonded chains of Mo^V dimers through preferential hydrogen bonding between H(7) and O(8) shown. This could have prevented the formation of localised high molybdenum concentrations in the molten acid solution promoting higher distribution prior to calcination.

**Figure 5.6.** Structural representation of $[\text{Mo}_2\text{O}_4\text{Br}_4(\text{CH}_2\text{C}_2\text{O}_4\text{H})]^{3-}$ anion, hydrogen bonding between H(7) and O(8) shown as dashed line.²⁰

5.2.3.2. Thermogravimetric Analysis

The DTG of uncalcined MM samples shown in Fig. 5.7 and corresponding TGA results summary in Table 5.2 presented clear differences between MM samples prepared using different iron precursors. The malonate products were interpreted at the same temperature ranges as shown in Section 4.3.4.2.

Isolated molybdenum malonate decomposition (168-210 °C) was most predominant in Phosphate MM, Acetate MM and Sulphate MM where it was the dominant carboxylate decomposition product observed. Nitrate MM, Oxalate MM and Chloride MM also presented large amounts of molybdenum malonate but it was not the dominant decomposition product.

The isolated decomposition of iron malonate (263-358 °C) was shown to decrease in significance between the materials the following order Chloride MM > Acetate MM ≈ Oxalate MM > Nitrate MM > Phosphate MM > Sulphate MM. Chloride MM presented clear separation of iron malonate with a sharp change observed in DTG results which were not presented in other samples.

The overlap between the two malonate decompositions (210-263 °C), which was suggested to be due to the activation of iron malonate by the exothermic decomposition of molybdenum malonate, was shown to decrease in significance in the following order Nitrate MM > Oxalate MM > Chloride MM > Sulphate MM > Acetate MM > Phosphate MM. The Oxalate MM and Acetate MM present possible evidence of their original iron precursors within this region with peaks at 217 °C and 240 °C indicating iron (II) oxalate^{21,22} and iron (III) acetate²³ decomposition respectively.

A 23.0 % mass reduction was observed in Phosphate MM results between 125-180 °C peaking at 170 °C which was not observed in other examples, this was suggested to be due to the dehydration of iron phosphate dihydrate.²⁴

Based on DTG/TGA results, iron malonate production was limited with the use of iron (II) sulphate, iron (III) phosphate and iron (III) acetate precursors possibly due to the lack of ligand substitution between the malonate and the original anionic species in the molten acid

mixture. A similar observation using iron (II) sulphate was observed by Rao and Khopkar²⁵ who saw the precipitation of iron malonate was prevented in solution.

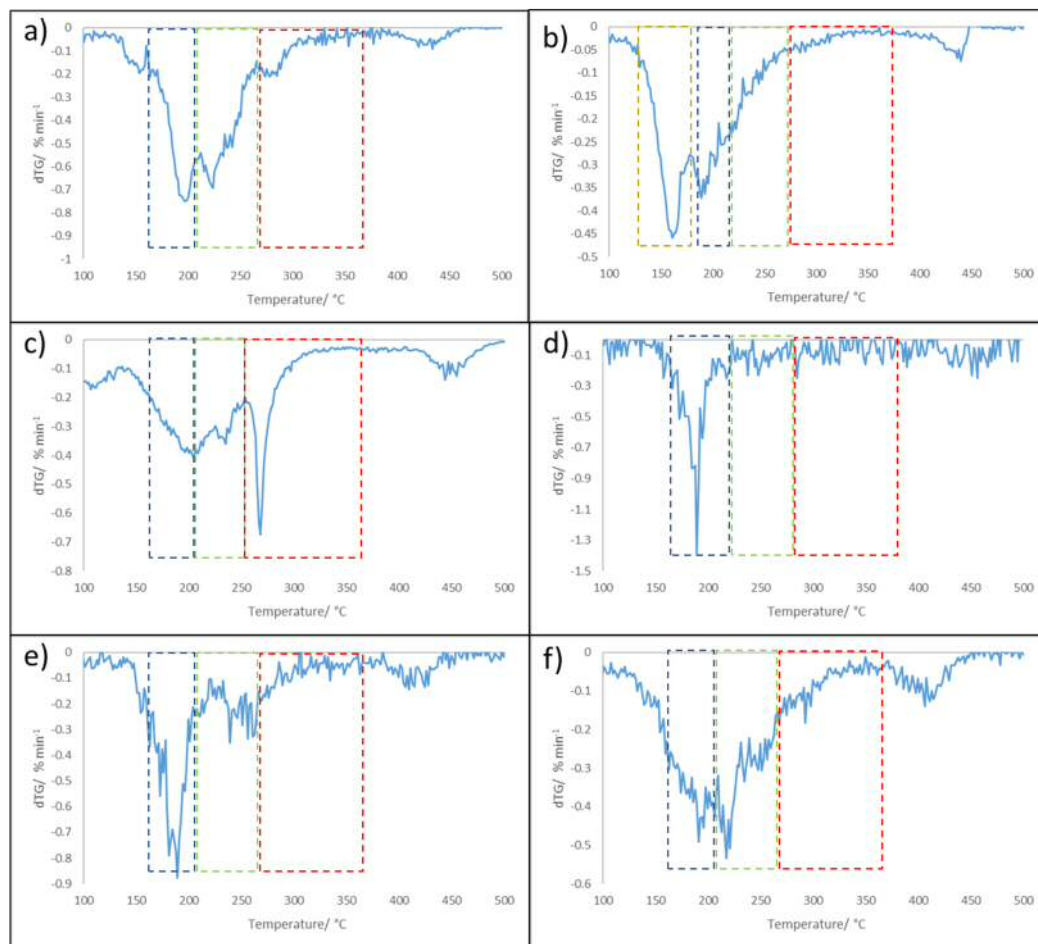


Figure 5.7. DTG Analysis of uncalcined MM samples using various iron precursors ranging from 100-500 °C using a ramp rate of 5 °C min⁻¹ (a) Nitrate MM, b) Phosphate MM, c) Chloride MM, d) Sulphate MM, e) Acetate MM and f) 1:2.2 Oxalate MM)

Table 5.5 TGA summary of MM samples produced using different iron precursor corresponding to DTG highlighted regions in Fig. 5.9. (+ Phosphate MM was tested between 125-180, 180-210, 210-263 and 263-358, * Chloride MM was tested between 168-210, 210-254 and 254-358)

TGA Temperature Range/ °C	Percentage Weight Loss/ %					
	Nitrate MM	Phosphate MM ⁺	Chloride MM *	Sulphate MM	Acetate MM	Oxalate MM
125-180	-	23.0	-	-	-	-
168-210	23.3	23.3	24.2	15.0	23.7	17.4
210-263	26.3	6.5	22.6	9.0	11.1	18.7
263-358	7.4	5.4	24.1	2.8	9.0	8.6

5.2.4. In-Situ Reduction Study

Investigation into the efficiency of surface reoxidation via the Mars-van Krevelen mechanism^{18,26} of iron molybdate samples gives a good indication how the samples will perform over prolonged operation at high conversion. To understand this in greater detail in-situ XRD reduction experiments at extreme reductive conditions were undertaken. This was due to reaction mechanism as stated in Chapter 1 where by the reduction of surface α - MoO_3 to MoO_2 subsequently oxidised by the bulk $\text{Fe}_2(\text{MoO}_4)_3$ as simplified in the following¹⁸:



The reoxidation of surface MoO_3 and thus the selective and active component of the catalyst in reductive conditions, such as those in high turnover or oxygen lean conditions, were tested using a reducing atmosphere. Zhang *et al.*²⁷ found that H_2/N_2 at 450 °C presented similar reductive potential to anaerobic methanol conditions at 350 °C²⁶ which saw the start of the degradation of the active catalyst due to the production of MoO_2 and so this was used as substitute in this investigation.

All samples were heat treated at a constant 450 °C for over 5 h while phase compositions were monitored regularly using XRD analysis. Chloride MM, Nitrate MM, Acetate MM and Oxalate MM all displayed a sharp decline in $\text{Fe}_2(\text{MoO}_4)_3$ initially as MoO_3 and $\beta\text{-FeMoO}_4$ content increased over time. A reduction in MoO_3 and a rise in MoO_2 content was detected as the reduction of $\text{Fe}_2(\text{MoO}_4)_3$ plateaued for each sample indicating the limit of MoO_3 reoxidation, this point varied between precursors with Chloride MM (226 min) able to maintain the MoO_3 for the longest time. The Nitrate MM (136 min) sample was next best with both Oxalate MM and Acetate MM reached that point at 118 min.

The reduction in $\text{Fe}_2(\text{MoO}_4)_3$ content up to this point may also indicate how homogeneous the mixing of the MoO_3 and $\text{Fe}_2(\text{MoO}_4)_3$ were, this is due to the greater access of the MoO_3 surface layer to the $\text{Fe}_2(\text{MoO}_4)_3$. The reduction of $\text{Fe}_2(\text{MoO}_4)_3$ content up to the plateau point highlighted was highest for Chloride MM (39.8 %) followed by Nitrate MM (29.7 %) and Oxalate MM (28.2 %) with Acetate MM (23.4 %) reducing the least. No significant changes in Fe_2O_3 content throughout were observed in all four samples.

Phosphate MM presented a similar trend with the increase in the relative MoO_3 phase content observed like other MM samples, however due to the apparent lack of $\text{Fe}_2(\text{MoO}_4)_3$ it appears the FePO_4 acted as the bulk oxygen source as a gradual reduction was observed producing Fe_2O_3 . This was similar to results shown by Ai who observed positive synergy between FePO_4 and MoO_3 .^{28,29} The point of MoO_3 decrease occurred at 190 min which was higher than many MM samples which may explain why such high formaldehyde selectivity was observed throughout.

The Sulphate MM sample in contrast to other MM samples maintained no stability at 450 °C using the H_2/N_2 atmosphere with a rapid decline of MoO_3 as MoO_2 dominates by 64 minutes, this may be caused by the lack of $\text{Fe}_2(\text{MoO}_4)_3$ in the sample with the composition formed of isolated MoO_3 and Fe_2O_3 on the surface preventing the reoxidation of MoO_3 .

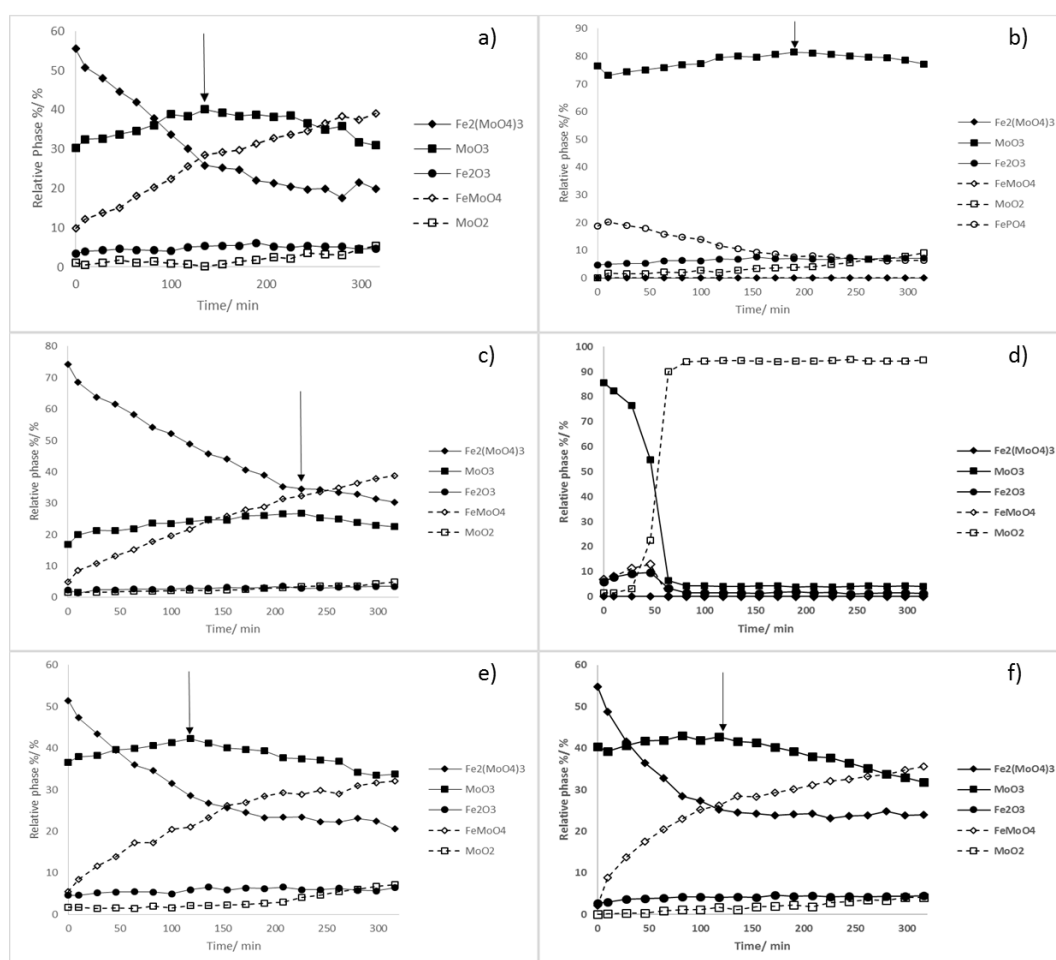


Figure 5.8. In-situ XRD reduction at constant 450 °C using 30 ml min⁻¹ 10 % H_2/N_2 mixture of MM samples produced using various iron precursors (a) Nitrate MM, b) Phosphate MM, c) Chloride MM, d) Sulphate MM, e) Acetate MM and f) Oxalate MM).

5.2.5 Iron Precursor Discussion

The use of different iron precursors seems to have a dramatic effect on the overall morphology and composition of the iron molybdate catalysts produced using MM and by extension the methanol partial oxidation results.

The best catalytic performance was achieved by Chloride MM and Nitrate MM which attained 94.2 % and 93.9 % yield at 365 °C and 335 °C respectively. Both samples presented high formaldehyde yields (>93 %) over an extended temperature ranges which were not observed by the other samples. Possible reasons for this increased formaldehyde selectivity presented at higher conversions may be due to the superior iron and molybdenum distribution observed in characterisation results. Both samples displayed the highest $\text{Fe}_2(\text{MoO}_4)_3$ content of the MM samples tested in XRD and Raman results, EDX mapping presenting largely homogeneous distribution of iron and molybdenum over the surface of the samples. In-situ XRD further supported the superior distribution of MoO_3 and $\text{Fe}_2(\text{MoO}_4)_3$ with both samples maintaining MoO_3 content for the longest time in reducing conditions through the Mars-Van Krevelen reoxidation of surface molybdena,¹⁸ this is thought to be due to the greater access of the $\text{Fe}_2(\text{MoO}_4)_3$ to the surface MoO_3 .²⁷

The next best catalyst was Oxalate MM which attained 89.5 % formaldehyde yield at 320 °C, Oxalate MM presented higher activity but formaldehyde selectivity was not maintained at higher temperatures. These changes may be due to lower distribution of iron and molybdenum observed with lower $\text{Fe}_2(\text{MoO}_4)_3$ in XRD and Raman spectral mapping, also highlighted with areas of Fe_2O_3 on the surface of the catalyst observed in microscopy results very similar to OM samples presented in Section 3.3. These Fe_2O_3 areas could have caused the larger surface area and by extension the higher activity observed by the catalyst but limiting the formaldehyde selectivity.³⁰⁻³²

The Phosphate MM was the most selective towards formaldehyde of the catalysts tested but was also the least active and maximum formaldehyde yields were not reached within the limits of the reactor (87.3% at 410 °C). Possible reasons for the lower activity observed may be due to the lack of phosphate removal from the iron which prevented the formation of $\text{Fe}_2(\text{MoO}_4)_3$ as observed in characterisation results. FePO_4 has been observed as largely inert towards methanol partial oxidation by Al^{3+} , a synergistic relationship between MoO_3 and FePO_4 has been observed similar to $\text{MoO}_3/\text{Fe}_2(\text{MoO}_4)_3$. The regeneration of surface MoO_3 by a Mars Van Krevelen mechanism with oxygen supplied from FePO_4 as suggested by observations in in-situ XRD results and literature examples.^{28,29} In this mechanism, it is the

crystalline MoO_3 which is the active species which is far less active than combination of amorphous surface MoO_3 supported on $\text{Fe}_2(\text{MoO}_4)_3$ due to limited number of terminal $\text{Mo}=\text{O}$ active sites.^{18,34}

The worst formaldehyde yields were attained by Acetate MM (83.9 % at 305 °C) and Sulphate MM samples (87.0 % at 350 °C) both produced large quantities of CO_x throughout. This was thought to be due to large quantities of Fe_2O_3 on the surface of the samples with large isolated areas of crystalline MoO_3 observed in microscopy results. Sulphate MM especially showed near complete segregation with no $\text{Fe}_2(\text{MoO}_4)_3$ in XRD and only trace amounts in Raman spectral mapping indicating poor mixing of iron and molybdenum. Acetate MM presented higher amounts of $\text{Fe}_2(\text{MoO}_4)_3$ in XRD and Raman spectral mapping than both Phosphate MM and Sulphate MM but it was significantly lower than the other MM samples with MoO_3 remaining the dominant species observed in characterisation.

The compositions of the catalysts were thought to be dependent on the mixing of the malonates prior to calcination. All samples were found to produce molybdenum malonate independent of the iron precursor used based on findings in DTG/TGA analysis.

Iron malonate production was shown to be highly dependent on the precursor. Iron (II) sulphate, iron (III) phosphate and iron (III) acetate caused little iron malonate formation due to the lack of displacement of the anionic species. The decomposition of both iron acetate and iron sulphate during calcination may have caused the formation of Fe_2O_3 on the surface of both samples.

Iron (II) oxalate was found to produce a mixture of both iron oxalate and malonate based on DTG/TGA analysis which may promote the mixing in the molten malonate mixture. The preservation of iron oxalate beyond the mixing step may have caused the similarities in both reactivity and morphology between Oxalate MM and OM samples shown in Section 3.3.

Iron (III) chloride and iron (III) nitrate usage produced the largest amounts of iron malonate, both of these samples produced the highest distribution of iron and molybdenum which may indicate that the formation of iron malonate may be required to achieved these high distributions. An increase in $\text{Fe}_2(\text{MoO}_4)_3$ content was observed in Chloride MM which may be due to the increase in Mo^{V} in the uncalcined mixture, this was suggested to form the $[\text{Mo}_2\text{O}_4\text{Cl}_4(\text{CH}_2\text{C}_2\text{O}_4\text{H})]^{3-}$ anionic species by Modéc *et al.*²⁰ which could promote mixing by preventing the formation of hydrogen bonding between molybdenum malonate dimers.

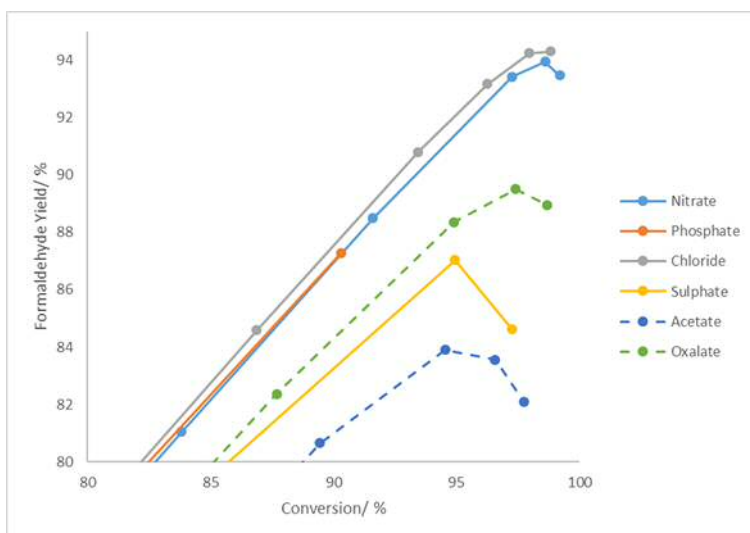


Figure 5.9. Methanol oxidation reaction summary of MM samples produced using various iron precursors.

5.3 Effect of Calcination Conditions on The Malonate Decomposition Method Using Iron (III) Chloride

5.3.1 Introduction

An investigation into the effect of calcination condition on the composition and by extension the reactivity of the Chloride MM samples was undertaken. The study used the same conditions as described in Section 4.4.

5.3.2.1 BET Surface Area and XPS Surface Analysis

The results of BET surface area analysis of Chloride MM samples using various calcination conditions are presented in Table 5.6. Samples calcined at 450 °C and 500 °C both present similar surface areas with the differences between the samples within experimental error. The most substantial changes were observed using 600 °C calcination where a $\approx 38\%$ reduction in surface area was observed compared to the other Cl samples.

Table 5.6. BET surface area and XPS surface ratio comparison for Chloride MM samples prepared using various calcination conditions.

Sample	BET Surface Area/ m ² g ⁻¹	XPS Surface Ratios	Rel. Surface Mo Excess/ %
		Fe:Mo	
Cl 500 2 h	2.2 ± 0.1	1:2.6	18.2
Cl 500 4 h	2.7 ± 0.4	1:2.6	18.2
Cl 500 6 h	2.1 ± 0.3	1:3.1	40.9
Cl 450 2 h	2.6 ± 0.2	1:2.7	22.7
Cl 450 4 h	2.8 ± 0.1	1:2.9	31.8
Cl 450 6 h	2.0 ± 0.3	1:2.7	22.7
Cl 600 2 h	1.4 ± 0.3	1:3.1	40.9
Cl 600 4 h	1.7 ± 0.2	1:3.0	36.4
Cl 600 6h	1.2 ± 0.1	1:3.2	45.6

Molybdenum surface content observed in XPS results were shown to vary as calcinations were changed. Cl 500 2 h, Cl 500 4 h, Cl 450 2 h and Cl 450 6 h were comparable with the differences between the samples within experimental error. All four samples presented a small excess of molybdenum relative to their theoretical bulk content.

The Cl 500 6 h, Cl 450 4 h and the three Cl 600 samples were also comparable presenting nearly double the molybdenum excess relative to the bulk of the previous samples. In the case of Cl 500 6 h and the Cl 600 samples, this may be due to the preferential molybdenum migration from the bulk towards the surface at higher temperatures as observed by Xu *et al.*³⁵

5.3.2.2 Powder XRD Crystallography

The XRD results shown in Fig. 5.10 and summarised in Table 5.7 present significant differences between the Chloride MM samples calcined at different conditions. All samples were comprised of a combination of Fe₂(MoO₄)₃, MoO₃ and Fe₂O₃. The Fe₂(MoO₄)₃ content was shown to decrease in the following order as MoO₃ content increased, Cl 500 2 h > Cl 600 4 h > Cl 450 4 h > Cl 600 2 h > Cl 600 6 h > Cl 500 4 h > Cl 450 6 h > Cl 500 6 h > Cl 450 2 h.

The Fe₂O₃ content was largely unchanged by calcination with all catalysts presenting between 1.0-1.5 %. A significant change was however observed as calcination lengths were

increased at 500 °C, a steady increase in Fe₂O₃ content in conjunction to a sharp rise in MoO₃ content from as the calcination length was extended from 2 h – 4 h – 6 h indicating Fe₂(MoO₄)₃ production limitation.

Low Fe₂(MoO₄)₃ content observed in Cl 450 2 h may be due to the low rate of the solid state reaction between Fe₂O₃ and MoO₃ at this 450 °C with some authors suggesting temperatures exceeding 470 °C are required to form large amounts of Fe₂(MoO₄)₃.^{36,37} Larger quantities of iron molybdate were observed as calcination was continued.

Very little variance was observed as calcination conditions were continued at 600 °C but all three samples were observed to contain over 80 % Fe₂(MoO₄)₃.

Table 5.7 Relative phase composition of Chloride MM samples produced using various calcination conditions corresponding to XRD results shown in Fig. 5.12.

Sample	Relative % Phase Based On Powder XRD Results		
	Fe ₂ (MoO ₄) ₃	MoO ₃	Fe ₂ O ₃
Cl 500 2 h	88.1	11.1	0.7
Cl 500 4 h	79.4	19.1	1.5
Cl 500 6 h	71.1	26.8	2.1
Cl 450 2 h	70.7	27.9	1.4
Cl 450 4 h	82.1	16.9	1.0
Cl 450 6 h	77.5	21.3	1.2
Cl 600 2 h	81.2	17.7	1.1
Cl 600 4 h	83.6	15.3	1.1
Cl 600 6 h	80.9	18.1	1.0

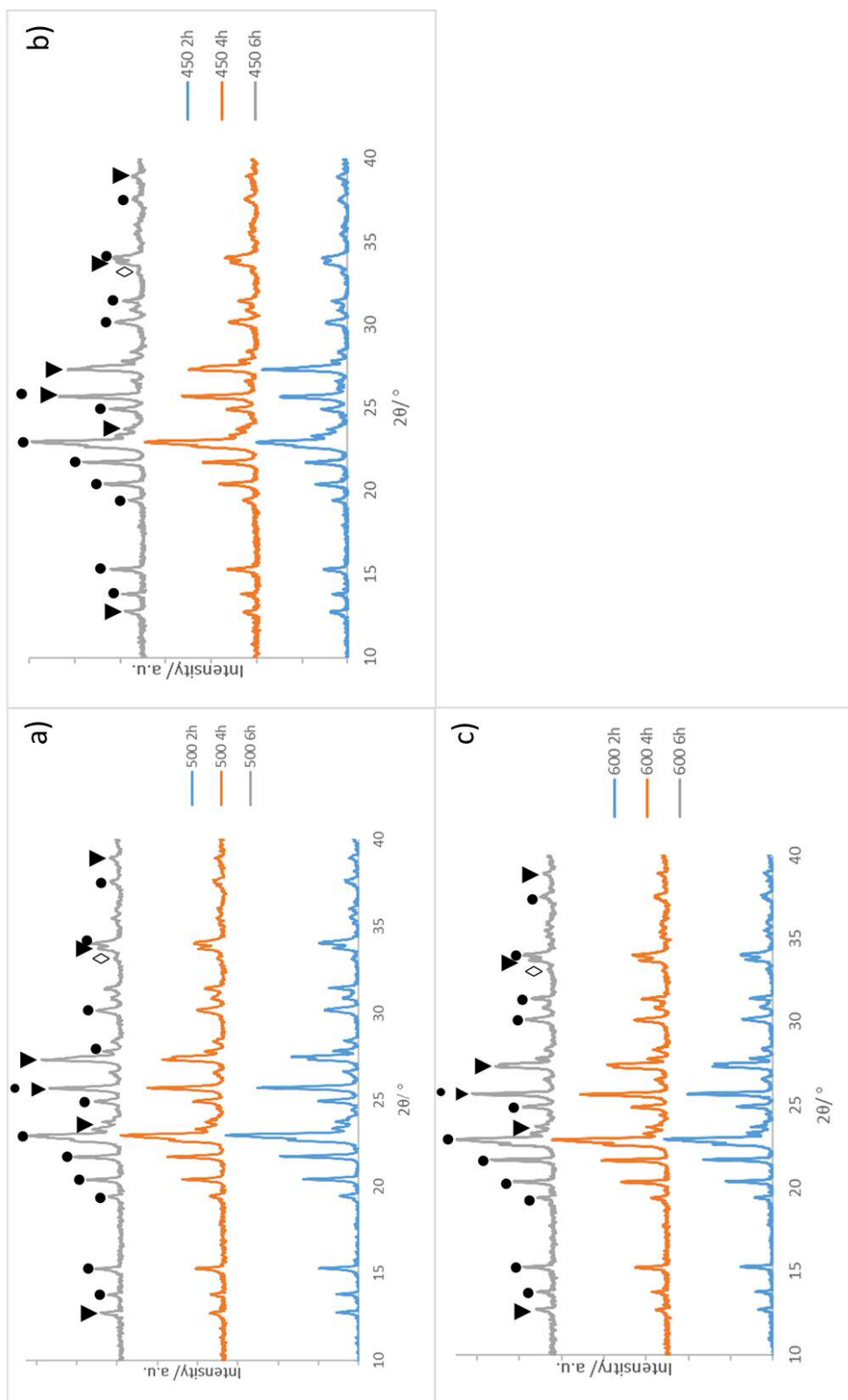


Figure 5.10 Powder XRD patterns of Chloride MM samples produced using different calcination lengths and temperature, (a) 500 °C, (b) 450 °C and (c) 600 °C. (Key: ▼ MoO₃, ● Fe₂(MoO₄)₃ and ◇ Fe₂O₃).

5.3.2.3 Raman Spectral Mapping

The Raman spectral mapping comparison of the CI 500 samples (Fig. 5.11) presented high $\text{Fe}_2(\text{MoO}_4)_3$ content in all samples, a gradual increase in MoO_3 content was observed as calcination lengths were extended in the general composition of the samples (Fig. 5.11.a, 5.11.d and 5.11.g for CI 500 2 h, CI 500 4 h and CI 500 6 h respectively). Areas of even higher MoO_3 content were also observed (Fig. 5.11.e and 5.11.h) and in greater numbers especially for CI 500 6 h which presented the greatest discrepancy between the points surveyed.

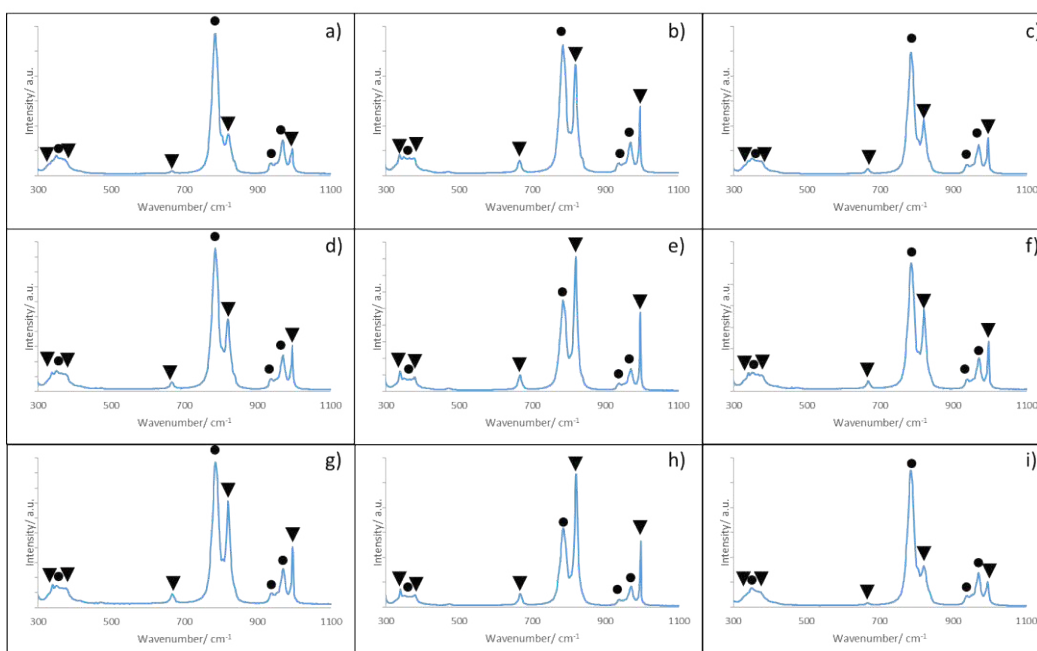


Figure 5.11 Raman spectral mapping comparison between Chloride MM samples produced using different calcination lengths at 500 °C (a-c) CI 500 2 h, d-f) CI 500 4 h, g-i) CI 500 6 h). (Key: ▼ MoO_3 and ● $\text{Fe}_2(\text{MoO}_4)_3$).

The highest average MoO_3 content in Raman spectral results was observed for the CI 450 2 h example (Fig. 5.12.a) which supports observations in XRD results. As calcinations were extended $\text{Fe}_2(\text{MoO}_4)_3$ content was shown to rise rapidly in the average composition of the samples (Fig. 5.12.d and 5.12.g for CI 450 4 h and CI 450 6 h respectively). Areas of very high MoO_3 content were observed for both CI 450 4 h (Fig. 5.12.f) and CI 450 6 h (Fig. 5.12.h) examples which were not seen in other Chloride MM samples, these areas were however rarely presented.

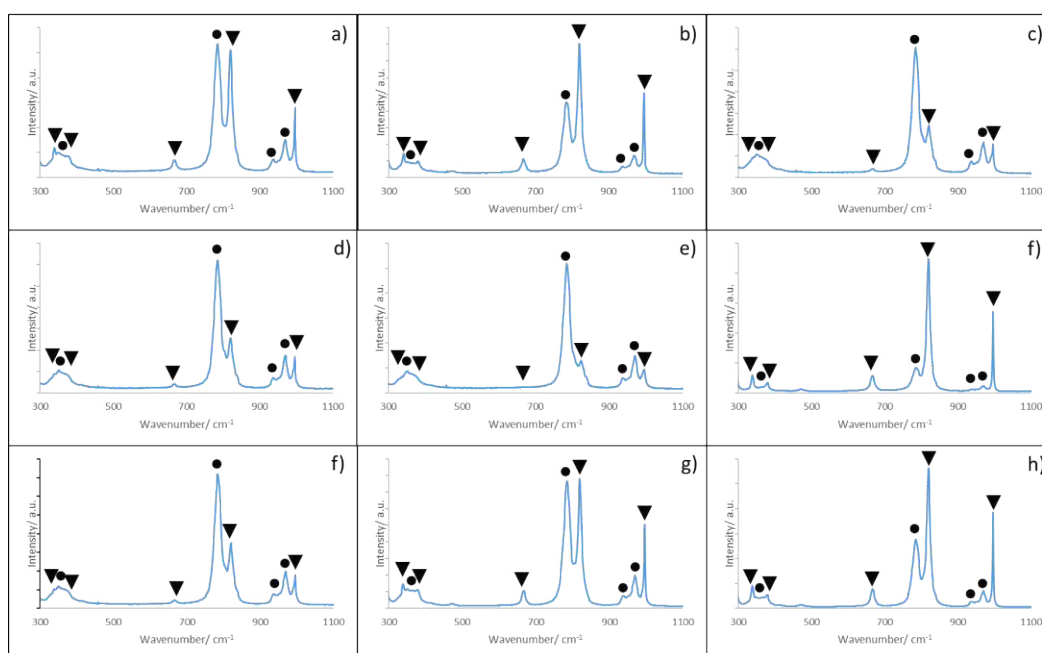


Figure 5.12 Raman spectroscopy mapping comparison between Chloride MM samples produced using different calcination lengths at 450 °C (a-c) CI 450 2 h, d-f) CI 450 4 h, g-i) CI 450 6 h). (Key: ▼ MoO₃ and ● Fe₂(MoO₄)₃).

The CI 600 samples presented the highest Fe₂(MoO₄)₃ content on average in Raman spectral mapping. The general composition of the CI 600 samples are shown in Fig. 5.13.a, 5.13.d and 5.13.g respectively. Similar to CI 500 samples, MoO₃ was shown to increase relative to Fe₂(MoO₄)₃ content as calcinations were extended. There was some discrepancy between the points with higher MoO₃ content observed in some areas, this was most prevalent in CI 600 4 h with many points presenting as 5.13.e.

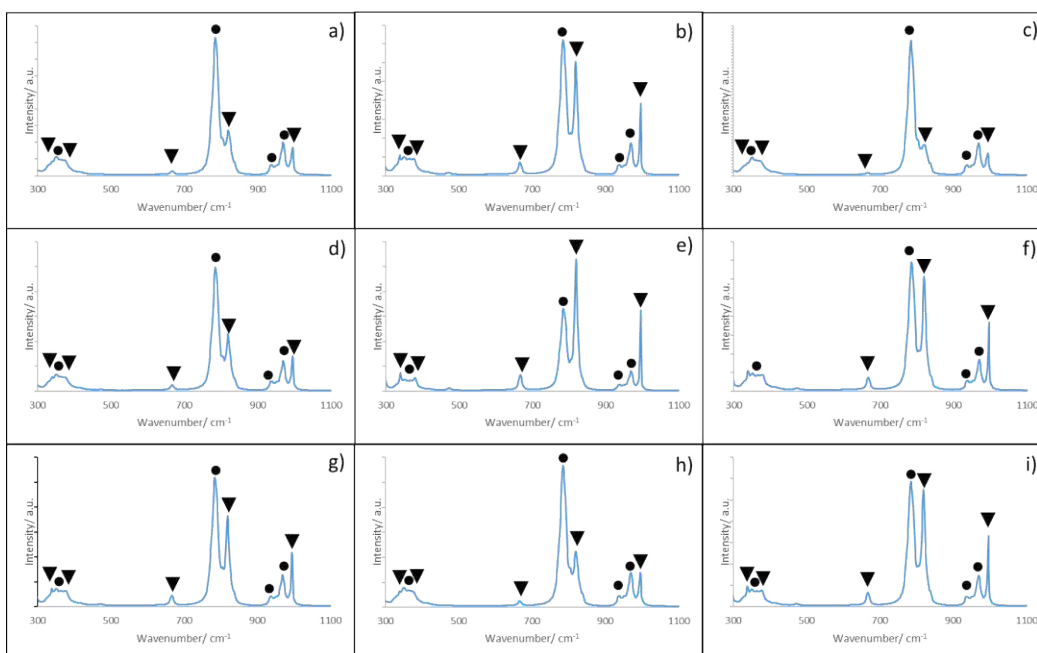


Figure 5.13 Raman spectroscopy mapping comparison between Chloride MM samples produced using different calcination lengths at 600 °C (a-c) CI 600 2 h, d-f) CI 600 4 h, g-i) CI 600 6 h). (Key: ▼ MoO₃ and ● Fe₂(MoO₄)₃).

5.3.2.4 SEM and EDX Elemental Mapping

Morphological changes were observed as calcination were extended at 500 °C, initially the formation of regular, ordered plate like structures in a lamellar like formation was shown. As calcinations were extended, a breakdown of the regular structures was observed with the formation of larger, more agglomerated structures observed in CI 500 6 h.

EDX mapping of the corresponding images showed an increase in elementally exclusive Mo areas as highlighted in the form of MoO₃ crystallites as calcinations were extended from 2 h. Large areas of high iron enrichment were also observed on the surface of CI 500 6 h which may indicate the formation of Fe₂O₃ on the surface of the sample.

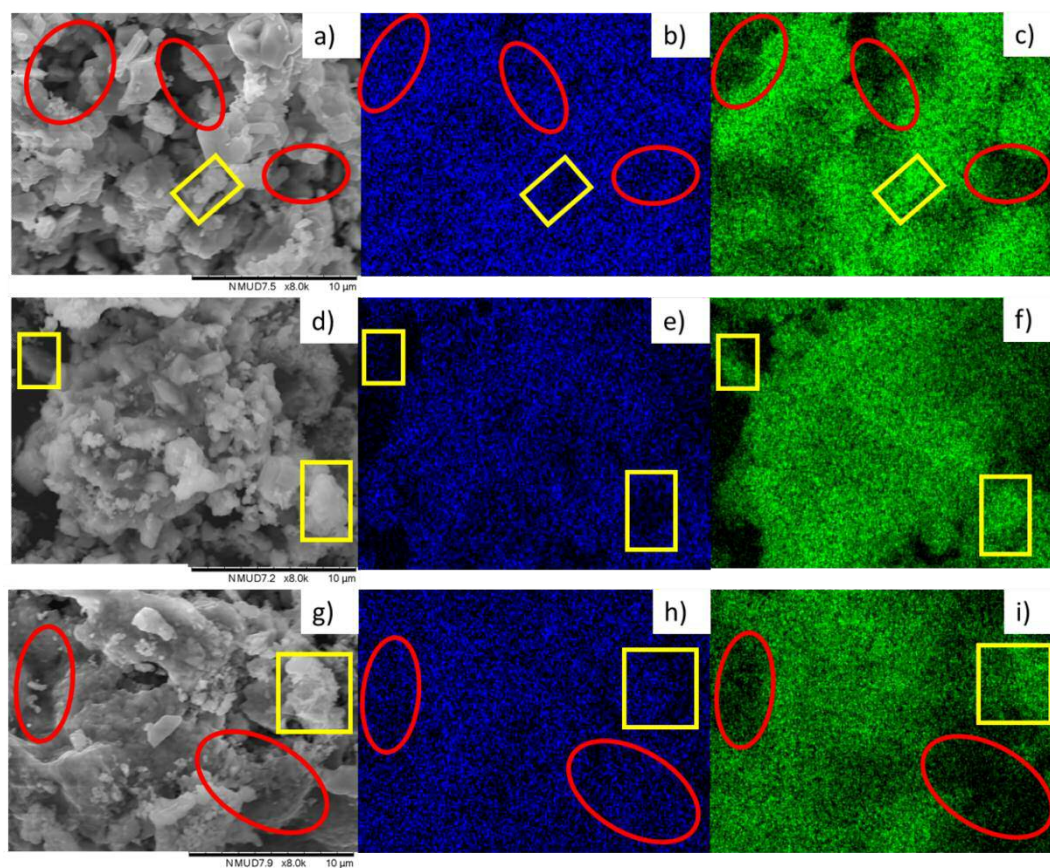


Figure 5.14 SEM and EDX elemental mapping comparison of Chloride MM samples calcined at 500 °C for a variety of different times. (a) SEM image of Cl 500 2 h, (b) EDX map showing Fe content of Cl 500 2 h, (c) EDX map showing Mo content of Cl 500 2 h, (d) SEM image of Cl 500 4 h, (e) EDX map showing Fe content of Cl 500 4 h, (f) EDX map showing Mo content of Cl 500 4 h, (g) SEM image of Cl 500 6 h, (h) EDX map showing Fe content of Cl 500 6 h and (i) EDX map showing Mo content of Cl 500 6 h. Highlighted Fe rich (red circles) and Mo rich (yellow squares).

Sponge-like morphologies were observed over much of the surfaces of Cl 450 samples (Fig. 5.15), large crystallite structures were also displayed in both Cl 450 2 h and Cl 450 6 h examples. EDX mapping of the structures found that the overall composition of the sponge-like structures were largely homogeneous with a mixture of both iron and molybdenum. The crystallite structures were observed to be molybdenum exclusive as highlighted suggesting the formation of MoO_3 on the surface of the samples. Iron enriched areas were observed on all three samples but as calcination were extended molybdenum content in these areas increased.

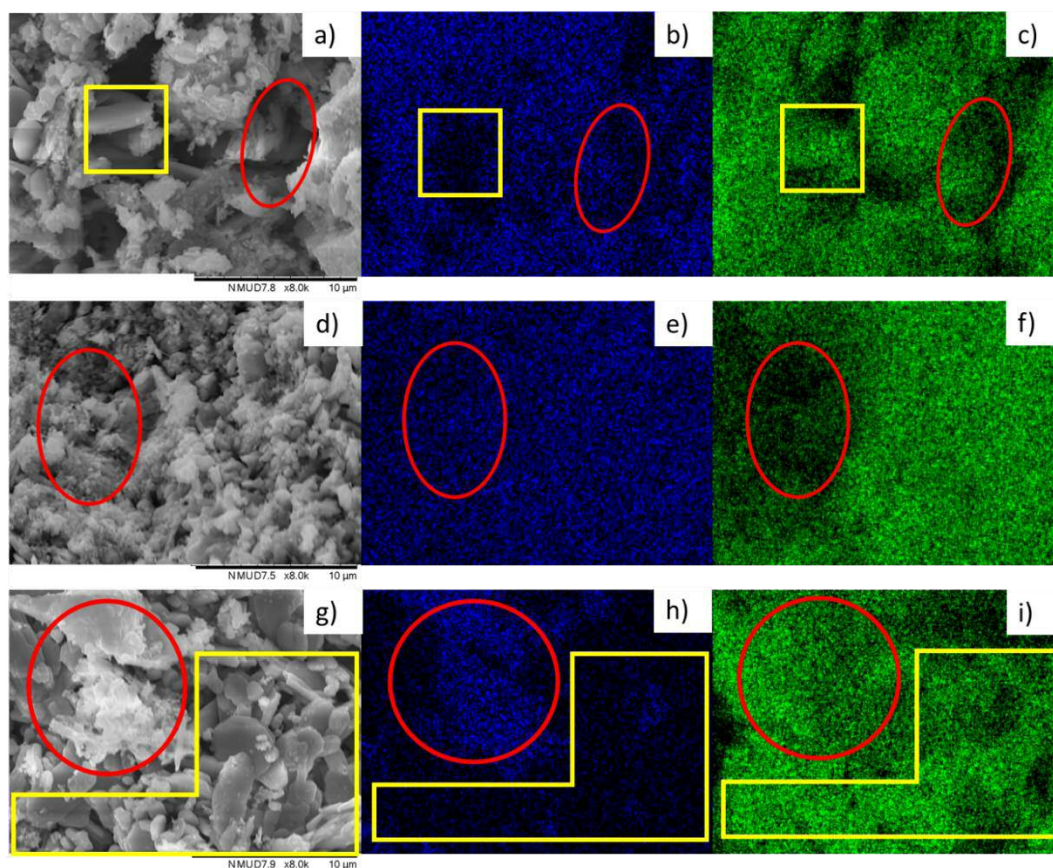


Figure 5.15 SEM and EDX elemental mapping comparison of Chloride MM samples calcined at 450 °C for a variety of different times. (a) SEM image of Cl 450 2 h, (b) EDX map showing Fe content of Cl 450 2 h, (c) EDX map showing Mo content of Cl 450 2 h, (d) SEM image of Cl 450 4 h, (e) EDX map showing Fe content of Cl 450 4 h, (f) EDX map showing Mo content of Cl 450 4 h, (g) SEM image of Cl 450 6 h, (h) EDX map showing Fe content of Cl 450 6 h and (i) EDX map showing Mo content of Cl 450 6 h. Highlighted Fe rich (red circles) and Mo rich (yellow squares).

The Cl 600 2 h sample was highly similar to Cl 500 2 h with the formation of a regular crystallite plate like morphology, evidence of agglomerated particles at the edges of these crystallites was also observed. As the calcination was continued, the crystallite morphology was lost in favour of large compact particles, these were found to agglomerate forming a lamellar structure. Crystallites were observed on the surface of both Cl 600 4 h and Cl 600 6 h which were shown to dramatically increase in size (2 μm increased to 5 μm diameter) as calcination was extended.

EDX mapping of the three samples showed an overall homogeneous distribution of both iron and molybdenum was observed over the surface. Areas of iron enrichment were observed in all three samples as highlighted but these areas were rarely observed, Cl 600 4 h displayed small areas of near iron exclusivity which could indicate Fe_2O_3 formation on the surface. The crystallite formation on the surface of both Cl 600 4 h and Cl 600 6 h were found to be

molybdenum dominated suggesting crystalline MoO_3 formation, possibly caused by the migration of amorphous MoO_3 towards the surface forming crystalline MoO_3 as suggested by Xu *et al.*³⁵

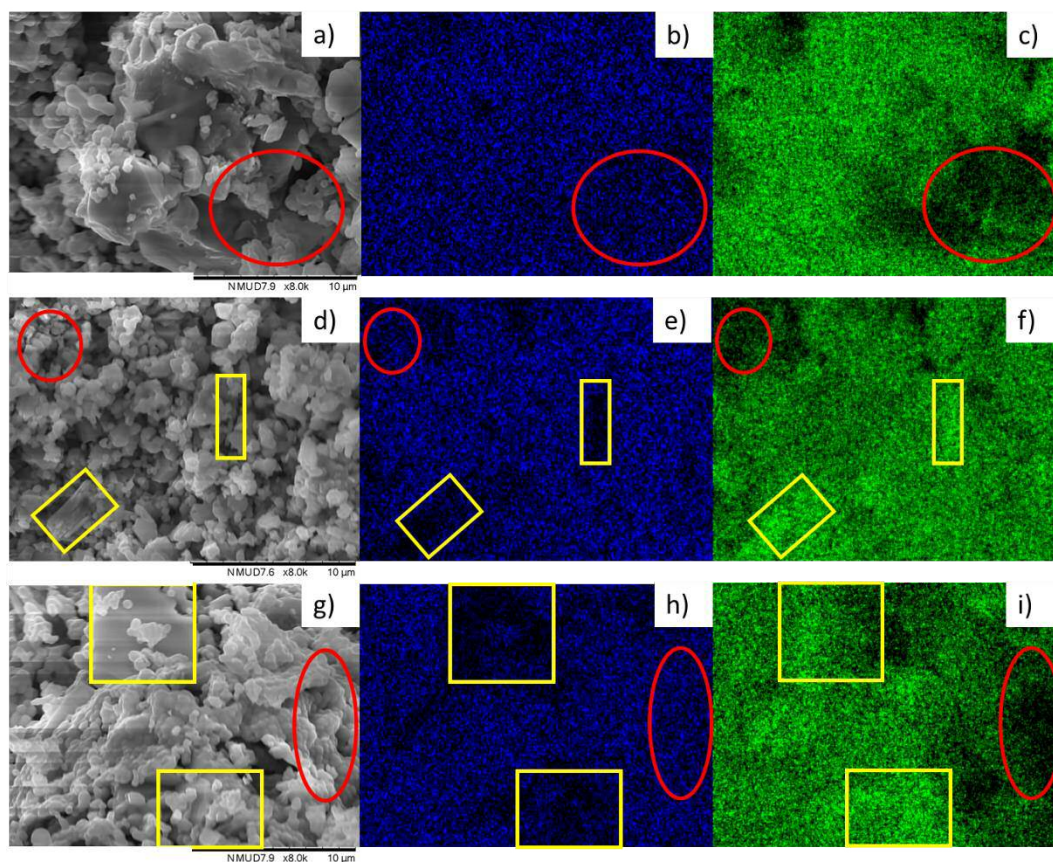


Figure 5.16 SEM and EDX elemental mapping comparison of Chloride MM samples calcined at 600 °C for a variety of different times. (a) SEM image of Cl 600 2 h, (b) EDX map showing Fe content of Cl 600 2 h, (c) EDX map showing Mo content of Cl 600 2 h, (d) SEM image of Cl 600 4 h, (e) EDX map showing Fe content of Cl 600 4 h, (f) EDX map showing Mo content of Cl 600 4 h, (g) SEM image of Cl 600 6 h, (h) EDX map showing Fe content of Cl 600 6 h and (i) EDX map showing Mo content of Cl 600 6 h. Highlighted Fe rich (red circles) and Mo rich (yellow squares).

5.3.3 Methanol Partial Oxidation

Methanol partial oxidation of Chloride MM samples prepared using different calcination conditions displayed significant variance between the materials as shown in Fig. 5.17.

The activity of the samples was shown to decrease in the following order Cl 450 4 h > Cl 450 2 h > Cl 500 6 h > Cl 450 6 h > Cl 500 4 h > Cl 600 4 h > Cl 600 6 h > Cl 500 2 h = Cl 600 2 h.

A wide range of conversions (28.2-59.1 %) were observed between the samples at 260 °C as reaction temperatures were raised conversion increased dramatically. The three Cl 450 and Cl 500 6 h samples all attained over 90 % conversion at 305 °C, these same conversions were

reached by Cl 500 4 h and Cl 600 4 h at 320 °C. Cl 500 2 h, Cl 600 2 h and Cl 600 6 h required temperatures exceeding 335 °C.

The formaldehyde and CO_x selectivity also varied between materials, Cl 500 6 h presented the lowest formaldehyde selectivity overall dropping below 90 % before 260 °C in favour of CO_x. Cl 450 2 h and Cl 600 4 h were the next best attaining high formaldehyde selectivity (>95 %) at 260 °C before decreasing steadily in favour of CO_x, at 320 °C Cl 600 4 h decreased more rapidly dropping to below 80 % at 350 °C. Both Cl 450 4 h and Cl 500 4 h were able to maintain high formaldehyde selectivity up until 320 °C before a gradual decrease was observed. The best formaldehyde selectivity was maintained by Cl 500 2 h, Cl 450 6 h, Cl 600 2 h and Cl 600 6 h which presented high selectivity well above 350 °C.

Table 5.8 Maximum formaldehyde yield summary of Chloride MM samples calcined using various conditions.

Sample	Maximum Formaldehyde Yield/ %	Temperature / °C
Cl 500 2 h	94.3	365
Cl 500 4 h	88.8	335
Cl 500 6 h	77.6	320
Cl 450 2 h	88.6	320
Cl 450 4 h	93.4	320
Cl 450 6 h	94.4	335
Cl 600 2 h	94.4	380
Cl 600 4 h	80.5	320
Cl 600 6 h	91.7	365

The effect these changes in reactivity had on maximum formaldehyde yield is summarised in Table 5.8. The lowest yields were achieved by Cl 500 6 h and Cl 600 4 h due to the low formaldehyde selectivity presented by both catalyst. The Cl 500 4 h and Cl 450 2 h samples were comparable although due to the higher activity displayed by Cl 450 2 h, the same formaldehyde yield was attained at lower temperatures. Cl 600 6 h was the next best with high formaldehyde yields achieved at high temperatures which was stabilised over a range of temperatures (350-380 °C). The best performing samples were Cl 500 2 h, Cl 450 4 h, Cl 450 6 h and Cl 600 2 h, all four samples maintain very high yields over a wider range of temperatures especially Cl 450 6 h which maintained over 93 % yield between 320-380 °C.

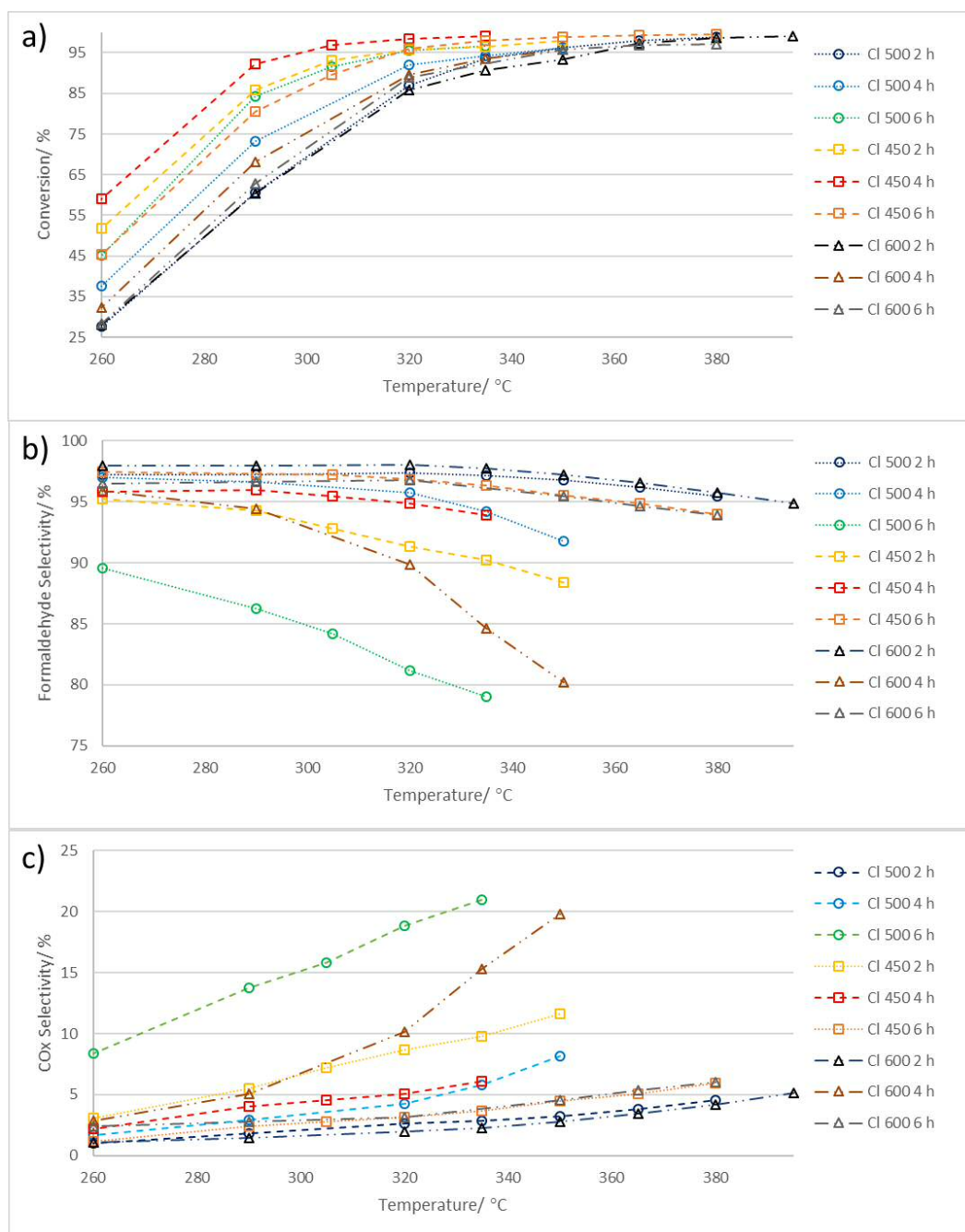


Figure 5.17 Methanol partial oxidation reaction comparisons of Chloride MM samples prepared using various calcination conditions using various reaction temperatures. (a) Methanol Conversion, (b) Formaldehyde Selectivity and (c) CO_x selectivity).

5.3.4 Discussion of the Effect of Calcination Conditions for MM Using Iron (III) Chloride

Based on catalytic results, the Chloride MM samples are highly sensitive to calcination conditions.

Extended calcination at 500 °C caused a significant decrease in formaldehyde yield from 94.3 % (CI 500 2 h), 88.8 % (CI 500 4 h) and 77.6 % (CI 500 6 h). Possible reasons for this is the reduction in $\text{Fe}_2(\text{MoO}_4)_3$ content with the formation of larger quantities of both MoO_3 and Fe_2O_3 . Fe_2O_3 content was observed on the surface of the CI 500 6 h sample in microscopy results which may be formed out of the migration of MoO_3 similar to observations by 500 4h MM sample presented in Section 4.4. where amorphous MoO_3 present in interstitial spaces of the $\text{Fe}_2(\text{MoO}_4)_3$ lattice were found to sublime similar to results shown by Xu *et al.*³⁵

The CI 450 samples catalytic performance was shown to improve as calcination time was extended with formaldehyde yields increasing from 88.6 % (CI 450 2 h), 93.4 % (CI 450 4 h) and 94.4 % (CI 450 6 h). Possible reasons for these changes may be due to the increase in $\text{Fe}_2(\text{MoO}_4)_3$ content observed by both CI 450 4 h and CI 450 6 h formed out of the solid-state reaction.³⁸ A gradual decrease in iron exclusive areas were also observed in microscopy results as calcinations were continued, this may have been due to migration of MoO_3 from the bulk covering exposed iron centres over time by the Kirkendall effect also observed by other authors using prolonged calcinations.³⁹⁻⁴¹ This could have caused the increased formaldehyde selectivity presented by both CI 450 4 h and CI 450 6 h samples.

Lower $\text{Fe}_2(\text{MoO}_4)_3$ content observed by all samples calcined at 450 °C may be due to the inadequate temperature for the solid-state reaction between the Fe_2O_3 and MoO_3 as suggested by some authors,^{36,37} who indicated significant $\text{Fe}_2(\text{MoO}_4)_3$ content was only achieved with calcination temperatures exceeding 470 °C.

The CI 600 samples presented significant changes, the maximum formaldehyde yield attained was shown to decrease in the following order 94.4 % (CI 600 2 h), 91.7 % (CI 600 6 h) and 80.5 % (CI 600 4 h). Possible reasons for this variation in catalytic performance may be due to the change in morphology going from CI 600 2 h – CI 600 4 h -CI 600 6 h. Starting with CI 600 2 h which presented similar morphology to CI 500 2 h with the formation of ordered crystalline plate structures which were shown to be evenly composed of both iron and molybdenum. As the calcination was extended, the formation of large particles was observed

similar to CI 500 4h with increase formation of MoO₃ crystallites on the surface of the catalyst. This in conjunction to an increase in overall MoO₃ content in Raman spectral mapping. This lack of homogeneity could have caused the exposure of Fe₂O₃ observed in microscopy towards the surface causing the increase in CO_x selectivity. The CI 600 6 h samples presented further MoO₃ production in the form of large crystallites observed in microscopy results and an indication of more MoO₃ in Raman spectral mapping. The morphology of the sample had also changed forming agglomerated layered structures of the particles observed in CI 600 4 h. The structures were not as homogeneous as the CI 600 2 h sample with areas of high iron content observed which may have limited the formaldehyde selectivity presented at higher temperatures.^{32,42}

5.4 The Effects of Calcination Conditions on The Malonate Decomposition Method using Iron (II) Oxalate

5.4.1 Introduction

The use of different calcination conditions was studied using the Oxalate MM mixture to ascertain if changes in calcination conditions may change the composition of the catalyst. Due to the relatively high Fe₂O₃ and MoO₃ content of the sample, it may be suggested that higher temperature calcinations may be preferential similar to samples produced using physical grinding methods.^{36,37}

5.4.2 Characterisation

5.4.2.1 BET Surface Area and XPS Surface Analysis

The BET surface area results presented in Table 5.9 presented significant differences between the Oxalate MM samples calcined using various conditions. Ox 450 samples presented the highest surface area independent of calcination time followed by the Ox 500 and the Ox 600 samples which presented a large reduction in surface area. Shorter calcination lengths were shown to promote surface area improvements at all temperatures.

The XPS surface results of the same materials presented minimal difference between surface Fe:Mo content between all the Ox 450 and Ox 500 samples and were within error of the technique. All the Ox 450 and Ox 500 samples presented with a small molybdenum excess on the surface compared to the theoretical bulk content. A sharp rise in molybdenum surface content was observed as calcination conditions were increased to 600 °C with no significant difference observed as the calcination was extended at this temperature. This may indicate a higher temperature requirement for molybdenum migration from the bulk to the surface, this was similar to results obtained by Xu *et al.*³⁵ who only observed significant molybdenum surface excesses only at temperatures exceeding 500 °C.

Table 5.9 BET surface area and XPS surface ratio comparison for Oxalate MM samples prepared using various calcination conditions.

Sample	BET Surface Area/ m ² g ⁻¹	XPS Surface Ratios	Rel. Surface Mo Excess/ %
		Fe:Mo	
Ox 500 2 h	7.7 ± 0.5	1:2.4	9.1
Ox 500 4 h	4.9 ± 0.6	1:2.4	9.1
Ox 500 6 h	4.9 ± 0.4	1:2.6	18.2
Ox 450 2 h	9.0 ± 0.6	1:2.4	9.1
Ox 450 4 h	7.9 ± 0.4	1:2.6	18.2
Ox 450 6 h	7.9 ± 0.5	1:2.4	9.1
Ox 600 2 h	1.9 ± 0.2	1:3.1	40.1
Ox 600 4 h	1.5 ± 0.2	1:2.9	31.8
Ox 600 6h	1.3 ± 0.3	1:3.0	36.4

5.2.2.2 Powder XRD Crystallography

The XRD patterns of Ox samples shown in Fig. 5.18 presented a mixture of Fe₂(MoO₄)₃, MoO₃ and Fe₂O₃ phases. The relative phase composition based on the XRD patterns is presented in Table 5.10.

The relative $\text{Fe}_2(\text{MoO}_4)_3$ content was shown to decrease as MoO_3 increased between samples. $\text{Fe}_2(\text{MoO}_4)_3$ content decreased in the following order, Ox 600 6 h > Ox 600 2 h > Ox 600 4 h > Ox 500 6 h > Ox 500 4 h > Ox 500 2 h > Ox 450 6 h > Ox 450 2 h > Ox 450 4 h.

Fe_2O_3 content for all samples was fairly similar ranging between 2.1-2.7 % except for Ox 600 2 h (4.3 %) and Ox 450 6 h (1.2 %).

Based on these results, 600 °C calcinations seem to be beneficial with the highest $\text{Fe}_2(\text{MoO}_4)_3$ content observed. Extended calcination at 500 °C also presented with higher $\text{Fe}_2(\text{MoO}_4)_3$ although none matched the Ox 600 samples. 450 °C calcinations caused lower $\text{Fe}_2(\text{MoO}_4)_3$ content to be produced which remained largely unchanged as calcination lengths were extended, this may be due to the low rate of solid state reaction between MoO_3 and Fe_2O_3 , similar observations have been found in other studies which suggested that $\text{Fe}_2(\text{MoO}_4)_3$ formation is limited at temperatures under 470 °C.^{36,37}

Table 5.10 Relative phase composition of Oxalate MM samples produced using various calcination conditions corresponding to XRD results shown in Fig. 5.20.

Sample	Relative % Phase Based On Powder XRD Results		
	$\text{Fe}_2(\text{MoO}_4)_3$	MoO_3	Fe_2O_3
Ox 500 2 h	62.2	35.6	2.2
Ox 500 4 h	62.6	34.7	2.7
Ox 500 6 h	64.5	33.0	2.5
Ox 450 2 h	61.1	36.7	2.2
Ox 450 4 h	59.6	37.8	2.6
Ox 450 6 h	61.9	36.3	1.2
Ox 600 2 h	66.4	29.3	4.3
Ox 600 4 h	65.0	32.8	2.2
Ox 600 6 h	70.4	27.5	2.1

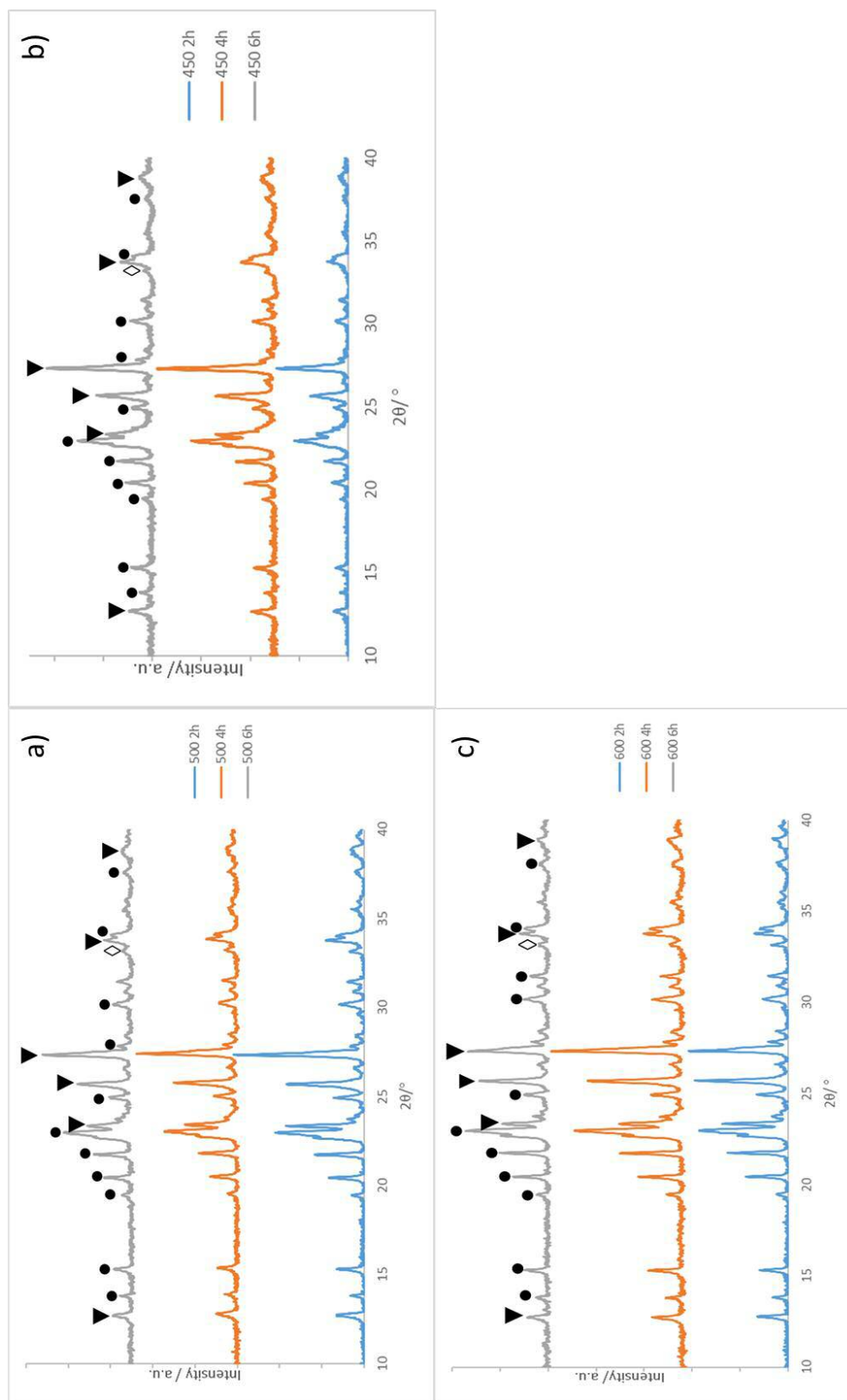


Figure 5.18 Powder XRD patterns of Oxalate MM samples produced using different calcination lengths and temperature, (a) 500 °C, (b) 450 °C and (c) 600 °C. (Key: \blacktriangledown MoO_3 , \bullet $\text{Fe}_2(\text{MoO}_4)_3$ and \diamond Fe_2O_3).

5.4.2.3 Raman Spectral Mapping

Ox 500 2 h showed the highest average $\text{Fe}_2(\text{MoO}_4)_3$ content of the Ox 500 samples in Raman mapping results shown in Fig. 5.19. Both Ox 500 4 h and 6 h presented higher MoO_3 content in the majority of the points surveyed. A small amount of variance between the points surveyed but largely unchanged suggest homogenous distribution. Regions of high $\text{Fe}_2(\text{MoO}_4)_3$ content shown in Fig. 5.19.i. may indicate the formation of iron molybdate at iron rich areas via the solid state reaction between migrating MoO_3 and Fe_2O_3 .

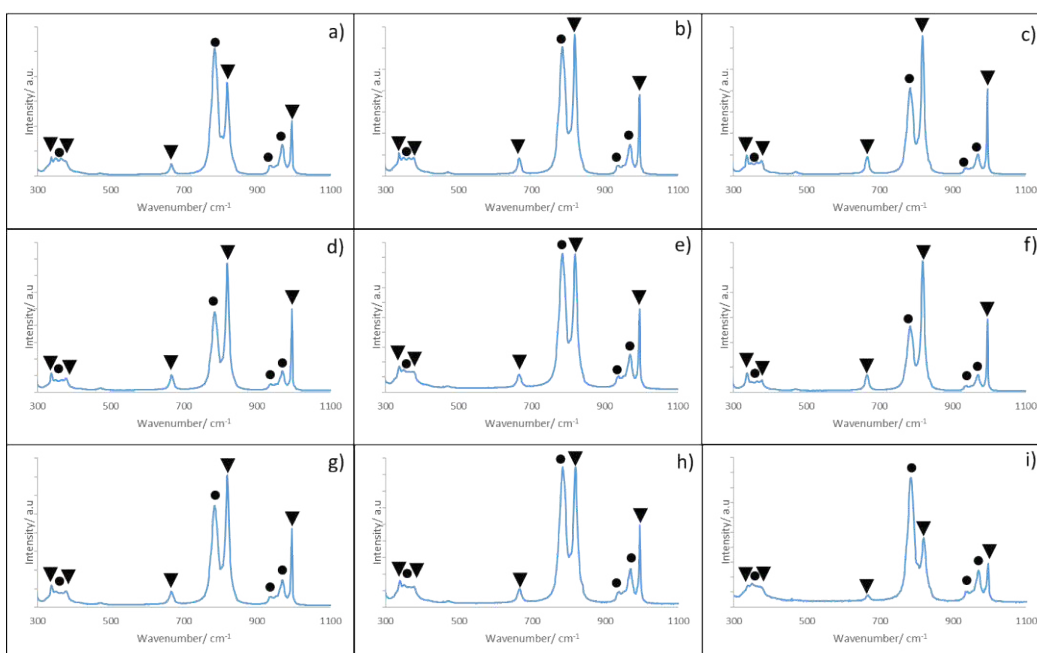


Figure 5.19 Raman spectral mapping of Oxalate MM samples produced using different calcination lengths at 500 °C (a-c) Ox 500 2 h, d-f) Ox 500 4 h, g-i) Ox 500 6 h). (Key: ▼ MoO_3 and ● $\text{Fe}_2(\text{MoO}_4)_3$).

The Raman spectral mapping results of Ox 450 samples (Fig. 5.20) presented the lowest $\text{Fe}_2(\text{MoO}_4)_3$ content of the Oxalate samples in their general composition, as show in Fig 5.20.a, 5.20.d and 5.20.g representing Ox 450 2 h, Ox 450 4 h and Ox 450 6 h respectively. A small increase in $\text{Fe}_2(\text{MoO}_4)_3$ content was observed for Ox 450 6 h but the change was minimal.

A small number of areas of far higher MoO_3 content were observed in the survey of each sample which could indicate a lack of homogeneous mixing of the samples with isolated MoO_3 presence.

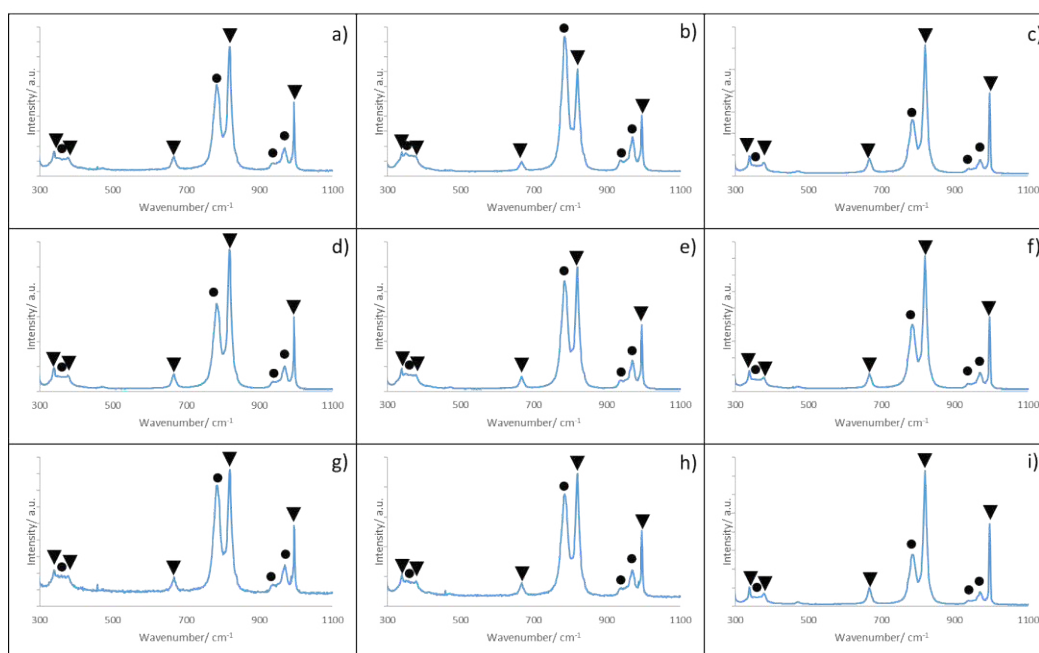


Figure 5.20 Raman spectral mapping of Oxalate MM samples produced using different calcination lengths at 450 °C (a-c) Ox 450 2 h, d-f) Ox 450 4 h, g-i) Ox 450 6 h). (Key: ▼ MoO₃ and ● Fe₂(MoO₄)₃).

Raman mapping comparison of Ox 600 samples shown in Fig. 5.21 supports XRD results shown in 5.18. Fe₂(MoO₄)₃ appeared in larger quantities in the majority of points represented as 5.21.a, 5.21.d and 5.21.g for Ox 600 2 h, Ox 600 4 h and Ox 600 6 h respectively.

Isolated areas of high MoO₃ content presented in previous Ox samples were shown to decrease as calcinations at 600 °C were extended. Regions of near exclusive Fe₂(MoO₄)₃ content like those observed in Ox 500 6 h were observed in all Ox 600 samples.

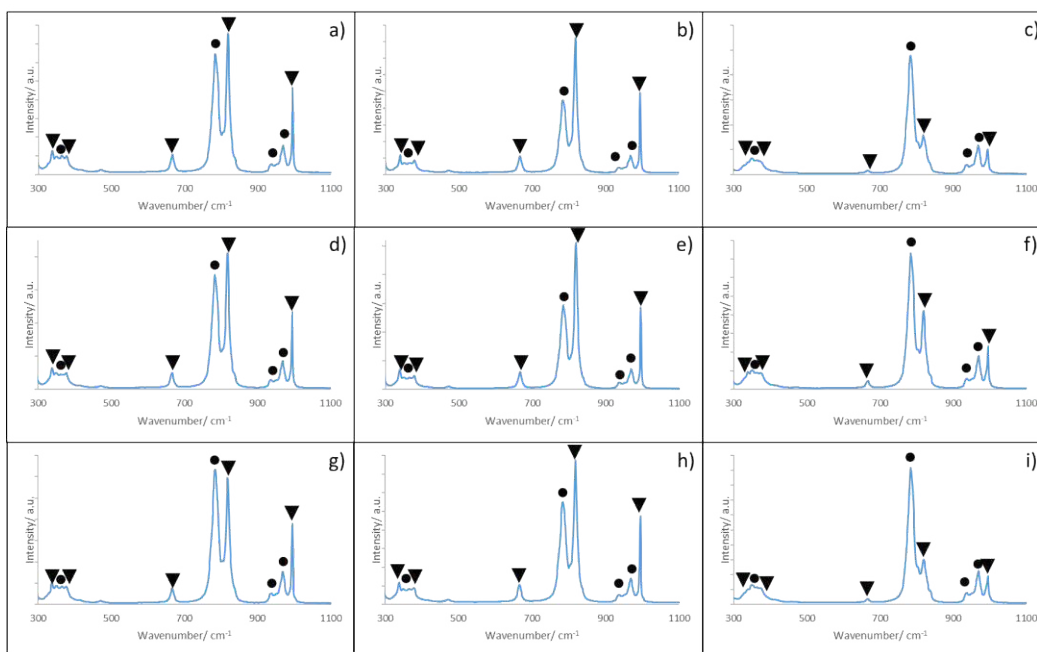


Figure 5.21 Raman spectroscopy mapping comparison between Oxalate MM samples produced using different calcination lengths at 600 °C (a-c) Ox 600 2 h, d-f) Ox 600 4 h, g-i) Ox 600 6 h). (Key: ▼ MoO₃ and ● Fe₂(MoO₄)₃).

5.4.2.4 SEM and EDX Elemental Mapping

Microscopy results of Ox 500 and Ox 450 shown in Fig. 5.22 and Fig. 5.23 respectively present minimal change in morphology with both calcination temperatures producing samples with sponge-like morphologies, these were probably formed out of the decomposition of the carboxylates similar to results found by Soares *et al.*^{11,43} utilising a sol-gel method.

EDX mapping of the corresponding micrographs did present some significant differences, higher molybdenum content was observed in Ox 450 samples with more areas of near molybdenum exclusivity observed on the surface indicating MoO₃ production. Limited evidence of MoO₃ formation on the surface was observed in the Ox 500 samples with only Ox 500 4 h displaying areas of molybdenum enrichment over the surface. Areas of iron enrichment were observed on the surface of all Ox 450 and Ox 500 samples although both the frequency and the size of these areas decreased in the Ox 500 samples.

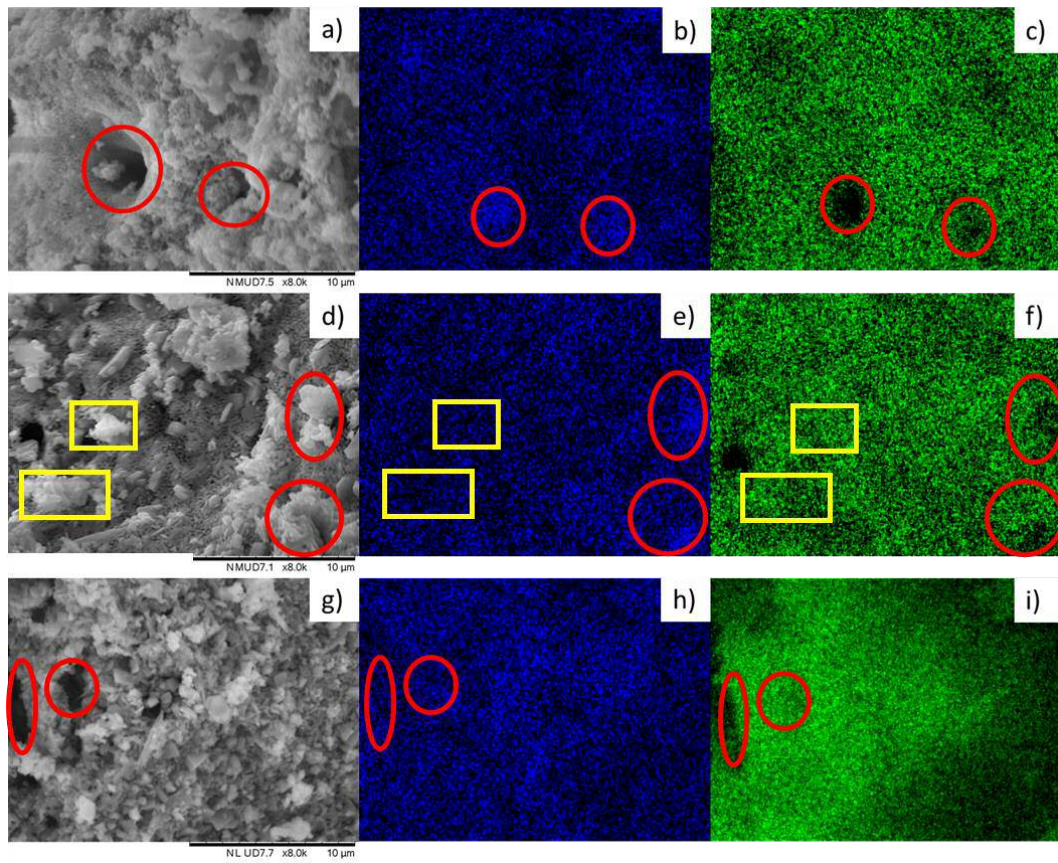


Figure 5.22 SEM and EDX elemental mapping comparison of Oxalate MM samples calcined at 500 °C for a variety of different times. (a) SEM image of Ox 500 2 h, (b) EDX map showing Fe content of Ox 500 2 h, (c) EDX map showing Mo content of Ox 500 2 h, (d) SEM image of Ox 500 4 h, (e) EDX map showing Fe content of Ox 500 4 h, (f) EDX map showing Mo content of Ox 500 4 h, (g) SEM image of Ox 500 6 h, (h) EDX map showing Fe content of Ox 500 6 h and (i) EDX map showing Mo content of Ox 500 6 h. Highlighted Fe rich (red circles) and Mo rich (yellow squares).

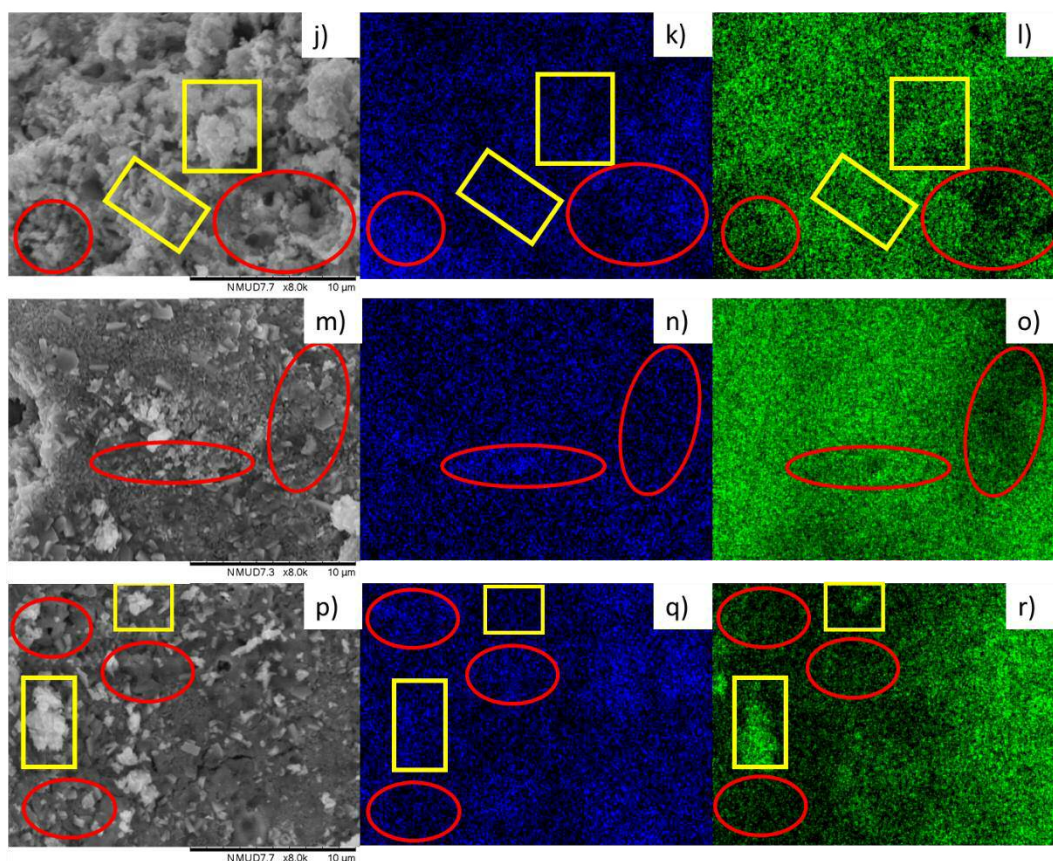


Figure 5.23 SEM and EDX elemental mapping comparison of Oxalate MM samples calcined at 450 °C for a variety of different times. (a) SEM image of Ox 450 2 h, (b) EDX map showing Fe content of Ox 450 2 h, (c) EDX map showing Mo content of Ox 450 2 h, (d) SEM image of Ox 450 4 h, (e) EDX map showing Fe content of Ox 450 4 h, (f) EDX map showing Mo content of Ox 450 4 h, (g) SEM image of Ox 450 6 h, (h) EDX map showing Fe content of Ox 450 6 h and (i) EDX map showing Mo content of Ox 450 6 h. Highlighted Fe rich (red circles) and Mo rich (yellow squares).

Large changes in morphology were observed in microscopy results of Ox 600 samples (Fig. 5.24). The formation of large particles which were observed to be evenly Fe:Mo distributed were seen in Ox 600 2 h sample results. Upon further calcination, agglomeration of these particles was shown to occur forming a layered agglomerated surface.

Areas of both iron and molybdenum enrichment was observed in corresponding EDX results for Ox 600 6 as highlighted but none of these areas were elementally exclusive. Overall, all three samples presented the most homogeneous composition of the Ox samples. The general composition of the surface shown in EDX mapping showed significant increases in molybdenum surface content compared to the previous Oxalate MM samples supporting XPS results.

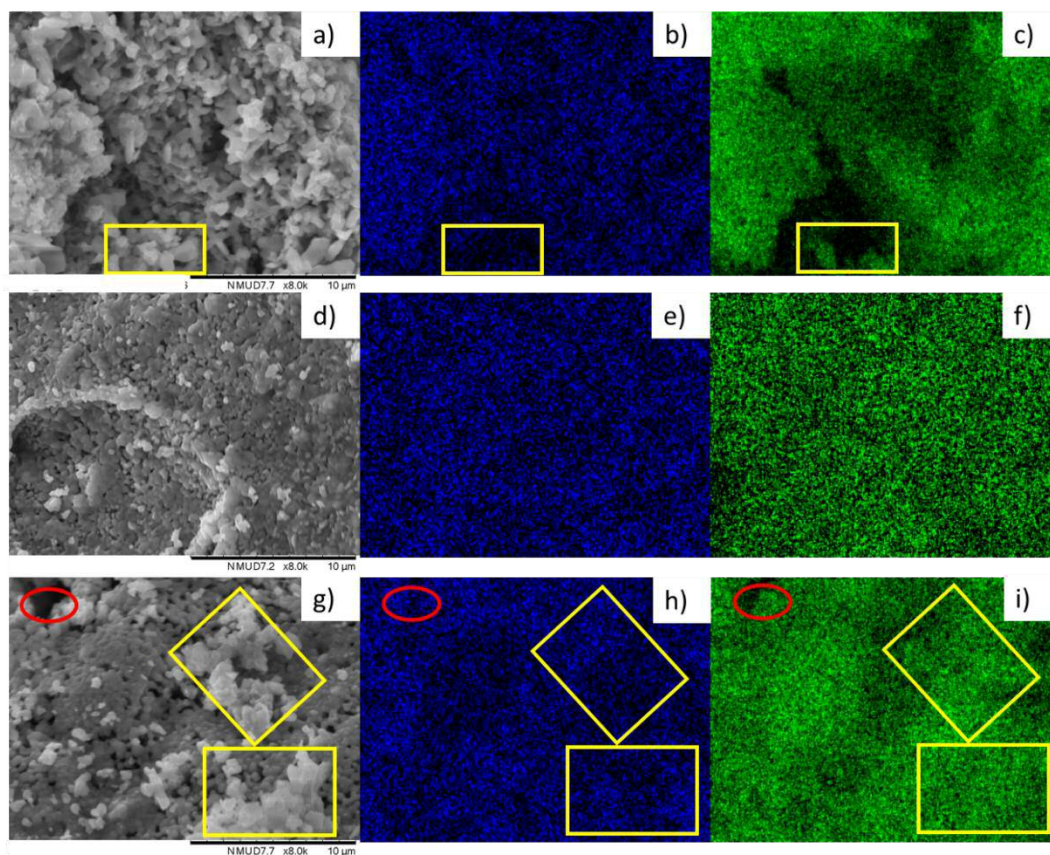


Figure 5.24 SEM and EDX elemental mapping comparison of Oxalate MM samples calcined at 600 °C for a variety of different times. (a) SEM image of Ox 600 2 h, (b) EDX map showing Fe content of Ox 600 2 h, (c) EDX map showing Mo content of Ox 600 2 h, (d) SEM image of Ox 600 4 h, (e) EDX map showing Fe content of Ox 600 4 h, (f) EDX map showing Mo content of Ox 600 4 h, (g) SEM image of Ox 600 6 h, (h) EDX map showing Fe content of Ox 600 6 h and (i) EDX map showing Mo content of Ox 600 6 h. Highlighted Fe rich (red circles) and Mo rich (yellow squares).

5.4.3 Methanol Partial Oxidation

Methanol partial oxidation results shown in Fig 5.25 present significant differences between Oxalate MM samples calcined at different temperatures.

The activity of the catalysts seems to be highly effected by calcination temperature but not by calcination duration. Ox 450 samples presenting the highest activity with all three samples attaining high conversion (>93 %) by 290 °C, similar methanol conversions were attained by Ox 500 samples at 305 °C. Ox 600 samples were the least active with high conversions attained at 320 °C by Ox 600 4 h and at 335 °C Ox 600 2 h and Ox 600 6 h.

Formaldehyde selectivity was shown to vary as calcination temperatures were altered, all samples present over 90 % selectivity at 230 °C. The Ox 450 samples presented with the

lowest formaldehyde selectivity decreasing steadily from 260 °C in favour of CO_x, selectivity increased by 2 % between Ox 450 2 h and Ox 450 6 h samples from 260 °C onwards.

The Ox 500 samples were the next best presenting a 2 % increase in formaldehyde selectivity from Ox 500 2 h (94.2 %) and Ox 500 4 h (93.9 %) and a further 2 % from Ox 500 6 h (95.9 %) at 260 °C. This selectivity was largely maintained at 290 °C before steadily decreasing in favour of CO_x dropping by 4 % by 350 °C.

The Ox 600 4 h sample displayed comparable selectivity to Ox 500 6 h throughout with over 95 % selectivity maintained up to 305 °C before decreasing in favour of CO_x products. The most selective samples were Ox 600 2 h and Ox 600 6 h both attaining over 96 % selectivity which was maintained up until 335 °C where Ox 600 2 h saw a reduction in favour of CO_x. Ox 600 6 h remained highly selective(>96 %) until 380 °C.

Due to these differences in methanol partial oxidation results, substantial changes were observed in maximum formaldehyde yields obtained as summarised in Table 5.11. Ox 450 samples all reached their maximum formaldehyde yields at 290 °C but were all limited to under 84 %. An improvement was observed as calcination temperatures were increased to 500 °C with all samples reaching between 89.4-89.5 % but due to the lower activity these were attained at 320 °C.

Table 5.11 Maximum formaldehyde yield summary of Oxalate MM samples prepared using different calcination conditions.

Sample	Maximum Formaldehyde Yield/ %	Temperature / °C
Ox 500 2 h	89.5	320
Ox 500 4 h	89.4	320
Ox 500 6 h	89.5	320
Ox 450 2 h	81.5	290
Ox 450 4 h	81.6	290
Ox 450 6 h	83.9	290
Ox 600 2 h	91.3	365
Ox 600 4 h	91.6	335
Ox 600 6 h	93.4	365

Ox 600 samples presented the highest formaldehyde yield due to the increased formaldehyde selectivity observed throughout, these higher yields were attained at higher temperatures due to the lower activity of the samples. Unlike the other Ox samples, extended temperatures ranges of over 90 % formaldehyde yield were achieved by Ox 600 2 h (350-380 °C), Ox 600 4 h (320-350 °C) and Ox 600 6 h (335-380 °C) indicating superior stability.

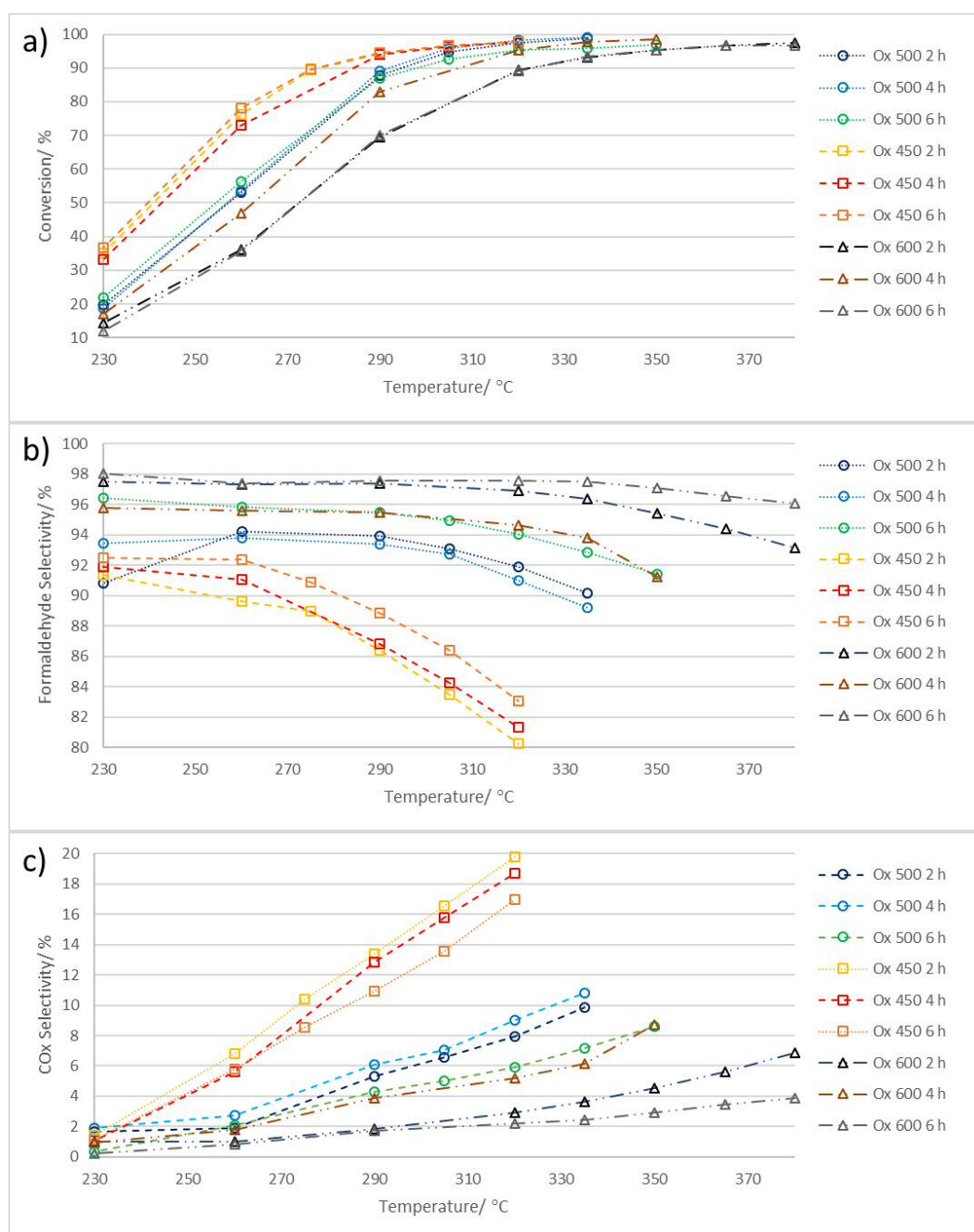


Figure 5.25 Methanol partial oxidation reaction comparisons of Oxalate MM samples prepared using various calcination conditions using various reaction temperatures. (a) Methanol Conversion, (b) Formaldehyde Selectivity and (c) CO_x selectivity).

5.4.4 Discussion of the Effect of Calcination Conditions for MM Using Iron (II) Oxalate

The performance of the iron molybdate samples prepared using MM with iron (II) oxalate were found to be highly sensitive to calcination temperature. The best performance was observed by the Ox 600 samples, all three produced over 91 % formaldehyde yield with the highest production from the Ox 600 6 h catalyst (93.4 %) yield. All three samples also produced high formaldehyde yields (>90 %) over an extended temperature range which indicates an increase in stability of the samples. The Ox 600 samples were however the least active of the Oxalate MM samples with high conversion only attained at temperatures exceeding 320 °C.

Possible reasons for the increased formaldehyde selectivity observed using the 600 °C calcination could be due to the highest $\text{Fe}_2(\text{MoO}_4)_3$ content produced using the higher calcination conditions presented in XRD and Raman spectral mapping. Molybdenum surface content was shown to increase in both XPS and microscopy results with limited iron enrichment observed in any of the Ox 600 samples, limited iron exposure to the surface as stated previously prevents production of CO_x products.^{32,42}

Lower activity of the Ox 600 samples may be due to the decrease in surface area possibly caused by change in morphology from sponge-like structures to large agglomerated particles similar to results shown by Huang *et al.*³⁷ this may also be due to lower exposure of iron towards the surface with both iron enriched surfaces and Fe_2O_3 which have been shown to present higher surface area and activity.^{32,34,42}

The next best calcination temperature for Oxalate MM samples was 500 °C with all three samples presenting 89.5 % formaldehyde yield with no significant change in catalytic performance as calcination duration was changed. Lower formaldehyde yield can be attributed to Fe_2O_3 content observed on the surface of the catalyst in microscopy results. An overall decrease in homogeneity was also observed in Raman spectral mapping and XRD with the formation of larger quantities of MoO_3 which did gradually decrease as calcinations were extended at 500 °C. Higher activity achieved by the Ox 500 samples may be attributed to the increase in surface area of the catalysts which could be due to the sponge-like morphology observed similar to results shown by Soares *et al.*^{11,43} It may also be due to the exposed iron rich regions which have been shown to increase activity of samples but also favour CO_x production.^{32,34,42}

The worst calcination conditions based on catalytic performance was 450 °C with formaldehyde yields varying between 81.5-83.9 % achieved at 290 °C. Formaldehyde selectivity was shown to increase slightly as calcination length was extended but overall changes were minimal. The reduction in formaldehyde selectivity and increase in activity observed may be due to the increase in iron rich and iron exclusive areas over the surface of the sample presented in microscopy results. The lower temperature calcination caused the lowest production of $\text{Fe}_2(\text{MoO}_4)_3$ content as observed in both XRD and Raman spectral mapping.

The variation observed as calcination temperatures were increased were very similar to results obtained by Huang *et al.*³⁷ utilising a physically ground mixture of Fe_2O_3 and MoO_3 . In their study, a combination of both thermal spreading of MoO_3 over the surface of the Fe_2O_3 and the solid-state reaction between Fe_2O_3 and MoO_3 caused an increase in $\text{Fe}_2(\text{MoO}_4)_3$ as calcination temperatures were increased. Similar observations were seen in the Oxalate MM samples, Fe_2O_3 containing areas were shown to decrease in number and frequency as molybdenum surface content was shown to increase in XPS results as calcination temperatures were increased. $\text{Fe}_2(\text{MoO}_4)_3$ content was also shown to increase substantially as calcination temperatures were raised indicating an increase in the rate of the solid-state reaction.³⁸

5.5 Conclusion

The malonate decomposition method has been found to be highly sensitive to changes in iron precursor used for the synthesis of iron molybdate catalysts for formaldehyde production. The use of iron (III) nitrate and Iron (III) chloride was shown to be beneficial with over 93.5 % formaldehyde yield achieved by both samples. This was caused by the superior mixing of the malonate precursors prior to calcination which then produced the most homogeneous iron and molybdenum distribution overall.

The use of iron (II) oxalate and iron (III) acetate precursors caused lower formaldehyde yields to be achieved with the formation of larger quantities of Fe_2O_3 on the surfaces of the catalysts with larger quantities of MoO_3 also present. This is thought to be due to the lack of ligand substitution between the malonate and the other carboxylates. This leaves isolated iron precursors in the molten malonate mixture which produced the Fe_2O_3 upon calcination

with limited migration from the MoO_3 to compensate for these preventing $\text{Fe}_2(\text{MoO}_4)_3$ formation.

The use of iron (III) phosphate and iron (II) sulphate caused lower catalytic performance with both samples presenting the lowest activity of the catalysts produced using malonate decomposition method. This was due to the MoO_3 dominated composition observed in both Phosphate MM and Sulphate MM samples. This was due to the complete lack of ligand substitution during the mixing step observed in both samples with phosphate and sulphate remaining complexed to the iron. Sulphate was removed from the Sulphate MM sample producing Fe_2O_3 during calcination, this caused higher CO_x selectivity observed throughout reactions lowering formaldehyde yields. Phosphate remained even after calcination leaving FePO_4 on the surface which was found to interact with MoO_3 in a synergistic manner promoting high formaldehyde selectivity similar to $\text{MoO}_3/\text{Fe}_2(\text{MoO}_4)_3$ although with far less activity.

Calcination studies conducted on Chloride MM and Oxalate MM samples showed that both were sensitive to calcination conditions. The Chloride MM samples calcined at $500\text{ }^\circ\text{C}$ presented lower formaldehyde selectivity as calcinations were extended as MoO_3 was shown to migrate to the surface forming crystallites leaving Fe_2O_3 exposed. Calcinations at $600\text{ }^\circ\text{C}$ presented similar results but evidence of molybdenum migration over the Fe_2O_3 areas with longer calcination times caused an increase in formaldehyde selectivity. $450\text{ }^\circ\text{C}$ 4 h and 6 h calcinations seemed to be beneficial for Chloride MM samples with the formation of highly active and selective catalysts which presented high stability to changes in reaction temperatures. This was thought to be due to the increase in MoO_3 surface coverage over iron centres preventing exposed Fe_2O_3 .

The Oxalate MM samples showed little effect of calcination duration but significant changes between calcination temperatures. $\text{Fe}_2(\text{MoO}_4)_3$ bulk and molybdenum surface content were shown to increase as calcination temperatures were raised. This caused a decrease in activity as surface area was reduced of the samples but also substantial increases in formaldehyde selectivity.

5.6 References

- (1) Camargo, J. A.; Alonso, Á. *Environ. Int.* **2006**, 32 (6), 831–849.
- (2) WHO/SDE/WSH/03 - nitratenitrite2ndadd.pdf
http://www.who.int/water_sanitation_health/dwq/chemicals/nitratenitrite2ndadd.pdf (accessed Jul 4, 2017).

- (3) Nitrogen Dioxide in the UK - Summary - nd-summary.pdf <https://uk-air.defra.gov.uk/assets/documents/reports/aeqg/nd-summary.pdf> (accessed Jul 6, 2017).
- (4) 139107.pdf <http://groundwaternitrate.ucdavis.edu/files/139107.pdf> (accessed Jul 6, 2017).
- (5) CHEMICAL ACCIDENT INVESTIGATION REPORT - TERRA INDUSTRIES, INC. NITROGEN FERTILIZER FACILITY PORT NEAL, IOWA | US EPA ARCHIVE DOCUMENT - cterra.pdf <https://archive.epa.gov/emergencies/docs/chem/web/pdf/cterra.pdf> (accessed Jul 6, 2017).
- (6) Dias, A. P. S.; Rozanov, V. V.; Waerenborgh, J. C. B.; Portela, M. F. *Appl. Catal. Gen.* **2008**, *345* (2), 185–194.
- (7) Volkovich, V. A.; Griffiths, T. R.; Thied, R. C.; Lewin, B. J. *Nucl. Mater.* **2003**, *323* (1), 93–100.
- (8) Aruanno, J.; Wanke, S. *Can. J. Chem. Eng.* **1975**, *53* (3), 301–307.
- (9) Thavornprasert, K.; Capron, M.; Jalowiecki-Duhamel, L.; Gardoll, O.; Trentesaux, M.; Mamede, A.-S.; Fang, G.; Faye, J.; Touati, N.; Vezin, H.; Dubois, J.-L.; Couturier, J.-L.; Dumeignil, F. *Appl. Catal. B Environ.* **2014**, *145*, 126–135.
- (10) Nikolenko, N. V.; Kozhevnikov, I. V.; Kostyniuk, A. O.; Bayahia, H.; Kalashnykov, Y. V. *J. Saudi Chem. Soc.* **2016**.
- (11) Soares, A. P. V.; Portela, M. F.; Kiennemann, A.; Hilaire, L. *Chem. Eng. Sci.* **2003**, *58* (7), 1315–1322.
- (12) Bersani, D.; Lottici, P. P.; Montenero, A. *J. Raman Spectrosc.* **1999**, *30* (5), 355–360.
- (13) Soares, A. P. V.; Portela, M. F.; Kiennemann, A.; Millet, J. M. M. *React. Kinet. Catal. Lett.* **2002**, *75* (1), 13–20.
- (14) Liu, H. *J. Nanoparticle Res.* **2010**, *12* (6), 2003–2006.
- (15) Gadgil, M. M.; Kulshreshtha, S. K. *J. Solid State Chem.* **1994**, *111* (2), 357–364.
- (16) Sklute, E. C.; Jensen, H. B.; Rogers, A. D.; Reeder, R. J. *J. Geophys. Res. Planets* **2015**, *120* (4), 2014JE004784.
- (17) Zhang, L.; Brow, R. K. *J. Am. Ceram. Soc.* **2011**, *94* (9), 3123–3130.
- (18) Routray, K.; Zhou, W.; Kiely, C. J.; Grünert, W.; Wachs, I. E. *J. Catal.* **2010**, *275* (1), 84–98.
- (19) Qin, G.; McGuire, M. J.; Blute, N. K.; Seidel, C.; Fong, L. *Environ. Sci. Technol.* **2005**, *39* (16), 6321–6327.
- (20) Modéc, B.; Dolenc, D.; Brenčič, J. V. *Inorganica Chim. Acta* **2007**, *360* (2), 663–678.
- (21) Hermanek, M.; Zboril, R.; Mashlan, M.; Machala, L.; Schneeweiss, O. *J. Mater. Chem.* **2006**, *16* (13), 1273–1280.
- (22) Riggs, W. M.; Bricker, C. E. *J. Inorg. Nucl. Chem.* **1971**, *33* (6), 1635–1647.
- (23) Habibi, M. H.; Kiani, N. *J. Therm. Anal. Calorim.* **2013**, *112* (2), 573–577.
- (24) Khachani, M.; El Hamidi, A.; Kacimi, M.; Halim, M.; Arsalane, S. *Thermochim. Acta* **2015**, *610*, 29–36.
- (25) Rao, R. R.; Khopkar, S. M. *Analyst* **1983**, *108* (1284), 346–352.
- (26) House, M. P.; Carley, A. F.; Bowker, M. *J. Catal.* **2007**, *252* (1), 88–96.
- (27) Zhang, H.; Shen, J.; Ge, X. *J. Solid State Chem.* **1995**, *117* (1), 127–135.
- (28) Ai, M. *Appl. Catal. Gen.* **2002**, *234* (1–2), 235–243.
- (29) Ai, M. *Catal. Today* **1999**, *52* (1), 65–69.
- (30) House, M. P.; Shannon, M. D.; Bowker, M. *Catal. Lett.* **2008**, *122* (3–4), 210–213.
- (31) Söderhjelm, E.; House, M. P.; Cruise, N.; Holmberg, J.; Bowker, M.; Bovin, J.-O.; Andersson, A. *Top. Catal.* **2008**, *50* (1–4), 145.
- (32) Bowker, M.; Brookes, C.; Carley, A. F.; House, M. P.; Kosif, M.; Sankar, G.; Wawata, I.; Wells, P. P.; Yaseneva, P. *Phys. Chem. Chem. Phys. PCCP* **2013**, *15* (29), 12056–12067.

- (33) Ai, M. *Catal. Today* **2003**, *85* (2–4), 193–198.
- (34) House, M. P.; Carley, A. F.; Echeverria-Valda, R.; Bowker, M. J. *Phys. Chem. C* **2008**, *112* (11), 4333–4341.
- (35) Xu, Q.; Jia, G.; Zhang, J.; Feng, Z.; Li, C. J. *Phys. Chem. C* **2008**, *112* (25), 9387–9393.
- (36) Dong, L.; Chen, K.; Chen, Y. *J. Solid State Chem.* **1997**, *129* (1), 30–36.
- (37) Huang, Y.; Cong, L.; Yu, J.; Eloy, P.; Ruiz, P. J. *Mol. Catal. Chem.* **2009**, *302* (1), 48–53.
- (38) Kostynyuk, A. O.; Gutenuar, F.; Kalashnikova, A. N.; Kalashnikov, Y. V.; Nikolenko, N. V. *Kinet. Catal.* **2014**, *55* (5), 649–655.
- (39) SEQUEIRA, C. A. C.; AMARAL, L. *Trans. Nonferrous Met. Soc. China* **2014**, *24* (1), 1–11.
- (40) Wang, L.; Peng, B.; Guo, X.; Ding, W.; Chen, Y. *Chem. Commun.* **2009**, No. 12, 1565–1567.
- (41) Shang, M.; Wang, W.; Ren, J.; Sun, S.; Zhang, L. *Nanoscale* **2011**, *3* (4), 1474–1476.
- (42) Bowker, M.; House, M.; Alshehri, A.; Brookes, C.; Gibson, E. K.; Wells, P. P. *Catal. Struct. React.* **2015**, *1* (2), 95–100.
- (43) Vieira Soares, A. P.; Farinha Portela, M.; Kiennemann, A. *Stud. Surf. Sci. Catal.* **1997**, *110*, 807–816.

Chapter 6

Conclusions and Future Work

6.1 Conclusions

The aims of this thesis were to establish the practical applications of molten dicarboxylic acid usage for the production of iron molybdate catalysts for methanol partial oxidation to formaldehyde. It has been established that the oxalate decomposition method (OM) described by Oudghiri-Hassani.¹ The sample produced (1:1.5 OM) was successful in the partial oxidation of methanol to formaldehyde with higher conversions obtained at lower temperature compared to a sample prepared using a more traditional coprecipitation methods. However the selectivity of the oxalate sample was significantly lower due to exposed Fe_2O_3 caused by non-homogeneous mixing of the iron and molybdenum.

Changes in Fe:Mo ratios on the composition of samples prepared using OM found significant differences as molybdenum content was changed. The best formaldehyde yields were achieved using 1:2.2 (92.6 %) and 1:1.7 (91.2 %) ratios with both surpassing the coprecipitated comparison example(90.0 %). This was due to a highly homogeneous composition thought to be due to the superior mixing of the oxalate produced prior to calcination suggested in a precalcination study. The use of 1:1.9 and 1:3.0 ratios caused lower formaldehyde yields due to the production of Fe_2O_3 and MoO_3 in larger quantities caused by the production of more isolated molybdenum oxalate. The use of 1:1.5 Fe:Mo ratio caused significant loss in formaldehyde selectivity due to areas of Fe_2O_3 exposed to the surface. This was thought to be caused by the inadequate mixing of the oxalates prior to calcination causing larger quantities of isolated iron oxalate decompositions to form Fe_2O_3 upon calcination.

Small water addition into the oxalate mixtures(1.25-2.5 ml per gram of oxalate mixture) was found to have a negative influence on composition with significantly lower $\text{Fe}_2(\text{MoO}_4)_3$ production thought to be due to the formation of larger quantities of isolated iron oxalate. This produced a large Fe_2O_3 content which caused the decrease in formaldehyde yield producing CO_x products throughout. Further water additions (3.75-6.25 ml per gram of oxalate mixture) lowered the amount of iron oxalate observed in the uncalcined mixtures. This may be due to the direct precipitation of $\text{Fe}_2(\text{MoO}_4)_3$ from solution. The results of this was highly dispersed iron and molybdenum in the calcined catalyst suggested by very high

$\text{Fe}_2(\text{MoO}_4)_3$ content observed in XRD and Raman spectral mapping. This caused an increase in formaldehyde selectivity observed by both samples although not surpassing samples prepared using no water addition.

Iron molybdate catalysts produced using malonate decomposition method (MM) have been found to outperform those produced by coprecipitation and OM with very high formaldehyde yields (93.9 %) attained. Unlike samples prepared using the other methods, MM catalyst produced high formaldehyde yields (>93 %) over extended temperature ranges indicating high stability of the catalyst. This was thought to be due to the superior distribution of the iron and molybdenum in the catalyst which prevented the formation of Fe_2O_3 exposed to the surface.

The malonate decomposition method was found to be more robust to changes in Fe:Mo ratio with only 1:1.7 producing formaldehyde yields under 92.6 %. This was due to the lower exposure of iron exclusive and iron rich areas towards the surface. This was thought to be due to the better mixing of the malonates precursors prior to calcination compared to the oxalate examples.

Calcination study of the 1:2.2 MM samples produced indicated that the samples were highly sensitive to changes in calcination conditions. The best conditions were found to be 500 °C 2h, 450 °C 4 h and 600 °C 4 h of those tested all of which attained over 93 % formaldehyde yield. Lower temperature, shorter calcinations caused less $\text{Fe}_2(\text{MoO}_4)_3$ production by the solid-state reaction between Fe_2O_3 and MoO_3 .² Extended calcination seemed to cause the production of large quantities of crystalline MoO_3 possibly from the migration from the bulk. Higher temperature calcination were suggested to cause sublimation of MoO_3 from the surface which caused lower formaldehyde selectivities as calcination were extended. Further investigation into the mobility of the molybdena species needs to be undertaken to ascertain what impact these changes may have on extended reactivity.

Changing of iron precursor used was investigated using MM. Substantial changes were observed in composition and reactivity of the samples as the precursors were altered. Both iron (III) nitrate and iron (III) chloride produced high amounts of $\text{Fe}_2(\text{MoO}_4)_3$ in the calcined samples which allowed for very high formaldehyde yields. Iron (II) oxalate was next best producing similar yields observed in OM examples. Iron (III) phosphate produced a combination of both FePO_4 and MoO_3 with little $\text{Fe}_2(\text{MoO}_4)_3$ production in the calcined samples, the effects of this was a highly selective but very low activity catalyst with the

reactive species shown to be crystalline MoO_3 . Low $\text{Fe}_2(\text{MoO}_4)_3$ content was also observed in samples produced using iron (III) acetate and iron (II) sulphate, both of which had large Fe_2O_3 and MoO_3 content which was exposed to the surface causing significant increases in CO_x selectivity. The lack of $\text{Fe}_2(\text{MoO}_4)_3$ production was thought to be due to the lack of ligand substitution during the mixing step between the iron precursors and the malonate for acetate, sulphate, phosphate and to a lesser extent oxalate. Both the chloride and nitrate were found substitute forming relatively large quantities of iron malonate prior to calcination.

A calcination study of the samples prepared using chloride found significant similarities with the 1:2.2 MM study with MoO_3 crystallite formation observed as calcination lengths were extended at temperatures exceeding $500\text{ }^\circ\text{C}$. This lead to areas of Fe_2O_3 exposed to the surface leading to lower formaldehyde yields. Lower temperature calcinations cause a gradual covering of iron rich areas as calcinations were extended increasing formaldehyde selectivity at lower temperatures.

The effect of changes in calcination conditions on the composition of MM samples produced using iron (II) oxalate were found to benefit with the use of higher temperature calcination as greater $\text{Fe}_2(\text{MoO}_4)_3$ content was produced. This allowed for higher formaldehyde yields to be achieved using the higher calcination temperature ($600\text{ }^\circ\text{C}$). Changes in calcination duration showed little effect on the overall performance of the samples.

6.2 Future Work

Work on these method is far from exhausted due to the versatility that the malonate decomposition method has presented. The highly mobile molybdena species observed using MM need to be investigated to ascertain whether it is beneficial for catalyst life time like those produced by Soares *et al.*³ through extended time on line analysis.

Better understanding of the species produced and lost during the calcination steps through in-situ studies may be highly advantageous to better understand why the distribution was so much better for the malonate samples over the oxalate.

Addition of dopants into the dicarboxylate mixtures to ascertain the whether they can be evenly distributed like the iron and molybdenum. This would be especially useful in possibly forming FeVMoO_x catalysts like those used as the current industrial standard

catalyst.⁴ But other additions such as bismuth may also be useful in the formation of multiple phase catalysts.

Testing of these approaches for other mixed metal oxide systems with the intention to develop new methods to produce well dispersed mixed metal oxides without the use of water. Many have already been tested with the use of citrate preparation methods^{5,6} but due to the controllability of these methods over citrates, they may be more suitable.

The use of longer chain diacids such as succinic may be advantageous with the substantial improvements observed using malonic vs oxalic which may be due to the chain length of the acid. Whether this has substantial effect is currently unknown.

6.3 References

- (1) Oudghiri-Hassani, H. *Catal. Commun.* **2015**, *60*, 19–22.
- (2) Kostynyuk, A. O.; Gutenuar, F.; Kalashnikova, A. N.; Kalashnikov, Y. V.; Nikolenko, N. V. *Kinet. Catal.* **2014**, *55* (5), 649–655.
- (3) Soares, A. P. V.; Portela, M. F.; Kiennemann, A.; Hilaire, L. *Chem. Eng. Sci.* **2003**, *58* (7), 1315–1322.
- (4) Andersson, A.; Holmberg, J.; Häggblad, R. *Top. Catal.* **2016**, *59* (17–18), 1589–1599.
- (5) Fuentes, R. O.; Baker, R. T. J. *J. Phys. Chem. C* **2009**, *113* (3), 914–924.
- (6) Khazaei, M.; Malekzadeh, A.; Amini, F.; Mortazavi, Y.; Khodadadi, A. *Cryst. Res. Technol.* **2010**, *45* (10), 1064–1068.